Smart Interactive Vessel Visualization in Radiology

DISSERTATION

zur Erlangung des akademischen Grades

Doktor der technischen Wissenschaften

eingereicht von

Dipl.-Ing. Gabriel Mistelbauer

Matrikelnummer 0326641

an der
Fakultät für Informatik der Technischen Universität Wien

Betreuung: Ao.Univ.Prof. Dipl.-Ing. Dr.techn. Eduard Gröller

Diese Dissertation haben begutachtet:

(Ao.Univ.Prof. Dipl.-Ing. Dr.techn. Eduard Gröller)	(Univ.Doz. Dipl.-Ing. Dr.techn. Miloš Šrámek)

Wien, 08.10.2013

(Dipl.-Ing. Gabriel Mistelbauer)

Smart Interactive Vessel Visualization in Radiology

DISSERTATION

submitted in partial fulfillment of the requirements for the degree of

Doktor der technischen Wissenschaften

by

Dipl.-Ing. Gabriel Mistelbauer

Registration Number 0326641

to the Faculty of Informatics
at the Vienna University of Technology

Advisor: Ao.Univ.Prof. Dipl.-Ing. Dr.techn. Eduard Gröller

The dissertation has been reviewed by:

_____
(Ao.Univ.Prof. Dipl.-Ing.
Dr.techn. Eduard Gröller)

_____
(Univ.Doz. Dipl.-Ing. Dr.techn.
Miloš Šrámek)

Wien, 08.10.2013

_____
(Dipl.-Ing. Gabriel Mistelbauer)

Erklärung zur Verfassung der Arbeit

Dipl.-Ing. Gabriel Mistelbauer
Löblichgasse 9/10, 1090 Wien

Hiermit erkläre ich, dass ich diese Arbeit selbständig verfasst habe, dass ich die verwendeten Quellen und Hilfsmittel vollständig angegeben habe und dass ich die Stellen der Arbeit - einschließlich Tabellen, Karten und Abbildungen -, die anderen Werken oder dem Internet im Wortlaut oder dem Sinn nach entnommen sind, auf jeden Fall unter Angabe der Quelle als Entlehnung kenntlich gemacht habe.

_____	_____
(Ort, Datum)	(Unterschrift Verfasser)

Acknowledgements

Abstract

Cardiovascular diseases occur with increasing frequency in our society. Their diagnosis often requires tailored visualization techniques, e.g., to examine the blood flow channel in case of luminal narrowing. Curved Planar Reformation (CPR) addresses this field by creating longitudinal sections along the centerline of blood vessels. With the possibility to rotate around an axis, the entire vessel can be assessed for possible vascular abnormalities (e.g., calcifications on the vessel wall, stenoses, and occlusions).

In this thesis, we present a visualization technique, called Centerline Reformation (CR), that offers the possibility to investigate the interior of any blood vessel, regardless of its spatial orientation. Starting from the projected vessel centerlines, the lumen of any vessel is generated by employing wavefront propagation in image space. The vessel lumen can be optionally delineated by halos, to enhance spatial relationships when examining a dense vasculature. We present our method in a focus+context setup, by rendering a different kind of visualization around the lumen. We explain how to resolve correct visibility of multiple overlapping vessels in image space. Additionally, our visualization method allows the examination of a complex vasculature by means of interactive vessel filtering and subsequent visual querying.

We propose an improved version of the Centerline Reformation (CR) technique, by generating a completely three-dimensional reformation of vascular structures using ray casting. We call this process Curved Surface Reformation (CSR). In this method, the cut surface is smoothly extended into the surrounding tissue of the blood vessels. Moreover, automatically generated cutaways reveal as much of the vessel lumen as possible, while still retaining correct visibility. This technique offers unrestricted navigation within the inspected vasculature and allows diagnosis of any tubular structure, regardless of its spatial orientation.

The growing amount of data requires increasing knowledge from a user in order to select the appropriate visualization method for their analysis. In this thesis, we present an approach that externalizes the knowledge of domain experts in a human readable form and employs an inference system to provide only suitable visualization techniques for clinical diagnosis, namely Smart Super Views. We discuss the visual representation of such automatically suggested visualizations by encoding the respective relevance into shape and size of their view. By providing a smart spatial arrangement and integration, the image becomes the menu itself. Such a system offers a guided medical diagnosis by domain experts.

After presenting the approach in a general setting, we describe an application scenario for diagnostic vascular visualization techniques. Since vascular structures usually consist of many vessels, we describe an anatomical layout for the investigation of the peripheral vasculature of the human lower extremities. By aggregating the volumetric information around the vessel

centerlines in a circular fashion, we provide only a single static image for the assessment of the vessels. We call this method Curvicircular Feature Aggregation (CFA). In addition, we describe a stability analysis on the local deviations of the centerlines of vessels to determine potentially imprecise definitions. By conveying this information in the visualization, a fast visual analysis of the centerline stability is feasible.

Kurzfassung

Kardiovaskuläre Krankheiten treten immer häufiger in unserer Gesellschaft auf. Zu deren Diagnose werden spezielle Darstellungsmethoden benötigt, um z.B. den Blutfluss im Falle von luminalen Verschlüssen zu untersuchen. Ermöglicht wird dies unter anderem durch die Technik der Curved Planar Reformation (CPR), welche longitudinale Schnitte entlang der Mittellinie von Blutgefäßen erzeugt. Durch die Möglichkeit, um eine Achse zu rotieren, kann das gesamte Gefäß auf eventuell vorhandene vaskuläre Abnormitäten untersucht werden (z.B. Verkalkungen an den Gefäßwänden, Stenosen und Verschlüsse).

Wir präsentieren in dieser Arbeit eine Visualisierungstechnik namens Centerline Reformation (CR), welche es erlaubt, das Innere von Blutgefäßen zu untersuchen, unabhängig von ihrer räumlichen Orientierung. Ausgehend von den projizierten Mittellinien der Gefäße kann das Lumen jeder Ader durch Wellenausbreitung in der Bildebene erzeugt werden. Um die räumlichen Distanzen in dichten Gefäßsystemen besser anzuzeigen, kann das Gefäßlumen optional durch ein Halo abgegrenzt werden. Unsere Methode folgt dem Prinzip von Fokus und Kontext durch Anwendung verschiedener Darstellungsmethoden rund um das Lumen. Wir erläutern, wie die korrekte Sichtbarkeit von mehreren sich überdeckenden Gefäßen in der Bildebene gewährleistet werden kann. Darüber hinaus ermöglicht unsere Visualisierungstechnik die Untersuchung eines komplexen Gefäßsystems mittels interaktivem Auswählen von Gefäßen und nachfolgenden visuellen Abfragen.

Eine verbesserte Version der Centerline Reformation (CR), welche ebenfalls in dieser Arbeit präsentiert wird, ermöglicht eine vollständige dreidimensionale Reformation von Gefäßstrukturen mit Hilfe des Sehstrahlverfahrens. Wir bezeichnen diesen Prozess als Curved Surface Reformation (CSR). Bei dieser Methode breitet sich die Schnittfläche nahtlos bis in das umliegende Gewebe der Blutgefäße aus. Zusätzlich legen automatisch generierte Ausschnitte so viel wie möglich des Gefäßlumens frei, immer unter Gewährleistung der korrekten Sichtbarkeit. Diese Technik ermöglicht eine uneingeschränkte Navigation innerhalb des zu inspizierenden Gefäßsystems und erlaubt die Diagnose von allen tubulären Strukturen, unabhängig von deren räumlicher Orientierung.

Mit der immer größer werdenden Datenmenge wird von Seiten der Benutzer mehr Fachwissen benötigt, um die jeweils passende Darstellungsmethode für die Analyse der vorliegenden Daten auszuwählen. Wir präsentieren in dieser Arbeit einen Ansatz, der Expertenwissen in eine für Menschen einfach lesbare Form auslagert, und ein Inferenzsystem, das automatisch die für die jeweilige klinische Diagnose passende Darstellungsmethode bereitstellt. Die vorgestellte Methode trägt den Namen Smart Super Views. Die Ansichten der automatisch vorgeschlagenen Darstellungen werden aufgrund ihrer Relevanz, durch Anpassung ihrer Form und Größe, un-

terschiedlich kodiert. Mit Hilfe einer intelligenten räumlichen Anordnung und Integration wird das Bild selbst zum Bildschirmmenü. Ein solches System bietet eine von Experten angeleitete medizinische Diagnose.

Der vorgestellte Ansatz wird zuerst allgemein präsentiert, und dann durch Beschreibung eines konkreten Anwendungsfalles für die diagnostische Darstellung von Gefäßen untermauert. Vaskuläre Strukturen bestehen üblicherweise aus einer Vielzahl von Gefäßen. Um diesem Umstand gerecht zu werden, beschreiben wir eine anatomische Anordnung zur Untersuchung des Gefäßsystems der menschlichen unteren Gliedmaßen. Durch kreisförmige Aggregation der räumlichen Information um die Mittellinien der Gefäße stellen wir ein einzelnes Bild für deren Untersuchung zur Verfügung. Wir nennen diese Technik Curvicircular Feature Aggregation (CFA). Weiters wird eine Stabilitätsanalyse über lokale Abweichungen der Mittellinien von Gefäßen erörtert, welche es ermöglicht eventuelle ungenaue Definitionen zu lokalisieren. Durch die Präsentation dieser Information in der Darstellung ist eine schnelle visuelle Erfassung der Stabilität der Mittellinie realisierbar.

Contents

List of Figures

List of Tables

List of Abbreviations

AVG	Average Intensity Projection
CFA	Curvicircular Feature Aggregation
CFD	Computational Fluid Dynamics
CPR	Curved Planar Reformation
CR	Centerline Reformation
CSR	Curved Surface Reformation
CT	Computed Tomography
CTA	Computed Tomography Angiography
DICOM	Digital Imaging and Communications in Medicine
DSA	Digital Subtraction Angiography
DVR	Direct Volume Rendering
FIS	Fuzzy Inference System
FMM	Fast Marching Method
FWHM	full width at half maximum
HU	Hounsfield Units
HUD	Head-up Display
HT	Hysteresis Thresholding
LOD	Level of Detail
MIDA	Maximum Intensity Difference Accumulation
MinIP	Minimum Intensity Projection
MIP	Maximum Intensity Projection
MRI	Magnetic Resonance Imaging
MRA	Magnetic Resonance Angiography
mpCPR	Multipath Curved Planar Reformation
PACS	Picture Archiving and Communication System
ROI	Region-of-Interest

CHAPTER **1** ■

Introduction and Overview

IMPROVEMENTS in medical imaging advance along with the development of modern computer systems. However, before dealing with current and future technologies, we should first take a look at the past. Starting with historical aspects of medical imaging acquisition, X-rays are one of the most important discoveries of modern medical imaging. Moving on to the area of angiography, we give a short outline of its historical highlights and describe its acquisition protocol. We then advance to tomographic modalities, as most of the contributions of this thesis are based on them. Since we examine very specific medical aspects, we provide an introduction to the medical domain. Outlining not only vascular diseases and their diagnosis and treatment, we give a high-level description of the medical basics and a comprehensive overview of vessel visualization techniques. We describe our software framework, developed in cooperation with our medical partners and give a short outline, how this fits into the working process of the daily clinical routine. As final remarks of this chapter, we briefly summarize the structure and scope of this thesis.

1.1 Medical Data Acquisition Foundations

Computerized medical imaging would not be possible without data. Therefore, we give a short historical outline of the most prominent discoveries of medical data acquisition. We focus on the ones used throughout this thesis and give only a brief description of possible alternatives.

1.1.1 History of X-Rays

In 1895 the German physicist Wilhelm Conrad Röntgen (1845-1923)[1] was studying the aspects accompanying the passage of electric current through gas of extremely low pressure inside a Crookes tube. This was a highly popular and active research area in those days. Röntgen discovered that invisible rays were emitted from the discharged tube, when placing a paper plate,

---

[1] Nobel Prize in Physics 1901

Figure 1.1: An X-ray image of a human forearm. (Image courtesy of RÜDIGER SCHERN-THANER, Medical University of Vienna, Austria)

coated with barium platinocyanide, in the path of the rays. He called these rays X-rays, the X because of the unknown type of radiation. To avoid any light from interfering with the discharged tube, it was placed in a sealed carton. Röntgen observed that invisible rays were passing through the box, rendering the plate fluorescent in a darkened room. The only factor influencing the illuminance is the thickness of possible objects between the tube and the plate. Röntgen took the first radiograph ever of his wife's hand. Soon after, he submitted his first manuscript "on a new kind of rays" to the journal of the Würzburg's Physical-Medical Society [128]. Interestingly, even twenty years after Röntgen's discovery, it was still doubtful, whether the manuscript was about waves or particles [52]. In fact, this type of radiation exhibits both properties (wave-particle duality). An X-ray image of a human forearm is shown in Figure 1.1 as an example.

1.1.2 Angiography

Angiography[2] describes a medical imaging technique of blood vessels in the human body. In 1896, shortly after the discovery of the X-rays, Haschek and Lindenthal [51] created the first angiogram of an amputated hand at the physical institute of Vienna. Since the attenuation of the blood vessels did not differ significantly from the surrounding tissue, a Teichmann's solution, a mixture of chalk, red mercury and petroleum, was injected into the arterial system. Röntgen observed that salts in liquids cause attenuation of X-rays according to their permeability [128]. To enhance blood vessels in vivo, the administered solution, called *contrast agent* or *contrast medium*, must be applicable to the human being without harm and has to attenuate radiation. In 1923, the first in vivo angiography on a human being, demonstrating the arterial blood supply of the thumb, was performed by Berberich and Hirsch [7]. Later in 1924, Brooks [13] was first able to create radiographic imaging of blood vessels.

X-rays can only distinguish between various types of tissue in case they exhibit natural contrast. A clear delineation of two different types of tissue can be observed in the radiograph, if their densities differ considerably, or if their atomic numbers are different. For example, soft tissue consists of elements with a low atomic number and bone partly of calcium, having a sig-

---

[2]Angiography stems from the Greek words *aggeion*, meaning "vessel" or "bucket", and *graphein*, meaning "to write" or "to record". The image of blood vessels is called *angiograph* or *angiogram*.

nificantly higher atomic number. To distinguish blood vessels from their surrounding tissue, a liquid medium has to be injected into the patient's arterial system to opacify the vessels. Such a liquid should have a significantly higher atomic number than blood (e.g., iodine) to increase the atomic number of vessels, rendering them distinguishable in the radiograph. There are two categories of contrast agents: ionic and nonionic ones. Although the former have been developed and clinically applied first, the latter are less harmful and presently used in the clinical routine [71]. The process of making vessels distinguishable by contrast agents is referred to as *vessel enhancement* or *vessel opacification*.

Subtraction Angiography. Studies on cadavers considerably improved the knowledge of the anatomy of the human vasculature. In order to allow feasible in vivo angiography for diagnosis and intervention, development of relatively safe contrast agents and advance in radiological equipment are necessary. A significant improvement over conventional angiography was introduced by *photographic subtraction*. This technique makes the visibility of contrast enhanced vessels possible by masking out undesired background structures. A native X-ray image, acquired before the administration of the contrast agent, is subtracted by photographic means from a series of subsequent images. Meanwhile, the contrast agent continuously flows through the arterial system of the patient [115]. As the native image acts as a mask for background structures, its common term is *mask image* and the other images are called *live images*. Another significant advance in angiography was the introduction of the catheter technology. It allows the injection of contrast agents farther away from the location of the punctuation through the insertion of a catheter.

Digital Subtraction Angiography. The advance of digital computer systems introduced the era of Digital Subtraction Angiography (DSA) [81]. It requires the injection of a contrast agent into the arterial system of a patient in order to opacify the vessels of interest. It is an invasive procedure due to the punctuation of the artery and the intra-arterial application of the contrast agent. Advantages of DSA are images with high spatial and temporal resolution and objects obstructing the vessels of interest are removed due to the subtraction operation [135]. This procedure is considered the *gold standard* for vascular imaging. Nevertheless, it exhibits a certain risk for patients, since DSA is an invasive procedure due to the administration of the contrast agent by means of a catheter. Possible motion artifacts caused by movement of the patient during the acquisition period can be corrected in post-processing operations [100]. Figure 1.2 presents a continuous series of images acquired with DSA. It is clearly visible when the contrast agent is passing through the captured vessels. Since DSA produces only luminograms, information about the components of plaque and the surrounding tissue of vessels cannot be provided [117].

1.1.3 Computed Tomography

In 1917, the Austrian mathematician Johann Radon (1887-1956) proved that any function in $\mathbb{R}^2$ is well defined by all line integrals of the function itself. Despite being a purely theoretical approach, it provided the mathematical basis for further development in the direction of Computed Tomography (CT). More specifically, the process of reconstructing spatial information
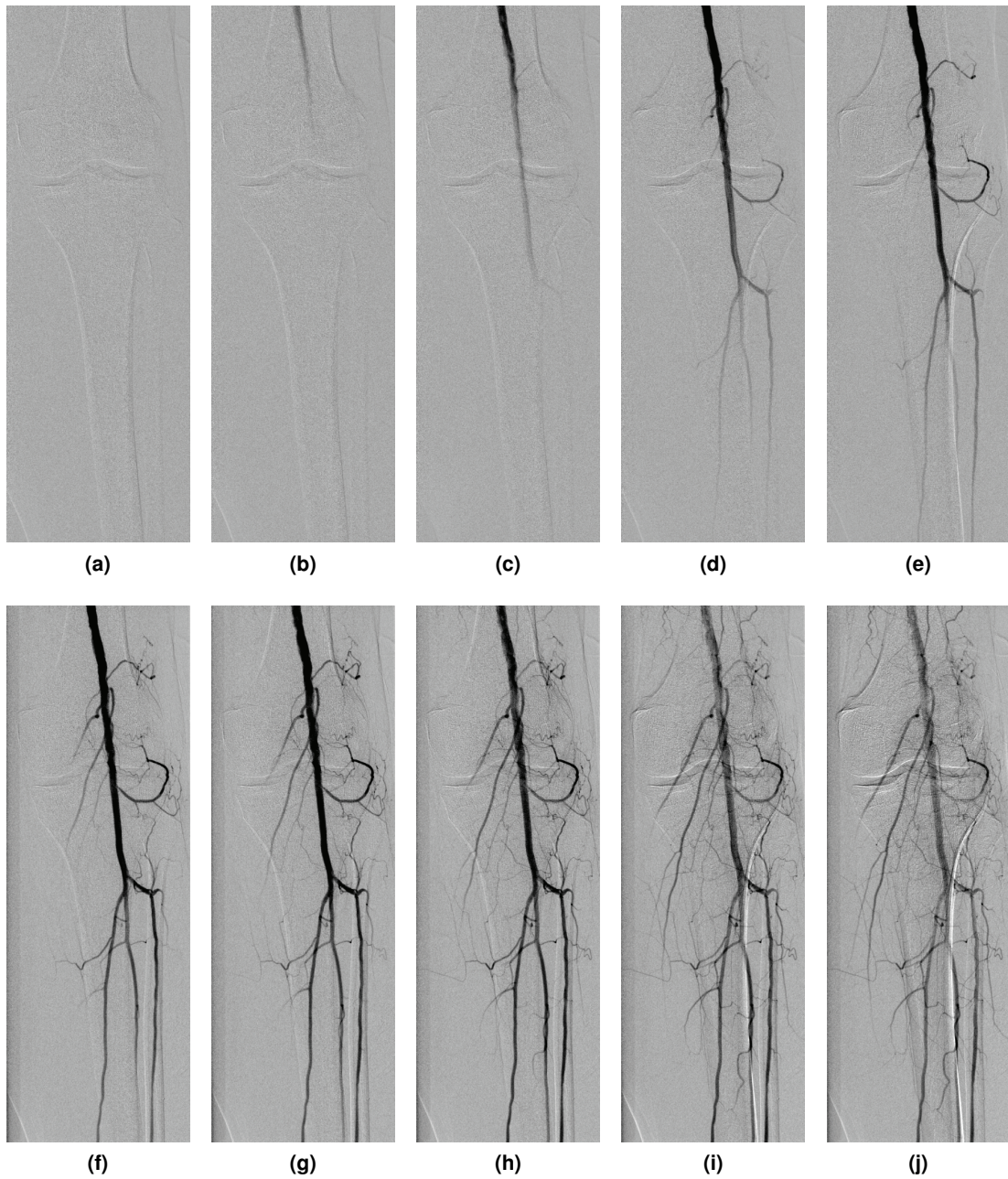
Figure 1.2: A series of DSA live images (or frames) showing the flow of the contrast agent through the vessels of the human left knee region. **(a)**-**(g)** show the inflow of the contrast agent, whereas in **(h)**-**(j)** it is reaching the capillary vessels and flowing out of the captured region. The bony shades are caused by the movement of the patient during acquisition. (Images courtesy of RÜDIGER SCHERNTHANER, Medical University of Vienna, Austria)

from a series of projections is called *Radon transform* [104]. Almost half a century later, Allan Cormack (1924-1998) made initial experiments with X-ray absorption on phantom data sets made of materials like wood or aluminum. In 1963, he published his work on the absorption distribution of radiation in the human body on transmission measurements. Godfrey Hounsfield (1919-2004) successfully built a prototype of a Computed Tomography (CT)[3] device in 1968. In 1972, the first clinical prototype was created and the first patient was scanned. This led to an advance in medical imaging as well as steady improvements of image quality and acquisition time. In 1979, both, Cormack and Hounsfield, shared the Nobel Prize in Physiology or Medicine for their contributions. In the late 1980s, the helical CT modality was developed, allowing the continuous movement of the patient through the gantry of the scanning device, in contrast to a fixed relation to the X-ray source as in previous devices. The acquired data now consists of spiral or helical cuts through the patient and the true sections are obtained during the reconstruction process by interpolation along the direction of the table movement. This facilitated the reconstruction of images at arbitrary positions within the patient and provided a higher data resolution. In practice, samples are reconstructed at discrete positions of a regular grid. This offers the possibility to inspect the interior of a specimen in a non-destructive way. Another improvement was the multi-slice CT, where multiple row detectors allow the acquisition of interleaved helical sections. This results in increased image resolution and reduced scanning time.

The basic principle of CT is the measurement of X-ray attenuation through materials with different attenuation coefficients. The most notable attenuation effects are the photo-effect and scattering (Compton effect). As the speed of the electrons depends on the strength of their surrounding electric field, X-rays generated with more than 100 kV are called *hard beam X-rays*, otherwise they are called *soft beam X-rays* [115]. If using hard beam X-rays, scattering is most dominant and the rays are only absorbed in very dense materials. Hence, this can be used for capturing bony structures, whereas soft tissue can be represented mostly by soft beam X-rays. Since most of the intensity of X-rays is absorbed in the soft tissue, soft beam X-rays are more harmful and beam hardening artifacts more distinct [104]. When traversing an X-ray through a material, it is attenuated according to the attenuation coefficient μ at every spatial point along the ray. The total attenuation I of a ray with length d is defined as:

$$I = I_0 \cdot e^{-\int_{0}^{d} \mu \cdot ds},$$ (1.1)

where I_0 is the initial intensity of the X-ray, dropping exponentially to zero. However, the attenuation coefficient $\mu(x, y)$ is unknown at any specific spatial position (x, y). According to Radon's theorem, the distribution of $\mu(x, y)$ is well defined by an infinite number of line integrals of $\mu(x, y)$. Although the total attenuation I is represented as an integral of $\mu(x, y)$, only a finite number of measurements are acquired while rotating the gantry of the scanner around the scanned object. The obtained reconstruction is therefore an approximation of the object represented by the values of $\mu(x, y)$.

---

[3]The term *tomography* stems from the Greek word *tome*, meaning "a cutting, section", and *graphein*, meaning "to write" or "to record"

Scanning Parameters. The volumetric data sets acquired by CT scanners exhibit a certain resolution, described by the *number of slices*, the *image matrix* (i.e., pixels per slice) and the *voxel distances*. The usual image matrix of current CT scanners is 512×512, whereas recently 1024×1024 are showing up. The distances between voxels are divided into the *pixel distance* and the *inter-slice distance*. The former specifies the distance of consecutive pixels within one slice, whereas the latter defines the distance between subsequent slices. If all distances are the same, the volumetric data set is isotropic, otherwise, and more commonly, it is anisotropic. Usually, the inter-slice distance is larger than the pixel distance. Another important scanning parameter is the *slice collimation* (or *slice thickness*). If it is larger than the inter-slice distance, an overlap of data is acquired during scanning. This has to be taken into consideration during volumetric data reconstruction. The rotating emitter/detector part of a CT scanner through which the patient table is moved is called *gantry*. Other important scanning parameters are the *tube voltage* (usually 80-140 kV), the *amperage* (150-350 mA), and the *gantry rotation speed* (i.e., the time for a complete $360°$ rotation of the gantry). The translation of the table per $360°$ gantry rotation is referred to as *table increment*. The *pitch p* of the CT scanner is defined as $p = d/(M \cdot S)$, where d is the table increment, M is the number of acquired slices per rotation (one for a normal multi-slice helical CT scanner and four for a four-slice multi-slice helical CT scanner) and S is the slice thickness [115]. Configurations of these parameters are summarized and stored in a *scanning protocol*. With the development of multi-slice helical CT scanners, precise three-dimensional medical imaging of the peripheral arteries of the human lower extremities is possible within 40 seconds [135].

Hounsfield Units. Since the measured physical quantity μ depends on the used spectral energy, it is difficult to compare images from different CT scanners. Therefore, the computed intensity values of the scanned objects are normalized into Hounsfield Units (HU)[4], relative to the attenuation coefficient of water. This normalization maps the data range to 12 bits, with the intensity of water being zero and air being –1000 (cf. Table 1.1). To simplify volumetric data access, these values are usually packed into 16 bits (2 bytes), although the dynamic range of their intensity values covers only 12 bits. The intensity I_T of a tissue T with attenuation coefficient μ_T is computed by the following equation [65]:

$$I_T = \frac{\mu_T - \mu_{water}}{\mu_{water}} \cdot 1000 \text{ HU}. \tag{1.2}$$

Due to the normalization, standardized data ranges can be defined for several types of tissue or organs (cf. Table 1.1 for the most common ones). Since different organs or types of tissue exhibit overlapping or similar intensity values, they are not distinctly separable by simple thresholding. This is one of the reasons why segmentation in medicine is a difficult and challenging task.

---

[4]Named after Godfrey Hounsfield

Table 1.1: Several types of tissue and their corresponding data range in HU [115, 145].

Tissue Type	HU
Air	−1000
Lung tissue	−900…−170
Fat tissue	−220…−30
Water	0
Pancreas	10…40
Liver	20…60
Heart	20…50
Kidney	30…50
Blood	40…100
Enhanced blood	150…500
Soft plaque	0…200
Calcified plaque	500…1000
Bones	45…3000
Metal	>3000

Windowing Function. In order to display the 12 bit intensity values on the screen, they need to be mapped to 8 bits, i.e., 256 gray levels. To minimize the necessary interaction, simple windowing is applied. This technique is characterized by two parameters, the window center C and the window width W, which can be compared to changing contrast and brightness of an image. The data range of these two values is 12 bits (i.e., between zero and 4095). For an intensity value I the corresponding grayscale value G is defined by the following linear transformation:

$$G = \begin{cases} 0 & \text{if } I \leq C - W/2 \\ \frac{I-C-W/2}{W} & \text{if } I > C - W/2 \wedge I \leq C + W/2 \\ 1 & \text{if } I > C + W/2 \end{cases} \tag{1.3}$$

A common interaction is sliding this window through the intensity domain, by, e.g., horizontal mouse movement changing the center and vertical movement changing the width. Figure 1.3 shows the same axial slice with two different windowing functions.

1.1.4 Computed Tomography Angiography

In addition to the scanning parameters of CT, Computed Tomography Angiography (CTA) requires the specification of the injection flow rate [mL/s] and injection duration [s] of the contrast agent. Peripheral CTA data are acquired by moving the patient through the gantry of the scanner, while simultaneously and continuously administering the contrast agent into the venous system, e.g., through the arm of the patient, to enhance the arterial system. Although DSA is considered the gold standard for vascular imaging, several studies have shown that CTA provides almost equally accurate diagnoses and treatment decisions for peripheral arterial occlusive diseases, while being less invasive [134, 135, 136].
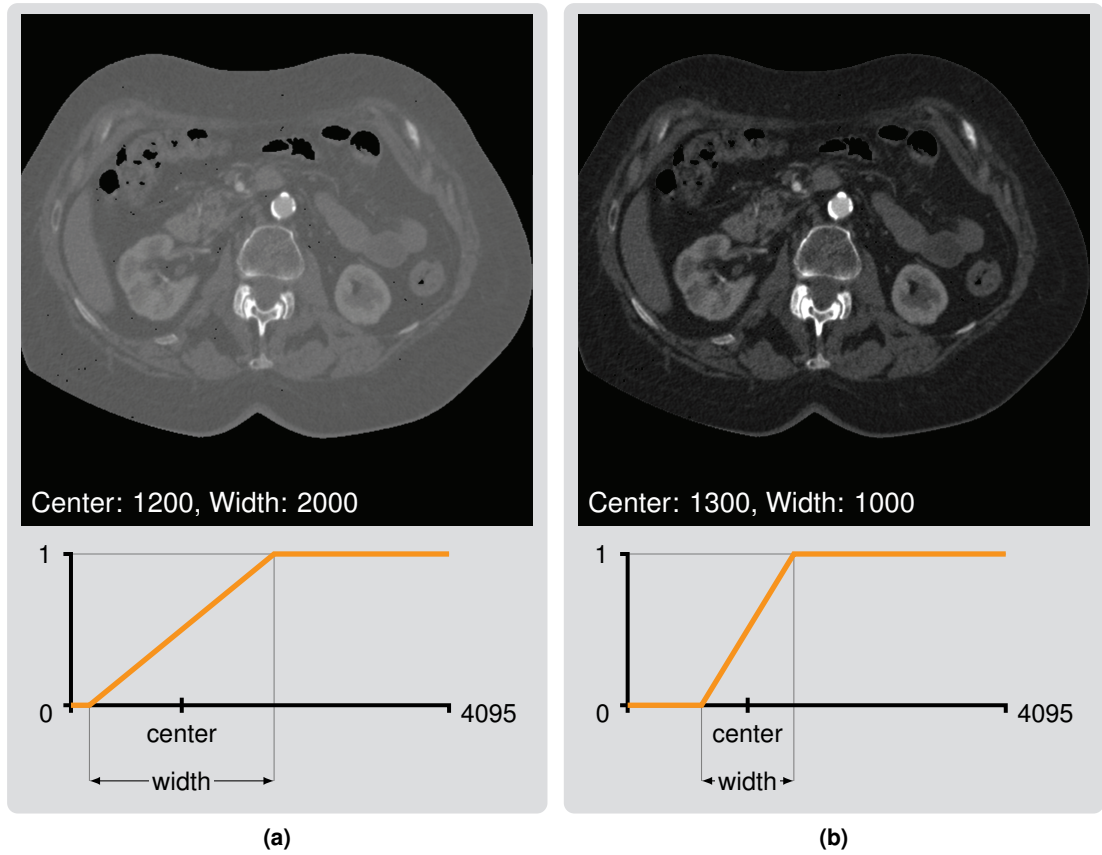
Figure 1.3: Demonstration of two different windowing functions of an axial slice of a human thorax. **(a)** has significantly less contrast than **(b)**, but it is brighter.

As opposed to DSA, which requires the contrast agent to be injected into the arterial system of a patient, in CTA the contrast agent is administered intravenously, a less invasive and harmful process. Before the contrast medium reaches the arterial system for the first time (*first pass*), it travels from the veins of the arm to the right atrium and the right heart ventricle, the lung, and the left atrium and the left heart ventricle [40, 41]. Since the contrast agent re-enters the right atrium and the right heart ventricle after being distributed throughout the organs (*recirculation*), vessels are cumulatively enhanced, i.e., they do not share the same range of intensity (HU) values. The reason for this is that the bolus (a bolus is an amount of liquid given intravenously in a short period of time) travels at different speeds through the different organs of the body. To provide a uniform vessel opacification, biphasic and multiphasic injection protocols have been studied [4, 40]. They require a high initial administration of contrast agent followed by either a constantly lower (biphasic) or continuously decreasing (multiphasic) injection rate, until the end of the scanning procedure. To obtain a uniform vessel enhancement, a biphasic protocol should be applied [43]. The mathematical foundations of optimized arterial enhancement using biphasic

contrast agent injection protocols can be found in the work of Fleischmann and Hittmair [42]. Having a uniform vessel opacification throughout the entire region of interest is particularly important for image post-processing or segmentation approaches [40, 41, 44].

1.1.5 Magnetic Resonance Imaging

An alternative to CT is Magnetic Resonance Imaging (MRI) that exploits properties of tissue under the influence of a strong magnetic field. The principle works as follows. Spinning hydrogen nuclei can be considered as small magnetic dipoles, aligning themselves to a strong externally created magnetic field. By employing pulses of electromagnetic energy (radio frequency pulses) the alignment of the magnetic field is altered and some initially magnetically aligned nuclei enter a temporal non-aligned high-energy state. This excitation is followed by a relaxation and realignment of the nuclei to the initial magnetic field. During this process, energy is emitted, which can be recorded and transformed into spatial information by using a Fourier analysis. Volumetric information can be acquired by using orthogonal magnetic field gradients as well as phase encoding. The homogeneity and strength of the magnetic field influence the quality of the obtained volumetric data, and the contrast depends on involved time constants of the excitation and relaxation cycles. Angiographic data can be acquired by the administration of commonly gadolinium-based contrast agents [136].

The main advantage of Magnetic Resonance Angiography (MRA) compared to CTA is the absence of ionizing radiation and potentially nephrotoxic (toxic to the kidneys) contrast agents [136, 171]. Contraindications are older, so-called non-MRA compatible, pacemakers, implants made of ferromagnetic materials, or cochlear implants. According to the study by Willmann et al. [171], advantages of CTA compared to MRA include the highest patient acceptance and a better assessment of vessels with small diameters (e.g., in the calves) owing to a higher resolution. CTA is seen as more comfortable by patients than MRA due to less noise, shorter examination time and a large diameter of the gantry board.

1.2 Vascular Imaging Foundations

In this section, we provide an outline of vascular diseases by describing their causes, symptoms, diagnosis and treatments. Since we deal with very specific medical aspects in the subsequent chapters of this thesis, this should aid the understanding of the basic medical terms. We concentrate first on a broad spectrum of atherosclerosis and do not focus solely on the investigation of peripheral arteries. Additionally, we briefly mention embolisms, as we show how we are able to present visualization techniques to visually explore and locate the embolisms even within a dense and complex vasculature.
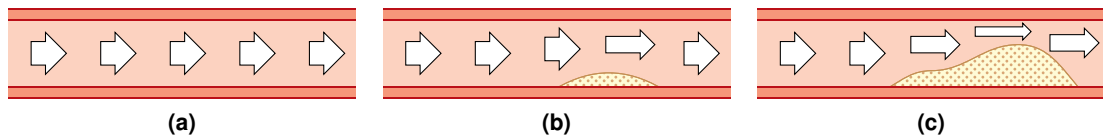
Figure 1.4: Illustration of the atherosclerotic process. **(a)** shows a healthy vessel without any occlusions of the blood flow. **(b)** displays a narrowed vessel with an initial buildup of plaque, whereas **(c)** demonstrates a vessel stenosis (>50% narrowing of the vessel).

1.2.1 Vascular Diseases

Vascular diseases are becoming an increasing concern in our aging society and they exhibit a severe impact on the human's health state. Atherosclerosis is a chronic inflammatory disease, primarily affecting large to medium-sized vessels. The main cause is the progressive accumulation of atherosclerotic plaque on the vessel walls, preventing blood from flowing. Clinical signs and symptoms of atherosclerosis belong to the group of *cardiovascular diseases*. These diseases have high incident rates in developed countries [33], leading to an important and relevant medical field, as they exhibit a significant risk for human life. A specific domain in medicine, radiology, is concerned with the causes, the progression and the prevention as well as the treatment of vascular diseases. Since such investigations require the precise analysis of vessel dysfunctions, visualization techniques can be of essential assistance to determine the severity and extent of the disease prior to the treatment of the patient [135].

Cardiovascular diseases are generally caused by a remodeling of the vessels due to subsequent buildup of plaque on the intimal layer of the arterial walls (cf. Figure 1.4). This process is referred to as *hardening* of vessels and consists of the following three stages:

1. A fatty deposit, i.e., *lipid plaque*, is built on the wall of a blood vessel. Such plaque is characterized by lipids, cholesterol, calcified deposits and other cellular residues. The resulting narrowing of the vessel is referred to as *stenosis* (cf. Figure 1.4c). With time this alters to:

2. A *fibrous plaque*, increasing the stiffness and decreasing the elasticity of the artery wall. It consists of tough, rigid collagen around the soft plaque. Later, parts of the plaque might change into:

3. A *calcified plaque* usually occurring in the thickest region of the sclerosed vessel wall. It is formed from a mineral deposition or possibly an ossification (the buildup of bony tissue).

Depending on the consumed cross-sectional size of the plaque, it is called *stenosis* in case of a luminal narrowing or *occlusion* when the complete vessel is obstructed by a clot and blood is unable to flow farther. As described by Schernthaner et al. [135], stenotic lesions can be categorized depending on their percentage of cross-sectional area coverage and their hemodynamic significance: 0% (healthy), 1-49% (patent), 50-69% (not hemodynamically significant), 70-99% (hemodynamically significant), and 100% (occlusion). The hemodynamic properties of

vessels can be assessed by measuring the blood pressure before and after the stenotic lesion. If the pressure after the lesion is significantly less than the one before, blood accelerates in this part, leading to a significant stenosis. The occurrence of hemodynamically significant stenoses ($\geq 70\%$) leads to a reduced blood supply of the corresponding organs. Such an ischemia (lack of blood supply) might not be immediately noticeable, possibly only during or after increased physical effort.

The manifestation of cardiovascular diseases depends on the affected organ or region of the human body, leading to a broad spectrum of symptoms and implications. The most important types of cardiovascular diseases are the following:

- A *cerebrovascular atherosclerotic disease* can manifest as a short transient ischemic attack, also referred to as mini-stroke. Symptoms of a stroke are local numbness, paralysis of one body side, blurred or double vision, or loss of speech.

- If a reduction of blood supply manifests as sudden chest pain (angina pectoris), it is known as *coronary artery disease*, caused by ischemia of the heart muscles. Possible conditions of the ischemia are significant stenoses or spasms of the blood vessels.

- In case of *peripheral arterial occlusive disease*, atherosclerosis in the arterial system of the lower limbs can cause pain, crippling or numbness due to *intermittent claudication*. It is manifested by muscular leg pain or discomfort when walking and vanishes during or after a short rest [107]. Usually, intermittent claudication is difficult to diagnose at this stage. Advancing to the next stage of severity, the legs might hurt even while resting, known as ischemic rest pain. Developing further, if the metabolic demand of muscle or tissue is not satisfied anymore, it is known as critical limb ischemia. At this stage, without intervention to improve the arterial perfusion, amputation of the affected region might be the last opportunity. [107].

For an elaborate survey on the symptoms and diagnoses of peripheral arterial diseases, we refer to the work of Norgren et al. [107].

Regardless of naturally conditioned risk factors such as the possibly advanced age of a patient, a potential risk factor for all cardiovascular diseases is *smoking*, with an even higher risk for the peripheral limbs [107]. Another significant risk factor is *diabetes mellitus* that leads to a more aggressive development in the peripheral arteries by involving even small vessels at earlier stages. It increases the risk of peripheral arterial diseases about three- to four-fold. According to Norgren et al. [107], insulin resistance has a considerable impact even on subjects without diabetes (increasing the risk about 40% or 50%). Another risk factor for peripheral arterial diseases is *obesity*. Compared to smoking or diabetes, a relatively lower risk is encountered by *hypertension*, but it is prevalent for all kinds of cardiovascular diseases [107].

The treatment of cardiovascular diseases depends on their manifestation and affected organs or regions of the patient. The most prominent clinical treatment strategies, ranked according to their invasiveness, are the following:

- *Conservative treatment* aims to avoid any radical medical measures or surgical procedures, e.g., guided exercises with simultaneous drug therapy.
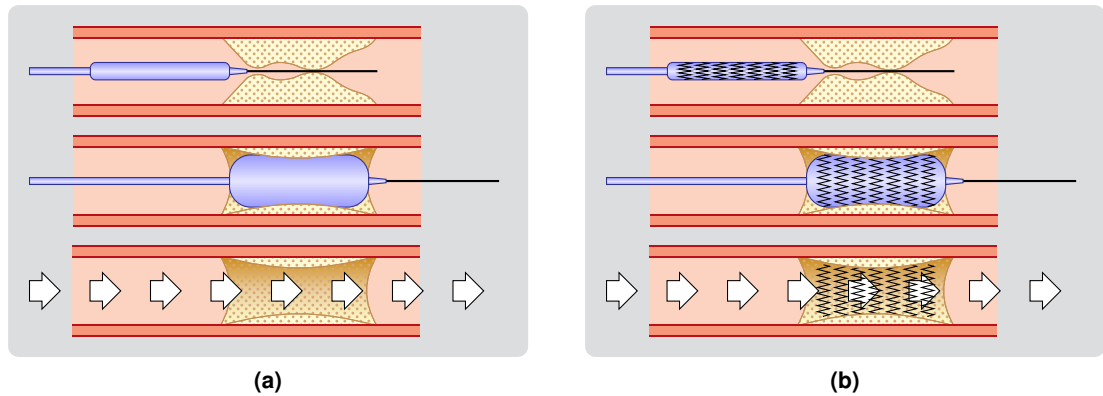
Figure 1.5: Illustrations of percutaneous transluminal angioplasty. **(a)** demonstrates the balloon dilatation procedure. A balloon is inserted into a vessel until the target location is reached. Subsequently, the balloon is inflated in order to compress its surrounding plaque. If the vessel is unstable, a wired mesh tube, as shown in **(b)** could be added for stabilization. (Illustrations adapted from Netzer [106])

- *Percutaneous transluminal angioplasty* is the insertion of a small catheter surrounded by a balloon into the vascular system of the patient (cf. Figure 1.5). At the location of the stenosis, the balloon is inflated by high pressure, compressing the atherosclerotic plaque while simultaneously stretching the artery wall (cf. Figure 1.5a). Additionally, an expandable wired mesh tube (called *stent*, cf. Figure 1.5b) could be implanted to prevent the recently stretched artery from collapsing inwards [96, 107, 143].

- *Surgical revascularization* is the restoration of the blood flow of a stenosed vessel by means of vascular grafting. The stenotic region of the vessel is circumvented with a bypass consisting of either the patient's own vein or synthetic material (e.g., Gore-Tex) [107].

- *Amputation*, as the last option, might be necessary to avoid sepsis in case of necrotic tissue and gangrene.

For extensive and elaborate information regarding treatment possibilities and their recommendations, we refer to the work of Norgren et al. [107]. Since the planning of a treatment procedure requires precise knowledge of the manifestation of a disease, it is necessary to establish the exact location and length of the lesion, as well as the lumen of the diseased vessel or if it is entirely occluded. It is important to know if a percutaneous transluminal angioplasty is sufficient, or if a surgical bypass grafting has to be applied. The acquisition of such precise information requires adequate visualization techniques of the vasculature. Hence, vascular imaging is an important part of radiology and visualization techniques can aid therapeutic decision making and treatment planning. As non-invasive diagnostic procedures are beneficial to the patient's health, we focus on medical data acquired with tomographic modalities, such as CTA, in this thesis.

Embolism. An *embolism* is a detached clot of hardened plaque, blood, or gas that has entered the blood stream. This might cause a blockage of blood (vascular occlusion) affecting a certain organ or part of the body, not necessarily close to the originating region. Such an occlusion can be the cause of a pulmonary embolism, blocking a part of the peripheral pulmonary vessel tree from the blood supply. Depending on the blood stream they enter, one can distinguish between arterial and venous embolisms. An arterial embolism can lead to a stroke if lodging in the brain due to ischemia. If a venous embolism is transported to the lung, it is a pulmonary embolism, reducing the blood supply to the lung. This vascular obstruction, or in the worst case occlusion, might lead to lung haemorrhage or reduction of the gas exchange surface. Embolisms might originate as a consequence of detached thrombi in the lower limbs or in the pelvic region [46, 47]. Since embolisms interfere with the blood stream, this should be conveyed by the visualization of the respective vessel lumen. In this thesis we demonstrate visualization techniques that are capable of reformatting the vessel lumen of carotid or peripheral pulmonary arteries (cf. Chapter 2 and 3).

Visualization. Visualization techniques can exploit certain properties of the different stages of plaque to provide a comprehensible visual interpretation for medical personnel. For example, when investigating CTA data, calcified plaque can be visualized with Maximum Intensity Projection (MIP), since it exhibits mostly high intensities, whereas soft plaque within the vessel might be captured with Minimum Intensity Projection (MinIP) due to its low intensity. In this thesis, we utilize such features to design tailored visualization techniques conveying this information to the user. Moreover, we present an aggregation, making the rotation around the vessel unnecessary (cf. Chapter 5).

1.2.2 Vessel Representation

The basic representation of vascular structures uses a cylindrical or tubular vessel model. The vasculature usually exhibits the topology of a tree, and is therefore referred to as *vessel tree*. It consists of a root with various branches, but does not contain any loops. The vessel tree can be viewed as an acyclic graph, where its nodes are branching points, not necessarily binary. These branching points are referred to as *control points*. The edges of the graph, spanned between two branching points, are called *vessel segments*. These vessel segments are usually not linear, rather curves, and are therefore resampled at constant, equidistant intervals. These resampled positions are referred to as *centerline points* and the linear segments spanned between two consecutive points are called *line segments*. All details of the underlying volumetric data are retained by choosing the length of the line segments to be smaller than the respective minimum voxel side length. The complete vessel tree consists of several curved vessel segments that are approximated with a multitude of small linear line segments (cf. Figure 1.6). A *vessel path*, in turn, is spanned between the root and a leaf vessel segment of the respective vessel tree.

Depending on the region of the body, for different types of vascular diseases, different vessels are clinically relevant. These need to be remodeled in the clinical routine work, to obtain tailored visualizations for inspection and treatment planning purposes. Throughout this thesis we
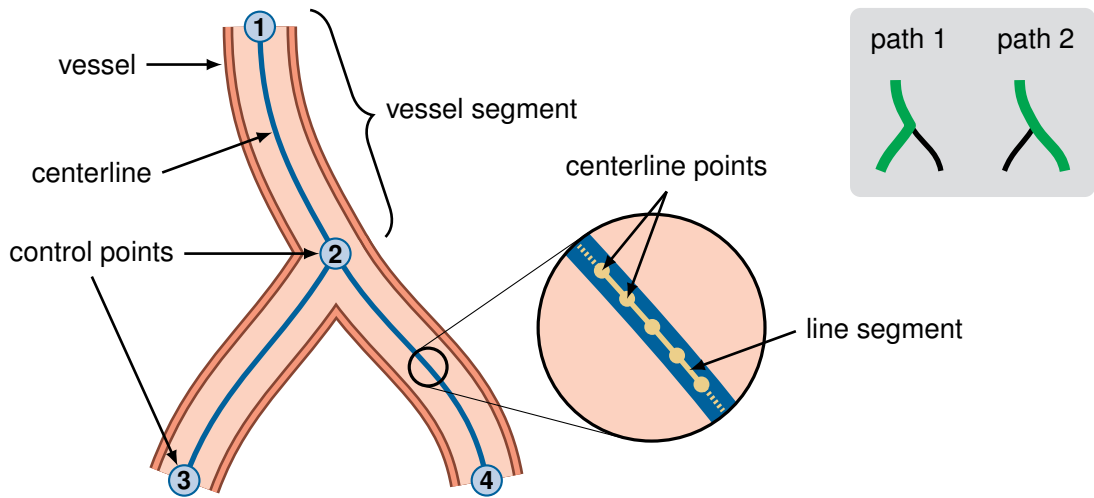
Figure 1.6: Illustration of the vessel representation. Control points are defined at the branching locations of vessels, each with a unique identifier. Vessel segments are spanned between two control points, consisting of many small line segments (cf. zoom-in). These are spanned between centerline points. There are two possible paths, one from control point 1 to 3 and another one from 1 to 4, as illustrated on the top-right in green.

demonstrate visualizations on several different important cases, for which we shortly describe the required information:

- For *cerebrovascular diseases*, the common carotid artery, the internal carotid artery and the intracranial arteries are of special interest. A blockage of these vessels has a severe impact on the patient's health state due to brain ischemia.

- For the investigation of *pulmonary embolisms*, the pulmonary vessels, the pulmonary artery as well as the peripheral pulmonary arteries are of interest. This leads to a complex vessel tree with many branches.

- For the investigation of *peripheral arterial occlusive diseases* of the human lower limbs, the abdominal aorta is chosen as the root vessel segment. Advancing down, only the most important vessels are remodeled to be included in the vessel tree, i.e., the iliac arteries, left and right. These lead to the femoral arteries, which then split into the peroneal, posterior and anterior tibial arteries, again, left and right. Overall, this leads to six clinically relevant vessel paths for the investigation of the human lower limbs, all starting from the aorta as root reaching down to the feet.

The choice of the root vessel segment usually depends on the investigated region of the human body and the vessels of interest.

1.3 Vessel Visualization

The visual representation of vessels serves many different aspects. For educational purposes, realistic or even illustrative renderings of vascular structures might be suitable, whereas clinical techniques are designed for the investigation of vascular pathologies. In this section, we give a general overview of the most important aspects of vessel visualization. Then, we explain vessel reformation techniques, as they provide an insight into the vessels. Finally, we discuss how to enhance spatial relationships between vessels when projected into image space.

Model-free visualization approaches use solely the underlying data without any further requirements. Marching cubes, proposed by Lorensen and Cline [94], is the standard choice for surface construction based on iso-values. As an extension, Pöthkow et al. [114] proposed probabilistic marching cubes by incorporating uncertainty information of the underlying volumetric data. Cebral and Lohner [23] describe another iso-surface extraction algorithm for mesh generation in Computational Fluid Dynamics (CFD) with applications in blood flow simulations. Schumann et al. [138] proposed a model-free surface rendering method that generates high-quality surfaces from segmented vessels. Starting from a binary vessel segmentation, they compute a point cloud which is transformed into a surface representation by means of multi-level partition of unity implicits [109]. Läthén et al. [85] describe an approach that provides a homogeneous visual representation of vessels by employing volume rendering. Usually, vessels are not entirely represented by common transfer functions, since the contrast agent is not distributed uniformly within the vessels. By applying an optimization strategy on local adaptations of the transfer function, vessels are visualized uniformly. Correa and Ma [28] proposed a technique that incorporates the maximum response of a multi-scale analysis into transfer functions in order to enhance features of certain sizes in volumetric data.

Model-based techniques require knowledge of the centerline and the radius of the vascular structure. Bloomenthal and Shoemake [11] describe *convolution surfaces*, as convolving a low-pass filter with the skeleton of a shape, followed by a subsequent polygonization according to a corresponding iso-value. When applied to vascular structures, a smooth and seamless visualization is obtained. However, vessels in close spatial proximity might merge. The surface of vessels can be approximated by geometric primitives such as generalized cylinders, presented by Kim et al. [73], or subdivision surfaces, described in the work of DeRose et al. [32] and Felkel et al. [39]. Pommert et al. [112] use splines for the approximation of surfaces of small vascular structures. Hahn et al. [50] describe *truncated cones* for vascular modeling and visualization. By assuming circular cross-sections, cones are defined by sweeping those along the vessel. To provide a smooth appearance, half spheres are added at the end of the vessels. Despite having artifacts at branching locations, the method provides a fast and good visual representation of vascular structures. Wua et al. [172] present a surface rendering approach for visualizing vascular structures defined by their centerlines and radii. The authors proposed a bidirectional adaptive sampling strategy to generate a topologically-correct base mesh. The complex topology of vascular structures is handled with modified normal calculations at bifurcations. They exploit local curvature information in order to obtain a high-quality surface visualization with as few polygons as possible. For further information on vessel visualization and quantification, the reader is kindly referred to the surveys by Bühler et al. [19] and Preim and Oeltze [116].

1.3.1 Vessel Reformation and Flattening

Reformation is a visualization technique to display interpolated values along a cutting surface. Multi-planar reformation is a traditional technique that creates orthogonal and later also oblique cutting planes through volumetric data. The most commonly used technique for the diagnosis of vascular diseases is Maximum Intensity Projection (MIP). The interpretation of spatial relations can be hindered by artifacts due to inhomogeneities in the distribution of the contrast agent and aliasing problems caused by the data resolution [75]. The problem when using MIP and Direct Volume Rendering (DVR) for the investigation of blood vessels in order to identify possible lesions is that bones usually obstruct vessels, unless they are segmented beforehand. Another issue in handling CTA data together with MIP is that calcified plaque exhibits almost the same intensity as bone and a higher intensity than that of opacified blood, possibly obstructing the interior (or lumen) of the vessels. However, it is of clinical relevance to assess the exact hemodynamic nature of a lesion to provide the correct decisions for further treatment. Bones provide a good context for orientation due to specific landmarks. Several approaches have been investigated for bone segmentation and vessel visualization, primarily for the peripheral arteries of the human lower limbs [66, 145].

In order to spare clinicians the cumbersome task of inspecting several hundreds of slices a curved plane is constructed to create longitudinal cross-sections through vessels. The approach of defining a curved cut plane through a vessel along its centerline (or central axis) is called Curved Planar Reformation (CPR), discussed by Kanitsar et al. [68]. These planar cuts through the volumetric data set are intended to provide more insight into otherwise obstructed internal structures. Kanitsar et al. [68] introduced three different types of CPRs (projected, stretched, and straightened), which exhibit distinct properties. The projected CPR is neither isometric nor conformal, whereas the stretched CPR is conformal. The straightened CPR is isometric and perspective obstructions due to rotations cannot occur, but the spatial perception of the vasculature as a whole is reduced. To compensate a possibly inaccurately defined centerline, a thick CPR has been developed. It employs a local MIP close to the cutting plane. The curved plane is extracted by a generating line, or *line-of-interest*. This leads to the issue that CPRs provide an accurate cut only for vessels with one predominant direction. This holds true in most cases of the peripheral arteries of the human lower extremities, which this method has been particularly designed for. In Chapter 2 and 3 we discuss how to remedy this issue and extend the approach to other fields such as pulmonary or cervical vessels. Moreover, since CPR is an image space technique, we present a method that operates entirely in 3D.

Since CPR is capable of generating the cutting plane only along a single vessel path, Kanitsar et al. [68, 70] proposed Multipath Curved Planar Reformation (mpCPR), the extension to multiple vessels. This technique renders a CPR for every vessel segment independently and exploits the specific geometry and spatial orientation of the vasculature to merge these CPRs into the final image. However, the visibility of multiple vessels overlapping due to the projection cannot be resolved properly. The same as with its predecessor, it is also designed for the investigation of peripheral arterial occlusive diseases of the human lower limbs. An evaluation of mpCPR has been done by Roos et al. [129]. This method partitions the final image according to the branches of the vessel tree and, therefore, it requires all vessels to be connected. If selecting different vessels by, e.g., visual querying, this constraint might not be satisfied, since possibly

disconnected vessels might be selected. In this thesis, we describe an extension that does not rely on this assumption.

Kanitsar et al. [69] describe the *untangled* CPR, an approach that projects the vessel tree into image space while avoiding obstructions by applying spatial deformations. Although this technique provides an occlusion-free visualization of the vessel interior of the entire vessel tree, it lacks spatial context due to the deformation. To model the complete interior of a vessel, Kanitsar et al. [69] proposed a *helical* CPR that presents the interior of a vessel by flattening it along a spiral, starting at the vessel's centerline. This approach preserves isometry, but lacks spatial context.

Lampe et al. [84] introduced a more general curve-centric reformation that allows transforming the space around a curve. Their method produces visualizations similar to planar reformations used for virtual endoscopy. Lee and Rasch [87] describe a tangential curved planar reformation by sweeping the Frenet frame along the projected centerline of a vessel. This creates artifact-free visualizations of the vessel lumen, but not of the surrounding tissue. Jianu et al. [60] explore the brain connectivity by projecting three-dimensional fiber tracts into 2D and subsequently cluster them, with each cluster having one centroid and many non-centroid tracts. They account for visibility by depth sorting the centroid tracts according to the depth of the center of the corresponding three-dimensional segments. We propose an approach (cf. Chapter 2) that uses the distance along the graph of all projected vessels together with the depth of a projected centerline voxel to determine proper visibility. This leads to a smooth lumen visualization at the connections of consecutive vessel segments.

Termeer et al. [151] proposed the volumetric bull's eye plot, a visualization technique for investigating coronary artery diseases. It provides an overview of healthy and scar tissue together with the coronary arteries by unfolding and reformatting the myocardium to a cylinder and projecting it along its major axis. Anatomical context is provided by mapping the coronary arteries on top of the projected tissue plot.

Methods for virtual endoscopy often use flattening methods based on nonlinear rendering, more specifically curve-centric radial ray casting. These visualizations usually map the volume to two-dimensional reformations. The horizontal axis represents the position along the centerline and the vertical axis represents the angular position of the flattened tubular structure displayed from the perspective of the centerline. Saroul et al. [132] proposed a technique for flattening free-form surfaces of anatomical medical structures that minimizes distortion along a user-specified curve or direction [133]. The surface is spanned between boundary curves, defined by users interactively placing markers within the volumetric data set. Bartrolí et al. [6] discuss a two-step method for colon flattening. In the first step they create a parametrization of the colon surface by casting nonlinear rays in the opposite direction of the gradient obtained from the distance field due to the centerline of the colon. This avoids intersections of consecutive cross-sections, but leads to a nonuniform sampling of the inner colon surface. Secondly, the colon surface is flattened by applying nonlinear two-dimensional scaling and subsequent resampling. Hong et al. [54] proposed a method for conformal colon flattening that minimizes global distortion. Williams et al. [170] present a combination of CPR and DVR for virtual endoscopy of the colon. Their technique performs a local DVR inside the colon and shows the CPR outside the colon as contextual information.

1.3.2 Context and Illustrative Rendering

Context rendering aims to enhance the spatial as well as the structural perception of particular regions or objects, which are focused on by the user. Additional visual cues can enhance the structural perception of an object and can provide important landmarks for navigating within volumetric data. This is especially relevant for designing clinically diagnostic visualization methods.

Straka et al. [146] proposed the VesselGlyph to establish focus+context rendering for CPR and mpCPR. Since cutting along a vessel makes it difficult to assess the spatial location of the surrounding tissue outside the vessel lumen, the VesselGlyph remedies this issue. The cut along the vessel is only shown within the lumen, whereas outside the vessel lumen various other volume rendering techniques can be applied. Several transition possibilities between the focus object and the context visualization are described. Such transitions can exhibit either a sharp border (no transition) or a linear interpolation between the focus and the context (smooth transition). In addition, vessels occluded by bones can be indicated by a so-called foreground-cleft, suppressing the object in front of the focus region. Optional occlusion lines might further visually indicate that the focus region is behind the occluding object [145]. Throughout this thesis we provide extensive discussion and examples of context visualizations.

Viola et al. [160] describe a technique for enhancing certain important objects within volumetric data sets by means of importance functions. Increasingly important objects create cutaway views to become visible to the viewer. Contextual information is provided around the important features [159]. Continued by Viola et al. [161], they discuss a method for retaining context while refocusing on different structures of interest within a volumetric data set. By defining an important object, the view, as well as visual parameters, are smoothly adapted to highlight the relevant object. We discuss in Chapter 3 how we employ an importance function to visualize the interior of blood vessels by simultaneously providing a smooth transition to their surrounding tissue.

Everts et al. [38] describe a general setup for enhancing the spatial and depth perception of dense line fields by halos along neural pathways. The geometric setup of a halo is defined by a depth displacement starting from the centerline. Depending on the relative distance between two lines, the width of the halos varies. This provides good visual cues and enhances the depth perception if dense line fields are rendered. In addition, the thickness of the lines is reduced with increasing distance to the viewer. For investigating dense vascular structures, such an approach provides a reasonable visual enhancement of depth and spatial relations. Bruckner and Gröller [16] describe an approach to enhance depth perception in volume rendering by employing volumetric halos. Halos are generated during the rendering process with view-aligned slices and the halo size is obtained by an iterative seeding approach. In order to provide uniform halos for objects of different sizes, the halos are computed on the gradient image. In addition, a broad spectrum of halo styles can be achieved by employing *halo profile functions* [14]. Ritter et al. [126] present hatching strokes to encode the spatial distance in shadows in a halo-like fashion. They use hatched shadows as indicators of the depth relationships of complex vascular structures. In addition, they provide a comprehensive quantitative evaluation of the effects of stroke hatching and their distance-encoded shadows. Interrante and Grosch [58] mention halos as an enhancement of depth perception in three-dimensional flow visualizations. Wenger

et al. [169] give a volumetric approach for halos in order to improve the visualizations of blood flows or neural pathways resulting from diffusion tensor imaging. We describe in Section 2.3.3, how we augment the visualization of a vessel's interior with halos.

Illustrative visualization aids the understanding of shape and its relation to the overall view. Bruckner [14] extensively describes several techniques for illustrative visualization of volumetric data. By introducing the notion of *style transfer functions* a number of different shading styles can be incorporated within a single rendering [17]. DeCarlo et al. [31] present *suggestive contours* as the non-photorealistic rendering of lines to provide enhanced visual cues of a shape. Suggestive contours augment true contours by conveying more details of the structure of an object. We employ silhouettes (cf. Section 3.2.3.5) to delineate and convey spatial discontinuities to the user in a comprehensive way.

1.4 Medical Data Processing Workflow

To allow the assessment of vascular diseases, clinically applicable images have to be provided. Therefore, the acquired volumetric data of a patient needs to be post-processed to extract the relevant information. Such a data processing workflow (cf. Figure 1.7) typically consists of the following tasks:

1. Starting with the **scanning** of the patient according to a certain protocol, tomographic imaging modalities (e.g., CTA or MRA) can be used for data acquisition. The scanning process is usually monitored by physicians and, in most cases, a series of axial (or transverse) slice images is obtained as a result. These images are usually stored in the Digital Imaging and Communications in Medicine (DICOM) image format and are sent to the Picture Archiving and Communication System (PACS) server for further processing or inspection.

2. The **reconstruction** step uses the information of the multitude of axial slice images to create a volumetric representation of the acquired region of interest.

3. In the **segmentation** step, undesired objects, such as the patient table, are removed first from the volumetric data set by masking the respective voxels. Then, different types of tissue, such as vessel or bone, are segmented in a semi-automatic procedure. This information is used to provide an obstruction-free analysis of blood vessels.

4. Vessels are **modeled** by employing a cylindrical model. The centerlines and radii of the vessels are specified in order to obtain a vessel tree of the patient's vasculature. Only the clinically relevant vessels are modeled, since their centerlines are necessary for specific visualization techniques.

5. In the next step, diagnostic **visualizations** are generated for the previously modeled vessel tree. Among these visualization techniques are CPR, mpCPR and MIP. The resulting images are sent to the PACS server for later retrieval for inspection.

6. Finally, the images are **interpreted** by radiologists at their workstations using a DICOM viewer. In most cases, the images are fetched from the PACS server and a report is usually recorded using the software from the corresponding vendor of the system.

19

AngioVis

Scanning	Reconstruction
– data acquisition – scanning of the region of interest	– many slice images as input – creates a volumetric data set

Segmentation
– removal of the patient table
– vessel & bone segmentation

Modeling
– modeling of vascular structures
– creates the relevant vessel tree

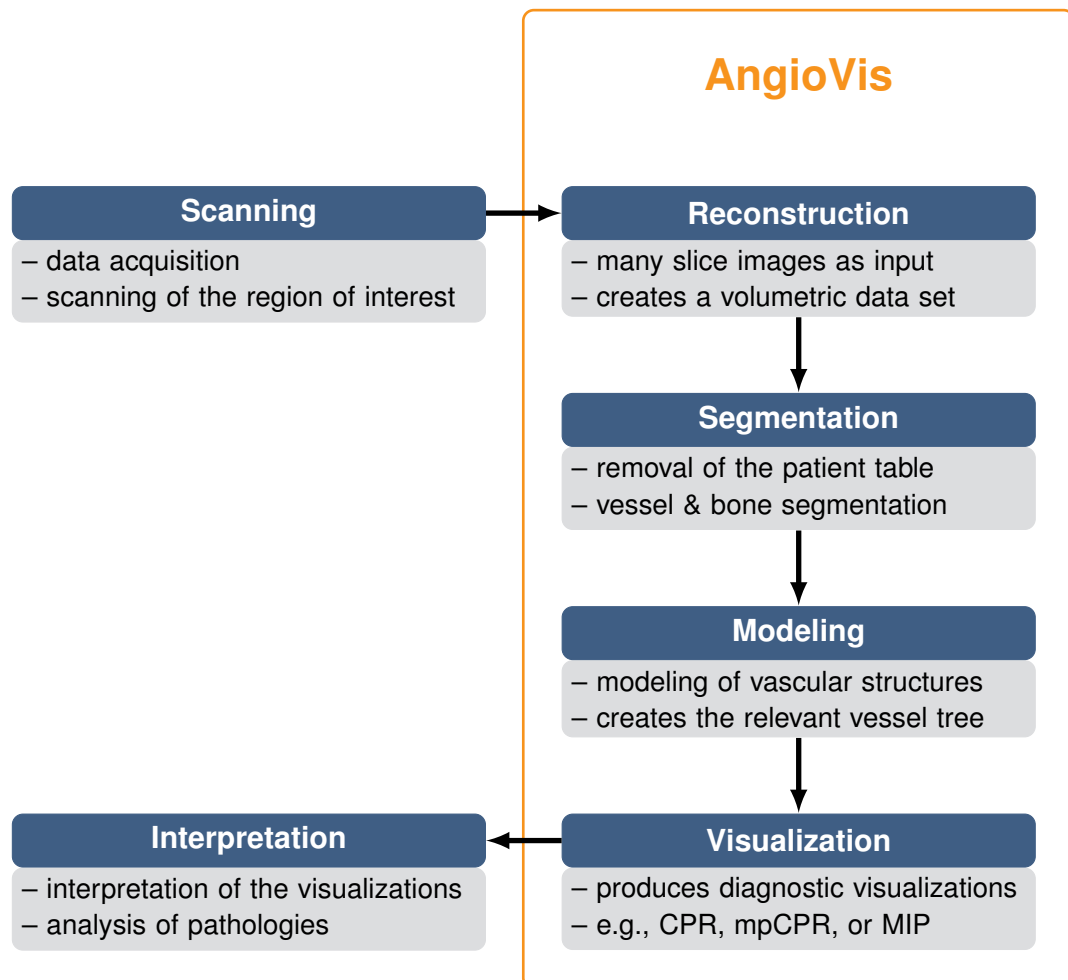| Interpretation	Visualization
– interpretation of the visualizations – analysis of pathologies	– produces diagnostic visualizations – e.g., CPR, mpCPR, or MIP

Figure 1.7: Illustration of the medical data processing workflow. The orange frame covers the steps of our framework, *AngioVis*, which has been developed during several research projects. In this thesis we focus on visualizations and how they might aid the interpretation and investigation of vessel pathologies.

In this thesis, we mainly focus on the visualization part and discuss method of how to aid radiologists during image interpretation and on how to reduce the number of images to inspect.

During several multidisciplinary projects between medical doctors and computer scientists, a prototype workstation, AngioVis [2], has been developed. This framework provides support for the aforementioned tasks of the clinical workflow, and is used in the hospitals of our medical collaborators in the daily routine and for research purposes. Throughout this thesis all techniques have been implemented in this framework as extensions (plugins).

1.5 The Scope of this Thesis

In this thesis, we address two important fields in medical visualization. First, diagnostic vessel visualization is discussed, especially reformation techniques for assessing vessel pathologies not only in the human lower extremities, but also in pulmonary and cervical vessels. The second field deals with aspects of interaction, namely how to support domain experts with smart interfaces and how to reduce required interaction while still providing all clinically relevant details.

The first area is covered by Chapters 2 and 3, where the focus is on the assessment of pathologies that hinder blood from flowing, e.g., stenoses or occlusions of vessels. Chapter 2 describes a technique, called Centerline Reformation (CR), that allows the visualization of the lumen of arbitrarily oriented vessels, in contrast to CPR and mpCPR. This offers the possibility to inspect the lumen not only of peripheral vessels of the human lower limbs, but also of cervical vessels or pulmonary vessels. Going one step further, an extended version of this technique, called Curved Surface Reformation (CSR), is discussed in Chapter 3. While not only allowing free navigation (e.g., rotation around any axis), correct visibility of the vessel lumen together with the surrounding tissue is preserved.

The Chapters 4 and 5 investigate methods for reducing the necessary interaction in a smart, or knowledge-assisted way. Starting with general aspects, Smart Super Views target the application of many techniques, tailored for only very specific areas. For example, CPR is used for the investigation of the vessel lumen, hence, domain experts need to be aware of this knowledge. Smart Super Views aim to automatize this semantic mapping and provide a bridge between the knowledge, the domain expert and the target application. A specific scenario of interaction reduction is provided in Chapter 5. Since many images usually have to be inspected in the clinical workflow to assess vessel pathologies, reducing their number while still showing the necessary details is provided by Curvicircular Feature Aggregation (CFA). The rotations of a cut surface around the centerline of a vessel are aggregated into a single image.

To assess the clinical relevance of all previously mentioned techniques, studies with domain experts have been carried out. In order to document the results, all materials are provided as Appendices to this thesis.

Medicine, to produce health, has to examine dis-
ease; and music, to create harmony, must investi-
gate discord.

—Plutarch

<div align="right">

CHAPTER **2**

</div>

Centerline Reformations of Complex Vascular Structures

This chapter is based on the following publication:

Gabriel Mistelbauer, Andrej Varchola, Hamed Bouzari, Juraj Starinsky, Arnold Köchl, Rüdiger Schernthaner, Dominik Fleischmann, Meister Eduard Gröller, and Miloš Šrámek. Centerline Reformations of Complex Vascular Structures. In *Proceedings of IEEE Pacific Visualization Symposium 2012*, pages 233–240, 2012.

Visualization of vascular structures is a common and frequently performed task in the field of medical imaging. There are already well established and applicable methods such as Maximum Intensity Projection (MIP) and Curved Planar Reformation (CPR). However, when calcified vessel walls are investigated, occlusion hinders exploration of the vessel interior with MIP. In contrast, CPR offers the possibility to visualize the vessel lumen by cutting a single vessel along its centerline. Extending the idea of CPR, this chapter describes a novel vessel reformation technique, called Centerline Reformation (CR), which is capable of visualizing the lumen of spatially arbitrarily oriented vessels, not necessarily connected in a tree structure.

THE precise analysis and visualization of vascular structures play an essential role for therapy-centric visualizations in medicine. The understanding of the vessel morphology and the spatial relationships can improve the diagnosis and treatment planning. Vascular trees are often very complex, with hundreds of branchings, which might occlude each other in rendering. Their reconstruction and visualization is therefore a challenging problem [154].

This chapter consists of two parts. First, a vessel-detection pipeline is described, based on the work by Hahn et al. [50]. Medical volume data with a focus on vessels typically comes from clinical Computed Tomography (CT) or Magnetic Resonance Imaging (MRI) angiography. Although the vascular structures are usually contrast enhanced, their intensities are not perfectly
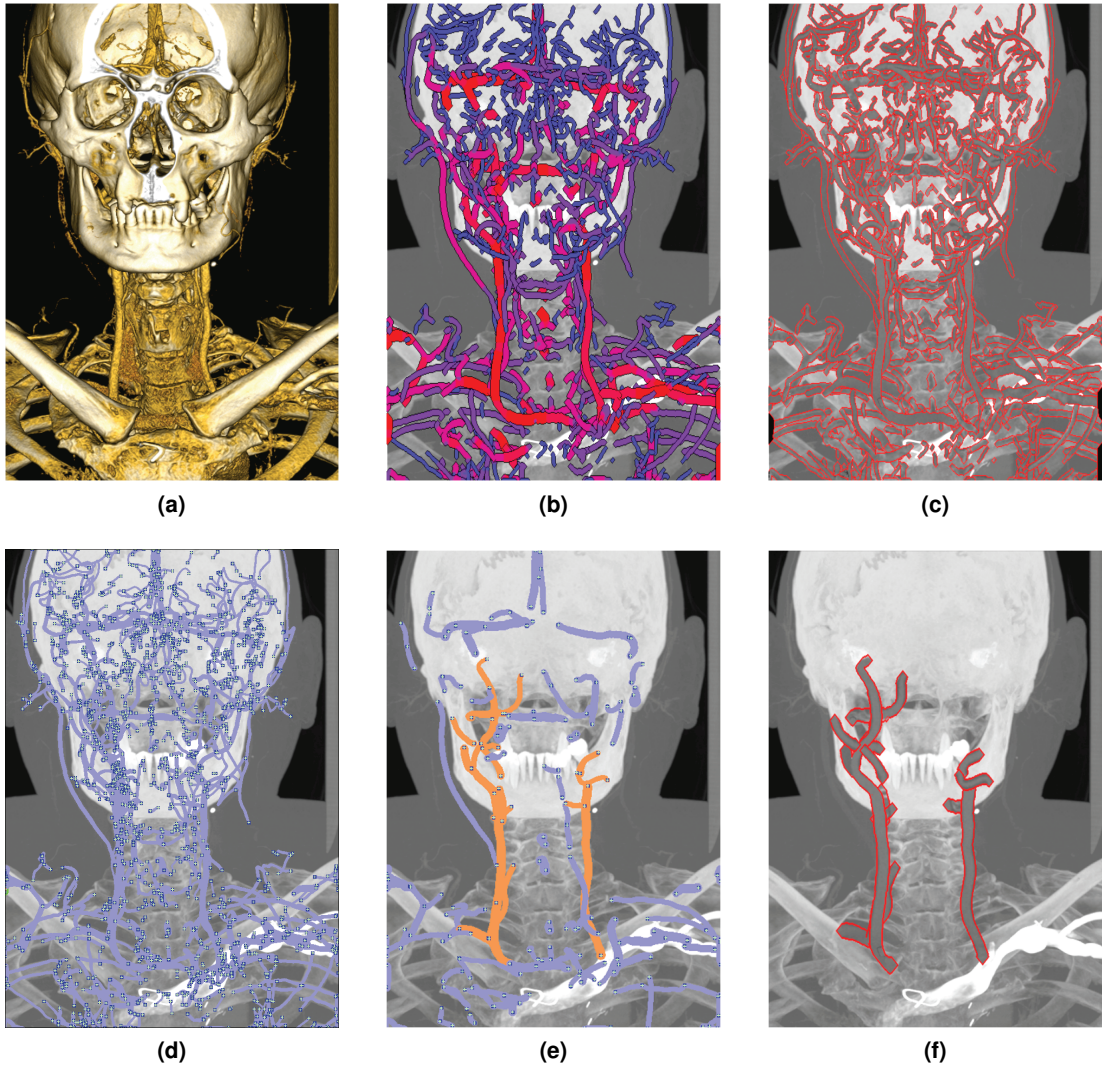
Figure 2.1: Overview of Centerline Reformation (CR). **(a)** shows a 3D visualization of a human head CTA data set. **(b)** visualizes automatically detected cervical vessels with size-based color-coding (thick vessels in red, thin ones in blue). **(c)** presents the vessel lumen of the whole vasculature with halos (red) and a context visualization (Maximum Intensity Projection), rendered with the proposed CR technique. **(d)** shows all automatically detected vessels (blue). **(e)** presents a subset of the vessels, filtered according to length and thickness in order to select specific vessels (orange). **(f)** displays the lumen of the carotid arteries, delineated with halos (red) and embedded into a context visualization (Maximum Intensity Projection).

(a) CPR (scanline) **(b)** CPR (normal vector) **(c)** CR (wavefront)
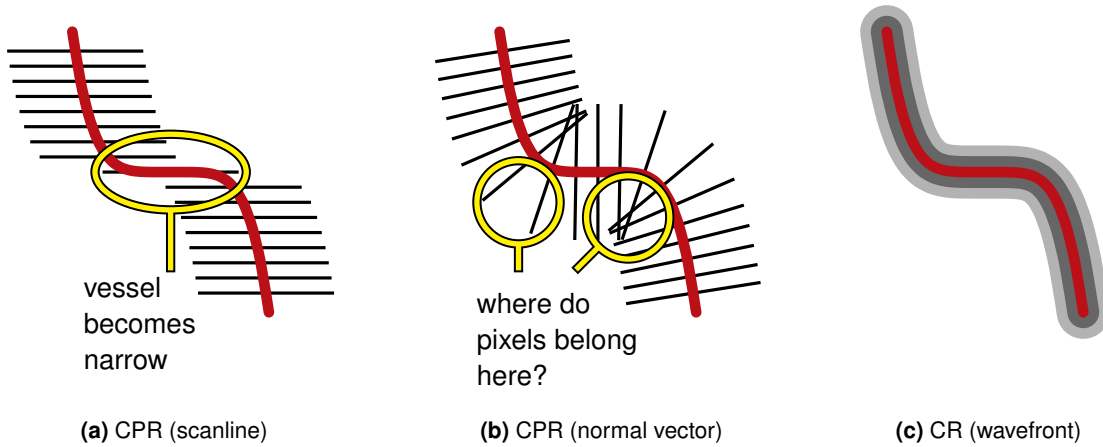
Figure 2.2: Comparison between CPR and CR. **(a)** demonstrates CPR using parallel scanlines as lines-of-interest, whereas **(b)** shows CPR using normal vectors as lines-of-interest [68]. **(c)** presents our proposed CR technique, employing wavefront propagation from the centerline outwards.

separated from other structures, such as bones. We present a pipeline that captures tubular structures, either bones or vessels, and determines the vessel centerlines. These are the prerequisites for vessel reformation techniques. Our goal has been the automatic detection of vessels to provide clinicians with an early estimate for further fine tuning and manual adjustment. This should advance the procedure for creating vessel reformation images, with a minimum of user interaction. However, further steps have not been investigated and the pipeline has not been evaluated; this is left open to future work. It has been our intention to demonstrate that the vessel reformation technique, which we describe in this chapter, is capable of rendering reformations of uncorrected, automatically detected, dense tubular structures.

The second and main part focuses on clinically relevant visualizations of tubular structures, specifically, vascular structures. In the case of pathologies that occur on vessel walls, such as plaque and calcifications, it is difficult to assess the vessel lumen, due to occlusion effects. Due to various limitations, in many cases conventional visualizations like iso-surface extraction, Maximum Intensity Projection (MIP), or Direct Volume Rendering (DVR) with simple transfer functions do not provide diagnostically satisfactory images. Curved Planar Reformation (CPR), proposed by Kanitsar et al. [68], is an advanced visualization method for the diagnosis of vessels, where a two-dimensional visualization of the vessel lumen is obtained by reformatting a curved cut along the vessel's centerline. The main contribution of this chapter is Centerline Reformation (CR), as a novel vessel reformation visualization technique, with the objective to visualize complex vascular structures for diagnostic purposes, as presented in Figure 2.1c on the example of cervical vessels. The method was motivated by the CPR technique introduced by Kanitsar et al. [68], but goes beyond its restrictions. The core novelty of the CR technique is the way how the lumen of vessels is reformatted (cf. Figure 2.2). A rotation independent approach is used, which is based on centerline reconstruction and wavefront propagation of the centerline infor-

mation within the vessel extent (radius). This new approach offers the possibility to reformat and visualize the lumen of spatially arbitrarily oriented vessels and arbitrarily complex vascular structures. The centerlines and radii are determined in a preprocessing step and are used for creating the lumen reformation. Their knowledge allows extending the visualization by halos, by vessel filtering according to various criteria and user interaction. Furthermore, the visualization of the vessel lumen can be augmented by means of a focus+context setup, for example, by the VesselGlyph technique [145, 146].

Compared to our previously developed method, discussed in the work of Mistelbauer [101], the technique described in this chapter has been completely redesigned by using the projected vessel graph in order to properly handle the visibility of multiple obstructing vessels. Previously, every vessel segment of the vessel tree was handled independently, leading to artifacts at branching points and incorrect visibility of overlapping vessels. Both issues have been significantly improved.

2.1 Related Work

Volume visualization plays an important role for the investigation of Computed Tomography Angiography (CTA) data sets. Quantification of vascular anomalies generally involves the definition of a centerline, which is a line-like representation of a three-dimensional object [147], either directly by path tracing, or indirectly by first segmenting the lumen [155].

A pipeline for vessel extraction is proposed by Selle et al. [139] and Hahn et al. [50]. Frangi et al. [45] describe a vessel-enhancement filter based on the eigenvalue analysis of the Hessian matrix in scale-space. Vessel-enhancement filters improve the visibility of vascular structures that are geometrically described as curved tubular objects [111]. The so-called *multi-scale analysis* is performed by first convolving the image with Gaussian derivative filters on different scales and subsequently analyzing the second-order derivatives, i.e., the Hessian matrix, at every image element [80, 92]. This approach is applied in our vessel-detection pipeline in order to retrieve vessels of various sizes. The high computational cost of the Hessian analysis on multiple scales in volumetric data can be reduced by performing local instead of global operations [3]. Lesage et al. [89] give an overview of techniques for segmenting the vessel lumen, including multi-scale analysis. Joshi et al. [63] describe a non-parametric entropy-based vessel detection that handles bifurcations better.

A comprehensive curve-skeleton survey can be found in the work of Cornea et al. [26, 27]. Thinning methods iteratively remove points from the boundary of an object while preserving its topology. We use such a skeletonization approach to retrieve the skeleton of vessels obtained from the multi-scale analysis. In distance-field methods, ridges in the distance field correspond to voxels that are locally centered within the object [118]. Tagliasacchi et al. [149] describe a method that uses the rotational symmetry axis of a point set to obtain its skeleton. Zhu et al. [178] proposed smooth harmonic skeletons of a triangulated representation of the vessel surface.

Jones et al. [62] give an overview of several techniques for computing distance fields. They distinguish between two approaches based on sweeping and on wavefront calculation. The first one calculates the distance field by sweeping through the data several times, whereas the second one propagates the distances from a starting point to its vicinity. Sethian [140, 141] describes

the Fast Marching Method (FMM), which is a wavefront method and used by our proposed CR technique for lumen rendering. Distances are computed by expanding the wavefront in the normal direction of a set of points. Telea and van Wijk [150] augment the FMM method for computing skeletons and centerlines.

In order to reduce the memory consumption of the vessel-detection pipeline, streaming approaches have been investigated. Law et al. [86] provide key principles for streamable data and describe a streaming technique that partitions a volume into blocks and performs subsequent operations on these blocks. Varchola et al. [158] describe slice-based streaming of volumetric data. Subsequent operations are carried out only on a specific set of slices, called *slabs*. If an operation requires neighborhood information, the required number of neighboring slices must be available and fetched. This is the approach we apply in the vessel-detection pipeline, which is described in the following section.

2.2 Vessel-Detection Pipeline

Since vessel centerlines are required to visualize the lumen, we have implemented a vessel-detection pipeline that is based on the work of Hahn et al. [50]. The pipeline uses multi-scale analysis of the data set to enhance tubular structures, followed by segmentation based on Hysteresis Thresholding (HT), skeletonization and, finally, conversion of the skeleton into a graph representation. This representation offers the possibility to filter vessels according to specific constraints during interactive visualization and allows the user to select vessels by visual queries utilizing brushing. The pipeline is additionally capable of handling large volumetric data sets by employing data streaming approaches [158].

In order to relieve clinicians of the time-consuming manual vessel segmentation, our pipeline provides them with a semi-automatic approach. The user input has been reduced to the necessary minimum which consists in specifying a range of vessel sizes (σ values) and two thresholds for HT that are used for vessel segmentation. In order to incorporate changes of these parameters, the pipeline needs to be re-run. Since clinicians usually do not want to specify and modify parameters, a default choice, adapted for their daily purposes, has been experimentally defined.

The workflow of the vessel-detection pipeline is outlined in Figure 2.3. It consists of three major steps, which are automatically executed: preprocessing, scale-space analysis and centerline generation. They will subsequently be discussed in more detail.

2.2.1 Preprocessing

To support input from various acquisition modalities, preprocessing is a necessary step to feed the pipeline with data in the required format and with certain expected properties. Owing to the fact that various scanners produce data with a different range of values, this step consists primarily of contrast enhancement, such that vessels remain the structures with the highest intensity. This may require remapping of the intensity values by a windowing function, in order to suppress other types of tissue with potentially higher intensity, such as bones [145]. Since various types of tissue are not distinguishable solely based on their intensity, undesired types of tissue are usually only partially suppressed.
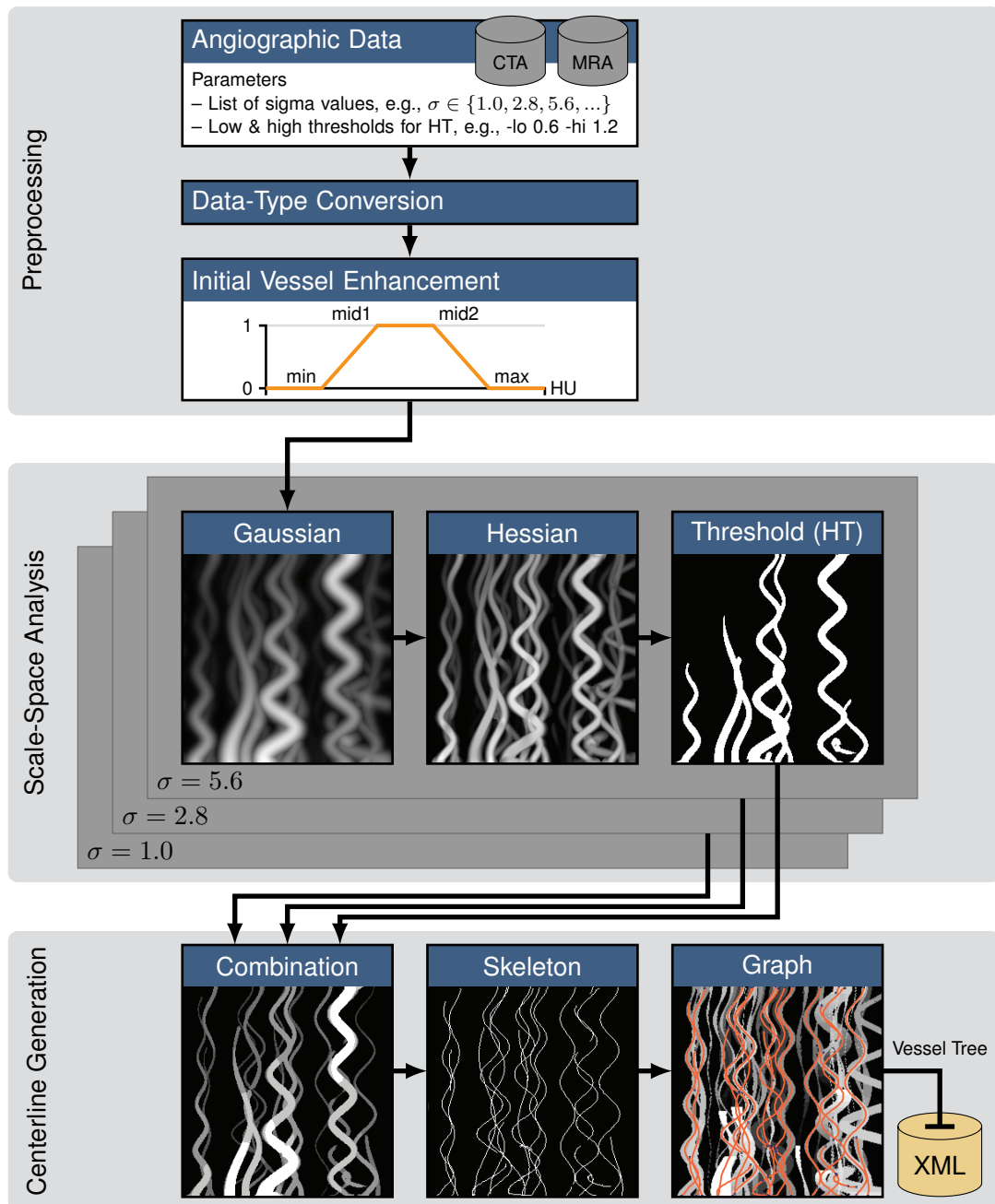
Figure 2.3: Workflow of the vessel-detection pipeline illustrated on an artificial data set. In the preprocessing step the data set is converted to the desired representation and vessels might be initially enhanced using a windowing function. During scale-space analysis, the Gaussian and Hessian filters followed by HT are applied for each scale in parallel (three scales are illustrated here). After combining all scales, the vessel centerlines are detected by skeletonization and finally converted into a graph representation.

2.2.2 Scale-Space Analysis

By employing scale-space analysis for vessel detection, only one parameter needs to be specified, namely the Gaussian standard deviation σ. The fact that it corresponds to the size of the detected vessels simplifies the user input for clinicians. Since vessels are tubular-shaped structures we enhance them with the vesselness operator that is based on an eigenvalue analysis of the Hessian matrix [45]. Other and more advanced vesselness operators are applicable here as well, e.g., the one by Pock et al. [111]. A vesselness operator enhances tubular-shaped structures of a certain scale and suppresses others. Thus, in order to enhance all vessels of interest within the volumetric data, a batch of filters has to be applied with values of the Gaussian σ covering the desired range of the vessels.

Vessel segmentation is based on the Hysteresis Thresholding (HT) from the Canny's edge detection framework [22]. This operation is applied to the respective results of the Hessian enhanced volumetric data sets. The results of the thresholding operations are binary volumes, where the foreground corresponds to the detected vessels of the appropriate scale, as shown in Figure 2.3 in the right image of the scale-space analysis plate. The advantage of HT resides in the suppression of spurious and not clearly pronounced structures and noise.

2.2.3 Centerline Generation

After all scales have been processed, they are represented as binary volumetric data sets. A mask of all vessels is obtained as a union of the vessel masks of the individual scales. Simultaneously, an auxiliary volume is created which stores for each foreground voxel the Hessian scale with the maximum response. If later a position is identified as a centerline voxel, this value is regarded as the *vessel radius* of the centerline at this voxel.

The centerlines of the previously segmented and combined vessels are determined by skeletonization in 3D using a thinning technique [88]. Although more elaborate methods exist, we used this one due to implementation simplicity. The result is a one-voxel thin 26-connected three-dimensional skeleton.

After analyzing the topology of the skeleton we represent it as a graph, which is done in a separate step, called graph conversion. A three-dimensional acyclic graph $G = (V, E)$, the vessel tree, is created, where the set of vertices V consists of branching points (with ≥ 3 neighbors) and endpoints (with exactly one neighbor). All other points have two neighbors and correspond to exactly one edge in the edge set E. We additionally compute the *thickness* of an edge as the average of the radii of all its points and the *length* as the number of all its points. These two properties are used for interactive filtering of vessels in order to select a specific subset of the whole vasculature.

2.3 Centerline Reformation

The major contribution of this chapter is the Centerline Reformation (CR), a vessel reformation technique to visualize the lumen of blood vessels and other vascular or tube-like structures given as volumetric data. The method belongs to the type of projected CPRs, as categorized by Kanitsar et al. [68], and therefore uses neither flattening nor straightening. The algorithm of CR can

be divided into four main steps (cf. Figure 2.4) with the vessel tree as input and the final image as output. First, in the *projection* step, the selected vessels or the entire vessel tree are projected into the view plane. In the second step, the *lumen rendering*, the projected vessels are grown until their extent is reached. Third, there is the option of rendering *halos* around the vessel lumen and, in the fourth step, a *context* visualization can augment the rendered vessel lumen. In the following sections each step is explained in more detail.

2.3.1 Projection

The first step of our algorithm is the projection. Input is a user-selected subset $sel(G)$ of the three-dimensional vessel tree G with centerlines e_i as its edges and $v_j \in e_i$ as their corresponding voxels. We project this subset into 2D using orthogonal projection

$$sel(G) \mapsto G^{2D} \tag{2.1}$$

with $e_i^{2D} \in G^{2D}$ as the projected centerlines, where each of them is a list of pixels $p_j = (x_j, y_j)$. Additionally, the adjacency information of G is used to build the graph G^{2D} in the 2D projection space. Then, we compute for every edge e_i^{2D} independently the arc-length, $l_{arc}(p_j)$, for every pixel $p_j \in e_i^{2D}$, by the following recursive equation

$$l_{arc}(p_j) = l_{arc}(p_{j-1}) + d(p_j, p_{j-1}), \qquad l_{arc}(p_0) = 0 \tag{2.2}$$

where $d(p, q)$ is the distance between two pixels, depending on the currently used distance metric (Manhattan or Euclidean) and neighborhood (4 or 8 connected). This is correlated to the arc-length parametrization of the edges e_i^{2D} and is similar to the approach proposed by Telea and van Wijk [150]. They parametrize the boundary of an object according to the arc-length and subsequently move inwards to compute the skeleton. Since we start from the centerline of a vessel and want to obtain the lumen, we advance in the opposite direction. Starting from the projected vessel tree, we propagate wavefronts outwards, until the extent of each vessel is reached.

Because multiple vessels might overlap in the 2D projection space, we use two buffers, a top-level buffer $B_T(p_j)$ and a candidate buffer $B_C(p_j)$ with pixels $p_j = (x_j, y_j)$, to correctly render the overlapping areas of vessels. The top-level buffer contains the currently visible vessel lumina. All the other vessels not yet in view are stored in the candidate buffer, since they might become visible when growing further. Both buffers have the resolution of the final image and store the following properties for every pixel, either only once in B_T, or in a list in B_C:

- a reference to the edge e_i^{2D} the pixel belongs to
- the depth value of pixel $p_j \in e_i^{2D}$
- the arc-length $l_{arc}(p_j)$ of pixel $p_j \in e_i^{2D}$
- the voxel $v_k \in e_i$ the pixel belongs to
- the vessel radius
- the type of the pixel (vessel, halo, background)

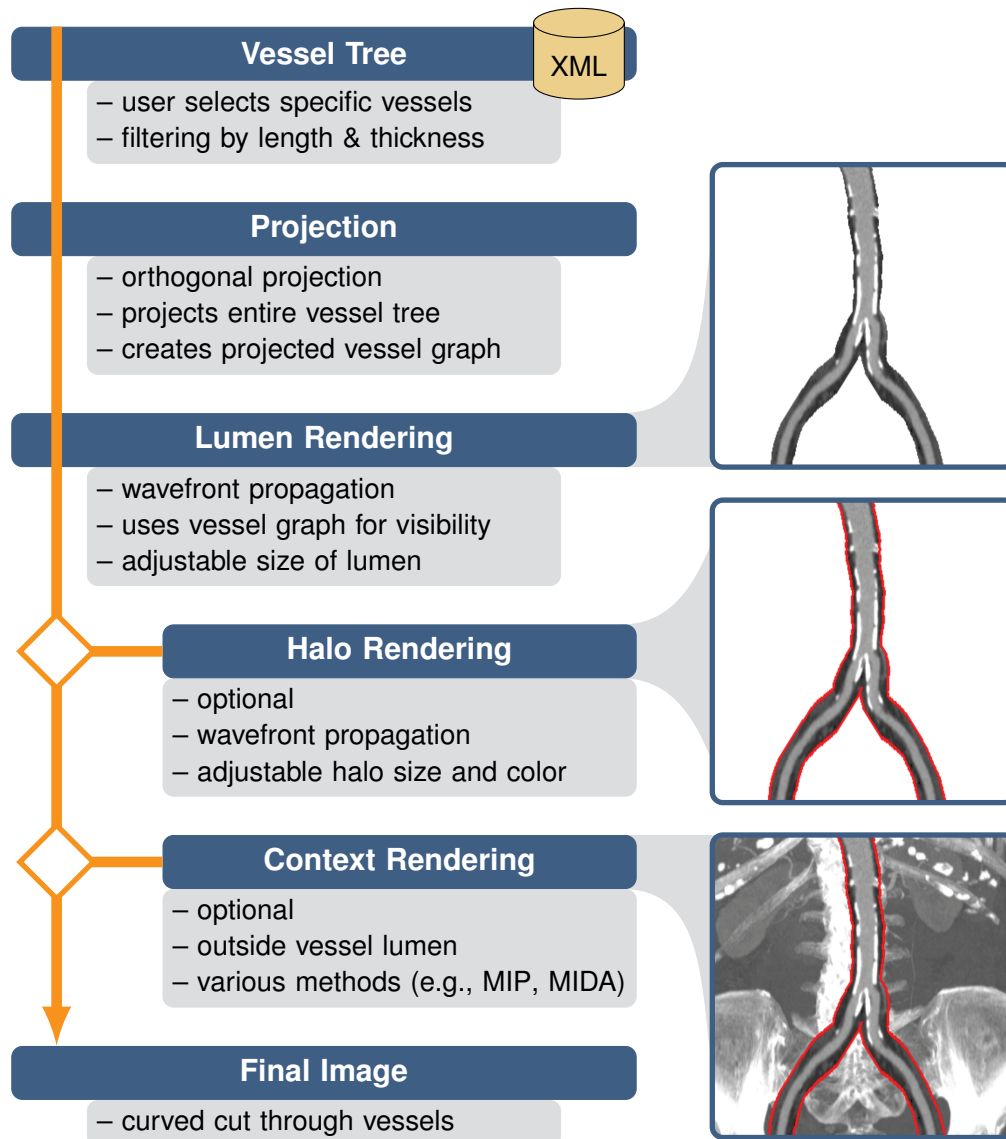**Figure 2.4:** Workflow of CR. The user is able to select specific vessels of the vessel tree and to filter them according to their length and thickness. These vessels are subsequently projected into the image space. The lumen is rendered using wavefront propagation and possibly enveloped by halos to enhance depth perception. The final image is composed by optionally adding a context visualization.

Whenever we refer to a pixel in one of these buffers in the remainder of this chapter, we mean the pixel's two-dimensional position together with the pixel's associated properties. The lists at every pixel of buffer B_C are additionally depth-sorted and contain the information of all candidate wavefronts, which are currently hidden, but might become visible when spreading further. A pixel of a currently hidden candidate wavefront can be rejected from advancing further, if its preceding pixel in the candidate list has a larger vessel radius, because the former pixel will always remain behind the latter. This reduces the total number of propagated wavefront pixels and, hence, increases overall performance. The computation of all candidate pixels of the initial wavefront, which is the projected vessel graph G^{2D}, is outlined in the subsequent code-snippet. There, U is a list of pixels where B_C needs to be investigated during the lumen rendering, since one pixel of each of these candidate lists might be closer to the view plane than the current top-level pixel.

$U \leftarrow \emptyset$ *list of pixels, whose candidate lists in B_C need to be investigated*
foreach $e^{2D} \in G^{2D} : \forall p \in e^{2D}$ **do**   *for all pixels of all projected edges*
    computeAndAddProperties(p) *compute every associated property*
    posInList $\leftarrow B_C(p) \cup \{p\}$ *insert pixel into candidates*
    if radius$(B_C(p)[\text{posInList} - 1]) \geq$ **radius**(p) **then**
        $B_C(p) \leftarrow B_C(p) \setminus \{p\}$ *reject candidate because of the smaller radius*
    else if $\#B_C(p) = 1$ **then**   *only one candidate in list so far?*
        $U \leftarrow U \cup \{(x(p), y(p))\}$ *add pixel's position*

It is sufficient to store the position of pixel p_j for every candidate in the list $B_C(p_j)$ only once in U. Finally, we receive all candidate pixels of the initial wavefront, $\forall p_i \in U : B_C(p_i) \neq \emptyset$.

2.3.2 Lumen Rendering

Our approach to reformat the lumen of the selected vessels is based on the Fast Marching Method (FMM) for propagating wavefronts, together with their properties, to neighboring pixels. We parametrize the edges of G^{2D} along their arc-length and extend this distance parametrization to the entire graph G^{2D}. In addition, we use this parametrization to determine the visibility of the vessels during lumen rendering.

Our method has been motivated by the observation that never altering a pixel once it has been spread to its neighbors, as done by the FMM, leads to visibility problems. These problems are illustrated in Figure 2.5a (highlighted with yellow circles). The reason for this is that a pixel of the same wavefront would not be changed, even if another one were closer to the view plane, since they are not depth-buffered. If only the depth information was used, the results would look like in Figure 2.5b. Always the pixels closest to the view plane are taken, regardless of the fact that they will overwrite the lumen of pixels behind them. Hence, using the depth information only is not sufficient to render the lumen correctly while accounting for proper visibility. Therefore, we have to find a more sophisticated way when altering an already grown pixel.

Before we can describe this, we need to define the distance between two points of the graph G^{2D} as illustrated in Figure 2.6. The distance between two points of the same edge $e^{2D} \in G^{2D}$,

(a) no arc-length, no depth buffer   **(b)** no arc-length, depth buffer   **(c)** arc-length, depth buffer
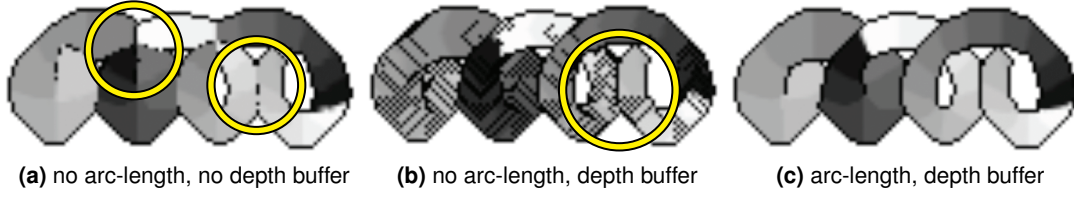
Figure 2.5: Comparison when using the arc-length parametrization or depth buffering for visibility. Since the grayscale gradients are stored in the data, they should be clearly reflected in the lumen visualization. Artifacts (highlighted with yellow circles) occur in **(a)** because pixels are never changed and in **(b)** since too many pixels are falsely overwritten. **(c)** shows the result of our proposed method.
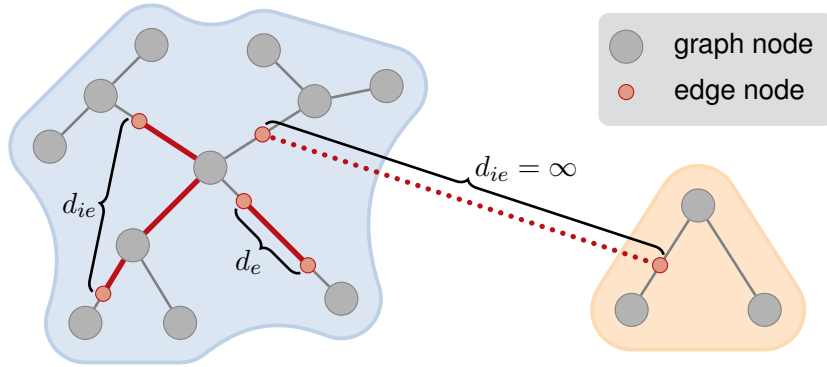
Figure 2.6: Distances d_{graph} between two points along the projected vessel graph G^{2D}, which consists of two disconnected graphs (highlighted in blue and orange).

called *edge distance* d_e, is computed as the arc-length difference of two points p and q by

$$d_e(p, q) = |l_{arc}(p) - l_{arc}(q)| \tag{2.3}$$

and the distance between two points of different edges, namely the *inter-edge distance* d_{ie}, is computed as

$$d_{ie}(p, q) = \begin{cases} \infty & \text{if } \nexists path(p, q) \\ \sum_{i=0}^{n-1} d_e(N_i, N_{i+1}), N_0 = p, N_n = q & \text{if } \exists path(p, q) \end{cases} \tag{2.4}$$

where $N_1 \dots N_{n-1}$ are the nodes of the graph G^{2D} along the path between the points p and q. The distance is computed by searching for a path in a depth-first fashion. If such a path exists, it is unique, because G^{2D} is acyclic. We can now define a distance metric over the graph G^{2D}, using these two distances, as

$$d_{graph}(p, q) = \begin{cases} d_e(p, q) & \text{if } edge(p) = edge(q) \\ d_{ie}(p, q) & \text{if } edge(p) \neq edge(q) \end{cases} \tag{2.5}$$

for any two points of G^{2D}. This distance metric is utilized during wavefront propagation to determine the visibility of colliding fronts.

The propagation of the wavefronts can be divided into two parts. First, in an update pass, all candidates of the list $B_C(p_j)$ of all pixels $p_j \in U$ are investigated and it is checked, whether they become visible and might contribute to $B_T(p_j)$. Since the list at $B_C(p_j)$ is depth-sorted, only the first element becomes visible if it is closer to the view plane than $B_T(p_j)$. Then, all candidates, including the first one, spread to their neighbors, unless they are discarded owing to a larger vessel radius of a preceding candidate. The following algorithm outlines how to determine the pixels that will spread to their neighbors by using the candidate pixel list U.

$P \leftarrow \emptyset$ *resulting list of pixels with their properties that need to be propagated*
foreach $p \in U$ **do** *for all pixels that need to be updated*
    first $\leftarrow B_C(p)[0]$ *take first candidate*
    top $\leftarrow B_T(p)$ *closest one is current top-level*
    if depth(first) < **depth**(top) **then** *first candidate closer than top?*
        $P \leftarrow P \cup \{B_T(p) \leftarrow \text{top} \leftarrow \text{first}\}$ *assign first to buffer and add to list*
        $B_C(p) \leftarrow B_C(p) \setminus \{\text{first}\}$ *remove first from candidates*
    foreach $c \in B_C(p)$ **do** *for all remaining candidates*
        if radius(c) ≥ **radius**(top) **then** *radius of candidate ≥ top?*
            $P \leftarrow P \cup \{\text{top} \leftarrow c\}$ *candidate becomes top and is added*
    $B_C(p) \leftarrow \emptyset$ *finally clear candidate list at pixel p in B_C*

When the update pass is finished, the second part, namely the propagation, is performed in a breadth-first processing of G^{2D}, starting with the propagation list P that has been obtained from the initial wavefront. Every pixel of the list P is spread to its neighbors, together with its properties. The vessel radius is decreased according to the chosen distance metric and when it reaches zero, the propagation is stopped. The user is able to offset the radius by a constant value. This is particularly useful if the vessel radius, which has been detected by our vessel-detection pipeline, is not sufficiently large to assess possibly suspicious regions on the vessel walls.

Since we propagate the wavefronts by simply iterating through their pixels, this might lead to different results when using another order, e.g., reverse iterate. To remedy this issue, if multiple pixels spread to the same neighbor and if they are close together according to d_{graph}, all their properties are interpolated. Figure 2.7 outlines how the wavefronts are propagated and when interpolation is taking place. A user-defined threshold, referred to as *arc-length threshold*, determines when two pixels are considered to be close together. To relieve clinicians from manually selecting this threshold, a default value tailored to their application purposes is given. During propagation, all candidates belong to the same wavefront, since the candidate buffer is cleared at every pixel after the update pass. However, one must be aware of the fact that interpolation might break the depth-sorted invariance of the candidate lists. Therefore, all interpolated pixels are removed and re-added later. The propagation is outlined in the following algorithm, where P is the current propagation list and U is the list of pixels for the next update pass.
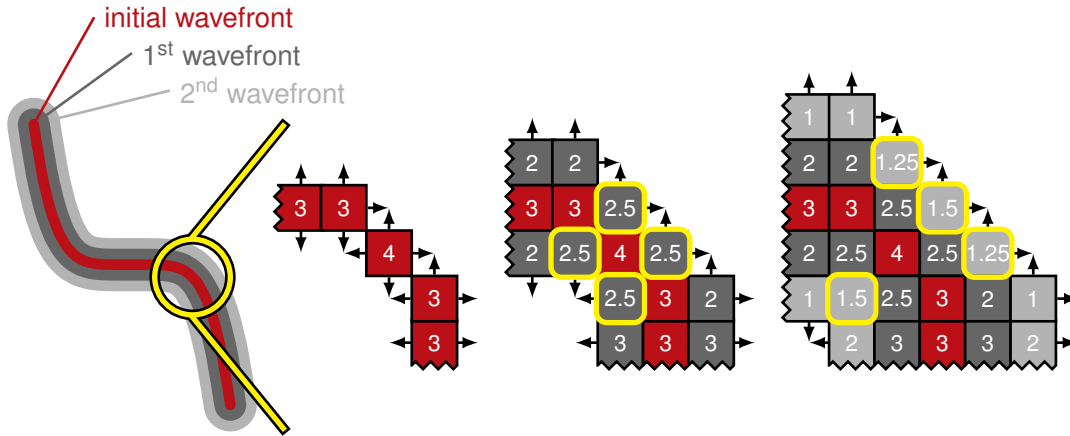
Figure 2.7: Illustration of the wavefront propagation. The pixels are spreading to their neighbors using the 4-neighborhood and Manhattan metric. The numbers indicate the vessel radius and interpolated pixels are outlined in yellow.

$U \leftarrow \emptyset$ *list of pixels whose candidates need to be updated*
foreach $p \in P : \forall n \in N_{neighborhood}(p)$ **do**   *for all neighbors of all pixels*
   $p \mapsto n$ *spread p to its neighbor n (radius$--$, if halo update depth, ...)*
   if $d_{graph}(n, B_T(n)) >$ threshold **then**   *neighbor away from top?*
      $A \leftarrow \emptyset$, neighborSkipped $\leftarrow$ false   *A is a list of changed candidates*
      foreach $c \in B_C(n)$ **do**   *loop through every candidate c of B_C at pixel n*
        if $d_{graph}(n, c) <$ threshold **then**   *neighbor close to candidate?*
          if **halo**$(n) \wedge \neg$**halo**(c) **then**   *skip halo if candidate is lumen*
            neighborSkipped $\leftarrow$ true   *halo does not overwrite lumen*
          else if $\neg$**halo**$(n) \wedge$ **halo**(c) **then**   *neighbor lumen, candidate halo?*
            $B_C(p) \leftarrow B_C(p) \setminus \{c\}$ *remove candidate from list*
            $A \leftarrow A \cup n$ *lumen can overwrite nearby halo*
          else if $($**type**$(n) =$ **type**$(c))$ **then**   *both same type*
            $B_C(p) \leftarrow B_C(p) \setminus \{c\}$ *remove candidate from list*
            $A \leftarrow A \cup$ **lerp**(c, n) *interpolate candidate with neighbor*

      if $\neg$neighborSkipped $\wedge (\#A = 0)$ **then**   *neighbor not interpolated?*
        $B_C(n) \leftarrow B_C(n) \cup \{n\}$ *add neighbor to candidates*
        if $\#B_C(n) = 1$ **then** $U \leftarrow U \cup \{(x(n), y(n))\}$
      else
        $B_C(n) \leftarrow B_C(n) \cup A$ *re-add interpolated candidates*
   else if $(\neg$**halo**$(n) \wedge$ **halo**$(B_T(n)))$ **then**   *neighbor lumen, top halo?*
      $B_T(n) \leftarrow n$ *lumen can overwrite nearby halo*
   else if $($**type**$(n) =$ **type**$(B_T(n)))$ **then**   *both same type*
      $B_T(n) \leftarrow$ **lerp**$(B_T(n), n)$ *interpolate top with neighbor*
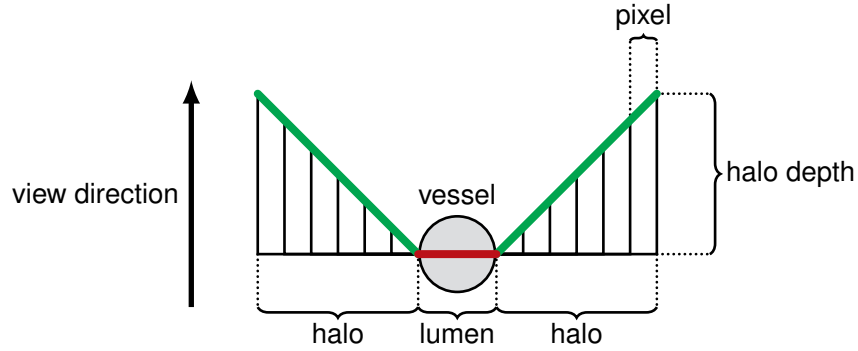
Figure 2.8: Illustration of halos (green) around the vessel lumen (red). The size of the halo is specified in pixels and the halo depth advances with increasing distance to the vessel lumen in view direction.

2.3.3 Halo Rendering

Once the vessel radius of a pixel from a wavefront reaches zero, the pixel is optionally added as halo for propagation again. The halos will augment the lumen visualization to delineate the visibility of different overlapping vessels, as illustrated in Figure 2.8 and presented in Figure 2.1c with halos in red. The user can specify the size of the halo in pixels. Although halos are rendered in the same way as the lumen, they are treated slightly differently. Their depth is increased proportionally to the distance from the centerline during spreading (indicated in the third line of the previous algorithm). Moreover, only pixels of the same type can be interpolated, namely if both are either halos or not halos.

2.3.4 Context Rendering

In order to provide an overview of the anatomical relation, a context visualization can augment the lumen visualization. If the lumen of every selected vessel has been rendered, possibly with halos, different tasks according to the type of every pixel p_j of the buffer $B_T(p_j)$ are performed. There are three possible types of pixels: vessel, halo and background pixels. If the pixel is a *vessel* pixel, the volumetric data is sampled at the stored voxel position. For *halo* pixels the user-specified halo color is assigned. If a *background* pixel is encountered in the top-level buffer, either a specific background color is assigned or a context is rendered, using MIP or Maximum Intensity Difference Accumulation (MIDA) [18]. Since orthogonal projection is used for the lumen visualization, we apply it for the context rendering as well.

Rendering of halos combined with the alternative rendering in the context area is similar to the focus+context rendering proposed by Straka et al. [146]. They introduce the VesselGlyph which combines DVR (context) together with CPR (focus) within a single image. While the VesselGlyph geometry is specified by means of a volumetric model based on vessel centerlines and corresponding three-dimensional distance fields, we distinguish between the vessel lumen, halo and background areas only in the two-dimensional projection space. Similar to the VesselGlyph, this offers the possibility to embed the lumen smoothly into the context area.

Table 2.1: Configuration of the vessel-detection pipeline for several processed data sets. The data sets are ordered from left to right according to the required computing time. The timings are given for a complete run-through.

	Artificial Helices	Pulmonary Vessels	Cervical Vessels	Human Lower Extremities
	Figure 2.9	Figure 2.12	Figure 2.1	Figure 2.10
Data Size	256^3	512^3	$512^2 \times 575$	$512^2 \times 1227$
#Scales	9	6	13	8
Lo / Hi HT	50k / 70k	0.6 / 1.2	0.6 / 1.2	0.6 / 1.2
Time PC1[1]	4.8 min	7.2 min	23.4 min[3]	21.6 min[3]
Time PC2[2]	1.3 min	4.3 min	7.4 min	7.7 min

[1] Intel Core2 @ 2.80GHz / 4GB RAM / GF 8800GTS 320MB
[2] Intel Core i7 @ 3.07GHz / 12GB RAM / GF 460GTX 1GB
[3] Individual scales were run sequentially (cf. Figure. 2.3), since in parallel their demands exceeded the GPU memory size.

2.4 Implementation

The technique has been implemented on the CPU due to various limitations of the software framework (AngioVis [2]) at the time of realization. However, we can visualize the vessel lumen at interactive frame-rates, where the performance is inversely proportional to the number and length of the rendered vessels. Although pixels can be rejected before spreading, the propagation consumes the major part of the rendering time. The time consumption of the projection and the vessel graph generation remain almost constant. The time of the update pass scales with the number of overlapping vessels, because more candidates have to be processed.

Since context rendering is also performed on the CPU, we accelerated it by pre-computing and caching ray directions just once for all slices. This is possible as we use orthogonal projection and allow rotations only around the z-axis.

2.5 Results

In this section several results of CR are presented, starting with the example of the human cervical vessels. Furthermore, CR is compared to Multipath Curved Planar Reformation (mpCPR) by use of a phantom data set that consists of many artificial helices, a standard medical case for angiography of the abdominal aorta, a special case of a cross-over bypass below the abdominal aorta, and a pulmonary embolism.

An overview of several data sets processed by the described vessel-detection pipeline is given in Table 2.1. The value ranges of the artificial helices and the CT data are largely different. Therefore, also the respective Hysteresis Thresholding (HT) differs considerably. If the scale-space computations are simultaneously performed for different scales, their entire mem-
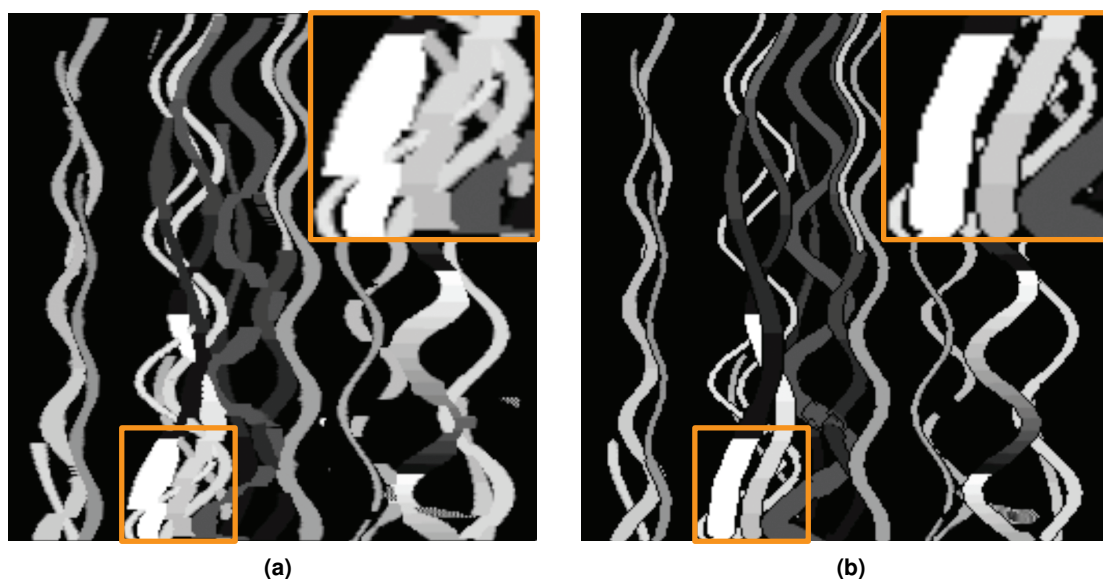
(a)   **(b)**

Figure 2.9: Comparison of mpCPR and CR based on a phantom data set that consists of many artificial helices with various grayscale values. **(a)** shows mpCPR and **(b)** presents CR. The zoom-ins demonstrate that CR accounts for the correct visibility of multiple overlapping vessels in 2D image space, in contrast to mpCPR.

ory demands might exceed the memory size of the GPU. In such cases, the scales are computed sequentially, consuming substantially more computing time. To support clinicians in the daily routine, default configurations of the vessel-detection pipeline for their common application scenarios are provided. This relieves them of the need to find suitable parameters.

A CTA data set showing the cervical vessels of a human head is presented in Figure 2.1. Domain experts see this application field as important and promising for reformation techniques. Figure 2.1a shows a 3D visualization of this data set, rendered with DVR. The lumina of all vessels are visualized with CR using size-based color-coding and MIP as context in Figure 2.1b, where red indicates bigger vessels and blue thinner ones. The size corresponds to the maximum scale where a vessel has been detected. Figure 2.1c presents the lumina of these vessels with a red halo and MIP as context visualization. Since the entire vasculature is quite dense (cf. Figure 2.1d) and not all vessels are of particular interest, they can be interactively filtered by the user according to length and thickness. Figure 2.1e demonstrates the result of such a filtering operation, where only thick and long vessels remain. The desired vessels are then selected using visual querying by brushing with the mouse (cf. Figure 2.1e, highlighted in orange) and their lumina are shown in Figure 2.1f.

Figure 2.9 presents a phantom data set that includes many artificial helices, consisting of various grayscale values. These are created on purpose in order to provide a possibility to verify if the lumen of such a helix is displayed properly (cf. Figure 2.5). Here, the visualization of many overlapping helices should be assessed. mpCPR does not account for proper visibility
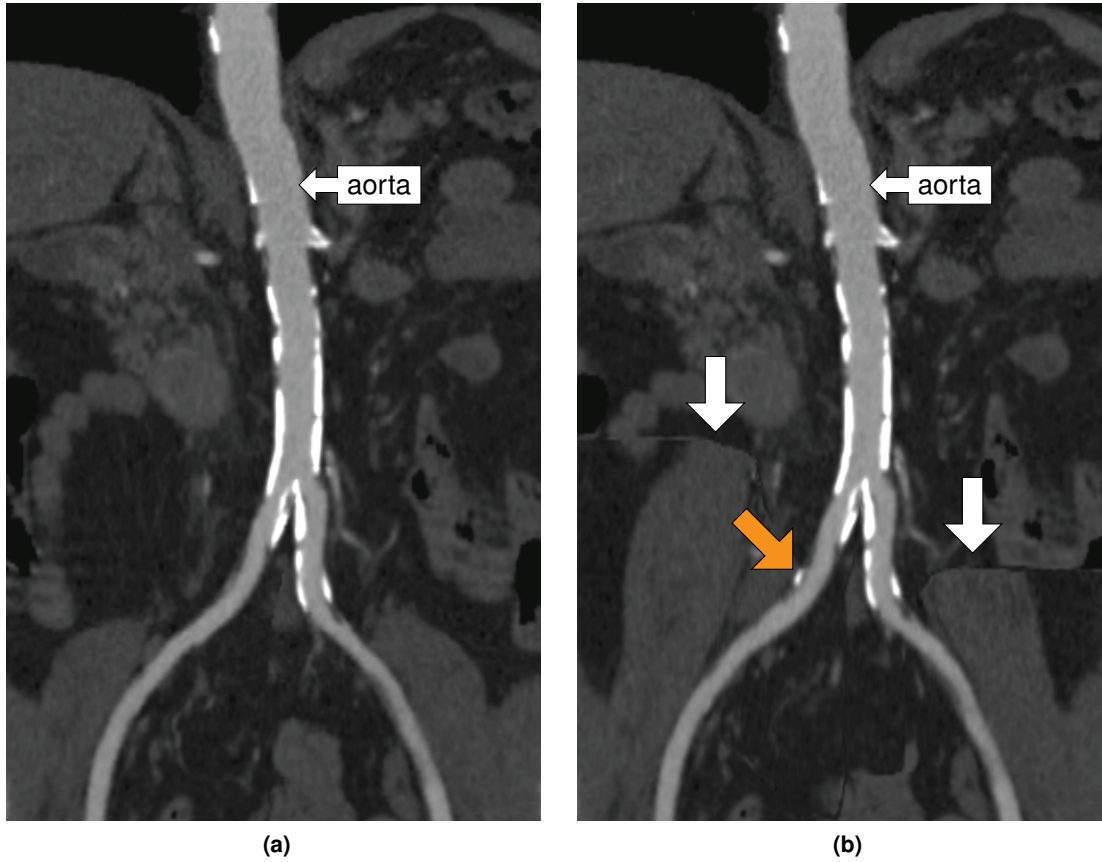
Figure 2.10: Comparison of mpCPR **(a)** and CR **(b)** of the abdominal aorta splitting into the iliac arteries left and right. The discontinuities (white arrows) result from the fact that the distance d_{graph} is used to determine whether a pixel is interpolated during spreading. However, they occur only in the surrounding tissue and do not affect the lumen itself. The bright calcification (orange arrow) is correctly shown by CR, because the depth of this region is obtained by wavefronts and not by horizontal lines-of-interest as in mpCPR.

of the helices (cf. Figure 2.9a) and which appear cluttered and without any depth cues. In contrast, CR shows the helices correctly according to the respective distance from the view plane, (cf. Figure 2.9b) and halos additionally enhance their delineation.

A comparison between mpCPR, using horizontal lines-of-interest, and CR is given in Figure 2.10 for a CTA data set of the human abdominal aorta. Since mpCPR is designed for the investigation of peripheral arterial occlusive diseases of the human lower limbs [66, 145], the lumina of vessels that exhibit one dominant direction are rendered with sufficient quality (cf. Figure 2.10a). CR displays the lumen of the vessel properly, since the calcification pointed out by the orange arrow (cf. Figure 2.10b) should be visible from this view direction. The white arrows show colliding wavefronts of different depths, resulting in perceivable depth discontinuities.
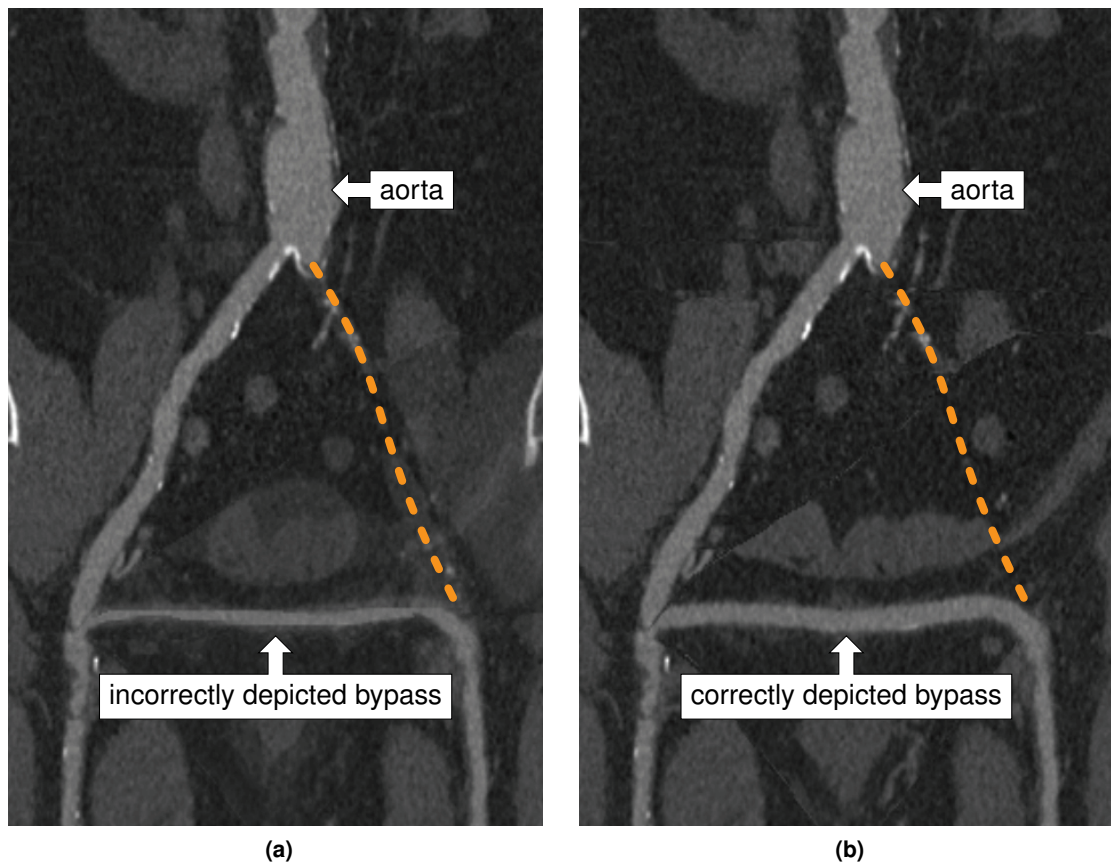
Figure 2.11: Comparison of mpCPR and CR based on a cross-over bypass below the bifurcation of the abdominal aorta. Because the left iliac artery (dashed line) is completely occluded, a bypass surgery was performed to provide the blood flow from the right iliac artery to the left femoral artery. **(a)** shows a mpCPR that incorrectly narrows the lumen of the bypass, whereas in **(b)** the CR clearly presents the lumen in its entire size.

Figure 2.11 presents a CTA data set with a cross-over bypass connecting both femoral arteries below the abdominal aorta. This demonstrates the advantage of CR, since horizontal lines-of-interest in case of mpCPR are not a proper solution here. The bypass is shown incorrectly narrowed and it is impossible to assess its vessel walls. CR correctly processes both vertical and horizontal vessels within one image, displaying the lumen of the bypass correctly. In order to visualize the surrounding tissue with CR, the vessel radius has to be increased accordingly. It is of clinical relevance to assess the lumen of the bypass as well, since pathologies within the bypass might prevent blood from flowing.

A CTA data set of the human thorax, including the pulmonary vascular system, is presented in Figure 2.12. Again, mpCPR is compared with CR (cf. Figure 2.12a and Figure 2.12b respectively). Both zoom-ins show the embolism that blocks blood from flowing through the vessel.
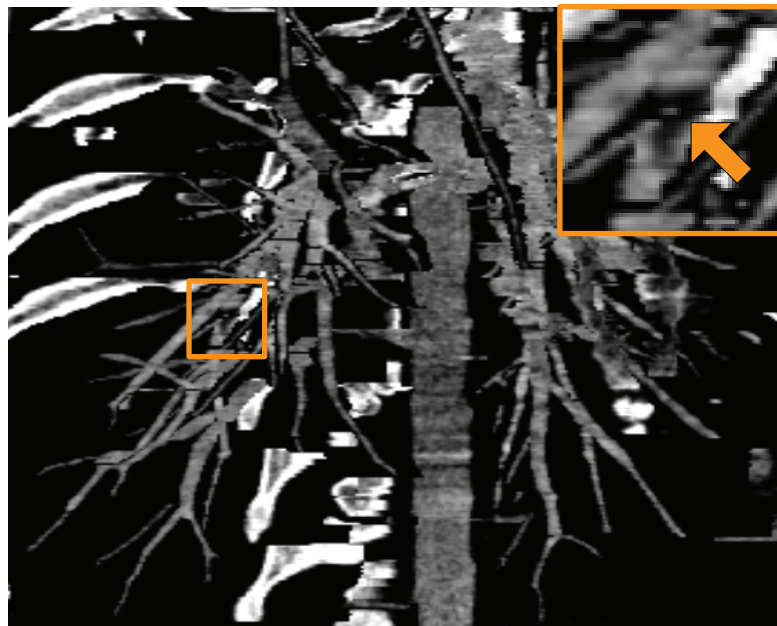
(a)
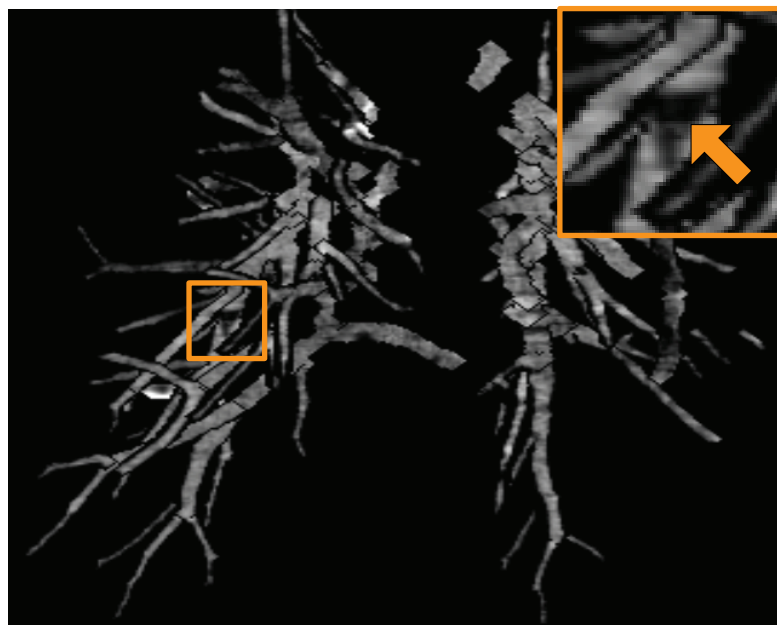
(b)

Figure 2.12: Comparison of mpCPR and CR based on pulmonary vessels. A pulmonary embolism is pointed out by the orange arrows in the zoom-ins. The lumen is rendered with mpCPR **(a)** and CR **(b)**.

(a)   **(b)**   **(c)**
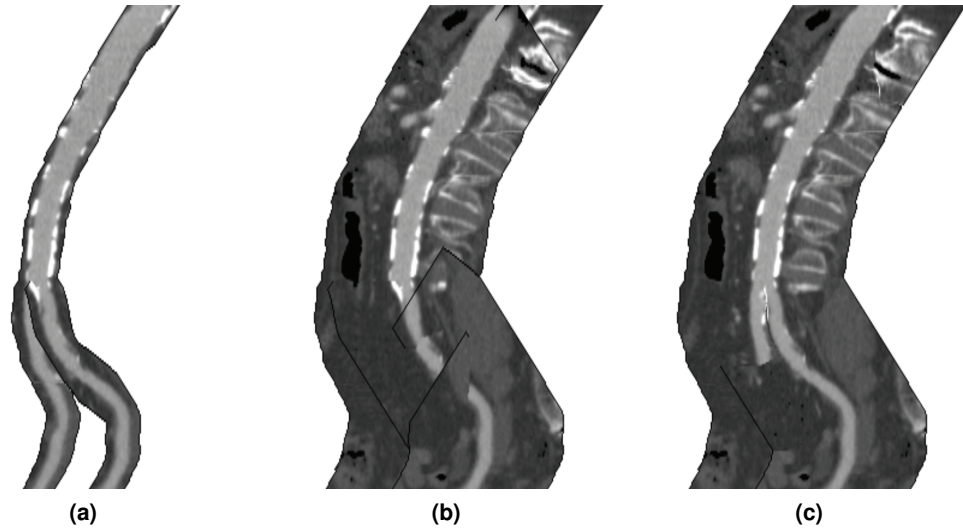
Figure 2.13: Demonstration of the trade-off between the displayed size of the surrounding tissue and the vessel visibility when using CR. **(a)** shows the lumen of the abdominal aorta and its branches with an arc-length threshold of 10 pixels. If the displayed size of the surrounding tissue is increased significantly, but the threshold is left unchanged, the visibility deteriorates, as presented in **(b)**. By increasing the arc-length threshold to 100 pixels as displayed in **(c)**, the visibility is restored, but the lumen of the vessel farther away from the viewer remains occluded.

While with mpCPR the vessels are not distinctly perceivable, CR preserves the visibility and delineates the embolism clearly. Since the peripheral pulmonary vessel tree is rather complex, selecting specific vessels may enable the user to quickly locate and identify pathologies, such as the embolism pointed out by the orange arrow in Figure 2.12.

2.6 Discussion

CR has to account for a trade-off between the displayed size of the surrounding tissue and the vessel visibility, as shown in Figure 2.13. In case of showing only the vessel lumen, a small arc-length threshold is sufficient to preserve the visibility (cf. Figure 2.13a). If increasing the displayed size of the surrounding tissue while leaving the arc-length threshold constant (cf. Figure 2.13b), the visibility of the vessel lumina deteriorates. The reason for this is that pixels farther away from the centerline collide with pixels that exhibit a large distance along the projected vessel graph. Hence, the arc-length threshold allows the surrounding tissue that is closer to the view plane to overwrite the vessel lumen farther away. To solve this problem, the arc-length threshold has to be increased simultaneously to correspond to the displayed size of the surrounding tissue (cf. Figure 2.13c).

In general, this trade-off results from the early discretization of the vessel geometry in 2D image space, since the 3D visibility information is lost. The technique we propose tackles this problem by using the depth information together with the projected vessel graph, but manual adjustment may still be necessary. Chapter 3 describes an approach that solves this issue by using a cost function and by computing the cut surface entirely in 3D without any manual interventions.

CPR and mpCPR have been designed for the investigation of vessels that mainly follow one principal direction. By allowing to rotate around one axis, the entire lumen of a vessel can be investigated. This is applicable for most vessels of the human lower limbs, but when considering other application areas, such as cervical or pulmonary vessels, an unrestricted navigation is required in order to entirely explore the respective vessel lumina. CR theoretically allows this, however, the arc-length threshold needs to be adjusted to provide a good balance between the vessel visibility and the displayed size of the surrounding tissue.

2.7 Evaluation

To assess the clinical relevance of visualizing spatially arbitrarily oriented vessels, we performed a study with six radiologists, based on a questionnaire (cf. Appendix A). CR is compared to CPR and mpCPR according to four different criteria with 34 questions. The following criteria have been identified (cf. vertical axis of Figure 2.14):

1. No significant difference between CPR and CR was found when visualizing a **single vertical vessel**. This should demonstrate that CR is capable of providing the same results for vertical vessels as the well tested and evaluated CPR technique [129]. Most participants see the visualization of the additional organs besides the vessels (surrounding tissue) as desired. Hence, the possibility to adjust the vessel radius in order to increase the displayed size of the surrounding tissue was rated very useful when using CR. This allows the compensation of a possibly too narrow vessel radius and the investigation of other pathologies or suspicious regions outside the vessel lumen.

2. For the assessment of **multiple vessels**, we presented to the participants visualizations of human peripheral pulmonary vessels and cervical vessels. In case of arbitrarily oriented vessels CR has been rated superior to mpCPR since it preserves the structure of the lumen while simultaneously accounting for correct vessel visibility. In fact, this was the key motivation for this technique. Moreover, the participants are particularly interested in the visualization of arbitrarily oriented vessels, since this offers them the opportunity to detect pathologies faster or at all. Hence, most participants rated the investigation of multiple vessels as very useful. When using CR, most of the vessels were shown without surrounding tissue. However, the majority of the participants rated the visualization of the surrounding tissue as shown by mpCPR as desired.

3. Generally, **halos** are desired by the majority of the participants to depict spatial relations and enhance the depth perception. A small halo size is considered to be sufficient and in the case of visual clutter it is helpful to be able to adjust the halo size.
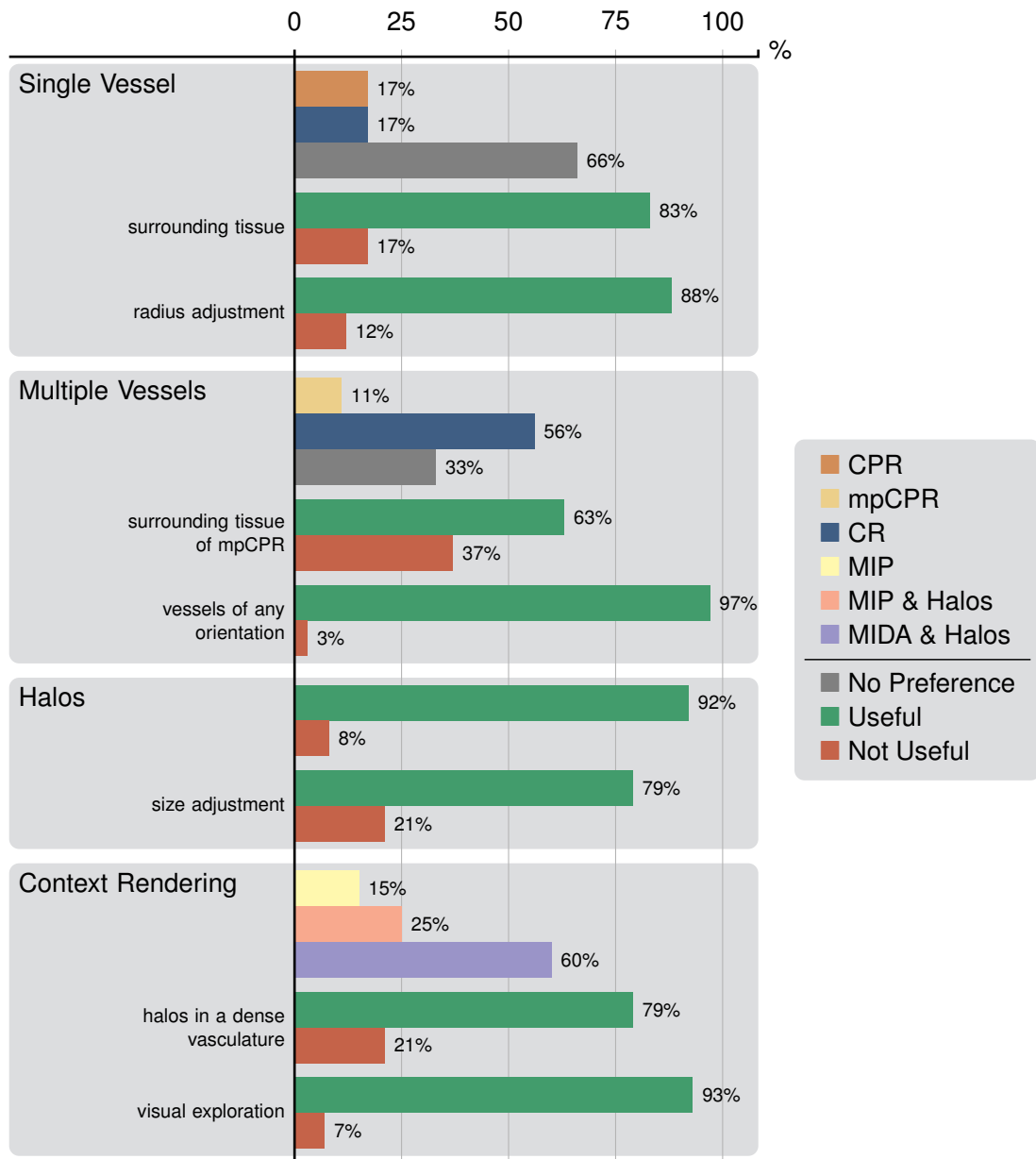
Figure 2.14: Evaluation of CR using a questionnaire (cf. Appendix A). It consists of 34 questions divided into four criteria (vertical axis). The horizontal axis shows the ratings of the participants in percent. There is no significant difference between CPR and CR if investigating the lumen of a single vessel. CR is the preferred choice for the assessment of multiple vessels. The visualization of the surrounding tissue is more preferred for a single vessel, since it becomes cluttered for multiple ones. Halos are rated overall very useful and MIDA was the preferred choice of context visualization.

4. In terms of **context rendering**, the participants rated MIDA better than MIP. However, both methods have no effect on the perception of the vessels. If investigating a dense vasculature together with a context visualization, halos are desired. The visual exploration of a dense vasculature by interactive selection and filtering of vessels is highly favored by the participants in order to detect pathologies or reveal them faster.

Concluding the evaluation, CR got a positive response, especially when investigating vessels of spatially arbitrary orientation. This would justify the application of CR, because handling such vessels is the main rationale of this technique. Enveloping the lumen with halos is also appreciated if investigating a dense vasculature.

2.8 Summary

In this chapter we described Centerline Reformation (CR), a technique for vessel lumen visualization and reformation of spatially arbitrarily oriented and branched vessels. This technique is based on vessel centerlines, which are determined by a vessel-detection pipeline and supplemented by an estimation of vessel radii. Subsequently, the centerline and radius information is used in the reformation, where vessel, halo and background areas are detected and rendered in different ways. Halos augment the vessel lumen in order to provide better visual cues if dense vascular structures are investigated. In order to increase the overall spatial awareness, the lumen visualization can be embedded into a context visualization. However, since this technique is operating in 2D image space, a trade-off between the displayed size of the surrounding tissue and the vessel visibility has to be taken into account. In Chapter 3 we describe an improvement by estimating and rendering the cut surface entirely in 3D.

He that will not apply new remedies must expect new evils; for time is the greatest innovator.

—Francis Bacon

3

Vessel Visualization using Curved Surface Reformation

Visualizations of vascular structures are frequently used in radiological investigations to detect and analyze vascular pathologies such as stenoses or occlusions. Curved Planar Reformation (CPR) is a wide-spread method that is designed for the investigation of blood vessels that exhibit one dominant direction. To analyze the lumina of arbitrarily oriented vessels, Centerline Reformation (CR) has been proposed (cf. Chapter 2). Both methods project the vessels into 2D image space in order to reconstruct their lumina. This chapter presents Curved Surface Reformation (CSR), a method that computes the vessel lumen entirely in 3D. This offers high-quality interactive visualizations of vessel lumina and remedies problems of previously established methods such as ambiguous visibility cues or premature discretization of centerline data. CSR maintains exact visibility information until the final query of the 3D lumina data.

VESSEL diseases, such as atherosclerosis or pulmonary embolisms, are becoming of an increasing medical concern in our aging society. Thus, the analysis of blood vessels for their diagnosis and treatment are important research fields of radiology. Angiographic interventions, such as stenting, balloon dilatation, or bypass surgery, need to be planned with care and precision, due to their major impact on the patient's health state. In order to optimally

---

[1]These authors contributed equally to this work. Thomas Auzinger provided the mathematical theory for the proposed technique, described in Sections 3.2.1 and 3.2.2.

(a)

(b)

(c)

(d)
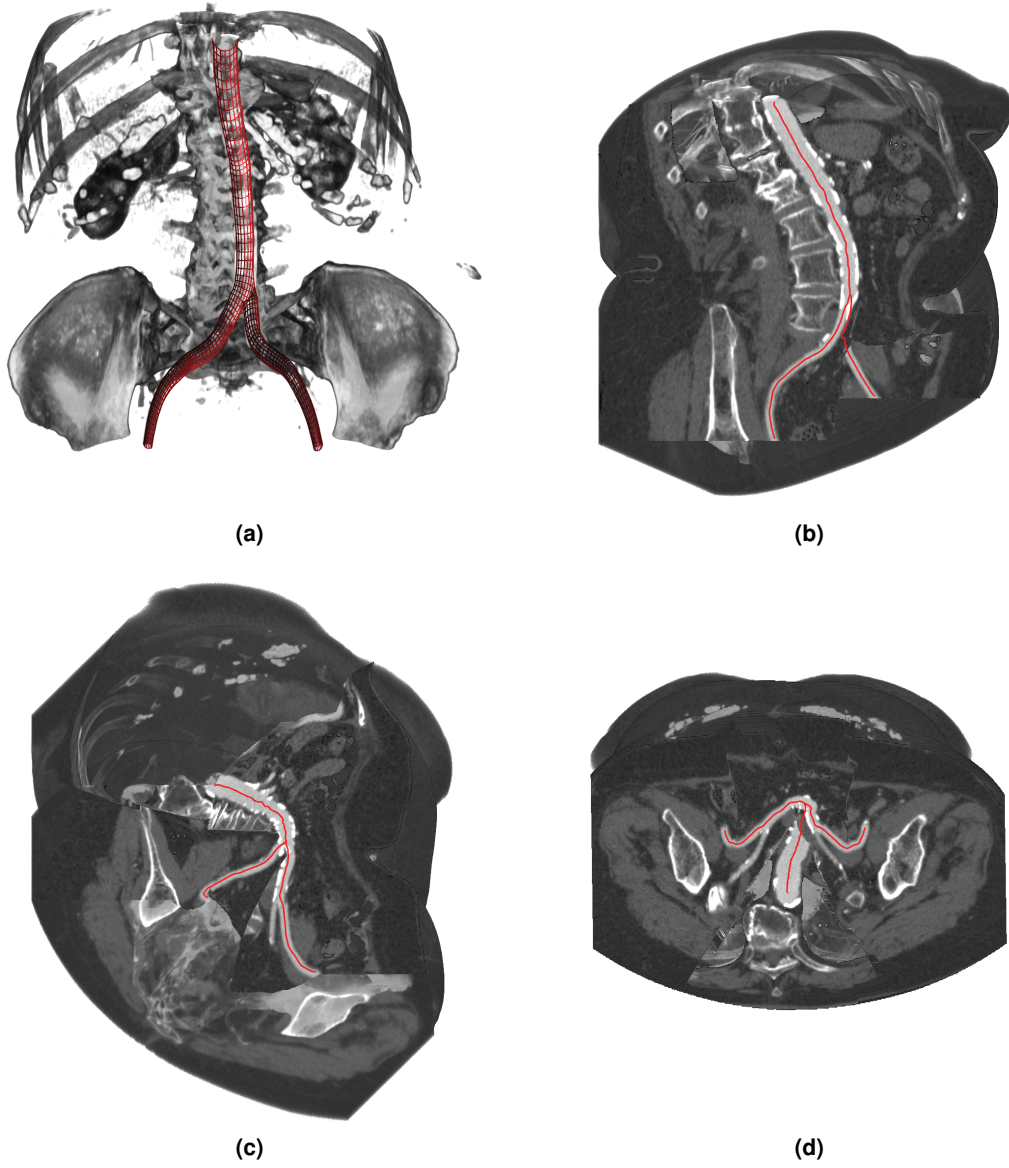
Figure 3.1: Demonstration of Curved Surface Reformation (CSR) based on the human abdominal aorta. **(a)** shows a 3D direct volume rendering of the data set together with the surface of the vessel tree (red wireframe). The remaining three images present our approach for visualizing the vessels' interior by generating a view-dependent cut surface through the vasculature. Our method features a smooth cut through surrounding tissue **(b)**, correct vessel lumen portrayal even at grazing angles **(c)** and the automatic placement of cutaways to allow inspections of large parts of the vasculature in a single view **(d)**. The visibility of the vessel tree is correctly resolved for every view direction.

Table 3.1: Aspects and improvements of Curved Surface Reformation (CSR) with respect to CPR and CR. Our method retains all positive properties of the most relevant state-of-the-art techniques and extends several aspects significantly.

	CPR	CR	CSR
Lumen Rendering	Pixel-Based	Pixel-Based	Ray Casting
Vessel Orientation	Restricted[1]	Unrestricted	Unrestricted
View Direction	Restricted[2]	Restricted[2]	Unrestricted
Visibility	None	Fair[3]	Good
Interactive	Yes	Fair	Yes

[1]vessels should run along one major direction
[2]rotation around one axis
[3]trade-off between visibility of lumen and surrounding tissue

decide on the therapeutic procedure, specific diagnostic methods are required. They assess the health state of blood vessels and answer clinically relevant questions such as, e.g., if blood is partially or entirely hindered from flowing through a vessel by calcifications or soft plaque.

The gold standard for angiographic imaging is DSA, a non-tomographic procedure. However, with the capabilities of modern medical scanners, less invasive tomographic data acquisition modalities, like CTA or MRA, are becoming increasingly popular. Both methods require the injection of a contrast agent into the patient's vasculature before the actual scan, to opacify the blood vessels in the obtained volumetric data set.

Confronted with a tomographic data set, special visualization techniques are required to assess possible vessel pathologies. Among these methods are Curved Planar Reformation (CPR) and Centerline Reformation (CR), which create a curved cut through a vessel along its central axis (*centerline*) to visualize its interior (*lumen*). Through cut surface rotation around the centerline of the vessel, they allow the identification of relevant blood flow obstructions or pathologies on the vessel walls. CPR has been initially designed for the visual analysis of peripheral arterial occlusive diseases, where the vessels are predominately oriented along the human lower extremities. In the majority of cases visualizing spatially arbitrarily oriented vessels with this method leads to artifacts. CR addresses this limitation by employing wavefront propagation for the lumen visualization. However, both methods operate in 2D image space, thus suffering from a premature discretization of the vessel geometry, like decreased precision of centerline location and loss of visibility information.

In this chapter, we describe Curved Surface Reformation (CSR), a vessel reformation technique that is designed to rectify these shortcomings (cf. Table 3.1). Our approach creates a view-dependent cut surface of the vasculature without the need to adjust any parameter. The main contributions of this technique are:

- A method to generate the cut surface along a vessel centerline completely in 3D, thus avoiding limitations of previous 2D methods.

- The correct handling of occlusions of different parts of the vasculature by employing a cost function on the cut surfaces.

- An automatic generation of cutaways on the cut surfaces to reveal as much of the vessel tree as possible.

- A Level of Detail (LOD) approach to smoothly extend the cut surface into the surrounding tissue.

- The ability to freely navigate (i.e., rotate, translate and zoom) within the vasculature at interactive frame rates.

- An outline of the corresponding rendering pipeline and its implementation as well as feedback by domain experts.

Additionally, we employ silhouette rendering to visually convey depth cues more prominently. Contextual information around the cut surface is provided by means of any common volume rendering technique, e.g., MIP, MIDA or DVR.

3.1 Related Work

The method proposed in this chapter extends several aspects of CPR (cf. Section 1.3.1) and CR (cf. Chapter 2), which are shortly described in this section.

3.1.1 Cutaways

Diepstraten et al. [36] present a set of rules for rendering interactive cutaways of polygonal data. Burns and Finkelstein [20] describe view-dependent cutaways for polygonal scenes. Li et al. [90] present a system for creating cutaways of complex objects in real-time. They apply visual styles from conventional illustrations such as various cutting types (box, tube, or window cuts), visual cues (edge shadows and shading) and inset cuts that cut deeper layers of an object with a smaller extent. Sigg et al. [142] proposed a degree-of-interest function for interactively specifying important features instead of manually placing them. In an iterative user-centric optimization process, cutaway primitives (cuboids, spheres, or cylinders) are optimally placed in order to allow a clear view of the desired object in the context of polygonal meshes and volumetric data. McInerney and Crawford [99] present a paint roller as an interaction metaphor for specifying the shape of the cutaway manually, while retaining ribbons of the occluding object. Burns et al. [21] use an importance function for generating volumetric contextual cutaways for medical visualization. They obtain a smooth transition between the occluder and the important object. Lidal et al. [91] give design guidelines with the aim to enhance shape and depth of the focused object in relation to its context. McGuffin et al. [98] use volume deformations and a set of interactive widgets to offer users the possibility to virtually browse through different layers of medical volume data. CSR will automatically create cutaways (cf. Figure 3.1d) to reveal occluded vessels by means of a cost function.

3.1.2 Volume Clipping

Konrad-Verse et al. [79] describe a virtual resection tool for organs employing user-placed meshes. After the user initially paints a stroke on the desired organ, a virtual cutting plane is computed via a principal component analysis. Additionally, the plane can be deformed in order to include or exclude objects from the cutting. Birkeland et al. [9] describe an illustrative clipping surface by means of physical properties of elastic membranes. It can serve as an illustrative slice with local DVR confined to its vicinity. User adjustment is facilitated by introducing additional force fields. To avoid cutting near objects, the surface adapts to salient features of the underlying data. Weiskopf et al. [167] describe interactive clipping of convex and concave objects from a volume, while accounting for proper volume shading. Wang and Kaufman [164] proposed a method for volumetric sculpting. They apply various operations on the volume at voxel level. Zhang et al. [176] present a real-time clipping strategy for visualizing data inside a volume. They compare several classifications for volume rendering with ray casting. For further information considering physically based deformable models, we refer to the survey by Nealen et al. [105]. In our approach, the volumetric data is cut by a curved surface.

3.1.3 Curve Simplification

In our technique, we simplify centerline curves to generate a coarse representation of the vessel tree to infer the large-scale behavior of the cut surfaces. As an old problem from computational geometry, it was already investigated by Imai and Iri [56, 57] for polygonal curves in the late 1980s. The most commonly used algorithm was developed by Ramer [121] and Douglas and Peucker [37]. Recent developments consider an improved distance metric [49] or utilize Bézier curves [25] for simplification.

3.2 Curved Surface Reformation

In the field of radiology, the diagnostic visualization of vascular structures plays a vital part in the investigation of certain vessel pathologies. Among occlusive diseases, stenoses are of particular interest. They can be caused by calcifications or soft plaque on vessel walls. The manual analysis of the raw medical imaging data of vessels is very time-consuming, and the use of medical visualization can dramatically improve its efficiency. Visualization methods usually require additional information on the imaging data, such as the locations of the vessel centerlines. These are modeled by radiological assistants in their daily clinical routine, in which they are assisted by semi-automatic detection methods such as the technique of Kanitsar et al. [67]. In the context of our visualization technique, centerline data is treated as input that was generated in a pre-processing step. Specialized visualization algorithms are then used for inspection of regions of interest and detection of pathologies.

General purpose methods can produce misleading visualizations. An example, if using MIP, is that vessels, which have concentric calcifications on their walls, incorrectly appear as completely occluded. To remedy this, planar reformations create a cut through the tissues or, as it is the case for vessel reformation, a cut along the vessels to visualize their interior. These

approaches provide a good overview of the vessel lumen and enable the specialist to deliver a qualified judgment on the severity of pathologies.

Different vessel reformation methods make various assumptions of the vessel geometry. CPR and its extension for multiple vessels, mpCPR [68], have been designed for the inspection of peripheral arterial occlusive diseases, where vessels strongly follow one principal direction. For display, the vessel is aligned with the up-axis $\mathbf{u}$, and the view direction is taken orthogonally to it. The cut surface is then spanned by the centerline and the direction that is orthogonal to both $\mathbf{u}$ and the view direction. This entails two major restrictions: the view direction can only rotate around the up-axis, and the cut surface degenerates if the vessel direction becomes orthogonal to $\mathbf{u}$. The latter case leads to excessive vessel thinning as shown in Figure 3.7a. A possible workaround to mitigate this effect is the stretching or straightening of the vessels. However, this interferes with the spatial perception of the displayed vessels, which is usually not desired by domain experts. Furthermore, the initial projection of the centerline into 2D discards the visibility information, and overlapping vessels cannot be kept apart.

CR (cf. Chapter 2) removes some of these drawbacks by using wavefront propagation on the projected vessel data. Although this allows the depiction of the lumen of arbitrarily oriented vessels, it still operates in 2D image space. This leads to a significant loss of visibility information due to the necessary projection. The cut surface is created by spreading the vessel locations to their surroundings. The visibility then has to be reconstructed by walking along the projected vessel tree. This leads not only to performance issues, but also requires the use of thresholds. They effectively determine the method's ability to either display the surrounding tissue or to correctly resolve the visibility. Figure 3.7b and Figure 3.9b provide an illustration of this trade-off.

To address these issues, we propose Curved Surface Reformation (CSR) to perform the lumen rendering entirely in 3D space. This new method allows the determination of the correct visibility of the various cut surfaces along the vessel tree. It also enables the extension of these surfaces into the surrounding tissue in a well-defined manner. In addition, we offer the possibility to use common interactions such as zooming, panning, or rotating around arbitrary axes in 3D for the first time in the field of vessel reformations. Our method builds on ray casting and is efficiently implementable on parallel hardware. We provide a CUDA implementation that runs at interactive frame rates.

In Section 3.2.1 the theory of our method is developed in a continuous setting. Its application on discrete input data is outlined in Section 3.2.2. Sections 3.2.3 and 3.2.4 discuss the resulting rendering pipeline (cf. Figure 3.4) and its implementation.

3.2.1 Theory

We employ ray casting of a surface defined by a cut through the vessel along its centerline, in order to render the lumen of a vessel. Since we do not require a fixed camera position and handle arbitrarily oriented vessels, the cut surface is dynamically generated, with its geometry depending on the view direction and the orientation of the corresponding vessel. In this section, we suppose as input to our method a set of differentiable three-dimensional curves, referred to as *vessel segments*, which constitute the centerlines of the relevant part of the vasculature for the visualization purpose. While our method does not require connected segments and is able

to handle arbitrary topologies of the vessel tree (cf. Section 1.2.2 for a detailed description), the common scenario is a connected set of vessel segments with possible branching points at their endpoints. Information on the radius of a vessel along its centerline is optional and can be used in the visibility computations (cf. Section 3.2.1.3). Since it is more comprehensible to demonstrate the geometrical concepts in a continuous setting, we take this route and present the adaptations to the actual, discrete input data in Section 3.2.2.

3.2.1.1 Surface Generation

Given the centerline curve $\mathbf{c}(t) : [t_0, t_1] \to \mathbb{R}^3$ of a vessel segment and a view direction $\mathbf{v}$, the *local (cut) surface* M is given by

$$M(s,t) = \mathbf{c}(t) + s\,\mathbf{v} \times \mathbf{c}'(t) \quad \text{with } t \in [t_0, t_1] \text{ and } s \in \mathbb{R}. \tag{3.1}$$

This definition is motivated by the requirements of having the local surface contain the centerline and be as perpendicular to the view direction as possible. In contrast, CPR and mpCPR use a fixed frame in the form of $\mathbf{c}(t) + s\,\mathbf{v} \times \mathbf{u}$, where $\mathbf{u}$ denotes the up-axis, and the view vector is constrained by $\mathbf{v} \cdot \mathbf{u} = 0$.

In order to display vessel cross-sections at the endpoints, we add two half-planes that are perpendicular to the view direction, i.e., for the start $\mathbf{c}(t_0)$ and endpoint $\mathbf{c}(t_1)$. The half-planes are given by

$$\mathbf{c}(t_0) + s\,\mathbf{v} \times \mathbf{c}'(t_0) + t\,\mathbf{v} \times (\mathbf{v} \times \mathbf{c}'(t_0)) \tag{3.2}$$

and

$$\mathbf{c}(t_1) + s\,\mathbf{v} \times \mathbf{c}'(t_1) - t\,\mathbf{v} \times (\mathbf{v} \times \mathbf{c}'(t_1)) \tag{3.3}$$

for $s \in \mathbb{R}$ and $t \in \mathbb{R}_+$. In the particular case of an alignment of the view direction and the centerline ($\mathbf{v} \times \mathbf{c}'(t) = \mathbf{0}$), a half-plane with a boundary perpendicular to the last non-aligned centerline direction has to be added. In case the centerline is parallel to the view direction at one of its endpoints, a plane perpendicular to the view direction in this point is added. This ensures that a projection of the resulting local surface covers the entire view plane at least once and that the vessel cross-section is visible if the centerline curve is collinear with the view direction.

This construction provides the correct cut surface for the corresponding vessel segment in a sufficiently small neighborhood of the centerline. For a finite extent of the vessel, however, this naive approach exhibits various deficiencies. In the following sections, we present how the approach we propose tackles these issues in order to create an entirely three-dimensional vessel reformation.

3.2.1.2 Main Challenges

The local surface M, as given in Equation 3.1, depends on both the view direction $\mathbf{v}$ and the local geometry of the centerline, which is specified by its tangent vector $\mathbf{c}'(t)$. Although this is reasonable for a small neighborhood of the centerline, this definition exhibits two types of undesired behavior with advancing distance from the centerline. Firstly, since the vessel lumen close to the centerline is the main focus, it should be visible whenever it is not directly occluded by either the same centerline or different vessel segments. However, this behavior is not shown

by M, since only the front-most parts of the entire vessel tree are visible. Secondly, small local details or noise are amplified at the outer regions of the surface, leading to self occlusions and depth discontinuities when viewed along the view direction $\mathbf{v}$ (cf. Figure 3.3). A solution to the first issue is given in Section 3.2.1.3 and to the second one in Section 3.2.1.4.

3.2.1.3 Cost Function

To allow the inspection of as many vessels as possible within the same view, it is advantageous to reveal the local surface of all those vessel segments that are not located behind other vascular structures in the current view. Thus, we generate cutaways on the local surfaces of vessel segments closer to the viewer, based on the following two principles:

1. The closer a point on a centerline is located to the viewer, the more relevant is the associated part of the local surface.

2. The closer a point on a local surface is located to its centerline, the more relevant it is.

It is possible to mimic this behavior by making use of spatial cost functions for all vessel segments. For each centerline c_i of the vessel tree, we define a cost function

$$C_i(\mathbf{x}) = C_{\|}(\mathbf{x}) + \lambda C_{i,\perp}(\mathbf{x}), \tag{3.4}$$

where λ denotes the weighting between the component parallel to the view vector $\mathbf{v}$, i.e., $C_{\|}(\mathbf{x}) = \frac{\mathbf{x} \cdot \mathbf{v}}{\|\mathbf{v}\|}$, and the one normal to it. The latter is given as the distance $dist_{\mathbf{v},\perp}(\mathbf{x}, c_i)$ between $\mathbf{x}$ and the image of curve c_i when both are projected onto a plane P perpendicular to $\mathbf{v}$. The intuitive explanation of this approach is that the parallel cost component penalizes the depth of surfaces while the normal component penalizes the distance from the respective centerline.

By evaluating the cost function on all local surfaces and projecting these values onto a plane P perpendicular to $\mathbf{v}$, we obtain several cost values per point on P. In fact, each local surface contributes one or more cost values to each point on P, since they cover the entire extent of P due to the nature of their construction. An example is given in Figure 3.2c, where a local surface contributes six cost values for each point on P in the center region of the trefoil knot. Another illustration can be found in Figure 3.5d. Subsequently, the smallest cost value is selected at each point and the corresponding surface location is marked as visible. Consequently, the visible local surface is selected for each point on the view plane and the global visibility is resolved (cf. Figure 3.2). Possible ambiguities arising from several identical cost values at the same point of P can be almost always neglected, since these are part of one-dimensional boundaries where the visibility changes between different centerlines. In very rare occasions it is possible that entire local surface regions contribute the same cost values and that artifacts similar to z-fighting arise. As we did not encounter such cases in any of our experiments and this behavior only occurs for specific view directions (we conjecture that these form a one-dimensional subset of the two-dimensional space of all view directions), we feel safe to ignore them.

The preference for broader or thinner surrounding surfaces around vessels is controlled by the parameter λ in the cost function. A large λ allows the cutaways of occluded vessels to reach close to the visible centerline, by strongly penalizing the projected distance. In contrast, a small λ leads to a more liberal occlusion of vessels behind the current centerline.

54
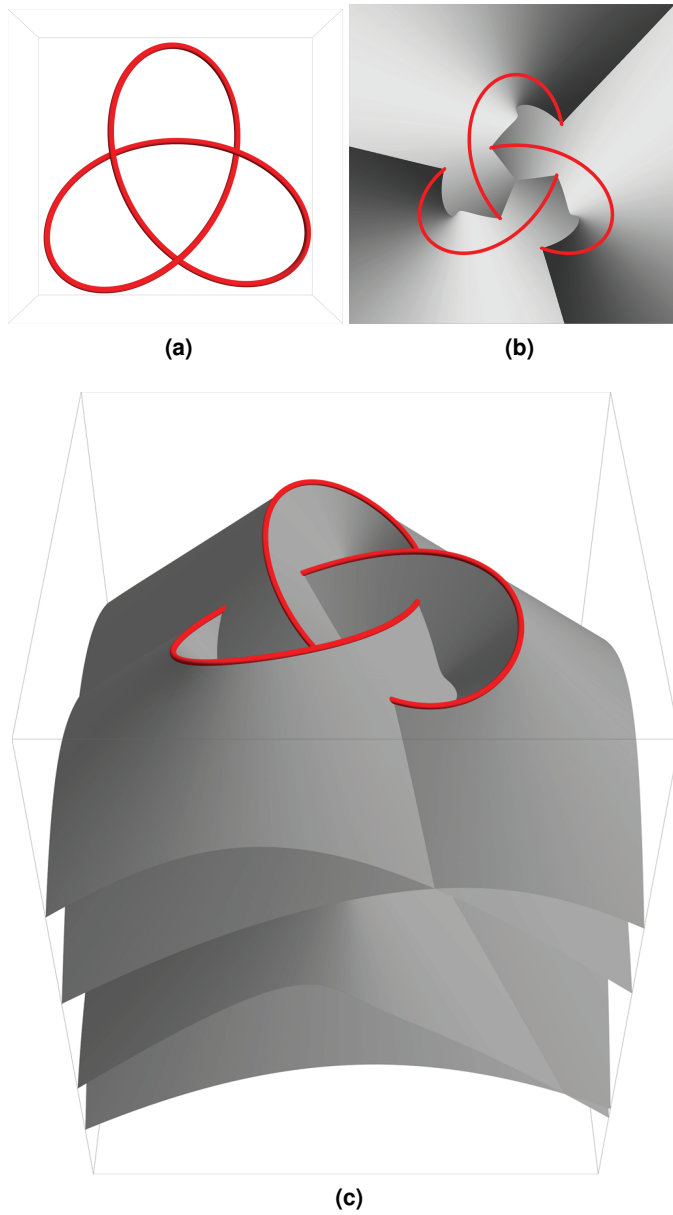
Figure 3.2: Illustration of the visibility resolution using a cost function. **(a)** shows a synthetic vessel input in the form of a trefoil knot. We use a cost function as given by Equation 3.4 defined on the generated local surface to determine its visible points, which are characterized by the lowest cost value along the view direction. The cost function for a frontal view of **(a)** is visualized in **(c)** by encoding the *cost value* as the depth of the local surface. Note that each vertical view ray intersects the local surface several times, and only the topmost intersection points constitute the visible surface. The final result in form of a depth image is given in **(b)**, where the grayscale encodes the depth of the local surface.

To guarantee the preservation of the full extent of vessels, so that cutaways do not cut into the vessel lumen of a visible centerline, a minor modification can be applied to the cost function. Such incidents can occur if two centerlines exhibit a small depth difference, since the cost function indicates a preference for choosing the occluded vessel very close to the centerline of the occluding vessel. These situations can be avoided by altering the normal component of the cost function to assign no distance cost to regions around the centerline within a certain vessel radius. This can be considered as placing a strip with possibly varying vessel radius around each centerline, in which the normal cost component of the associated cost function is zero. Consequently, a vessel behind another centerline will always have a higher cost, since both, the depth and distance component, contribute to its occlusion. In case of very dense vascular structures the local surface of the majority of visible vessels will not exceed the extent of the vessel itself, because a large number of cutaways is generated. In such occasions, our method would resemble dense line rendering and due to conceptual similarities, only slight modifications would ensure convergence to the illustrative method of Everts et al. [38].

Hence, our approach remedies the first problem with the initial definition of the local surfaces due to resolving the visibility of the local surfaces of the vessel tree. The second challenge, as described in Section 3.2.1.2, is tackled in the subsequent section.

3.2.1.4 Centerline Simplification

Although the local surface M, as defined in Equation 3.1, is geometrically appropriate in a neighborhood of its respective centerline, it nevertheless exhibits an undesired behavior globally (cf. Figure 3.3). The reason for this is the usage of centerline derivations in the definition of M, because small geometrical details along the vessel get amplified with increasing distance from the centerline. This leads, in general, to a multitude of undesired self occlusions of the local surface if viewed along the view direction $\mathbf{v}$.

To counteract this behavior, we propose a Level of Detail (LOD) approach based on centerline simplification. While small details of the centerline should be preserved in its close vicinity to provide a faithful representation of the vessel geometry, only the large-scale characteristics of the centerline should define the surface behavior in the surrounding volume. It would be possible to develop a theory of a continuous simplification of the centerline, yielding infinitely many LODs. However, justified by the discrete nature of the actual input data and the fact that the continuous formulation would not aid further understanding, we employ just a finite number of discrete levels to perform the simplification.

For a fixed number $(N + 1)$ of LODs, each centerline is simplified to obtain N increasingly smoothed versions of it, where the initial curve is preserved in level 0. The actual simplification method for discrete input data is specified in Section 3.2.2.2.

The visibility between the local surfaces of the smoothed versions of a centerline is again resolved with the aid of the cost function by evaluating it on the local surfaces of relevant LODs. Depending on the projected distance d between the centerline of a vessel segment and a point on the view plane, the two most relevant LODs k_0 and k_1 are determined by means of a selection function $f(d)$ to obtain

$$k_0 = \min(N, \lfloor f(d) \rfloor) \quad \text{and} \quad k_1 = \min(N, \lfloor f(d) + 1 \rfloor). \tag{3.5}$$
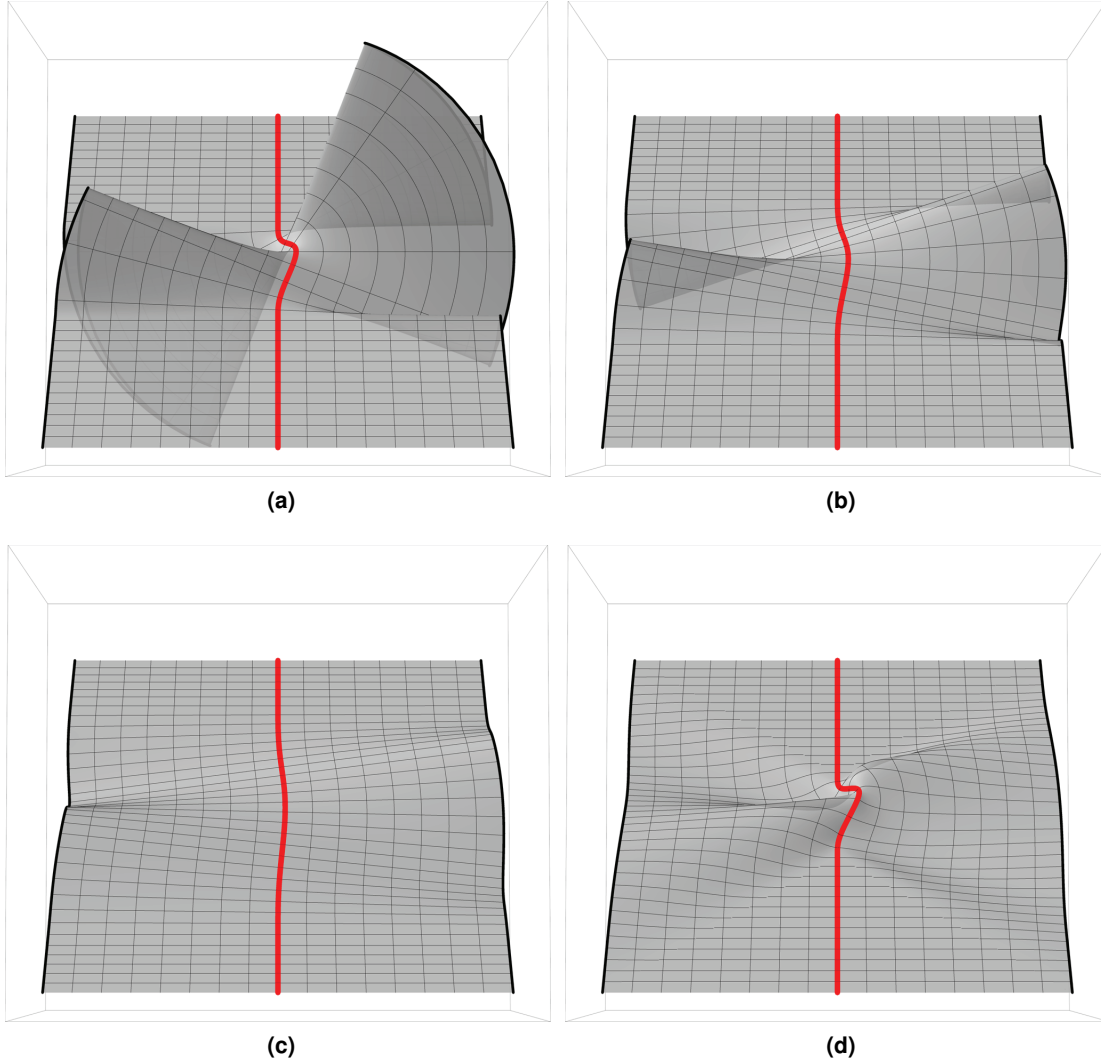
Figure 3.3: Illustration of the instability of the local surface with respect to small perturbations of the centerline (red). **(a)** exhibits severe distortions by a small scale detail of the centerline leading to multiple self occlusions of the local surface. These can be drastically reduced by progressive smoothing of the centerline as shown in **(b)** and **(c)**. Our proposed Level of Detail (LOD) method uses coarser and smoother representations of the centerline for increasingly distant parts of the surface. This eliminates the undesired self occlusions but preserves the detailed vessel geometry close to the centerline **(d)**.

We use a sublinear selection function to concentrate the initial LODs around the centerlines; in our implementation of the form $f(d) \propto \sqrt{d}N$.

As described in Section 3.2.1.3, we project the cost values of the two surfaces onto the view plane and, for each LOD separately, we chose the surface locations $\mathbf{i}_0$ and $\mathbf{i}_1$ with minimal cost for each point on the view plane. The final *cut surface* location $\mathbf{i}$ is then given as a linear blend of the two LODs, i.e.,

$$\mathbf{i} = (k_1 - f(d))\mathbf{i}_0 + (f(d) - k_0)\mathbf{i}_1. \tag{3.6}$$

This provides a smooth transition between the LODs and a gradual simplification of the local surface as a function of distance d. No blending is performed beyond the last LOD, since $k_0 = k_1 = N$. A representation of the result of this method is given in Figure 3.5e.

This concludes the theory section for our proposed method. Before describing the actual rendering pipeline, we outline the necessary adaptation of the aforementioned methods to handle discrete input.

3.2.2 Discrete Geometry

The theory in Section 3.2.1 was developed in a continuous setting that does not reflect actual computation hardware. This section covers the required discretization steps necessary for numerical processing.

3.2.2.1 Surface Generation

Assuming that a vessel centerline is given as a piecewise linear curve, the corresponding local surface consists of planar pieces, namely line stripes, connecting triangles and half-planes at the endpoints. In this section, we provide a brief description on how to generate such a local surface.

For a line segment, defined by the points $\mathbf{l}_0$ and $\mathbf{l}_1$, of the vessel tree, a line stripe is generated by extruding the line segment in direction $\mathbf{v} \times (\mathbf{l}_1 - \mathbf{l}_0)$ (cf. Figure 3.5a). Since this direction is perpendicular to the view direction $\mathbf{v}$, the stripe is located between the depths $d_0 = \mathbf{v} \cdot \mathbf{l}_0$ and $d_1 = \mathbf{v} \cdot \mathbf{l}_1$ along the view direction.

If two consecutive line segments L_0 and L_1, given by the three points $\mathbf{l}_0$, $\mathbf{l}_1$ and $\mathbf{l}_2$, are not collinear when projected onto the view plane, a gap would arise in the projected local surface in case only line stripes had been used. In order to avoid this, we use a triangle that originates in the connection point $\mathbf{l}_1$. The triangle edges extend along the boundaries B_0 and B_1 of the line stripes given by

$$B_0 = \{\mathbf{l}_1 + s\,\mathbf{v} \times (\mathbf{l}_1 - \mathbf{l}_0)\} \tag{3.7}$$

and

$$B_1 = \{\mathbf{l}_1 + s\,\mathbf{v} \times (\mathbf{l}_2 - \mathbf{l}_1)\}. \tag{3.8}$$

This ensures that the triangle covers the gap between B_0 and B_1. Since such a gap only occurs on one side (when projected onto the view plane), we choose either $s \in \mathbb{R}_+$ or $s \in \mathbb{R}_-$.

In order to complete the local surface, half-planes H_0 (respectively H_n) are added at the start and end point $\mathbf{l}_0$ (respectively $\mathbf{l}_n$) of a vessel segment. These are defined as

$$H_0 = \{\mathbf{l}_0 + s\,\mathbf{v} \times (\mathbf{l}_1 - \mathbf{l}_0) + t\,\mathbf{v} \times (\mathbf{v} \times (\mathbf{l}_1 - \mathbf{l}_0))\} \tag{3.9}$$

and, respectively, as

$$H_n = \{\mathbf{l}_n + s\,\mathbf{v} \times (\mathbf{l}_n - \mathbf{l}_{n-1}) - t\,\mathbf{v} \times (\mathbf{v} \times (\mathbf{l}_n - \mathbf{l}_{n-1}))\} \tag{3.10}$$

with $s \in \mathbb{R}$ and $t \in \mathbb{R}_+$.

In case a line segment L is collinear with the view direction, we add an additional half-plane using the definition of H_n above, but substituting the points $\mathbf{l}_{n-1}$ and $\mathbf{l}_n$ by the endpoints of the last non-collinear line segment before L along the centerline. An additional plane that contains the corresponding endpoint is created perpendicular to $\mathbf{v}$ if the first or last line segment of a centerline is collinear.

These constructions ensure that the piecewise planar surface of each centerline covers the entire view plane when projected onto it, as illustrated in Figure 3.5b. Due to the fact that we employ ray casting for evaluating the cost function on this surface, we can use simple geometrical intersection tests between the rays and the unbounded polygons. The cost function of Section 3.2.1.3 can be directly used for this purpose.

3.2.2.2 Centerline Simplification

The LODs of the vessel tree are computed in a preprocessing step. To generate coarser representations of the individual vessel segments, we employ progressive filtering with spline functions. The centerline of a given LOD is approximated by a cubic B-spline and resampled to generate the next LOD. The performance of this simple approach is sufficient, and the quality benefits by employing more sophisticated methods such as the curve simplification algorithm by Chuon et al. [25] are negligible. It is possible to faithfully represent the vessel segments with fewer line segments, due to the absence of fine details in higher LODs. In our implementation, we pursue an aggressive pruning as we drop half of the points for each successive LOD. For a sufficiently dense initial sampling of centerlines as in our input, we did not observe any artifacts resulting from this optimization, which drastically reduces runtime.

As described in Section 3.2.1.4, our LOD approach uses the selection function $f(d)$ depending on the projected distance d of the ray from the centerline. This value can easily be determined by computing the distance between the ray and the line segments of the initial centerline, i.e., the unsmoothed LOD 0.

3.2.3 Rendering

This section presents the rendering pipeline of CSR as outlined in Figure 3.4. It takes a vessel tree, consisting of line segments, and a volume representation of the surrounding tissue as input and generates an image of the cut surfaces along the vessel centerlines. As we employ ray casting at several stages of the pipeline, various buffers in the size of the final output image are used to store intermediate values. A sequence of such intermediate results is given in Figure 3.5. In the exceedingly rare case of z-fighting artifacts (cf. Section 3.2.1.3), we prevent their aggravation with temporal flickering by maintaining a strict rendering order of the input data. As a preprocessing step, the LODs of the vessel tree are computed as described in Section 3.2.2.2.
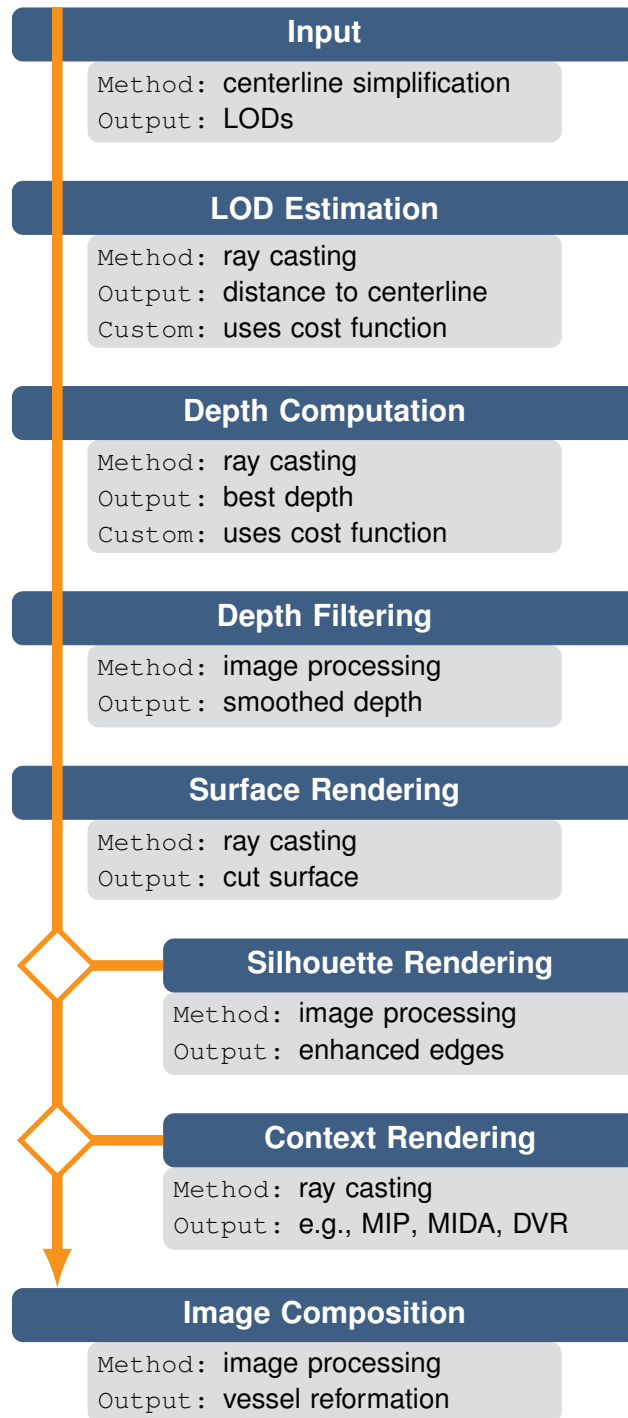
Figure 3.4: Rendering pipeline of Curved Surface Reformation (CSR). The first entry of every stage denotes the used method and the second item gives the output. The custom entry indicates the stages where the cost function is used.
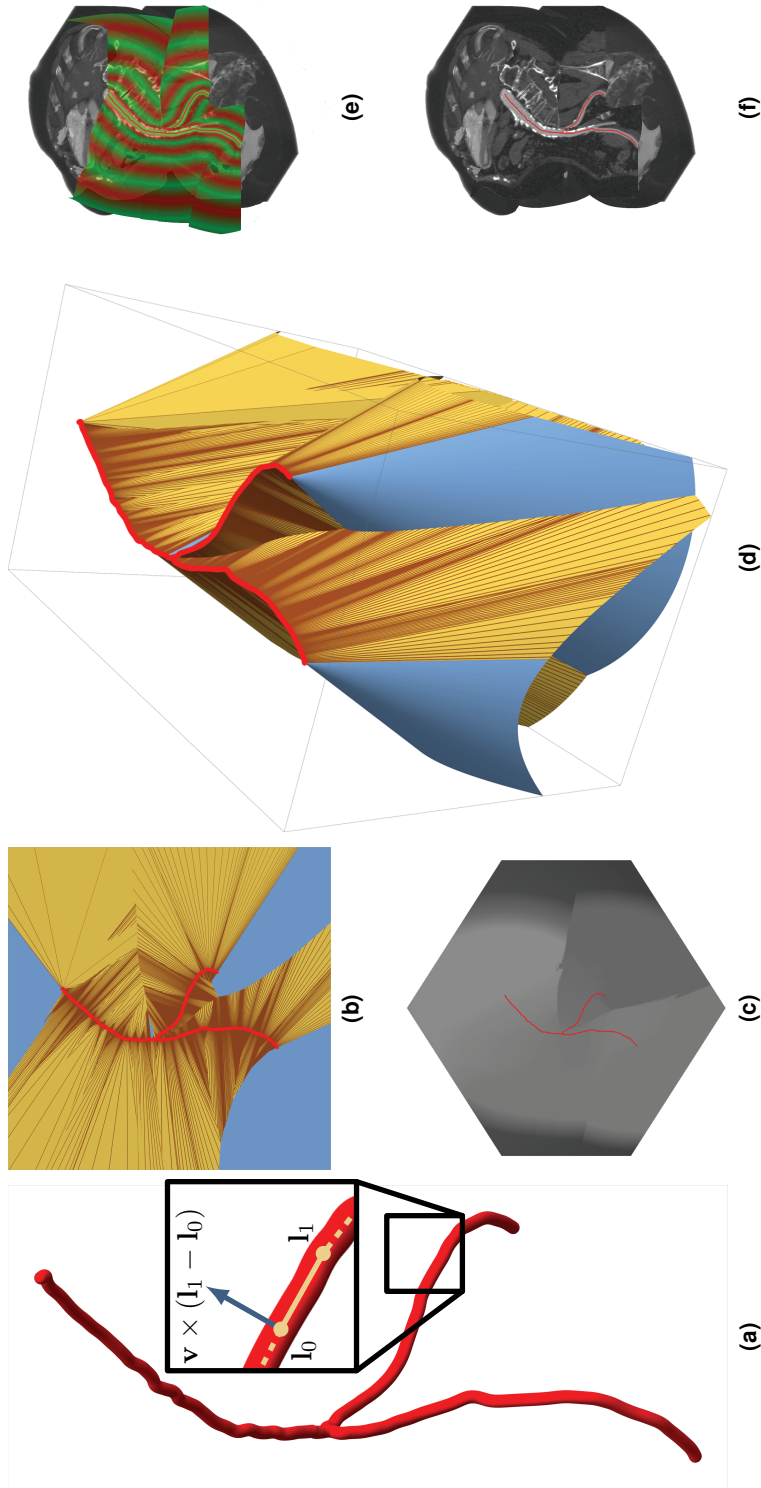
Figure 3.5: Illustration of the rendering pipeline. **(a)** depicts an input vessel tree consisting of 800 line segments. A detailed view of a single line segment illustrates the variables of Section 3.2.2.1 with the view direction piercing orthogonally through the paper. The geometry of the local surface of the unsmoothed centerlines is shown in **(b)** where the planar parts are colored according to their type—dark brown for line stripes, light brown for triangles and blue for the half-planes at the endpoints. The final depth buffer after the depth computation and filtering stages is depicted in **(c)** and the corresponding cost function is illustrated in **(d)**. **(e)** gives an overview of the LODs which are alternately colored in red and green. It also shows the part of the final output **(f)** that is covered by the cut surface whereas the other parts are generated by the context rendering stage.

3.2.3.1 LOD Estimation

This stage generates a distance buffer that stores the projected distance of each image location to the nearest centerline of the vessel tree. This data is used as the argument d for the LOD selection function $f(d)$ as described in Section 3.2.1.4.

3.2.3.2 Depth Computation

Using the distance information of the previous stage, we determine the two relevant LODs using the method of Section 3.2.1.4. By using ray casting, we collect the cost values for all intersection points with local surfaces along the ray. This is done separately for each pair of LODs, and we retain the intersection points with the minimal cost for each pixel. The final intersection point is a weighted blend between the respective LOD intersections to ensure smooth progressions from one LOD to the next. The output of this stage is the depth of the final intersection point in a depth buffer.

3.2.3.3 Depth Filtering

To remove aliasing artifacts that arise from undersampling of a high-frequency depth signal caused by fine geometric details of the vasculature, the depth image is convolved with a smoothing filter. This is necessary when sampling cut surfaces, which extend from centerlines that are nearly collinear with the view direction, since their planar parts shrink to sub-pixel sizes. We use a Gaussian filter kernel with standard deviation σ for this task and set its full width at half maximum (FWHM) in frequency space to half the Nyquist frequency of the output image, i.e., $\sigma = 2\sqrt{2\ln 2}/\pi$ pixel. The discrete version is cut off at 3σ, which gives a kernel size of 7×7. The output makes up the depth values of the desired cut surface (cf. Figure 3.5c).

If the filter size is significantly increased, the depth discontinuities between the visible cut surface regions of different parts of the vessel tree are smoothed. In the final rendering, this leads to steep 'slopes' between the regions. We do not utilize this fact in our method and leave it just as an observation.

3.2.3.4 Surface Rendering

A simple lookup into the volumetric intensity data set, which surrounds the vessel centerlines, is performed with the depth values of the cut surface. We use trilinear interpolation for this task and obtain the intensity values of the visible vasculature's lumen and of the surrounding tissue. Afterwards, we apply a user-specified windowing function to map these values to grayscale colors and opacities.

3.2.3.5 Silhouette Rendering

After determining the depth of the cut surface and the subsequent filtering step, depth discontinuities still remain. These are, however, intentional, and constitute the switch from the surrounding of one part of the vessel tree to another one. Since these important spatial cues might not be easily perceivable, we improve the three-dimensional visual perception of the cut surfaces
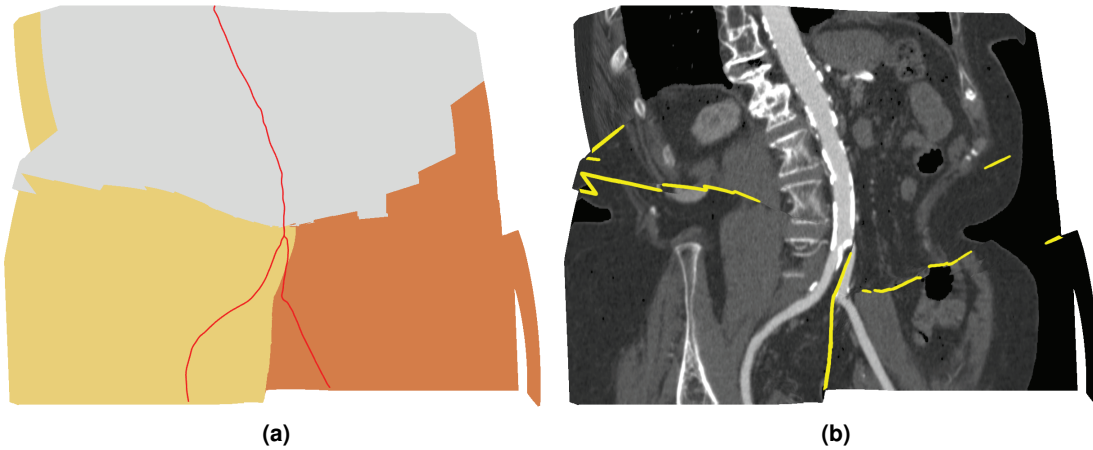
Figure 3.6: Silhouette rendering. **(a)** shows the color coded influence zones of the three vessel segments. Small depth discontinuities at the zones' borders and large discontinuities anywhere are presented as yellow silhouettes in **(b)** as an overlay of the cut surface.

by highlighting these discontinuities. This is achieved by modulating a user-specified silhouette color (yellow in our case) with the response of a customized filter function.

Large depth discontinuities are revealed by applying a Sobel edge-detection filter. However, small discontinuities between spatially close vessel segments from different parts of the vasculature are not captured. To identify these, every point of the projected cut surface is marked with a unique identifier of the corresponding vessel segment (cf. Figure 3.6a). Small depth discontinuities can only occur along the borders of these influence zones of the vessel segments while branching locations remain unaffected, since they are continuous in depth.

Thus, we amplify the response of the Sobel filter at these borders. We observed that a simple multiplication by a constant factor already yields adequate results and improves the depth perception of vessel occlusions near branching locations. A final smoothing of the combined filter response provides anti-aliasing of the discontinuity lines and gives our final color modulation (cf. Figure 3.6b). This allows for a better perception of depth discontinuities.

3.2.3.6 Context Rendering

Due to the fact that the cut surface displays only parts of the volume, the perception of the overview can suffer. To remedy this, we optionally add a final context visualization step to the CSR workflow. Straka et al. [146] propose a focus+context approach by embedding the vessel lumen (focus) into a volume rendering (context). We render a context behind the regions of cut surfaces at locations where they lie outside the volume. When rotating, the context visualization becomes apparent, and the domain expert can clearly perceive the spatial location of the region of interest within the data set. Figure 3.5f shows such a context visualization, using MIDA as proposed by Bruckner and Gröller [18]. Any other volume rendering technique could serve as context visualization as well.

Table 3.2: Performance timings in milliseconds per frame of CSR for the data sets presented in the results. The most time-consuming operations are the LOD estimation, as every line segment has to be evaluated during this stage, and the context rendering. The depth computation is less expensive and all other operations have negligible temporal cost.

	Figure 3.1	Figure 3.7	Figure 3.9
Data Size	$512^2 \times 256$	$512^2 \times 1305$	$512^2 \times 575$
LOD Estimation	97.8 ms	272.6 ms	133.0 ms
Depth Computation	13.5 ms	105.6 ms	39.0 ms
Depth Filtering	1.7 ms	1.7 ms	1.7 ms
Surface Rendering	0.9 ms	1.0 ms	1.1 ms
Silhouette Rendering	7.6 ms	7.7 ms	7.7 ms
Context Rendering	96.9 ms	270.7 ms	131.8 ms
Frame Time	218.4 ms	659.3 ms	314.3 ms

The context is displayed, whenever a ray hits the volume and the cut surface lies outside the volume at its pixel location or when the windowing function makes the cut surface completely transparent. In the first case, the rays traverse the whole volume, whereas in the second case, the rays start at the depth of the cut surface (cf. Figures 3.1b to 3.1d, 3.5f, and 3.8). The advantage of this context visualization is that it provides additional spatial cues when rotating while still depicting the occlusion-free cut surface.

3.2.4 Implementation

Our technique was implemented as part of the AngioVis [2] framework. The LODs of the vessel tree centerlines are generated on the CPU as a preprocessing step at startup and regenerated after changes to the vessel tree. The remaining stages of Section 3.2.3 are implemented in CUDA and use OpenGL just for computing the entry and exit positions of the rays. This allows the whole pipeline to make use of the parallel computing capabilities of current GPUs which leads to an interactive performance of our implementation.

We analyzed the computing times of all individual stages of the CSR rendering pipeline. The outcome is summarized in Table 3.2 with the timings given in milliseconds. The measurements have been taken on an Intel Core i7 with 3.07 GHz with 12 GB system memory and a GeForce 680GTX with 4 GB video memory. The LOD estimation is the most costly step, as each ray is checked with every line segment of the most detailed LOD of the vessel tree in order to compute an accurate distance. The performance of this step could be increased by gradually computing the distance from the coarsest to the finest LOD and updating only relevant distances in each step. The depth computation is less expensive, since only two coarse LODs are tested for most of the rays. The following operations consume nearly constant, insignificant amounts of time. Context rendering takes a considerable amount of time due to the ray marching of MIDA. Nevertheless, even our unoptimized implementation of CSR is capable of interactively rendering

the cut surface together with the context visualization. Ray casting could also be substituted by rasterization of the local surface primitives similar to the method of Hoff et al. [53]. A performance gain is not guaranteed, however, as the cost function methodology cannot rely on the hierarchical depth-buffering capabilities of graphics hardware.

3.3 Results and Discussion

In this section, several results that were obtained with our method are presented. The weighting $\lambda = 10$ in the cost function (cf. Equation 3.4) is used for all subsequent results. First, we present a small data set to illustrate the capabilities of our technique. With the second and third data set, we compare CSR with existing methods, such as mpCPR and CR, in order to highlight our improvements.

Figure 3.1 presents a CTA data set of a human abdominal aorta at its first bifurcation displayed for several view directions. A DVR visualization is shown in Figure 3.1a together with the vessel tree rendered as wireframe model in red. Figures 3.1b-3.1d give results of our method together with MIDA as context visualization. Visibility is correctly resolved in Figure 3.1b, as the left vessel branch is partially hidden due to its larger distance from the viewer. The cut surface is smooth even far from the vessel due to our LOD approach and exhibits intended jumps in depth when changing from the influence zone of one branch to another one. Figure 3.1c shows a view from bottom right, which depicts the vessel lumen and surrounding tissue. The reason for the smoothness is again the continuous transition between different LODs of the vessel tree. A view from the bottom is presented in Figure 3.1d. Here, a cutaway is generated to show the lumen of the aorta, which is located farther away from the viewer than its two branches.

Figure 3.7 shows a CTA data set of the vasculature of the human lower extremities with a cross-over bypass below the bifurcation of the abdominal aorta. We compare mpCPR (3.7a) with CR (3.7b) and CSR (3.7c). Although mpCPR provides a continuous cut surface through the vasculature and its surrounding tissue, it cannot visualize the lumen of the bypass adequately. The lumen is incorrectly narrowed, since the bypass runs horizontally, a situation that cannot be properly handled by mpCPR. This issue is addressed by CR, but a trade-off between the display of the surrounding tissue and the vessel visibility has to be made. This leads to artifacts, as pointed out in the zoom-ins, stemming from the fact that the information of the left vessel overwrites information of the right one. CSR avoids these issues by rendering the lumen entirely in 3D. Also the visibility of the denser vasculature in the lower legs is correctly preserved. Figure 3.8 shows several rotated views using CSR with MIDA as context visualization.

A CTA data set of the human cervical vessels, including the carotid arteries, is shown in Figure 3.9. With mpCPR (3.9a), visibility is not preserved and the lumen of horizontally running vessels is not rendered correctly (cf. zoom-in). The surrounding tissue is, however, shown. With CR (3.9b), a trade-off between the display of the surrounding tissue and the visibility of the vessels has to be done. This is the reason why one vessel is cut off, as the vessel lies behind the surrounding tissue (cf. zoom-in). Correcting the visibility would further limit the size of the visible surrounding tissue. CSR (3.9c) preserves the visibility as well as provides a smooth cut through the surrounding tissue.
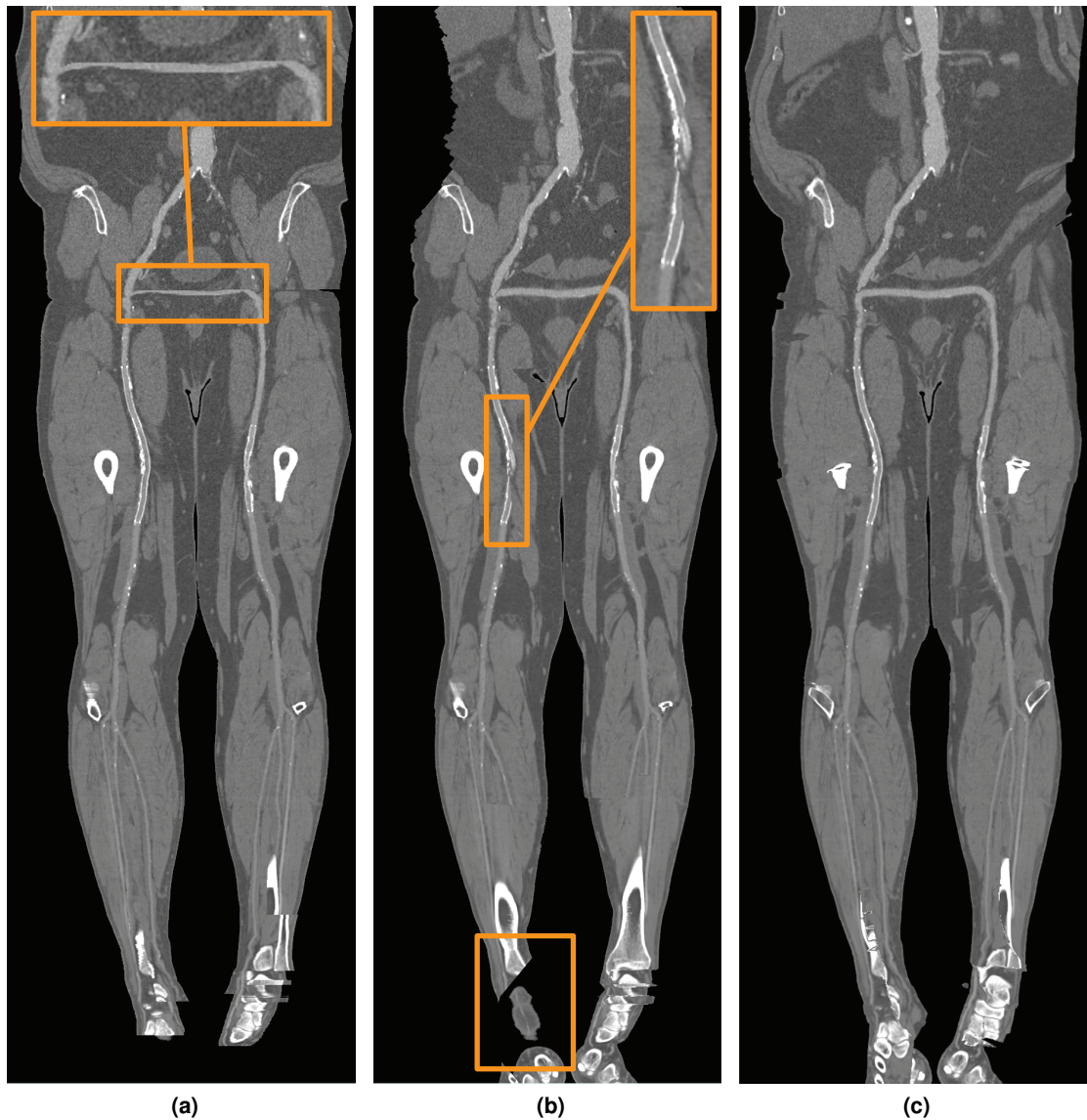
Figure 3.7: Comparison of mpCPR, CR and CSR based on a CTA data set of the vasculature of the human lower extremities with a cross-over bypass. **(a)** shows an mpCPR of the vasculature with an incorrectly narrowed lumen of the bypass (cf. zoom-in). **(b)** displays a CR which accounts for the correct lumen of the bypass, but shows artifacts resulting from the trade-off between vessel visibility and the displayed size of the surrounding tissue (cf. zoom-ins). The vessel radius is offset by 150 pixels and the arc-length threshold equals to 300 pixels. **(c)** presents CSR showing the correct lumen of the bypass and accounting for proper overall vessel visibility.

(a)   (b)   (c)

Figure 3.8: Several rotated views of the human lower limbs using CSR together with MIDA as context visualization. **(a)** shows a view from the right, **(b)** demonstrates a top-right view and **(c)** displays the vasculature from the top-left.
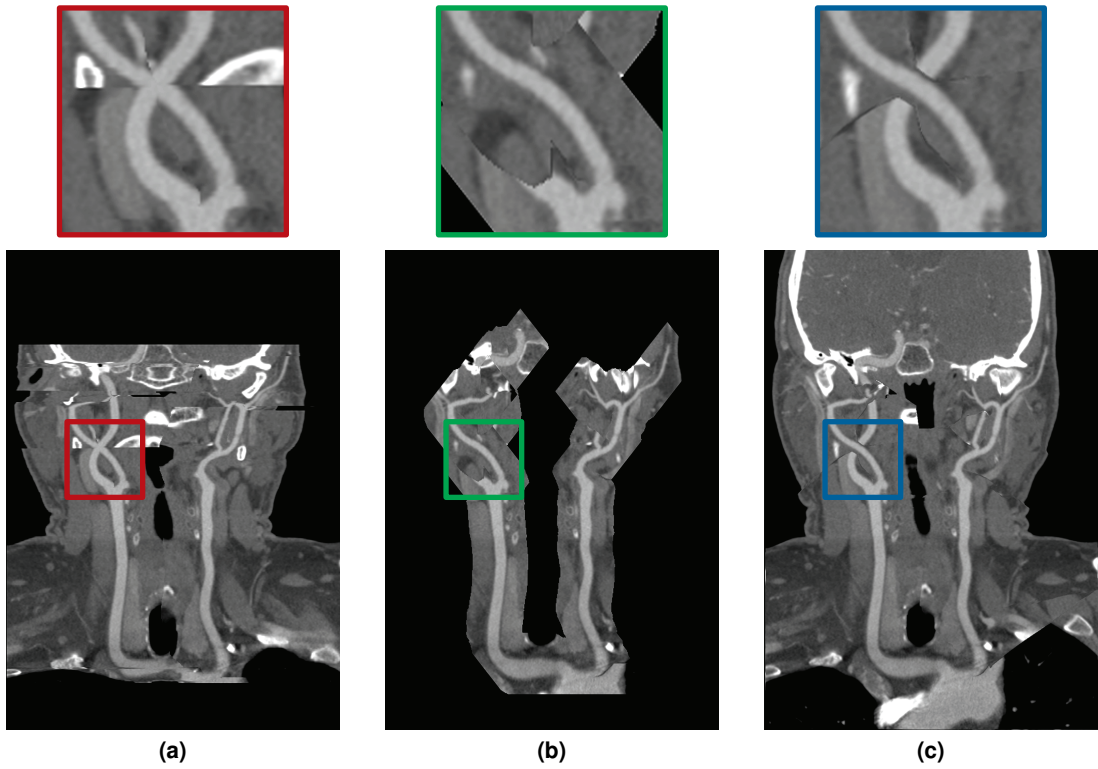
Figure 3.9: Comparison of mpCPR, CR and CSR based on cervical vessels of a human head CTA data set. **(a)** shows an mpCPR of the vasculature, which does not account for correct visibility (cf. zoom-in). **(b)** displays the lumina of the vessels using CR with a small vessel radius offset (50 pixels) and arc-length threshold (150 pixels) exhibiting a visibility artifact caused by the trade-off. **(c)** presents CSR generating a smooth cut surface through the vasculature and surrounding tissue while preserving the visibility (cf. zoom-in).

3.4 Evaluation

We consulted twelve radiologists from three different hospitals for an evaluation of CSR in comparison to mpCPR and CR based on a questionnaire (cf. Appendix B). The questionnaire consisted of 21 questions regarding five criteria (cf. vertical axis of Figure 3.10). Additionally, the usefulness of displaying the surrounding tissue, the visibility and the silhouettes were investigated, while the other two criteria are considered useful per se. The number of votes for the usefulness of the corresponding criterion is depicted by the green bar, while the red bar shows votes doubting its usefulness. The outcome of the evaluation of every criterion is subsequently summarized and discussed:

1. There is no clear preference for a reformation technique for inspecting the **vessel lumen** in a standard medical case. mpCPR is rated lowest, but most participants see no clear difference as indicated by the large gray bar. This question should test if our method is equivalent to currently used clinical methods for standard cases.

2. All participants preferred CSR for investigating the **surrounding tissue**, and the domain experts regard this criterion as very useful (green bar). One radiologist specifically mentioned that the vessel surroundings are beneficial to the detection of other pathologies. This supports the LOD approach for smoothly extending the cut surfaces into the surrounding tissue.

3. For assessing the **visibility** of overlapping vessels, we use a cervical vessel data set (cf. Figure 3.9). The majority of participants rated CSR highest. The other categories in order of popularity were no preference, mpCPR, and CR. Additionally, most domain experts considered a correct visibility as very useful (green bar). In fact, a smooth cut through the surrounding tissue while preserving the visibility of overlapping vessels was one of the motivations for developing our technique.

4. Regarding the **depth perception** of different vessels, CR and CSR are rated on the same level, mpCPR is rated worse.

5. **Silhouettes** were not rated as useful by most participants. We assume, however, that they could prove helpful after an accommodation period or for a complex vasculature, as specifically mentioned by one domain expert. A larger user study would be required to evaluate this effect as well as our context rendering.

Concerning the spatial orientation, domain experts pointed out that they use their anatomical knowledge to orientate themselves and navigate within the 3D data sets and images. One radiologist specifically mentioned that visualizing the lumen of arbitrarily oriented vessels and having the possibility of unrestricted rotations, has great potential. In fact, this is part of the rationale for developing this method.

The feedback from domain experts indicates that CSR compares favorably to mpCPR and CR. Moreover, CSR enhances the visualization of surrounding tissue and the visibility of multiple overlapping vessels.
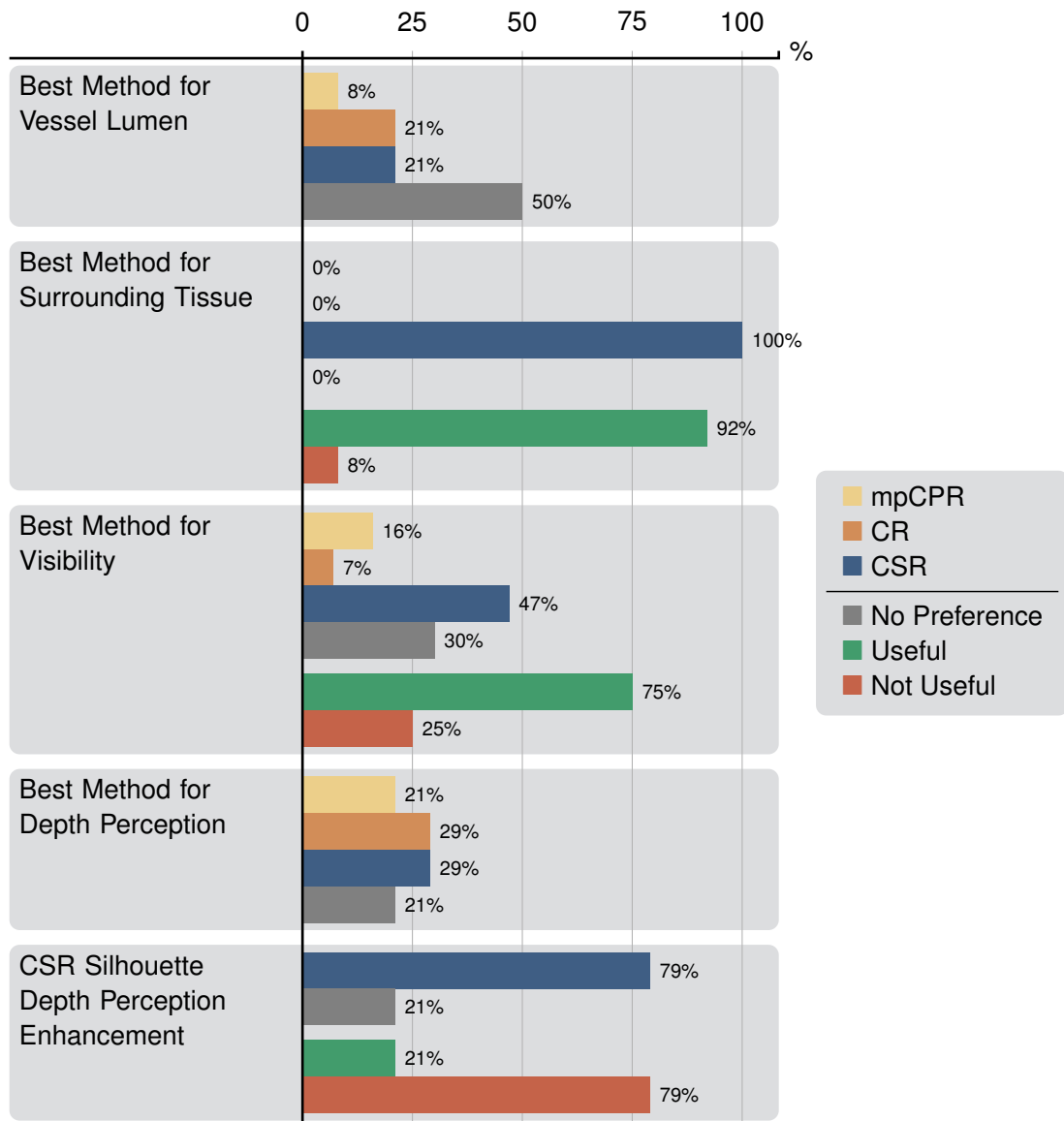
Figure 3.10: Evaluation of CSR in comparison to mpCPR and CR based on a questionnaire (cf. Appendix B). It consists of 21 questions divided into five criteria (vertical axis). The horizontal axis shows the ratings of the participants in percent. The preferences of the participants were evaluated in the first three criteria, while in the last two, the number of correct answers has been counted. While no technique has clear advantages for inspecting the vessel lumen in a standard medical case, our technique compares favorably concerning the depiction of surrounding tissue and vessel visibility. The depth perception was roughly equal for all techniques and silhouettes provided no additional benefits.

3.5 Summary

In this chapter, we proposed CSR, a novel reformation technique that generates a cut surface through the lumen of vessels entirely in 3D. It does not require adjustment of any parameters by the user, while preserving correct visibility of vessels and their surrounding tissue. Moreover, arbitrary rotations are supported, giving the user complete freedom to inspect the vessel lumina from every desired view direction. As our proposed technique has been implemented on graphics hardware, it offers interactive visual analysis of vessel pathologies.

We see several avenues for **future work** based on our method. As it allows the inspection of a complex vasculature in 3D, a given CSR view could be linked with a detailed view of a single vessel that contains aggregated information, such as based on CFA (cf. Chapter 5). The application to different curve-like anatomical structures such as nerves might be interesting. While we only evaluate our method's merits for vessel reformation, it is a general approach to generate view-dependent 2D surfaces along 1D curves that produces high-quality cuts through the surrounding 3D volume. The visualization of cut surfaces along curve-like features in scalar [29] and vector data [59, 72] in various scientific and technical domains are possible application scenarios.

At each increase of knowledge, as well as on the contrivance of every new tool, human labour becomes abridged.

—Charles Babbage

CHAPTER 4

Smart Super Views — A Knowledge-Assisted Interface for Medical Visualization

This chapter is based on the following publication:

Gabriel Mistelbauer, Hamed Bouzari, Rüdiger Schernthaner, Ivan Baclija, Arnold Köchl, Stefan Bruckner, Miloš Šrámek and Meister Eduard Gröller. Smart Super Views — A Knowledge-Assisted Interface for Medical Visualization. In *Proceedings of IEEE Conference on Visual Analytics Science and Technology*, pages 163–172, 2012.

Due to the ever growing volume of acquired data and information, users have to be constantly aware of recent methods for exploration and interaction, even though not each of these techniques might be applicable to the data at hand or might reveal the desired result. Owing to this, innovations may be used inappropriately and users may become skeptical. In this chapter, we propose a knowledge-assisted interface for medical visualization. It reduces the usual accommodation period for users with new visualization methods, by providing only the most relevant ones in a smart way. Consequently, we are able to expand such a system with innovations without users being aware when, where, and especially how they may or should use the techniques.

DUE to an advance in data acquisition modalities, the amount and versatility of available information increases. In the medical domain, these data have to be processed by clinicians, leading to a high workload and long reporting times. Various techniques [67, 68, 69, 70, 151] try to reduce the number of images to inspect in order to assess vascular pathologies. Nevertheless, with advancing technologies, new modalities are likely to emerge, leading to even more images. To enable clinicians to handle such a huge amount of data, the information must be meaningfully structured and reduced before presenting it to them.

Figure 4.1: Smart Super Views. The relevance of the views is mapped to a super-elliptical shape and decreases from top to bottom. The subsequent views are shown, starting from the top: The oblique slice view following the selected vessel in green **(a)**, the coronal **(b)**, sagittal **(c)** and axial **(d)** slice views in white, the bone view in blue **(e)**, the tissue view in yellow **(f)** and the vessel view in red **(g)**. The border colors additionally distinguish the different views.
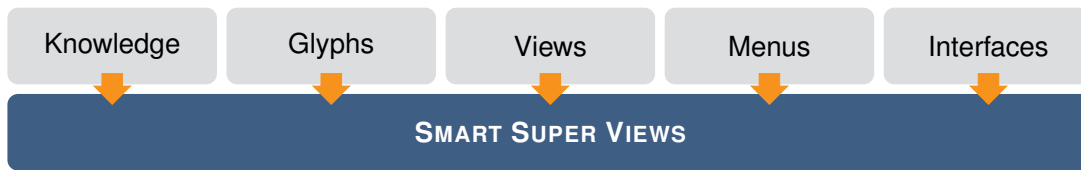
Figure 4.2: Various aspects of Smart Super Views.

Nowadays, there are several different kinds of visualization areas, each with its own set of techniques suitable for specific purposes. In the field of radiology, established methods such as MIP are widely applied and can be, for example, extended by MIDA [18]. Specific methods, such as CPR or mpCPR, proposed by Kanitsar et al. [68], are tailored to the investigation of calcifications on vessel walls. However, it is still the responsibility of the physician to decide which technique should be used when and especially where. For example, it may not be appropriate to use MIP for the assessment of a stent treatment, since a vessel could appear completely blocked, although it might only be calcified around the vessel wall. In such a case, blood might still be able to flow, a fact which could be revealed by inspecting an axial slice image or an image generated by CPR. This possible inadequate use should be avoided. With the increasing number of available visualization methods, such incidents will accumulate, because not every physician might be aware of a technique's intended application areas. Clinicians may not know all possible pitfalls, which could lead to negative consequences.

Common user interfaces exhibit several problems. For example, menus can become very long and cluttered and, therefore, it is often difficult to spot the desired option. Toolbars can contain too many buttons and, although one is able to adjust them manually, this is quite cumbersome. Popup menus try to focus on the most important options, but suffer from the same drawbacks, if overloaded. Hence, with increasing amounts of information and possibilities, it is a challenging task to provide only relevant options for every use case. In addition, interfaces may exhibit many technical terms and expressions, not everyone might be familiar with.

In this chapter, we propose a concept, where an image acts as a menu itself. The visualization becomes the main user interface, by augmenting it with dynamically generated integrated views. Once a user picks a Region-of-Interest (ROI) within the underlying data, only the most suitable visualization techniques are determined and presented. We call this approach *knowledge assisted sparse interaction*.

4.1 Related Work

Our approach aims to simplify the interaction of medical visualization systems by employing a smart system that is built upon the knowledge provided by radiologists. We incorporate aspects of several different research directions into our approach (cf. Figure 4.2).

4.1.1 Radiological Studies

Ota et al. [110] give a comprehensive evaluation concerning the reliability of multi-detector Computed Tomography Angiography (CTA) in comparison to the gold standard, Digital Subtraction Angiography (DSA). They assessed the importance of observing axial images and concluded that multi-detector CTA is a reasonable alternative to common diagnostic techniques for patients with arterial occlusive diseases in the lower limbs. Portugaller et al. [113] analyzed different visualization techniques for quantitative lesion assessment in lower extremity arteries with an area reduction of $\geq 70\%$, such as stenoses or occlusions. The result of their study shows that MIP together with axial images is most accurate in detecting cross-sectional lesions. Northam et al. [108] assessed in their study the reduction of the field-of-view from the whole data set to a specific region, in order to increase the spatial resolution. However, possible pathologies outside this limited view will be missed. Schertler et al. [137] demonstrated in their study the significant impact of non-vascular diagnosis even when using vessel CPRs. They show that axial images must always be taken into consideration. It is not enough to use CPR alone, as 27% of pathologies would remain unrecognized.

4.1.2 Multi-View Visualization

Visualization applications frequently make use of multiple linked views to simultaneously depict different representations of the data. The concept of linking and brushing connects these views by interactively highlighting selections in all views [127]. We also draw inspiration from super-views, introduced by Motro [102], which provide a homogeneous view while accessing multiple databases. Any interaction with the superview is decomposed into queries for each individual database. The outcomes are then assembled to provide the result for the initial query. Bier et al. [8] introduced toolglasses and magic lenses, which allows the depiction of alternative data representations in interactive see-through widgets. In the context of volume visualization, different types of magic lenses have been explored by LaMar et al. [83] and Wang et al. [163]. Inspired by traditional illustrations, Bruckner and Gröller [15] presented integrated contextual views in their VolumeShop system. Based on this concept, Taerum et al. [148] use contextual close-ups to present high-resolution sub-volumes of medical volume data. Ropinski et al. [131] proposed interactive close-ups for the visualization of multimodal data. Their work also presented a layout algorithm for the placement of these views. Balabanian et al. [5] describe integrated views in a graph layout in order to navigate through a volume hierarchy. They combine various types of interactions and visualizations in order to explore different regions of interest. Smart views, as presented by Radloff et al. [120], provide a refined view management in a multi-display environment. Recent work by Steinberger et al. [144] visually links selections in multiple applications to preserve context. In our work, we focus not only on how alternative views are presented, but also which views are most appropriate for different parts of the data.

4.1.3 Smart Navigation Techniques

Since orientation can be cumbersome when investigating three-dimensional data, several approaches have been presented to simplify navigation. McGuffin et al. [98] use deformations and a set of interactive widgets allowing users to virtually browse through different tissues of a medical volume data set. Tietjen et al. [152] presented LiftCharts as a simple tool for easing navigation when interacting with slice views of segmented medical data. Viola et al. [161] discussed a method for retaining context while refocusing on different structures of interest in a volume data set. Kohlmann et al. proposed LiveSync [76] and LiveSync++ [77], a method for interactively synchronizing a 3D view with 2D slice views. They automatically determine a good 3D view for a position selected on a 2D slice using local data properties. In further work, they also describe how to determine a 2D slice position from a single position on a 3D rendered image in different scenarios by matching ray profiles against a database [78]. Diepenbrock et al. [34] used a fisheye view in combination with preview images to ease navigation in virtual fly-throughs.

4.1.4 Knowledge-Assisted Visualization

The aim of knowledge-assisted visualization approaches is to improve visual exploration and analysis by utilizing information about the visualization process itself (e.g., a user's chosen visualization parameters and abstractions), and information about the scientific data to be visualized (e.g., high level abstract characterization and findings) [24, 166]. Tzeng et al. [153] use a painting metaphor to classify and visualize volumetric data. They feed the extracted information to an intelligent system, using a neural network or a support vector machine, in order to apply the classification to a new data set in a similar region. Rezk-Salama et al. [125] incorporated expert knowledge to develop a high-level interface for transfer function design. Their approach uses a principal component analysis to extract high-level parameters from a set of user-defined transfer functions. Nam et al. [103] proposed a method for extracting and indexing features to enable the automatic categorization of volume data sets. A knowledge-assisted system for the analysis of geological data was presented by Kadlec et al. [64]. Their approach captures the properties of seismic features to improve segmentation. One way to formalize domain knowledge is fuzzy logic [173, 175], which allows the specification of rules and relations using linguistic variables. Rautek et al. [122], for example, used a fuzzy rule base to map volumetric attributes to visual properties. They also extended their approach to incorporate interaction [123]. We also employ a fuzzy rule base, which enables us to represent the suitability of certain types of visualizations for different spatial regions based on domain expert knowledge.

4.2 Overview

We propose a smart user interface that intuitively presents only relevant options in contrast to, for example, a list view showing all possibilities. Our approach has been motivated by the fact that clinicians often base their reporting on inspecting a large number of images, either by quickly browsing through them or viewing them one by one. This is a cumbersome procedure, and optimizing the way of presenting these images would reduce the required reporting time. To shorten this procedure, we enhance our views with knowledge in order to provide users
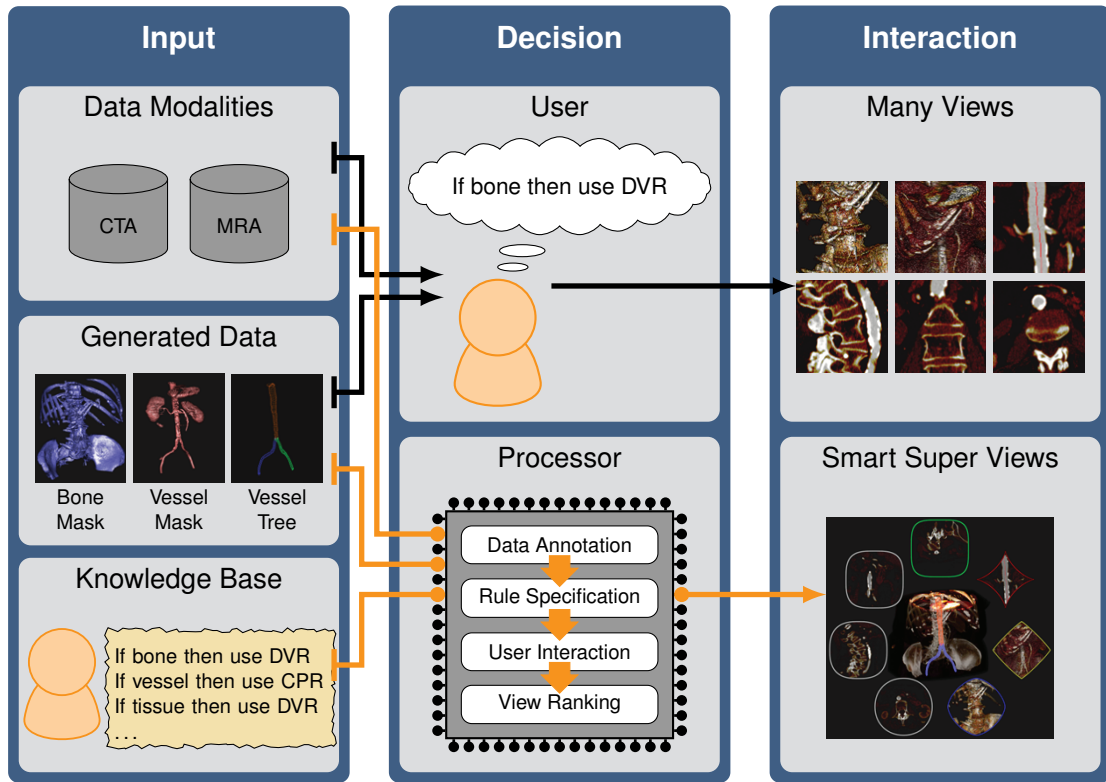
Figure 4.3: Usual workflow of medical reporting (black arrows). The clinician has to know which method is applicable to which region of the data and for which purpose it has been designed. Our system (orange arrows) supports clinicians by formalizing this expert knowledge as rules in the input step. A smart processor decides for a user-specified ROI which visualizations are suitable and should be presented. The clinician has then the possibility to interact with those suggested views in order to inspect the ROI in more detail.

only with relevant visualizations for interaction. Figure 4.3 presents the common workflow of medical reporting (black arrows) and demonstrates how our proposed system integrates therein (orange arrows). This system can be split into three main steps, each of which is subsequently briefly outlined. The most important and most notable difference between the conventional and our approach is that the user no longer needs to be aware of which method has to be used for a specific task or region of interest, since this knowledge is provided in a rule base, defined by domain experts.

Information is acquired and gathered from different sources in the **first step**. In addition to a volume data set, our application offers a bone mask, a vessel mask and a vessel tree as input. The bone and vessel masks are obtained by a semi-automatic segmentation procedure, usually done by radiological assistants. Then, they create a vessel tree by manually tracking vessels and specifying centerlines and radii accordingly. The outcome of this procedure is a vessel tree of the patient's vasculature, as shown in the vessel tree image in the *Generated Data* in Fig. 4.3.

This vessel information is used to differentiate bones from vessels and to separate them. Since the automatic process might not produce a perfect separation, manual fine tuning is carried out afterwards. Although this procedure is rather time-consuming, it is done for every patient in the daily clinical routine. Hence, we can utilize this additional information in our system. In contrast to the conventional approach, the most significant difference in this step is that domain experts have to define a set of rules, which maps the input to specific output. This offers a flexible solution for extending the output by incorporating new rules and visualizations.

Based on the previously described input information, a user decides, in the **second step**, where a ROI is located within a volumetric representation of a patient, and which specific visualization technique is applicable there. This requires significant expertise and experience from the user due to the required awareness of the algorithmic internals and the intention of the visualization technique. Our proposed system assists the user by employing an inference engine that processes the input together with a knowledge base. If the user selects a ROI, the most suitable visualization techniques are suggested automatically.

In the **third step**, the user interacts with the provided visualizations and inspects the ROI in more detail. In contrast to the common scenario, where the user has to choose a visualization technique for interaction, our system provides support by suggesting suitable choices, ranked according to their relevance. Additionally, interaction is reduced, since only a small set of relevant visualizations is suggested in each specific case. Among these relevant techniques for medical diagnosis are CPR, MIDA, MIP and DVR as well as axial, coronal, sagittal slices and an oblique slice following the currently selected vessel segment.

4.3 Smart View Inference

When the user is browsing through the three-dimensional data, our system determines the most relevant visualization techniques in the corresponding region. The processor shown in Figure 4.3 outlines how this is achieved by using four modules. Figure 4.4 gives a more detailed view of these modules, where the general workflow is top-down following the black arrows.

The first module is the *data annotation*, where semantic layers are extracted from various sources of input. In the *rule specification* module, human readable rules are specified or fetched from an external source, like a database. These rules define the connection between the input and output for a specific region the user is currently exploring. The third module bundles the information of the semantic layers according to the *user interaction* and feeds it to the fourth and final module, the *view ranking*. In this module, a Fuzzy Inference System (FIS) combines the condensed information using fuzzy logic and provides a ranking of important views only. The thinner black lines in Figure 4.4 illustrate the dependency between the input and the output.

4.3.1 Data Annotation

The goal of this module is to extract meaningful information in the form of semantic layers from the raw input data. Examples of semantic layers are the images in the data annotation of Figure 4.4. Their input can either originate from data acquisition modalities such as CTA or MRA, or can be manually specified, like the bone and vessel masks, by, for example, radiological
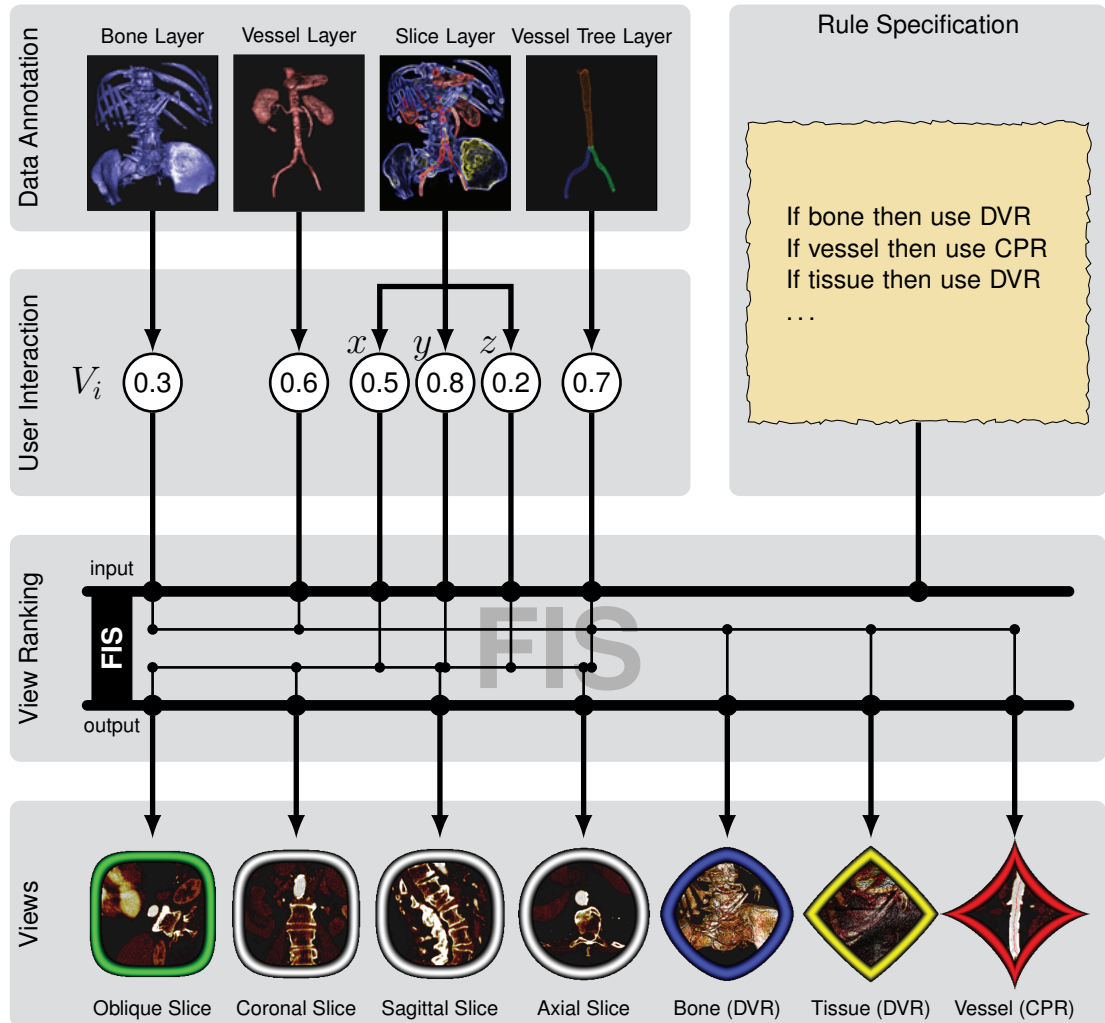
Figure 4.4: Workflow (black arrows) of the processor consisting of four modules. First, semantic layers are extracted by data annotation and, second, a rule base is defined or loaded. In the third module, the information of every semantic layer is condensed to a single value, according to user interaction. In the next module these values are fed to the Fuzzy Inference System (FIS) where they are fuzzified in order to evaluate the rules. The results of these rules are aggregated and used to determine a ranking of suitable visualizations. The two thick lines in the view ranking module indicate the input and output respectively. Once an output is derived and defuzzified, the resulting views are sorted. They exhibit a super-elliptical shape with their relevance mapped to the exponent of the super-quadrics definition.

assistants. Since these semantic layers (L_{Bone}, L_{Vessel}, L_{Slice} and $L_{VesselTree}$) are the basis of all subsequent operations, they should be determined carefully. In the following paragraphs we describe every layer in detail, namely, what kind of information it represents and what kind of input data it requires.

Bone & Vessel Layers. In order to interact with bones and vessels, we need to determine their depth values. Therefore, we employ ray casting and determine the first hit position with the segmentation masks of bones and vessels during rendering, in real-time. The obtained depth values are stored in two separate semantic layers for vessels and bones.

Slice Layer. We distinguish between two different categories of slices. The first category consists of axis-aligned slices such as the *axial*, *sagittal* and *coronal* slices. We use ray casting and estimate the importance of a slice along a ray in real-time by determining the first hit of a ray with an object, either vessel or bone. Then, the dot product between the corresponding slice axis and the gradient vector of the hit position determines the importance. If the dot product equals zero, the importance is highest, because the gradient vector lies within the slice plane. Otherwise the importance decreases with increasing dot product until it reaches zero in case the gradient vector coincides with the slice axis. The semantic layer for the axis-aligned slices stores a three-dimensional vector for every pixel, where each coordinate depicts the maximum importance of the corresponding slice along the ray. The (x, y, z) coordinates represent the importance of the sagittal, coronal and axial slices respectively. The second category includes the *oblique* slices that move perpendicularly to the direction of the currently selected vessel segment. To determine the relevance of the oblique slice view, we use the semantic layer of the vessel tree.

Vessel Tree Layer. In order to determine the user-selected vessel segment (cf. Figure 4.4, the orange segment of the vessel tree of the data annotation module) color picking is performed. The vessel tree is rendered by using a triangle mesh, with colors encoding the different vessel segments. By reading back the color at the pixel under the cursor in the current frame buffer, the corresponding segment can be identified. The semantic layer for the vessel tree is a binary mask, indicating if a segment was hit or not. It is not important where the vessel is exactly located spatially, but only if the user hovers over a vessel or not. This is the reason why the spatial information is not used.

4.3.2 Rule Specification

The rule specification module concerns the definition of the connections between the input data and the output visualizations. In order to model these connections we use a collection of *if-then* clauses and store these rules in a human readable form in an external file. The rules are defined by domain experts in order to provide specific mappings of input to output. These mappings should reflect, of course, the clinical protocol of their daily routine.

The antecedents of the rules can contain several logical combinations of the input semantic layers by using logic operations such as *and*, *or* and *not*. The consequent of every rule consists of a set of applicable visualization techniques (e.g., MIP, DVR, CPR). Linguistic variables, such as

bone, *vessel* or *tissue*, are used to define the rules in a human readable form. This facilitates the extension and maintenance of the system, even by non computer scientists. Due to the fact that our linguistic variables do not exhibit a binary state, either *true* or *false*, we use fuzzy logic [173] to process them accordingly.

This externally stored domain knowledge offers the possibility of incorporating changes easily, by simply adding or removing rules. Another advantage is the exchange of this knowledge in order to provide different modes for several application areas, for example, interdisciplinary medical discussion rounds between radiologists, clinicians and surgeons.

4.3.3 User Interaction

If the user interacts and requests suggestions for a specific region in the data, the proposed visualization techniques should correspond to the data contained therein. So far, we have the semantic layers and a set of rules defining the mapping from input to output. However, the definition of the input for the rules themselves is still pending. This input is a value that is subsequently fuzzified in order to be used in the evaluation of the antecedents of the rules. To distinguish between non-fuzzy and fuzzy values, the former are referred to as *crisp* values.

Region-of-Interest (ROI). The user defines a two-dimensional Region-of-Interest by the cursor position on the screen and a user-specified radius. Taking a small neighborhood into account avoids high variational changes of the suggested smart views due to data coherence.

The information of the semantic layers is used inside the ROI to derive a single crisp input value for every linguistic input variable. This is necessary to evaluate the rules accordingly. However, not every value of the semantic layers inside this region should have the same influence. The main focus should be at the cursor position. Thus, the crisp scalar input values, V_i, for every linguistic input variable are computed over the ROI by

$$V_i = \frac{1}{N} \cdot \sum_{(x,y) \in ROI} [C_i(x,y) \cdot S(x,y)] \tag{4.1}$$

where (x,y) is a pixel inside the ROI, $C_i(x,y)$ is a conditional term for modeling the correspondence of multiple semantic layers, $S(x,y)$ is a spatial influence function and N is the normalization factor, i.e., the area of the ROI in pixels. The following equations show, how the conditional term is computed at a pixel (x,y) using the information of the different semantic layers (L_{Bone}, L_{Vessel}, L_{Slice} and $L_{VesselTree}$).

$$C_{Bone}(x,y) = \begin{cases} 1, & \text{if } L_{Bone}(x,y) \leq L_{Vessel}(x,y) \\ 0, & \text{otherwise} \end{cases} \tag{4.2}$$

$$C_{Vessel}(x,y) = \begin{cases} 1, & \text{if } L_{Vessel}(x,y) \leq L_{Bone}(x,y) \\ 0, & \text{otherwise} \end{cases} \tag{4.3}$$

$$C_{SagittalSlice}(x,y) = L_{Slice}(x,y).x \in [0,1] \tag{4.4}$$

$$C_{CoronalSlice}(x,y) = L_{Slice}(x,y).y \in [0,1] \tag{4.5}$$

$$C_{AxialSlice}(x,y) = L_{Slice}(x,y).z \in [0,1] \tag{4.6}$$

$$C_{VesselTree}(x,y) = L_{VesselTree}(x,y), \ 0 \vee 1 \tag{4.7}$$

Figure 4.5: Common workflow of a FIS. First, crisp input values are fuzzified using fuzzy membership functions. Second, the antecedents of the *if-then* rules are evaluated using fuzzy set operators. The implications are evaluated with the minimum operator [97]. Third, the fuzzy implication results are aggregated and, fourth and finally, defuzzified using the centroid method to provide a crisp output.

The value for bone, for example, needs the information of the vessel and bone semantic layers, because both store the depth of the respective masks. C_{Bone} will be one, only if the depth value in its semantic layer is less than the value in the semantic layer of the vessel, at the same pixel position. In the case of the slices, only the value for the corresponding axis is taken. For the vessel tree, either one or zero is returned, because only a binary mask is stored. This mask indicates if a vessel is located under the current pixel.

Spatial Influence. Not every position inside the ROI should have the same influence on the result. Information in the near vicinity of the cursor position should contribute more. For example, if the user hovers over the aorta, the ROI might contain some bone, such as the spine. If the focus is on the aorta, then the bone should have less influence than the vessel and this should be reflected in the output visualizations. We model this by computing a weight for every pixel $p(x, y)$ of the ROI, with cursor position $\mathbf{c}$, according to the following function:

$$S(x, y) = \frac{1}{(1 + \frac{\lambda}{r}\|\mathbf{p} - \mathbf{c}\|_2)^\sigma} \tag{4.8}$$

with r being the radius of the ROI in pixels, σ controlling the speed of the influence decay and λ providing the weight at the boundary pixels of the region. The influence decreases with distance from the center. Experiments have shown that using $\sigma = 2$, $\lambda = 0.3$ together with $r = 10$ provides a good response, where the suggested views reflect the underlying data.

4.3.4 View Ranking

Once the crisp input values V_i (cf. Equation 4.1) have been determined for all linguistic input variables, they are fed to an inference engine together with the set of rules. Since fuzzy logic is used for rule evaluation, the inference engine is a Fuzzy Inference System (FIS). Figure 4.5 illustrates the common workflow of a such a system and in the subsequent paragraphs every step is explained.

Fuzzification. In the first step, the crisp input values are fuzzified using fuzzy membership functions. There are several different types of these functions, e.g., they could exhibit a triangular, trapezoidal or Gaussian shape. Throughout this chapter, triangular membership functions are used.

83

Implication Evaluation. Fuzzy logic offers the possibility to specify knowledge in the form of rules with linguistic variables and terms, rather than with exact numbers [174]. For the specification of these rules, we use the concept of the *if-then* rule with fuzzy antecedents and consequents. For every rule, its antecedent is evaluated using fuzzy set operators and the consequent is computed using the minimum operator [97].

Aggregation. Once all fuzzy consequents are obtained, they are aggregated by combining their fuzzy membership functions. Again, fuzzy set operators are used to aggregate these fuzzy consequents. The result of the aggregation step is one fuzzy output.

Defuzzification. In order to obtain a crisp output value from the aggregated fuzzy one, defuzzification is needed. Common defuzzification approaches are the centroid method, maxima decomposition, center of maxima calculation or height defuzzification. In all subsequent examples of this chapter, the centroid technique is used. The final crisp output value is utilized to determine the membership value of every linguistic output variable. This membership value is the relevance of the respective suggested visualization. Subsequently, the proposed views are sorted according to their relevance and presented to the user.

4.4   Visual Mapping and Interaction

The output of the smart view inference is a ranked list of suggested visualizations that needs to be presented to the user in a suitable way. Every visualization is shown in a separate view, embedded into the current user interface, analogous to a Head-up Display (HUD).

A HUD is a transparent display presenting data where the viewer does not need to look away from the usual focus area. It was originally designed for pilots in order to relieve them of looking down on their instruments. It allows them to look forward with the head positioned up. Hence the name Head-up Display. We use this analogy to present the relevant views embedded into the visualization the user is interacting with. This avoids interaction with other windows or menus, possibly distracting the user, and the focus remains in the same window. While the user is still able to see the ROI, the original view is enriched by additional so-called *smart views*. The term *smart view* has been chosen to reflect that the views have been determined in a knowledge-assisted, i.e., smart, way.

4.4.1   Visual Mapping

In order to visually convey the relevance, it is incorporated into the shape of a view. Several perceptual properties of glyphs, such as shape, size, color and orientation are described by Ropinski and Preim [130]. They state that the shape and size of glyphs are perceived *pre-attentively*, within the first quarter of a second. Hence, we employ certain properties of glyphs for our smart views as well. Concerning various kinds of shapes, Kindlmann [74] states that super-shapes convey information more clearly and precisely. Therefore, we use a super-elliptical shape for our smart views and, additionally, color the boundary of the shapes differently. Simultaneously, the relevance is encoded in the size of the area covered by the shapes on the screen. This is

intended to allow us an unambiguous identification of the most relevant views. Combining all these aspects, our views are suggested according to some underlying knowledge and exhibit a super-elliptical form, hence the name *smart super views*.

A super-ellipse is defined as the set of points (x, y) with

$$\left|\frac{x}{a}\right|^n + \left|\frac{y}{b}\right|^n = 1 \tag{4.9}$$

where $a, b > 0$. Since differences in shape and size are perceived pre-attentively [130], we map the relevance of a visualization to the exponent n of the super-ellipse. This leads to the following equation for our views

$$\left|\frac{x - x_{pos}}{size}\right|^{m(rel)} + \left|\frac{y - y_{pos}}{size}\right|^{m(rel)} \leq 1 \tag{4.10}$$

where $size$ is the chosen size of the view, $m(rel)$ is the relevance shape-mapping function with rel being the relevance of the corresponding suggested view and (x_{pos}, y_{pos}) is the position of the view. We empirically determined the shape-mapping function $m(rel)$ as

$$m(rel) = (0.5 + 2 \cdot rel)^\alpha \tag{4.11}$$

where α controls the speed how fast the shape of a suggested view becomes rectangular. Using $\alpha = 1.5$ covers most of the dominant shapes, i.e., rectangles, circles and stars. In addition, we omit very thin star shapes by shifting with 0.5 and scaling the relevance by two. Due to the α exponent, highly relevant views have a rectangular shape, whereas the least important one exhibits a star-like form. Owing to this mapping, a view's shape and area changes according to the relevance obtained from the ranking.

Spatial Arrangement. Once the shape of every view has been determined in terms of its relevance, the views need to be spatially arranged. We provide two possible layout strategies:

- In a *linear layout* all views are arranged along a horizontal line, starting with the most relevant view at the left and proceeding to the right with decreasing relevance (cf. Figure 4.6). In order to avoid overlapping with the ROI, the views are positioned at the bottom of the overall view they are embedded in.

- A *radial layout* positions the views in a circle around the ROI. The views are arranged in a counter clockwise fashion, with the most relevant view being placed above the ROI (cf. Figure 4.7). This avoids visual clutter in the case of many views.

4.4.2 Interaction

The user can hover over a specific smart super view and interact with it in the same way as with the overview visualization it is integrated in. No manual switching between the different views is required. This makes the interaction sparse and allows the user to immediately gain more insight into a specific region. We distinguish between two states of interaction. In the
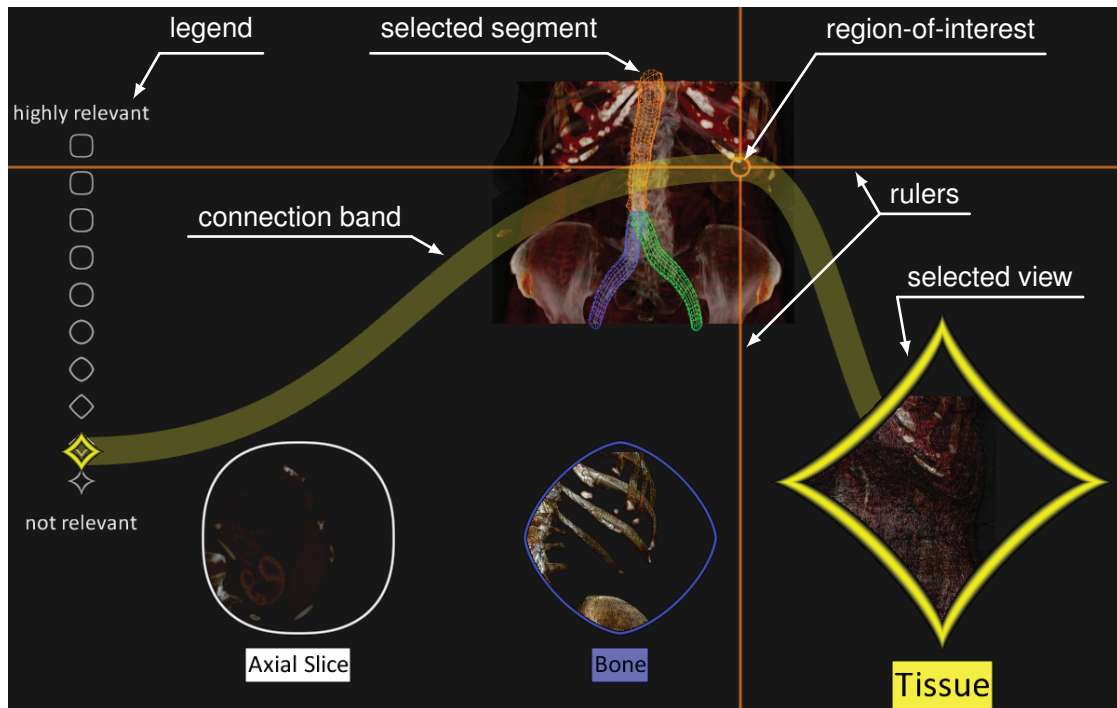
Figure 4.6: Smart super views arranged in a linear layout at the bottom of the window with the overview visualization being MIDA. The shape of the views changes with decreasing relevance from left to right. Tissue (yellow) is the least relevant view. It is selected and therefore enlarged. The yellow band connects the selected view with the ROI and the corresponding glyph in the legend.

overview state, the user navigates in the overview visualization without being guided by our system. Once a ROI has been identified and additional information is requested, in order to explore this region in detail, the user can switch to the inspection state. For every interaction in this state, the user gets immediate feedback in the form of smart super views. The user is still able to navigate within the overview visualization, but the suggestions are updated accordingly. This enables guided exploration of the underlying data with only relevant additional information being displayed. If a suggested view is selected by hovering over it, the user is able to inspect the visualization of the view by, e.g., zooming, panning and rotating. In addition, the size and border of a selected view are enlarged in order to give the user a visual feedback. When finished with guidance or inspection, pressing a key will return to the overview state and all smart super views will disappear.

Legend. In order to provide an overview of the entire range of the relevance, a legend of possible shapes is presented. This conveys the relevance visually and provides a context. If the user selects a smart super view, the corresponding glyph is indicated in the legend at the position of the respective relevance. Additionally, a connection band between the glyph in the legend, the

view and the ROI provides another visual cue. Following this band, one quickly perceives the overall layout and the selected view's relevance within the global ranking. Figure 4.6 demonstrates smart super views arranged in a linear layout, together with the legend on the left. The least relevant view (tissue) with the yellow border is selected and, following its connection band, one can clearly see the corresponding relevance. The legend shows the highest relevance at the top and the least at the bottom. To enhance the visual perception of the ROI, horizontal and vertical rulers are displayed (cf. Figure 4.6).

4.5 Results

Figure 4.1 presents an overview of possible views that our system can provide. The relevance decreases from left to right. In this example, the most relevant view is the oblique slice view, followed by the coronal, sagittal and axial slice views. Then, bone using DVR precedes tissue using DVR and the last view is the vessel view showing a CPR. High relevance leads to an almost rectangular shape, whereas the least important view looks like a star. The border colors additionally distinguish the various views, whereas the coronal, sagittal and axial slice views share the same color.

Figure 4.7 shows a data set of a human abdomen, rendered with MIP together with the vessel tree rendered in wire-frame mode. When hovering over the aorta, it is displayed in the suggested views, as shown in the vessel view at the bottom of the image with the red border. This smart super view allows the user to rotate the selected part of the aorta using CPR. In this scenario, tissue (yellow border) is ranked the least relevant view, which can be visually derived from its star-like shape. The two slice views (white borders) have quite similar relevance, as reflected in their circular shape.

Figure 4.8 gives an example where the user is hovering over a stent. As MIP is the underlying overview visualization, it initially seems that the stent completely blocks the vessel. However, when inspecting the vessel in the corresponding view with the red border using CPR, one can clearly see that this is actually not the case and the blood is able to flow through the stent.

Figure 4.9 shows several smart super views for different regions of a human lower extremity data set using MIDA as overview visualization. If the user moves over the aorta, slice, vessel and tissue views are suggested (cf. Figure 4.9a). These views are placed around the ROI in a radial layout and the sagittal slice view is selected, recognizable by the magnification of the view. The user is able to interact with this view by, e.g., scrolling through the slices or changing the windowing function. Another suggestion is given in Figure 4.9b, where the focus is on the pelvic bone. The bone view (blue border) is selected and has the highest relevance, followed by an axial and sagittal slice view. Only the bones defined by the bone mask are shown with DVR. Next, moving to the knee region, the vessel view and the selected oblique slice view (green border) are shown in Figure 4.9c, since the user hovers over a vessel. If moving a bit away from the vessel, other types of tissue are taken into account. This leads to the example in Figure 4.9d, where tissue and slice views are suggested. The tissue view (yellow) is selected and the knee is inspected more precisely using DVR.
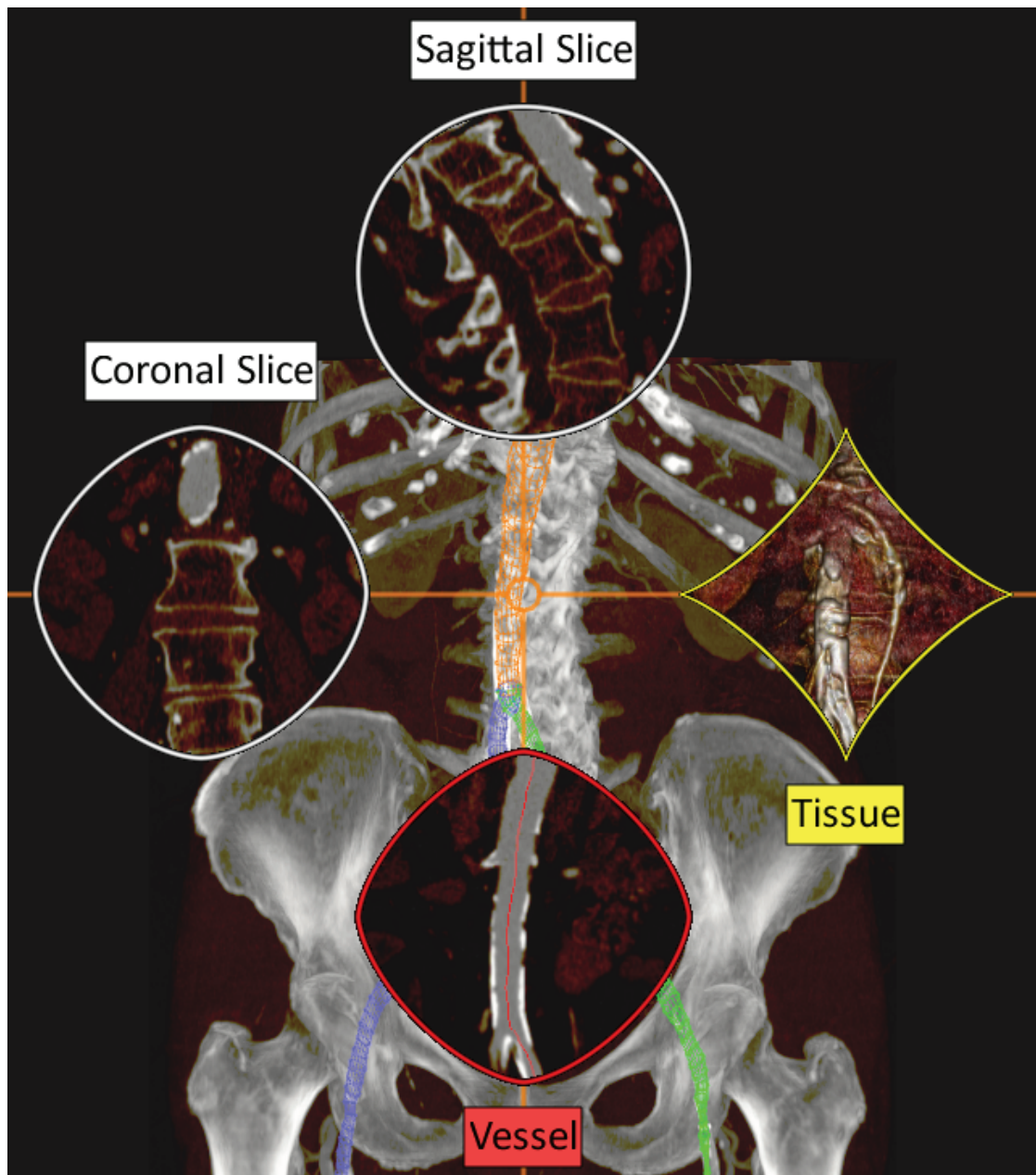
Figure 4.7: Smart super views presented in a radial layout around the ROI, while moving over the aorta of a human data set showing the abdominal region. The overview visualization is MIP. The sagittal slice view is the most relevant view, followed by the coronal slice view. The vessel view displays a CPR of the selected vessel segment (orange). The tissue view is ranked least relevant and presents a DVR.
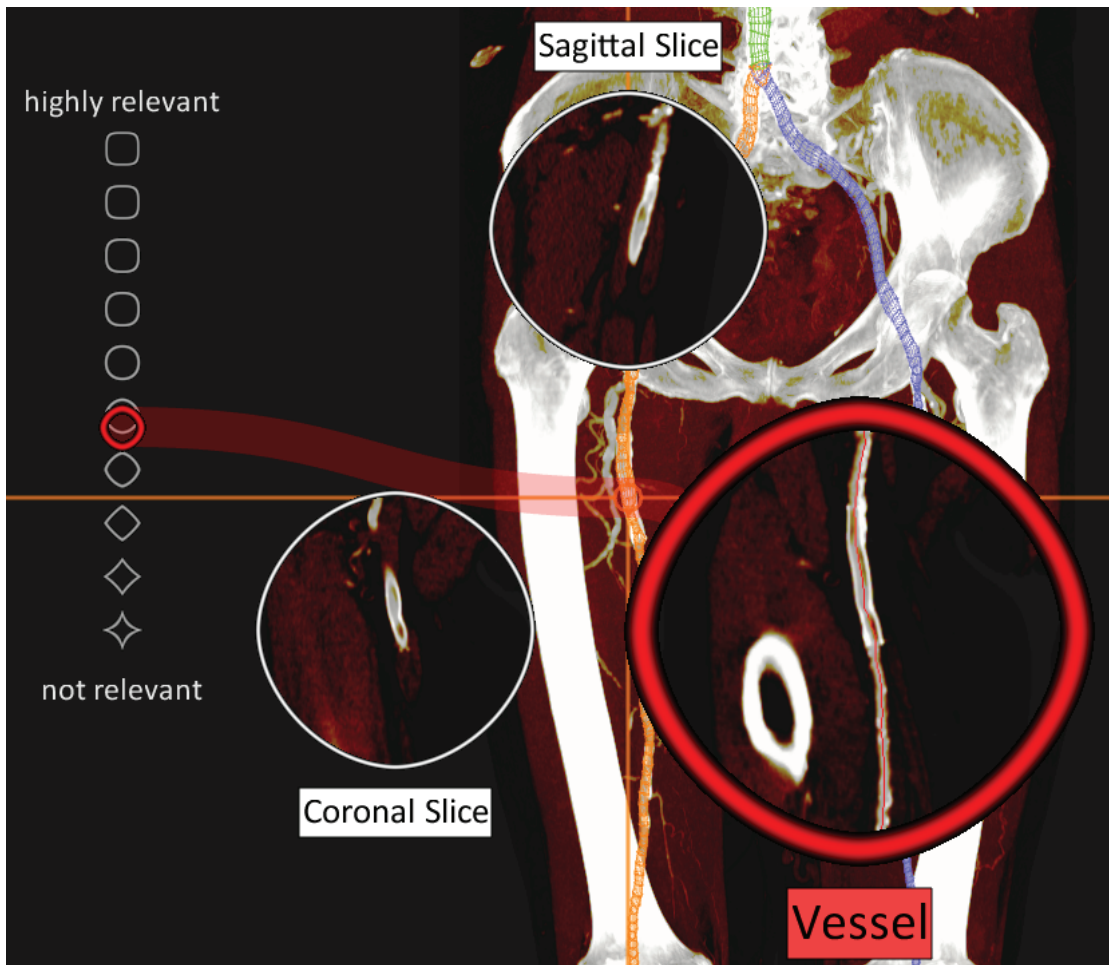
Figure 4.8: Detailed investigation of a stent in the vessel view (red border) using CPR. The user is able to rotate around the centerline of the vessel to verify if the blood is able to flow through the stent.

4.6 Implementation

We implemented our smart super view system in the AngioVis [2] framework. All visualizations, the overview one as well as the ones of the smart super views, are rendered into separate frame buffer objects using CUDA. The super-elliptical shapes together with the views and the legend are rendered using GLSL shaders. The rulers, the outlines of the ROI and the connection bands are drawn using the painting capabilities provided by Qt4.

The user can interactively move the ROI to obtain smart super views and then inspect a specific one. The inspection can be done in real-time by enlarging the active view in order to provide more space for investigation. Rotating, zooming, panning and changing the transfer and windowing functions are the default capabilities of every view.
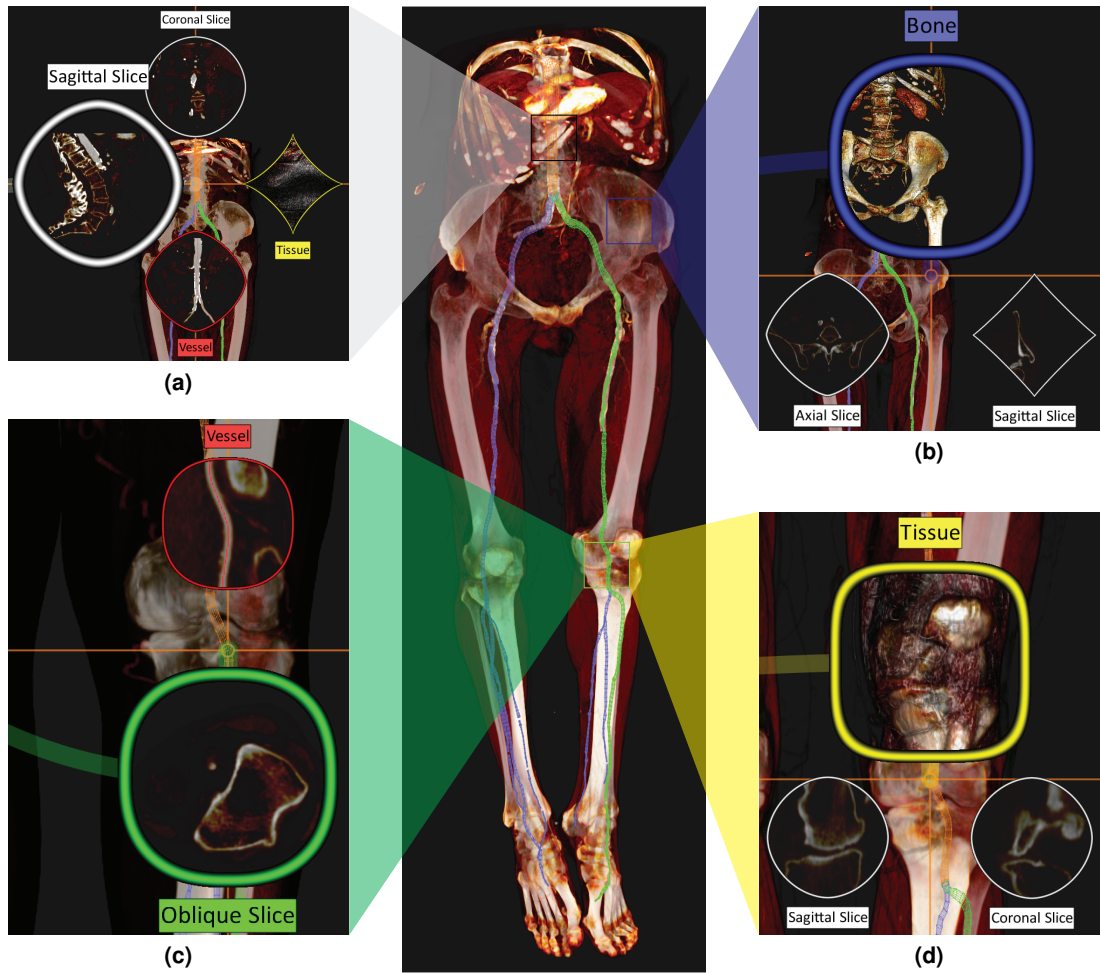
Figure 4.9: Various smart super views of different regions of a human lower extremity CTA data set. The overview visualization is MIDA in all examples. Selected is **(a)** the sagittal slice view, **(b)** the bone view, **(c)** the oblique slice view and **(d)** the tissue view.

We used the fuzzy-lite [119] library for integrating fuzzy logic into our application, since it provides an intuitive and fast C++ interface. The linguistic input and output variables as well as the membership functions are defined in the source code. The rules are stored in a text file and loaded during initialization of the smart super view plugin.

4.7 Evaluation

In discussions and semi-structured interviews with physicians, we acquired qualitative feedback on the applicability of our smart super views. We consulted two domain experts, i.e., radiologists. They mentioned that the initial goal of a visual workflow is the reduction of the number of slices to inspect. A common procedure is to investigate all slices of a patient's data set in order

to detect suspicious regions. This usually works well, but consumes a considerable amount of time. For the investigation of blood vessels, CPR and mpCPR have been proposed [68]. These techniques significantly reduce the number of images that clinicians have to inspect.

With the increased resolution of current scanners, the data sets consist of more slices and the amount of time required for an inspection increases. Additionally, the number of images increases as well with more techniques being available, even for specific purposes. For the investigation of blood vessels such techniques are, for example, various stretched, straightened or untangled CPRs. For every technique images have to be generated for a given set of view directions. The clinicians have to inspect all these generated images, as some pathologies, such as vessel occlusions, might remain unrecognized otherwise. This is a potential scenario of our proposed system, because it automatically provides only the relevant visualizations. In addition, clinicians are able to view the ROI from various view directions, because smart super views offer more interaction than static images.

According to the study by Portugaller et al. [113], specific combinations of views lead to more accurate reporting results. They conclude that using only axial slice images, CPR or MIP alone is not sufficiently accurate when judging a considerable number of pathologies. The outcome of the study is that MIP together with an axial slice view is the most precise procedure. Our system is able to provide this by adapting the rule base accordingly.

The domain experts also liked the possibility to additionally blend specific views into their workflow. Their workplace usually includes four displays, with three of them being used for the PACS workstation. The fourth and left most screen remains mostly unused. Here, they see some potential for our proposed system, as an extension of their current workstation. Having additional information on suspicious regions and getting only relevant views was considered to be a promising extension. Concerning the discrimination of the various views, the domain experts mentioned that it is intuitive for a user with some basic knowledge of the underlying algorithms. The interaction is seen as fairly easy.

The domain experts see further potential of our proposed system in interdisciplinary medical discussion rounds between radiologists, clinicians and surgeons. Our system can be adapted to their specific requirements by providing individual rule bases. By changing the rules, the system immediately adapts to the desired protocol. For example, a surgeon wants to see a vessel with DVR, whereas a radiologist prefers CPR.

According to the study presented by Northam et al. [108] and as a future extension, our system might use the full field-of-view of the underlying data for the overview visualization, while additionally providing smart super views using a high resolution but limited field-of-view. This would reduce the potential risk of missing pathologies along with showing the ROI in a high resolution.

The study by Schertler et al. [137] investigates the impact of axial slices on the localization of possible pathologies beyond the vessels in the chest region. Our system can account for such cases by defining an appropriate rule base. The potential risk to overlook pathologies is reduced by guiding the radiologist to certain views in specific regions. These views use only well-known and established visualization techniques according to the application scenario.

Summarizing the evaluation, the domain experts see our system as a promising addition to their current clinical workflow. They especially see a potential in the possibility to guide the
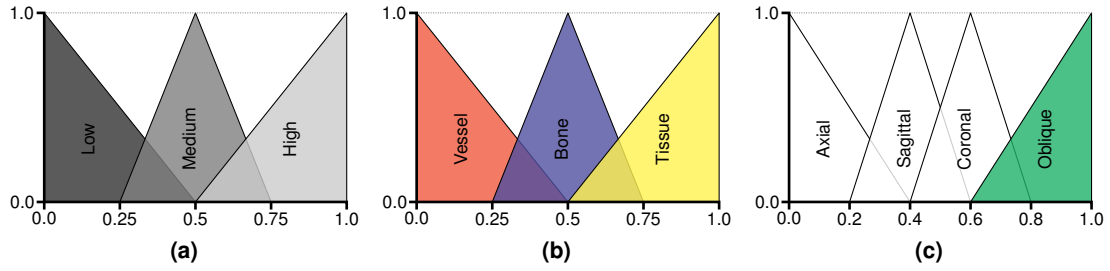
Figure 4.10: Linguistic variables with their terms and corresponding triangular membership functions used in the FIS. The left and right most terms are shoulder terms. The colors correspond to those employed in the user interface. **(a)** shows every linguistic input variable with the terms *Low*, *Medium*, *High*. **(b)** presents the linguistic output variable with the terms for the vessel, bone and tissue views. **(c)** shows the linguistic output variable with the corresponding terms for the slice views.

user to important views in order to minimize potential risk factors due to inadequate use. A comprehensive user study, with the aim to investigate the impact of our proposed system on the daily clinical routine, is still open.

4.8 Discussion

Among several possibilities of fuzzy membership functions, we chose triangular ones for every linguistic variable. All linguistic input variables exhibit the structure shown in Figure 4.10a and consist of the terms *low*, *medium* and *high*. These terms have triangular membership functions with the same area, but *low* and *high* are shoulder terms. The linguistic output variable for the vessel, bone and tissue views, called *Method*, has the corresponding visualizations as terms (cf. Figure 4.10b). The linguistic output variable for the slices, named *Slice*, consists of four terms and is shown in Figure 4.10c. The colors are the same as in the user interface of our system and as demonstrated in the results. The following rules are an outline of the *if-then* rules that are used to create the result images throughout this chapter. The values V_{Vessel}, V_{Bone} and $V_{VesselTree}$ are obtained by Equation 4.1.

if V_{Vessel} is Low **and** V_{Bone} is High **and** $V_{VesselTree}$ is Low **then** Method is Bone
if V_{Vessel} is Medium **and** V_{Bone} is Low **and** $V_{VesselTree}$ is Low **then** Method is Tissue
if V_{Vessel} is High **and** V_{Bone} is High **and** $V_{VesselTree}$ is High **then** Method is Vessel

The complete dependency of the output views on the semantic layers and their associated visualization techniques is given in Table 4.1. The vessel tree influences the oblique slice view and the vessel view, since both views need a representation of the underlying vessel. If most of the ROI is covered by the vessel tree, the vessel and oblique slice views will become highly relevant. If primarily bone is selected, the bone view will be ranked highest. If vessel, bone and vessel tree are captured within the ROI, the tissue view will be rated as relevant. The complete

Table 4.1: Views with their dependencies on the semantic layers and their associated visualization techniques. We distinguish between two different types of slice views, namely axis-aligned ones, where consecutive slices are parallel ∥, and an oblique one, following the currently selected vessel segment, being orthogonal ⊥ to it.

	Semantic Layer				
View	Bone	Vessel	Slice	Vessel Tree	**Visualization**
Oblique Slice			✗	✗	⊥ Slice
Coronal Slice			✗	✗	∥ Slice
Sagittal Slice			✗	✗	∥ Slice
Axial Slice			✗	✗	∥ Slice
Bone	✗	✗		✗	DVR
Tissue	✗	✗		✗	DVR
Vessel	✗	✗		✗	CPR

list of rules can be found in Appendix C, split into two sets of rules, one for each output linguistic variable (*Method* and *Slice*).

Providing the FIS with meaningful information often requires a considerable amount of information or even specific information, such as the bone and vessel masks. In general, we cannot assume that we have such annotated data available. However, our system is implemented in a framework that is used in the clinical routine of two hospitals. Radiological assistants create such annotations in their daily work. Hence, in our scenario, we have such data available. The tracking of the vessel tree is also done for every patient, therefore, we can use it in our system. Such a vessel tree consists only of the clinically relevant vessels. Concluding, the required data are available, without the necessity of any user adaptation or changes to the workflow.

4.9 Summary

In this chapter, we proposed a knowledge-assisted user interface for medical visualization. The user is able to hover over a specific region and gets only relevant visualizations presented in the form of smart super views. These views are integrated into the overview visualization and visually convey relevance by shape and color. In order to inspect a view in detail, the user just needs to hover over it. This allows the user to interact in the usual manner. Knowledge is provided by domain experts in the form of *if-then* rules. These are evaluated using fuzzy logic to obtain a ranking of suitable visualizations.

> Nature is an infinite sphere whose center is every-
> where and whose circumference is nowhere.
>
> —*Blaise Pascal*

CHAPTER **5**

Vessel Visualization using Curvicircular Feature Aggregation

Radiological investigations are common medical practice for the diagnosis of peripheral
vascular diseases. Existing visualization methods such as Curved Planar Reforma-
tion (CPR) depict calcifications on vessel walls to determine if blood is still able to flow.
While it is possible with conventional CPR methods to examine the whole vessel lumen
by rotating around the centerline of a vessel, we propose Curvicircular Feature Aggre-
gation (CFA), which aggregates these rotated images into a single view. By eliminating
the need for rotation, vessels can be investigated by inspecting only one image. This
method can be used as a guidance and visual analysis tool for treatment planning.

R ADIOLOGICAL investigations often require a fast and precise diagnosis for proper treat-
ment planning in order to minimize negative impacts on a patient's health state. One
particular field of radiology is the analysis of blood vessels, e.g., the identification of
deviations of the flow channel in case of peripheral arterial occlusive diseases. Blood flow de-
viations can be caused by pathologies on the vessel walls, such as calcifications or soft plaque.
Angiographic medical volume data are typically acquired using tomographic techniques, such
as Computed Tomography Angiography (CTA) or Magnetic Resonance Angiography (MRA).
These data consist of stacks of axial sections or slice images. The usual radiological diagnostic
procedure is the investigation of every axial slice image of a data set, one by one. This is a
time-consuming task, since a typical data set may consist of thousands of slices.
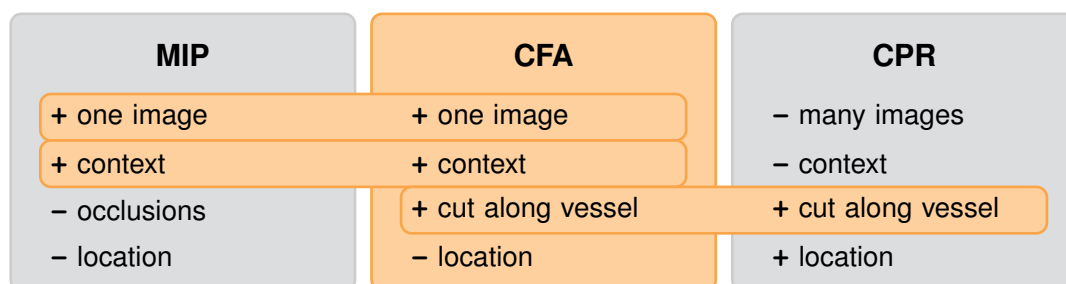
MIP	CFA	CPR
+ one image	**+ one image**	− many images
+ context	**+ context**	− context
− occlusions	**+ cut along vessel**	**+ cut along vessel**
− location	**− location**	+ location

Figure 5.1: Unifying aspects of Curvicircular Feature Aggregation (CFA) with respect to MIP and CPR.

In order to relieve clinicians of the task of inspecting data sets slice-by-slice, Maximum Intensity Projection (MIP) has evolved into a well-established visualization technique for medical investigation. It projects 3D information onto one static 2D image. Applied to CTA data, the method captures bones and calcifications, since they exhibit the highest intensity. However, one cannot distinguish between vessels being blocked by calcifications or vessels having calcifications only on their walls. To remedy this drawback, Curved Planar Reformation (CPR) techniques were investigated [68, 70]. These methods depict a curved cut through the lumen of a vessel along its centerline. By rotating around the centerline, the whole lumen of the vessel can be inspected. However, this approach still requires a substantial degree of interaction, making the analysis of a pathology a time-consuming process.

In this chapter, we propose a visualization technique called Curvicircular Feature Aggregation (CFA), designed for the investigation of blood vessels. The main idea of this method is the reduction of necessary interaction by performing an aggregation around the centerline of a vessel. The result is a single static image, making the rotation operation unnecessary. In addition, clinicians are supported by visual analysis tools for further inspection of interesting regions. Among these tools are linked views, such as an axial slice view. Contextual information outside the vessel lumen is provided by means of common visualization techniques such as MIP, MIDA or DVR.

5.1 Related Work

The technique proposed in this chapter combines several aspects of MIP and CPR, as outlined in Figure 5.1. The goal is to provide an overview of the whole vasculature and to support clinicians in identifying and reporting vessel pathologies within a single static image.

5.1.1 Nonlinear Rendering

Gröller [48] investigates methods for nonlinear ray tracing with iterative or hierarchical ray representations and discusses their possible applications for visualization of various dynamic systems. Kurzion and Yagel [82] present a space deformation for volume visualization based on ray deflectors. Weiskopf et al. [168] implement nonlinear ray tracing on the GPU. Their

approach consists of a ray setup according to camera parameters, ray integration, ray-object intersection, and local illumination. Wang et al. [162] discuss a method for volume visualization with nonlinear camera projections. The technique uses a lens-based deformation in order to magnify an interesting object in the scene. Cui et al. [30] present a technique which uses a curved ray camera with a bent view frustum in order to handle occlusions in complex three-dimensional scenes. Löffelmann and Gröller [93] describe an extended camera concept that is capable of creating artistic effects with ray tracing while maintaining an overview of the overall scene. Hsu et al. [55] proposed a rendering framework for multi-scale rendering of geometric and volumetric models. Their method can present complex structures with multiple levels of detail using a focus+context approach. They also employ artistic effects that are commonly used by illustrators. Diepenbrock et al. [35] proposed *normalized circular projection*, a technique that investigates the activity of a positron emission tomography outside the vessel wall (estimated by means of CT) of the carotid arteries of mice. The vessels are straightened and normalized to cylinders and, subsequently, projection operations are performed around these cylinders in concentric circles. This technique is similar to our approach presented in this chapter, but we investigate and analyze the properties of various aggregations along circular rays in CTA data. In addition, we provide a layout for multiple vessel branches. Nonlinear rendering methods, such as nonlinear ray tracing or ray casting, apply concepts of space deformation. In this chapter, we present a technique that uses nonlinear rays to obtain diagnostic visualizations for blood vessels.

5.1.2 Vessel Visualization Arrangement

Treemaps, originally proposed by Johnson and Shneiderman [61], represent a two-dimensional space-filling approach for visualizing trees. Each node of the tree is represented by a rectangle with its area being proportional to a specific data attribute. To visually convey the relation of parents and children nodes in a simple and comprehensible way, nested rectangles are used. With time, treemaps have been extended in order to enhance the interpretation of the data or to handle larger data sets. Van Wijk and van de Wetering [157] developed *cushion treemaps* that inherit the compactness, i.e., the space-filling property of hierarchical information, but provide a better understanding of the underlying hierarchy by means of intuitive shading. Radial space-filling techniques, described by Andrews and Heidegger [1] and Lou et al. [95], replace the orthogonal partitioning of rectangles with a radial layout. Van Ham and van Wijk [156] proposed *beamtrees* that represent a method for the visualization of hierarchical data where the nested rectangles of the original treemaps are replaced by overlapping beams. Nodes are represented by stacked cylindrical beams that depict both hierarchical structure and node characteristics such as size. Zhao et al. [177] proposed a combination of treemaps and node-link diagrams. They provide a space-efficient layout, while retaining the structural clarity of node-link diagrams [124]. So far, the focus has been on the layout design of treemaps. Blanch and Lecolinet [10] assess the interaction with treemaps to explore large data sets. They introduce the notion of *zoomable treemaps*, which represent a mixture between treemaps and zoomable user interfaces. Borkin et al. [12] proposed a two-dimensional vessel visualization method visually conveyed in a tree-like fashion. Their tree representation shows the entire vasculature within one image, while providing anatomical information such as vessel diameter and branching structure. Our approach renders the vessels straightened and arranges them horizontally in an anatomically sorted manner.

5.2 Curvicircular Feature Aggregation

Diagnostic visualization plays an important role in conveying the information of the underlying data to domain experts. In medicine, such data usually stem from angiographic imaging sources, where a contrast agent is simultaneously administered during the acquisition procedure to enhance the vasculature of the patient. The imaging source can be, for example, CTA or MRA. The current gold standard for vascular diagnosis is DSA, a non-tomographic technique. However, methods based on data from tomographic modalities, such as CPR, are gaining in importance. To investigate the lumen of a blood vessel, many CPR images have to be generated from different viewing angles. Clinicians usually scroll through these images, searching for possible pathologies. Motivated by this, we propose Curvicircular Feature Aggregation (CFA) that removes the need to rotate around the centerline of a vessel. It aggregates rotated views into a single static image. The workflow of CFA is outlined in Figure 5.2. The vessel centerlines and radii are obtained by radiological assistants in their daily clinical routine. Among many existing vessel tracking techniques, the assistants use a semi-automatic procedure, which is based on the work presented by Kanitsar et al. [67].

In order to aggregate around the centerline of a vessel, circular rays are cast. These rays are concentric circles with increasing radii, starting from the centerline of the vessel. This is an extension of the CPR technique in order to provide only a single image for several viewing angles. Rays with coinciding center are coplanar, i.e., lying in the same geometric plane. Throughout this chapter we refer to them as *sampling planes*. They can be either axis-aligned or perpendicular to their respective centerlines. The circular rays are sampled, either at a constant angle or a constant arc-length. As the latter sampling strategy leads to an increased number of samples on circles with larger radii, it consumes significantly more computing time. Next, the samples are aggregated into one value for every circular ray. This can be achieved by several methods, such as Maximum Intensity Projection (MIP), Minimum Intensity Projection (MinIP) or Average Intensity Projection (AVG). Basically, any common operator can be applied here. MIP and MinIP are of particular clinical relevance if using CTA data, as MIP depicts calcifications while MinIP provides information about soft plaque. Both pathologies are of high importance, since they hinder blood from flowing through a vessel. In order to provide additional information on how slight variations of the centerline affect the aggregation, we offer a stability visualization, combined with the CFA. Eventually, the CFA of the lumen can be embedded into a visualization of its anatomical context, if radius information is available.

Typical clinical reporting does not only consist of inspecting images generated from CPR or mpCPR, but also requires the consideration of axial slice images. As demonstrated in the study by Portugaller et al. [113], this has a significant impact on the outcome of medical reporting. It is not sufficiently accurate to base a report solely on CPR or MIP images. For this reason, we additionally provide a three-dimensional overview visualization of the vasculature and an axial slice view. By linking these views with the CFA, users are able to explore and navigate through the vessel tree in a comprehensive fashion. In the following sections, each step of Figure 5.2 is explained in detail.
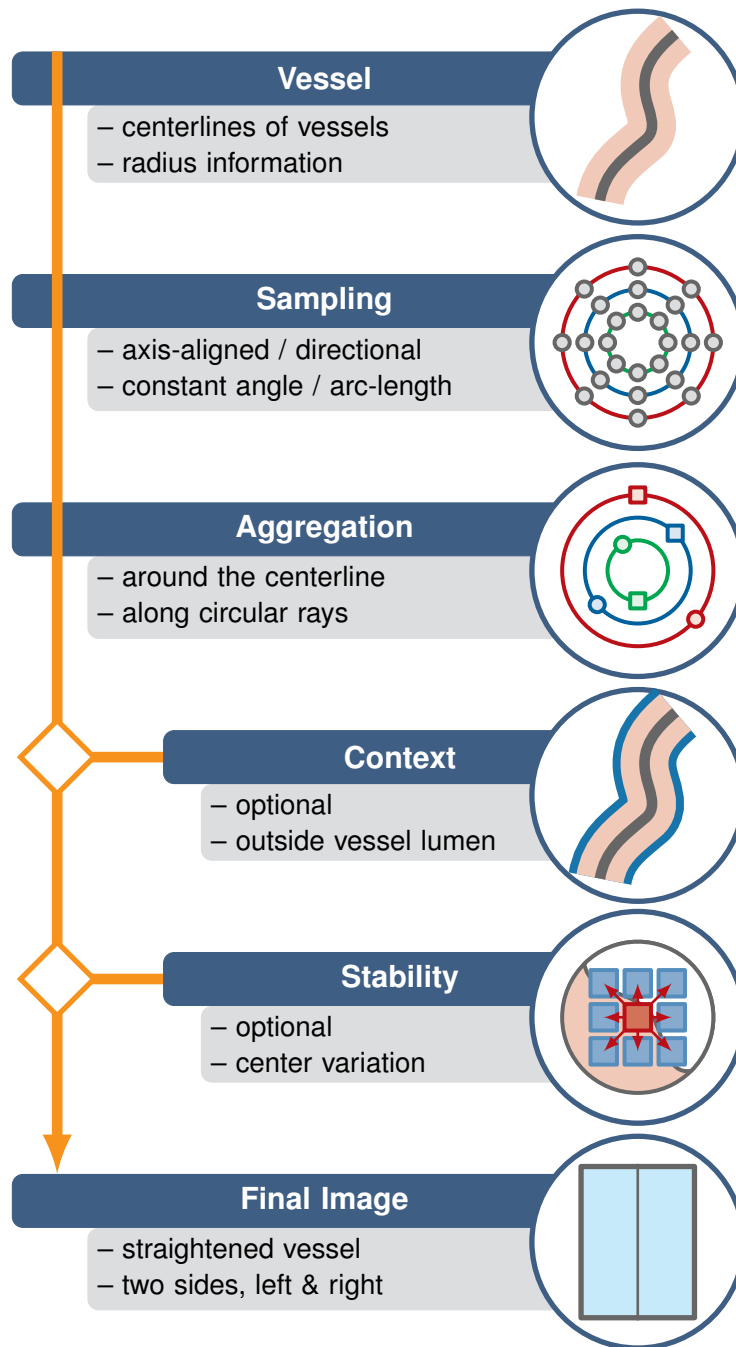
Vessel
– centerlines of vessels
– radius information

Sampling
– axis-aligned / directional
– constant angle / arc-length

Aggregation
– around the centerline
– along circular rays

Context
– optional
– outside vessel lumen

Stability
– optional
– center variation

Final Image
– straightened vessel
– two sides, left & right

Figure 5.2: Workflow of CFA.

5.2.1 Sampling

Starting with a vessel tree (cf. Section 1.2.2 for a detailed description) as input, several cross-sections can be defined along its vessel segments (cf. Figure 5.3a). These cross-sections constitute the sampling planes of the concentric circular rays (i.e., with coinciding centers) and are defined at every centerline point of a vessel segment. Subsequently, circular rays are emitted from these points within their respective sampling plane. To obtain an aggregated value along the circular rays, we use planar radial sampling due to the cylindrical geometry of the vessels and compute n samples $S_{n,\mathbf{X},\mathbf{r},\mathbf{s}}$ around a point $\mathbf{X}$ with radius R by

$$S_{n,\mathbf{X},\mathbf{r},\mathbf{s}} = \{\mathbf{X} + R \cdot (\cos(i \cdot \frac{2\pi}{n}) \cdot \mathbf{r} + \sin(i \cdot \frac{2\pi}{n}) \cdot \mathbf{s})\} \tag{5.1}$$

for $i \in \{0, \ldots, n-1\}$, where $\mathbf{r}$ and $\mathbf{s}$ are the orthogonal generating vectors of the corresponding sampling plane. For sampling around a centerline point $\mathbf{C}$ of a vessel, we distinguish two possibilities to determine the local sampling plane given by the vectors $\mathbf{r}$ and $\mathbf{s}$. First, they can be chosen to be axis-aligned, for example, coinciding with the axial slice plane, i.e., $\mathbf{r} = (1, 0, 0)$ and $\mathbf{s} = (0, 1, 0)$. This leads to homogeneous surrounding regions outside the vessel lumen. If the vessel orientation is not perpendicular to the axis-aligned plane, another sampling plane must be chosen, otherwise the surrounding information and the vessel lumen will be severely distorted. For this reason, and as the second possibility, we compute the rotation minimizing coordinate frame along the centerline using the double reflection method described by Wang et al. [165]. The circular rays are now orthogonal to the centerline (cf. Figure 5.3a). Hence, the lumen of vessels with arbitrary orientation will not be distorted.

The concentric circular rays can be sampled at either constant angle or constant arc-length, as mentioned by Kanitsar et al. [69] and demonstrated in Figure 5.3b. In the case of a constant angle ω, the sampling frequency remains fixed with increasing R, $n = (2\pi)/\omega$, but the distance between consecutive samples increases. If using constant arc-length sampling, $n = R \cdot U$, where U is the number of samples for $R = 1$. The sampling frequency increases with R, but the distance δ between two samples stays constant.

5.2.2 Aggregation

The common clinical reporting procedure of radiologists consists of browsing through many CPR images or axial slices. This approach can be cumbersome and time-consuming due to the high number of images to inspect. The technique described in this chapter remedies this drawback. It aggregates features around the centerline and represents them in a single static image. This makes the rotation operation unnecessary. Since the centerline is defined by a curve, the technique is called Curvicircular Feature Aggregation (CFA). After specifying the samples for every circular ray, a single value needs to be obtained for every ray by an aggregation operation. The goal is to extract relevant domain-specific information along these rays and visually convey it in the final image. Features of interest are mainly calcifications or soft plaque. In CTA data, calcifications are well-characterized by the maximum intensity (MIP) along the ray, while soft plaque can be depicted by showing the minimum intensity (MinIP). While the average value could also provide additional information, it has been considered less relevant by domain experts in our experiments.
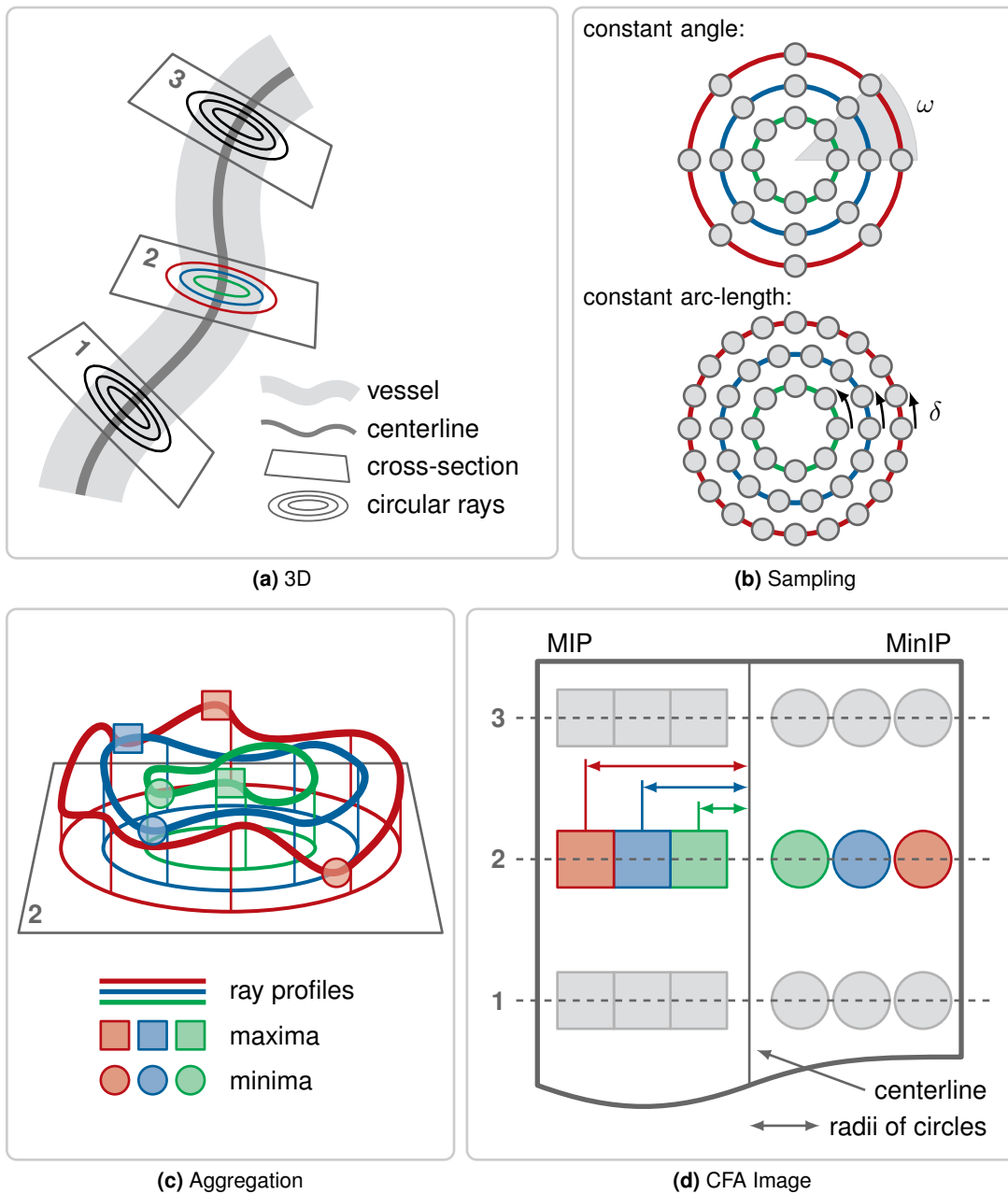
(a) 3D

(b) Sampling

(c) Aggregation

(d) CFA Image

Figure 5.3: Illustration of the sampling and aggregation around the centerline of a vessel. **(a)** displays a centerline with three cross-sectional planes. **(b)** demonstrates two sampling strategies, either with constant angle ω or with constant arc-length δ. **(c)** shows the circular ray profiles of the second cross-section with their maxima as squares and minima as dots. **(d)** presents the final image, where every cross-section corresponds to a row and every concentric circle to a column. The maxima are displayed on the left side of the centerline and the minima on the right side.
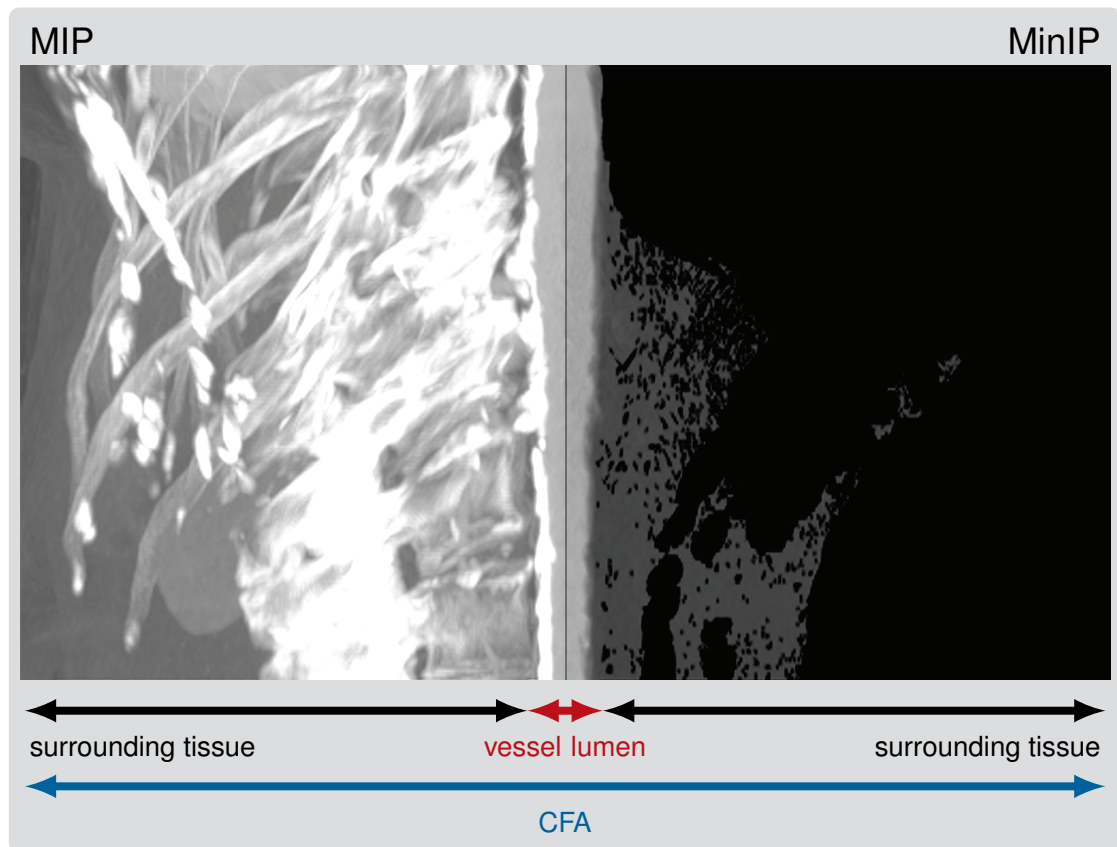
Figure 5.4: Example of CFA along a human abdominal aorta. The thin black centerline separates the image into two parts. MIP (left) shows how closely calcifications approach the centerline and MinIP (right) displays the soft plaque.

Figure 5.3 provides an overview of how the samples are aggregated and how the obtained values are placed in the resulting image. Figure 5.3a presents cross-sections along a vessel together with concentric circular rays and Figure 5.3b illustrates the two possible sampling strategies. Figure 5.3c shows the minima (dots) and maxima (squares) of the corresponding colored circular rays of cross-section two. Figure 5.3d shows the placement of these values in the final image. Since the rotation operation is not required, an orthogonal projection is used and the vessels are represented in a straightened way. Due to this straightening, the obtained image can be divided into two parts, left and right, separated by the centerline of the represented vessel. On the left side MIP is used and on the right MinIP. Both methods are *order independent*, i.e., regardless of the direction of aggregation along a circular ray, the result stays the same. For this reason, two methods can be incorporated into a single image side-by-side. In the case of an *order dependent* technique, the aggregated values of both directions would be shown on the left and right side of the image respectively.
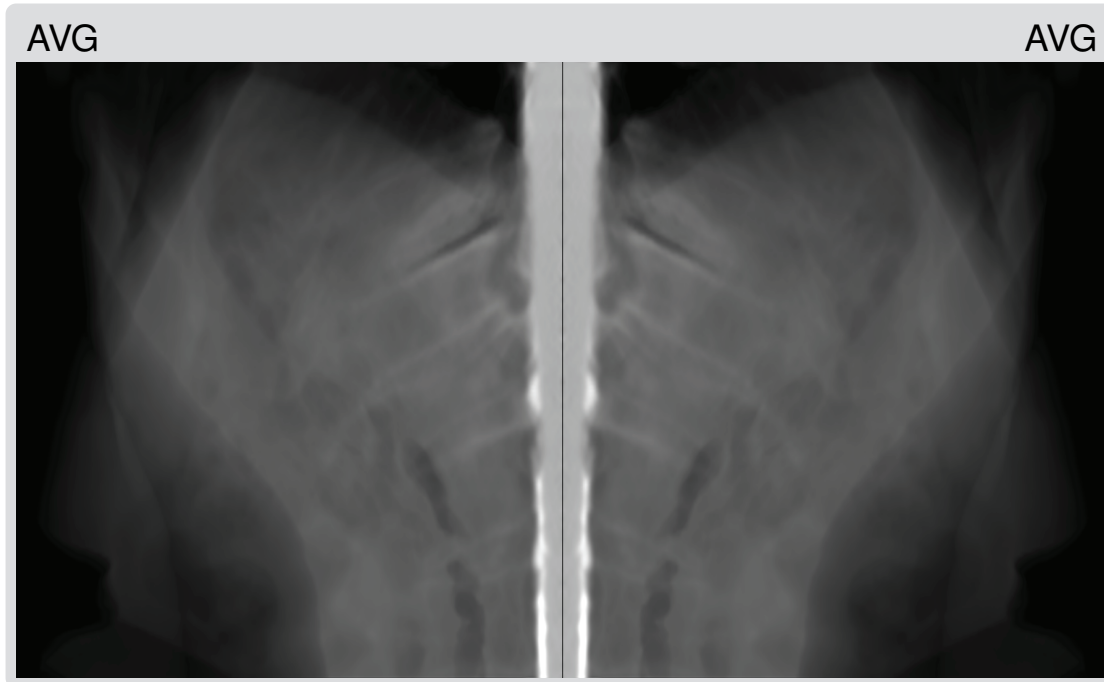
Figure 5.5: Example of CFA along a human abdominal aorta, using AVG as aggregation operation. Calcifications and soft plaque are not as clearly perceivable as in Figure 5.4.

The aggregation is defined as an operator $Op(S_{n,\mathbf{X},\mathbf{r},\mathbf{s}}) = Op(D(v))$ over the intensities $D(v)$ for the samples $v \in S_{n,\mathbf{X},\mathbf{r},\mathbf{s}}$ of a circular ray. Figure 5.4 gives an example of MIP ($Op = max$) on the left and MinIP ($Op = min$) on the right side of the centerline. The left side highlights calcifications, whereas the right side displays soft plaque. Both features are clinically relevant and interesting. If there are high intensity values close to the centerline in MIP, the centerline passes through a calcification. Such an incident cannot occur if the centerline is properly specified by going through the blood flow channel, unless the vessel is completely blocked by an occlusion. The same situation can occur also for low intensity values close to the centerline, depicted this time with MinIP. Another possibility of aggregating along a ray is Average Intensity Projection (AVG), where $Op = mean$. However, calcifications and soft plaque are not as distinctly visible as when using MIP or MinIP (cf. Figure 5.5). Additionally, no original data value is shown, which is not readily accepted in the medical domain.

By aggregating along the circular rays, the information is reduced to its essence. This enables very dense sampling of a vessel's cross-section. In the case of CPR, the images are generated for a predefined set of viewing angles around the vessel. In order to capture small details within the vessel, the angle has to be reduced, leading to an increased number of images. In contrast, CFA allows to capture even the finest details within a single image, which might have been missed if using a larger viewing angle.
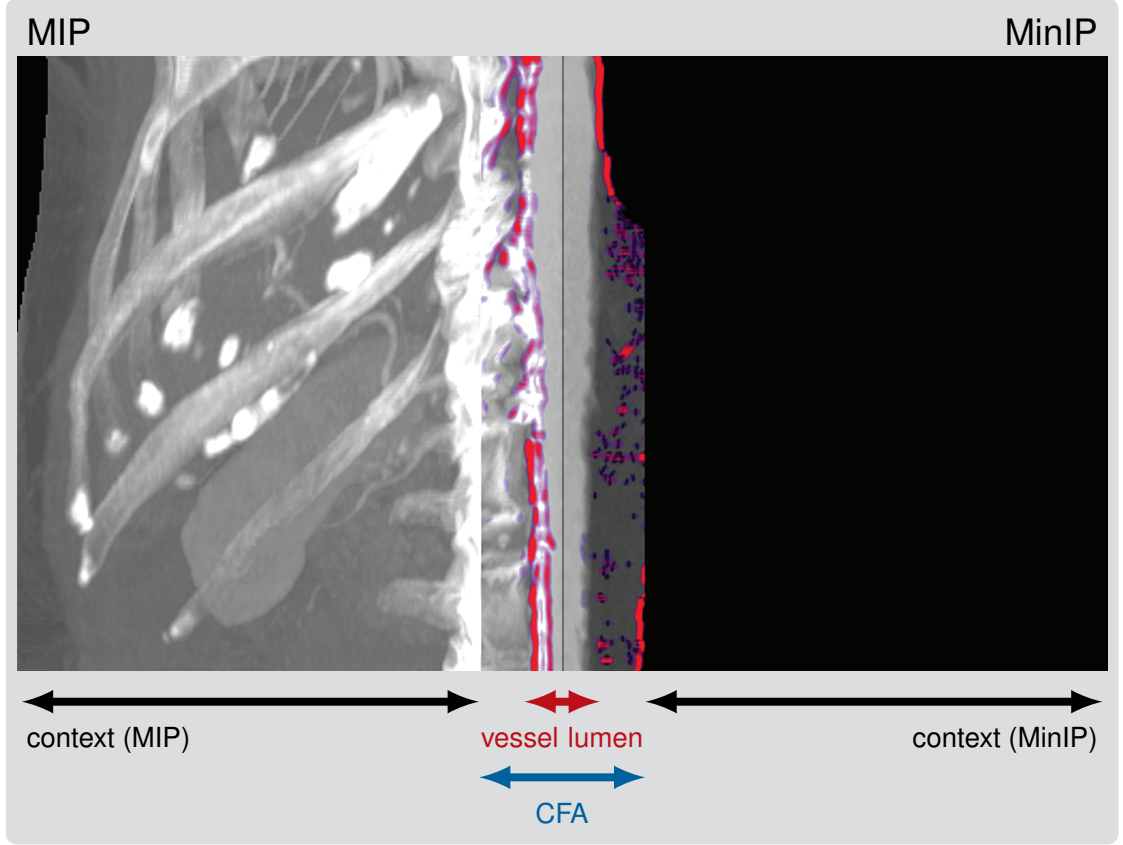
Figure 5.6: Example of a context visualization outside the CFA and a stability overlay (from red being unstable to blue being stable). The context rendering uses the same method as for the CFA.

5.2.3 Context

Since our method aggregates samples into a single value in a circular manner, the spatial perception is reduced with increasing distance from the center of a vessel. Motivated by the VesselGlyph [146] technique, which embeds a CPR (focus) into a MIP or DVR (context), we optionally augment the CFA (focus) of the vessel lumen with a context visualization of the vessel's surrounding tissue. This contextual information enhances spatial perception and, for example, provides surgeons with a better overview of the vasculature. Figure 5.6 shows an example of a CFA with context visualizations on both sides. The final image $I_F(x, y)$ is composed by

$$I_F(x, y) = \begin{cases} I_{CFA}(x, y) & \text{if } |x_{cl} - x| \leq R_{max} \cdot f \\ I_{CTX}(x, y) & \text{if } |x_{cl} - x| > R_{max} \cdot f \end{cases} \tag{5.2}$$

where I_{CFA} is the CFA image and I_{CTX} is the image of the context visualization, both with dimensions $W \times H$. The horizontal position of the centerline within the image is $x_{cl} = W/2$.

Because the vessel radius information is not always reliable, we multiply the maximum radius, R_{max}, of the current vessel branch by a user-specified factor f (2 in our implementation). This ensures that the context starts outside the vessel lumen. The context visualization is created by using axis-aligned ray casting (usually a frontal view of the data set).

5.2.4 Stability Analysis

Centerlines are typically available only with a certain accuracy, and CFA crucially depends on the location of the centerline. The stability of a CFA is determined by the magnitude of change that a slight variation of the centerline exercises on the resulting image. Since the centerline may not always be completely centered, we determine the stability of a CFA over a neighborhood of a centerline point $\mathbf{C}$. The neighbors $\mathbf{N}_{\mathbf{C},w}$ of $\mathbf{C}$ are computed as

$$\mathbf{N}_{\mathbf{C},w} = \{\mathbf{C} + i \cdot \mathbf{r}\} \times \{\mathbf{C} + j \cdot \mathbf{s}\} \tag{5.3}$$

for $i, j \in \{-w, \ldots, w\}$, where $w \in \mathbb{N}$ is user-specified and $\mathbf{r}$ and $\mathbf{s}$ are the orthogonal vectors generating the sampling plane normal to the centerline. For each element of $\mathbf{N}_{\mathbf{C},w}$ we apply planar radial sampling and an operator Op to finally obtain an intensity value. The local stability is now given by the variance of all these values and describes the local uniformity around $\mathbf{C}$. The stability is low if the variance is high and vice versa. We overlay the CFA with the variance mapped to red if it is high and blue if it is low (cf. Figure 5.6). A high variance close to the centerline indicates a badly estimated centerline. This can be used as an indicator for the centeredness of a centerline point.

5.3 Visual Mapping

Finally, the whole tree-like vasculature of the human lower extremities should be presented in a meaningful and comprehensible way. Borkin et al. [12] propose a method where the branches of the vessel tree are connected at the axial slice positions of their parent branches. In our case, due to vessel straightening, this layout can become rather long. For this reason, the CFAs of the vasculature are spatially sorted from left to right and grouped according to the anatomy. Figure 5.7 illustrates the layout for the abdominal aorta with its branches, the iliac arteries. The root of the tree is centered and subsequent branches are presented to the left or right as a group. Since we render the vessel lumen straightened using orthogonal projection, distances can easily be measured. Therefore, rulers are added to every CFA visualization inside the border around the image. To allow the investigation of a vessel branching location, every branch is pre-pended with a part of its parent vessel (10 centerline points in our implementation). This is visually conveyed and delineated by the transition margin, as indicated by the blue line in Figure 5.7b, leading to a 6mm overlap in our case. The anatomical layout of the entire vasculature of the human lower limbs is presented in Figure 5.8.

In addition to common interaction possibilities such as zooming, panning or changing the windowing function, whole branches of the vessel tree can be collapsed. By clicking on the image above the CFA, which shows an aggregation along the centerline, the visibility of the corresponding vessel branch is toggled. This might be particularly helpful if the vessel tree is
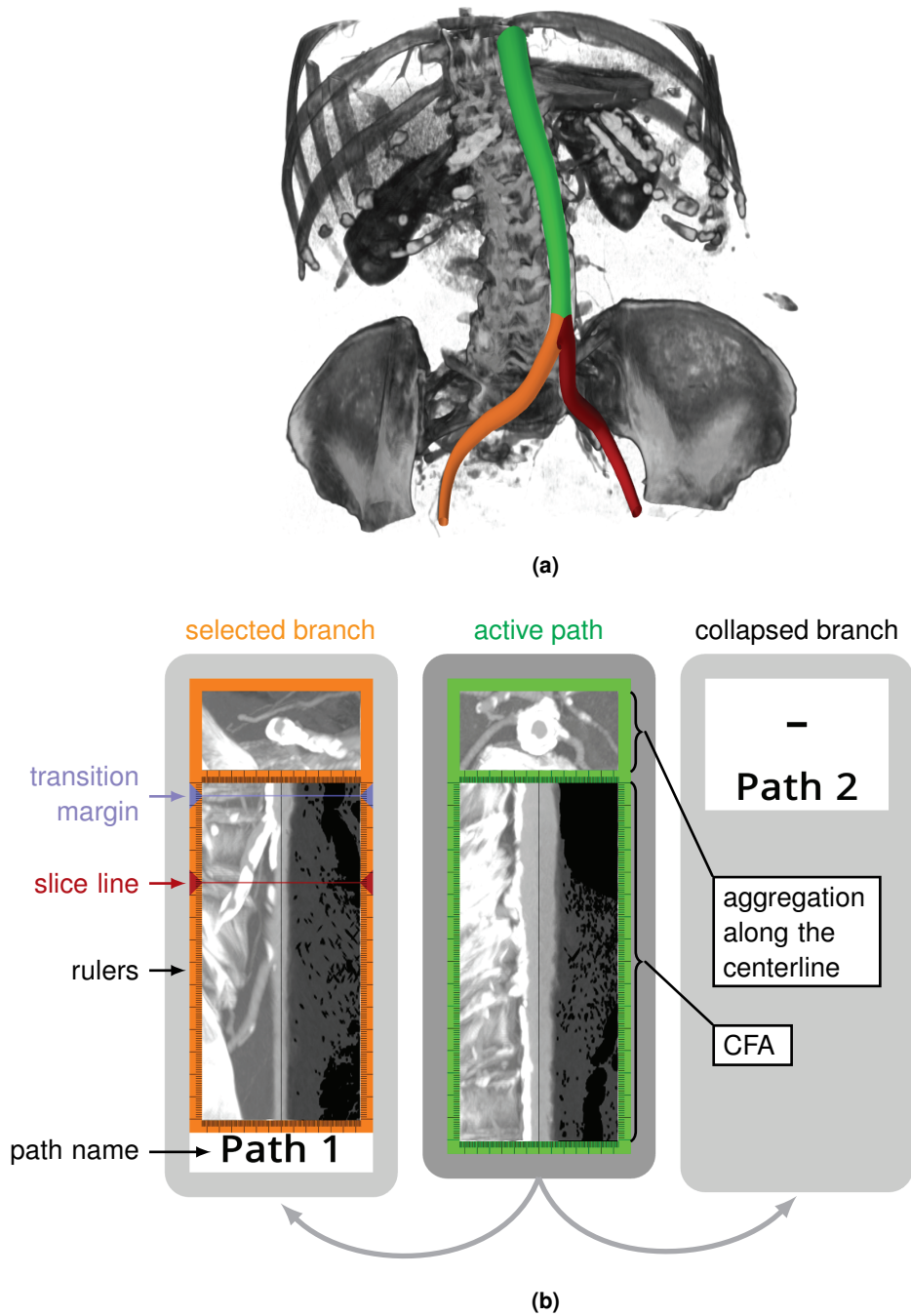
(a)

(b)

Figure 5.7: Illustration of the anatomical layout of the abdominal aorta and its branches. The vessel tree consists of three vessel segments, where the orange and green ones are part of the currently active path. **(a)** shows a 3D visualization together with the vessel tree. **(b)** presents the anatomical layout with the abdominal aorta (image with green border) in the middle and its branches placed to the left and right.
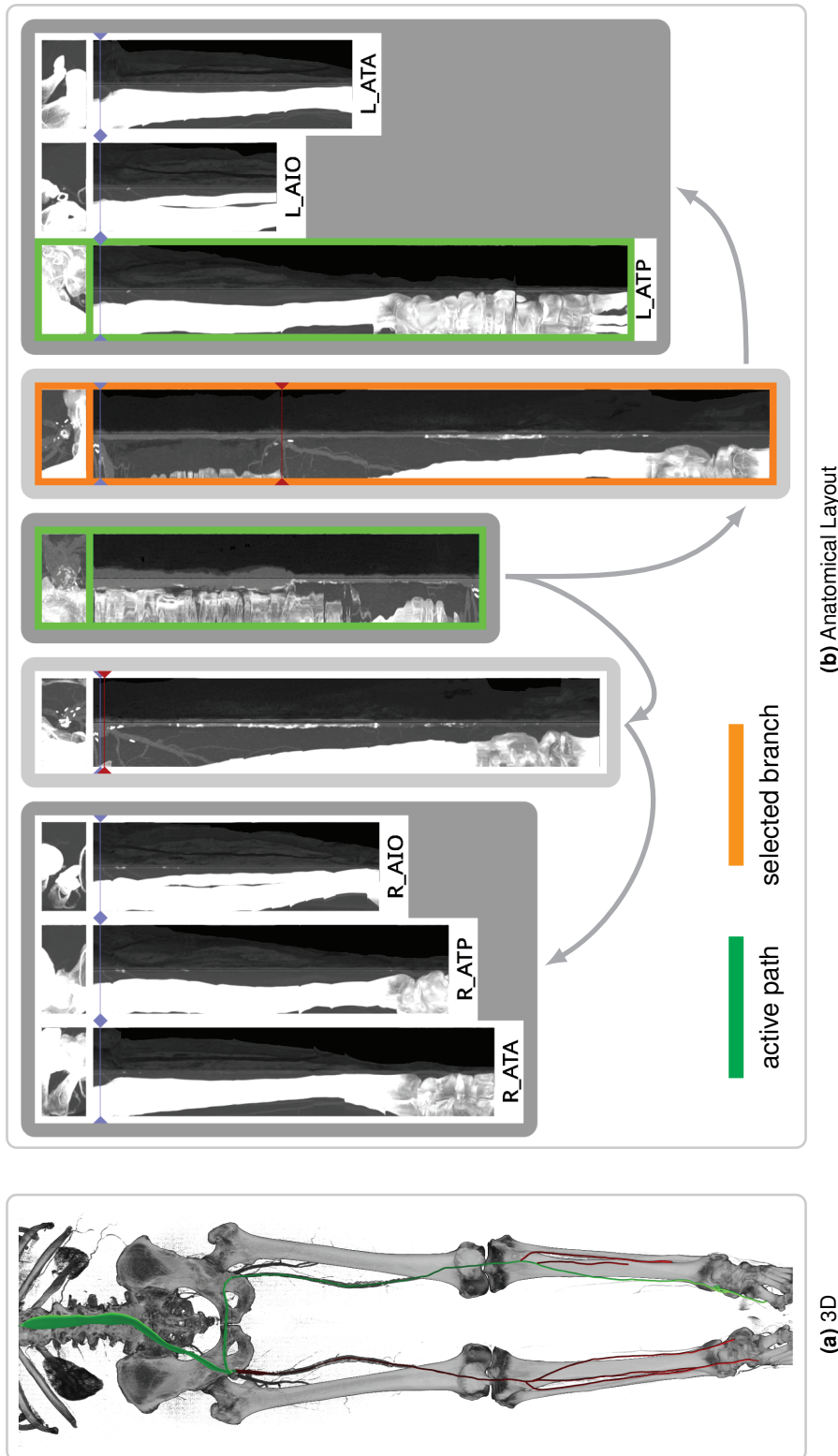
(b) Anatomical Layout

(a) 3D

Figure 5.8: Example of the anatomical layout of the vasculature of the human lower limbs, acquired with CTA. The patient has a cross-over bypass below the aortic bifurcation, connecting the right iliac artery with the left femoral artery. **(a)** shows a 3D visualization together with the vessel tree. **(b)** presents the anatomical layout with the abdominal aorta in the middle and its branches placed to the left and right. A sampling plane orthogonal to the centerline is used to properly create the CFA of the bypass (image with orange border).

rather complex. The currently user-selected vessel branch is highlighted in orange, whereas the vessel path including this branch is marked as active and shown in green (cf. Figures 5.7 and 5.8). Such a vessel path extends from the root to a leaf of the vessel tree. The context visualization and the centerline stability overlay can be interactively switched on and off by the user.

Zooming is usually done by scaling the CFA texture and using texture interpolation capabilities. We provide an additional zooming possibility by decreasing the distances between consecutive circular rays, starting from the centerline. This anisotropic zooming offers a denser sampling close to the centerline and provides a more precise zooming than texture interpolation. This changes only the horizontal scale and preserves the overview of the whole vessel branch.

5.4 Results

In this section, we present results of CFA with three examples. First, we illustrate and demonstrate our method on a phantom data set containing several important pathological features. The second example shows the vasculature of the human pelvis including a vessel stenosis. Third, a vessel occlusion is presented below the bifurcation of the human abdominal aorta. In all examples MIP, CPR and CFA are compared.

5.4.1 Phantom Data Set

A phantom data set is shown in Figure 5.9. The centerline runs straight through the artificial tube, from top to bottom. The bottom of the tube is shifted sideways to simulate a centerline being off-center. This can be seen by the orange centerline point inside the calcification at the bottom in Figure 5.9a. The following relevant pathological features are simulated (cf. Figure 5.9a):

- a small eccentric calcification,

- a concentric calcification,

- a big eccentric calcification,

- an eccentric soft plaque,

- a concentric stenosis and

- a small eccentric calcification, centerline off-center.

For every pathological case, a corresponding axial slice is presented on the left side, together with the position of the centerline, shown as an orange point. The aim of the phantom data set is the comparison of MIP, CPR and CFA for these important features.

In the MIP visualization in Figure 5.9b the concentric calcification seems to block the whole artificial vessel. Even the big eccentric calcification appears to completely prevent the blood from flowing. This can be clarified by using CPR or CFA. The CPR images in Figure 5.9c are generated for angles from $-90°$ to $90°$ with an $18°$ stepsize. It is cumbersome to inspect all these images and judge, for example, the centeredness of the centerline.

The CFA image is shown in Figure 5.9d with MIP on the left side and MinIP on the right side. The sampling planes of the circular rays coincide with the axial slice plane. All calcifications can
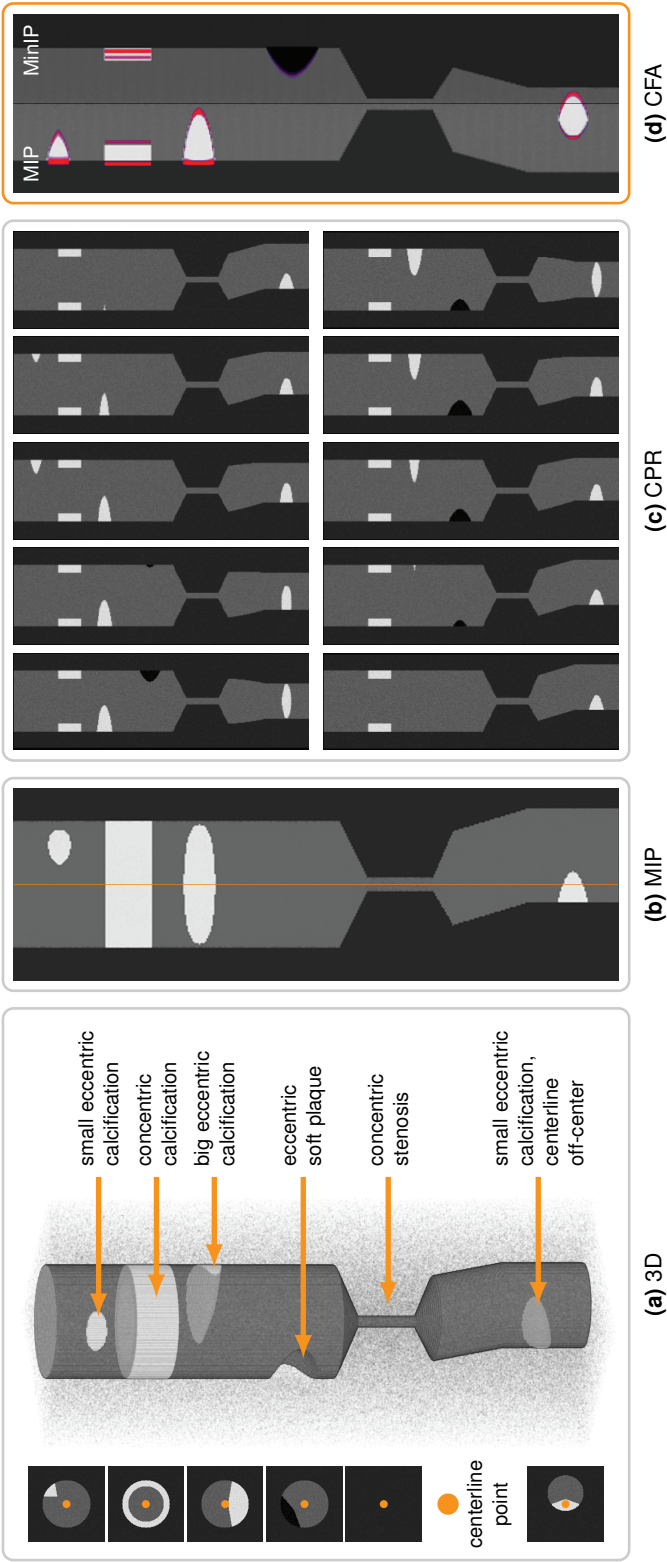
Figure 5.9: A tubular phantom data set. **(a)** shows a 3D visualization of all relevant pathological features. **(b)** presents a MIP of the whole data set with the centerline in orange. **(c)** displays the CPR images and **(d)** the CFA with MIP on the left and MinIP on the right showing all the features within one image. A high variance (red) close to the centerline indicates that it is not properly centered.

be seen on the left side of the CFA image and the soft plaque on the right side. If a calcification is visible in MIP and MinIP close to the vessel wall, it has to be a concentric calcification. If a calcification is only visible in MIP, it is an eccentric one. The same can be observed for soft plaque, but with MinIP.

Additionally, it is possible to judge the centeredness of the centerline. Since the eccentric calcification at the bottom also appears in the MinIP, but close to the centerline rather than close to the vessel wall, the centerline has to pass through this calcification, although it should not. Therefore, one can deduce that the centerline is not properly centered in this part, since it should always be in the lumen of a vessel. The high variance (red) at the centerline supports this conclusion, since the boundary of two different types of tissue is in its close vicinity, namely a calcification and opacified blood. Hence, a small alteration of the centerline would lead to a high variance.

5.4.2 Vessel Stenosis

Figure 5.10 shows a CTA data set of the human pelvis with a vessel stenosis. The position of the stenosis is pointed out by an arrow in the top-left 3D visualization. Next, axial slices at the beginning, at the center, and at the end of the stenosis are presented. They demonstrate how narrow the vessel lumen becomes in the center of the stenosis. In the MIP image the stenosis is hardly perceivable. The CFA image at the top-right shows a MIP on the left side and a MinIP on the right side. The sampling planes are chosen to coincide with the axial slice plane. It is well perceivable in the zoom-in, where and to what extent the vessel becomes narrow (orange arrow). The CPR images at the bottom of Figure 5.10 are generated for the angles between $-90°$ and $90°$ with a stepsize of $18°$.

5.4.3 Vessel Occlusion

Figure 5.11 presents a CTA data set of the human pelvis with a vessel occlusion inside a stent below the bifurcation of the abdominal aorta. The occlusion is highlighted by an arrow in the top-left 3D visualization and even clearly visible in the MIP image, but the lumen inside the stent remains obscured. The CPR images (between $-90°$ and $90°$ with an $18°$ stepsize) show the occlusion well, but many of them have to be inspected. In contrast, the CFA shows the entire occlusion within one image. Since soft plaque is visible on both sides up to the vessel wall and its intensity differs from blood, it can only be a concentric stenosis inside the stent obstructing the whole lumen and completely blocking blood from flowing.

5.5 Discussion and Limitations

We implemented the proposed technique in the AngioVis [2] framework. Although the framework is used in the daily routine, the proposed technique is not, since it would require an extensive clinical evaluation. We employed CUDA for computing the CFA images and GLSL for visualizing them anatomically sorted and grouped. The path names are rendered with the painting capabilities of Qt4.
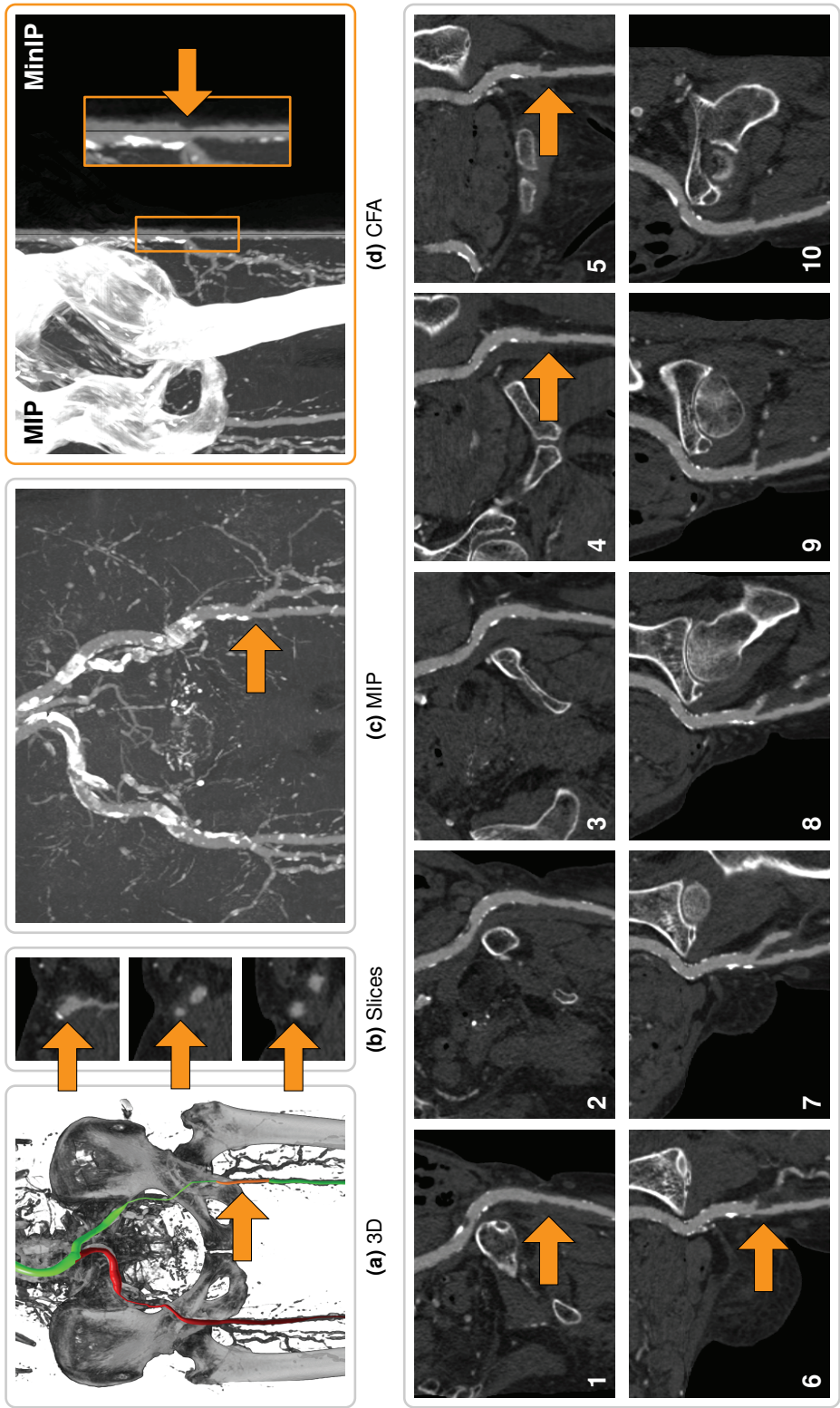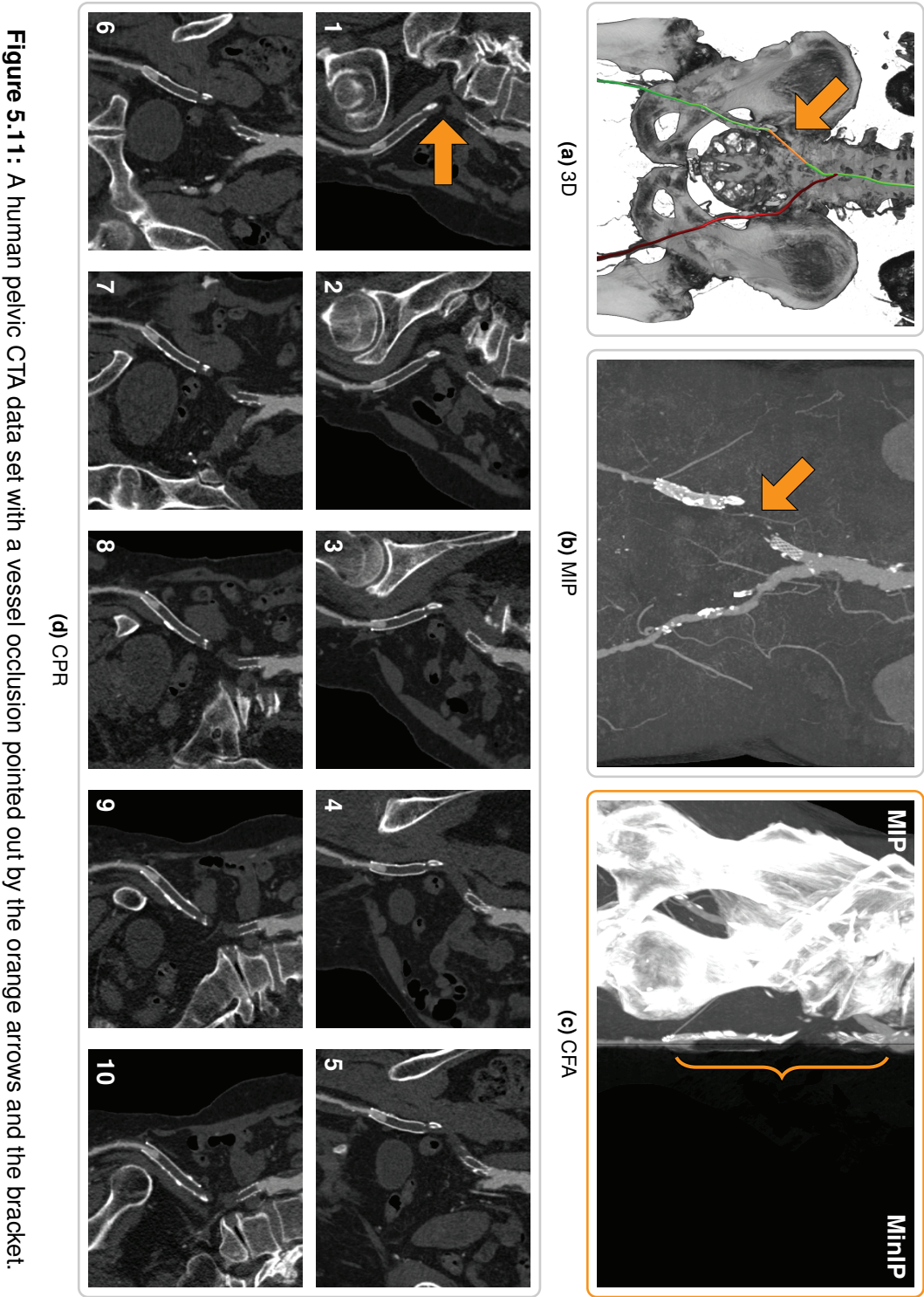
Figure 5.10: A CTA data set of the human pelvis with a vessel stenosis pointed out by the orange arrows.

Figure 5.11: A human pelvic CTA data set with a vessel occlusion pointed out by the orange arrows and the bracket.

One drawback of CFA originates from the aggregation along the circular rays. If using an order independent aggregation approach, the exact circular location of a feature is not conveyed in the final image. MIP, for example, captures only the maximum value along the ray, regardless of its position and size. To determine the exact location within a cross-section, we provide clinicians with additional linked views like, for example, an axial slice view.

Furthermore, CFA is much less sensitive to changes of the centerline than CPR and additionally provides information about the centerline stability by visually guiding users to highly varying regions. Large errors in the centerline detection cause problems, for example, if the centerline is outside the vessel lumen. However, with CPR the pathological feature at the bottom of the phantom data set (cf. Figure 5.9c) might be reported as a stenosis, although it is a pseudo stenosis. In fact, this case is one of the motivations for our technique, because through using MIP and MinIP it is possible to judge the centeredness of the centerline. Hence, the centerline stability is less of an issue for CFA.

5.6 Evaluation

We consulted nine radiologists for evaluation of CFA by means of a questionnaire (cf. Appendix D). We compared MIP with CPR and CFA in terms of the pathological features presented in the phantom data set (cf. Figure 5.9) and in terms of the vessel stenosis (cf. Figure 5.10) and the vessel occlusion (cf. Figure 5.11). Additional linked slice views were not used in this comparison. The following criteria or main points (cf. vertical axis of Figure 5.12) were assessed and discussed:

1. In the assessment of overall preference (labeled **General**), CPR performs better than CFA, and both are significantly better than MIP. The reason for this could be the fact that CFA is mostly new to the participants and MIP and CPR are already well known. The evidence for this assumption is given by the next criterion: Simplicity.

2. Regarding **simplicity**, the participants rated CPR as the most simple method, followed by MIP and finally CFA. More learning time is probably required to understand CFA and then interpret the images accordingly. Two radiologists specifically mentioned that, after the initial accommodation period, the technique shows great potential.

3. Assessing the **size** or **length** of a pathology along a vessel has been rated as useful by all participants. In fact, the possibility to immediately measure the size or length of a stenosis along the vessel is one of the strengths of CFA.

4. Although the cross-sectional **location** of a pathology is rated as useful by some participants, two radiologists confirmed that the position along the centerline is more important. The cross-sectional location of a pathology is not considered to be relevant for current therapeutic procedures in the clinical routine (e.g., balloon dilatation, stenting, and bypass surgery). As mentioned when discussing the limitations of CFA, the location of a pathology within a cross-section cannot be estimated properly without linked slice views. Hence, CPR performed best by far with regard to this criterion.
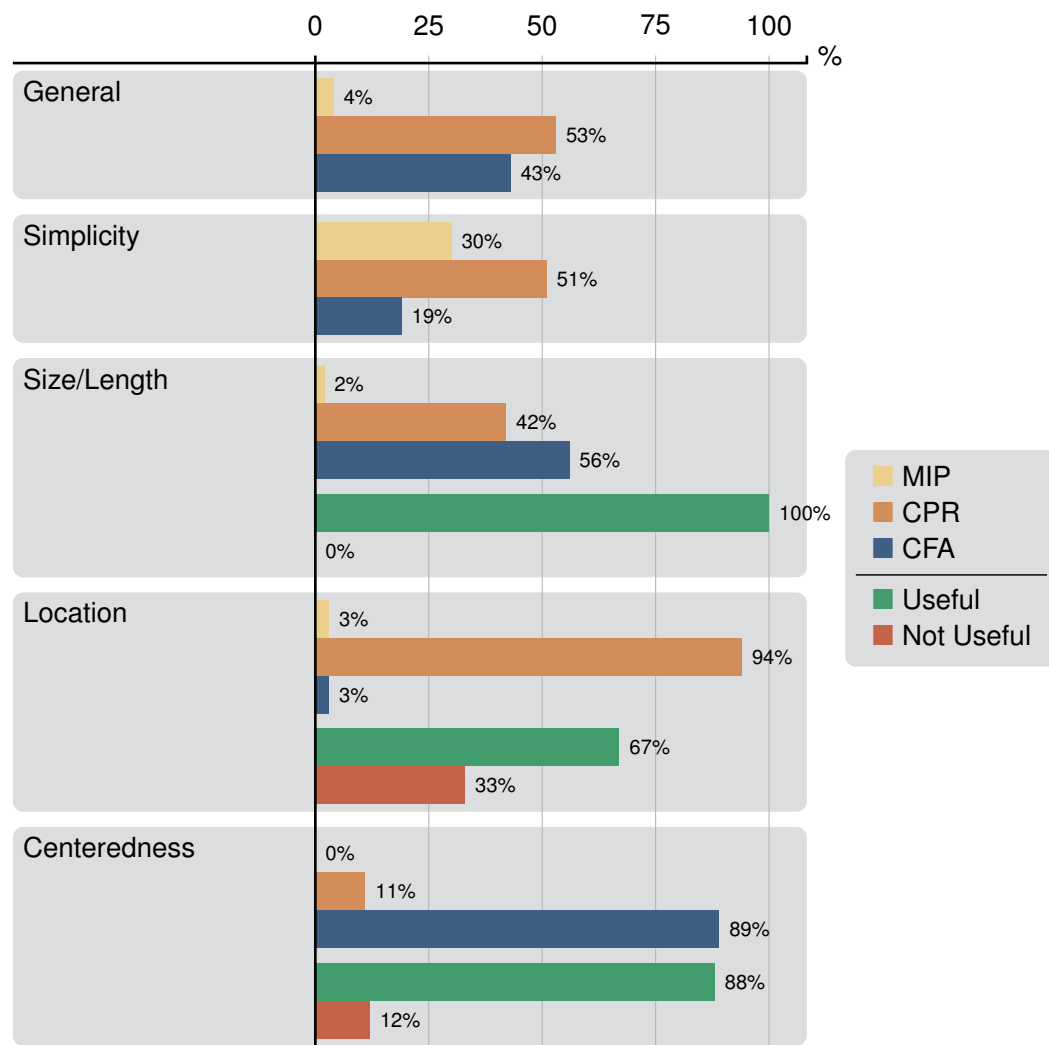
Figure 5.12: Evaluation of CFA using a questionnaire (cf. Appendix D). It consists of 48 questions divided into five criteria (vertical axis). The horizontal axis shows the ratings of the participants in percent. In addition, the clinical usefulness of three criteria (Size/Length, Location, and Centeredness) has been evaluated.

5. The visual analysis of the **centeredness** of a centerline is seen as useful by most partici-
pants. This is another key feature of CFA and it performed best concerning this criterion.
The reason for this is the opportunity to directly judge the centeredness of a centerline
within a single image.

Overall, CFA received a positive response and its strengths are well conveyed and seen as useful
by most participants. The feedback obtained from domain experts gives an indication that CFA
could be a valuable alternative to MIP and CPR in the clinical routine.

5.7 Summary

In this chapter, we introduced Curvicircular Feature Aggregation (CFA), a new technique for the
visualization of blood vessels. Our novel approach aggregates vessel features around the center-
line into a single static image. This avoids inspecting the vessel lumen from multiple viewing
angles. Furthermore, our method provides additional visual cues on the centerline stability. We
described how such an aggregation of a vessel tree can be presented anatomically sorted and
grouped and suggested linked views for further visual analysis. The feedback from domain
experts indicated that our technique can be an alternative to MIP and CPR.

We can only see a short distance ahead, but we can
see plenty there that needs to be done.

—Alan Turing

CHAPTER **6** ∎

Conclusion

THIS thesis addressed two parts of medical visualization, mainly demonstrated on CTA data. First, in the field of vessel reformation techniques, the assessment of the interior of spatially arbitrarily oriented vessels was investigated. Providing a satisfactory visualization of the vessel lumen while smoothly cutting into the surrounding tissue and retaining correct visibility of multiple vessels, was one of the main challenges. We proposed two novel vessel reformation techniques with the aim to progress towards a more general approach:

Centerline Reformation (CR) offers the possibility to render the lumen of arbitrarily oriented vessels, by using wavefront propagation in image space. Spatial relations of multiple vessels are enhanced with halos, and contextual information is demonstrated by embedding the lumen into any volume rendering. Although this technique generates acceptable results, it suffers from the trade-off between the displayed size of the surrounding tissue and the visibility of multiple vessels.

Curved Surface Reformation (CSR) improves CR by providing an entirely three-dimensional process of creating a cut surface through multiple vessels, while simultaneously cutting smoothly through their surrounding tissue. By means of a cost function along the cut surfaces, automatically generated cutaways reveal as much of the vessel lumen as possible. Moreover, unrestricted interaction allows a comprehensive exploration and diagnosis of vessels with any spatial orientation.

The second part dealt with reduction of clinical reporting time by decreasing the required interaction of medical systems. We described at first more general aspects of such a system, by proposing the *knowledge assisted sparse interaction* approach, with examples in the medical domain. With respect to vessels, we discussed a technique for vessel visualization and inspection, which is based on this approach. It combines several aspects of both, vessel reformations and interaction reduction. The following two contributions have been made:

117

Smart Super Views provide only the relevant visualization techniques in the form of super-elliptical views. The relevance is encoded in the shape and size of the view and we proposed two possible layout strategies, the linear and radial layout. This provides effective guidance of the user with knowledge defined by the respective experts of the application domain.

Curvicircular Feature Aggregation (CFA) reduces the number of images to inspect by aggregating the volumetric information in a circular fashion around the centerline of vessels. This leads to a single image, showing how close pathologies reach to the centerline. An inaccurately defined centerline can be assessed with the aid of the stability overlay of the respective centerline.

Although this thesis presented an advance towards general vessel reformations and interaction reduction in medical visualization, there is a lot of room for future improvements. We consulted many radiologists for their evaluations of our described approaches. Nevertheless, clinical studies are still left to be done as they are crucial in transferring the techniques into the daily clinical routine. Regarding vessel reformation techniques, different strategies for context rendering as well as enhancement of silhouettes can be investigated. Apart from the presented application fields of Smart Super Views, others can be explored, possibly even non medical ones, such as geographic maps or programs for computer-aided design. Other representations of knowledge or possibilities in machine learning can be considered to provide users with more opportunities in guided data exploration.

Imagination is more important than knowledge.
For knowledge is limited.

—*Albert Einstein*

APPENDIX **A**

Questionnaire of Centerline Reformation

T HE aim of this questionnaire should be the evaluation of our visualization technique, called Centerline Reformation. This method offers the possibility to inspect the lumen of arbitrarily spatially oriented vessels, due to a new way of creating the lumen. We will compare this method with Curved Planar Reformation (CPR) and Multipath Curved Planar Reformation (mpCPR). Furthermore, we will present different context visualizations in combination with CR. The questionnaire will assess the following points:

- Visualization of one vessel lumen

- Visualization of the lumen of many vessels

- Halos augmenting the vessel lumen

- Visualization of different context rendering methods

A.1 Single Vessel Visualization

The following two images show the lumen of one vessel visualized with two different methods.

(a) (b)

		a	x	b
1	Which image depicts the vessel best?	a☐	x☐	b☐
2	Which image visualizes the flow-channel qualitatively better?	a☐	x☐	b☐
3	Which image depicts the calcifications best?	a☐	x☐	b☐
4	Which image visualizes the additional organs besides the vessel qualitatively better?	a☐	x☐	b☐

		1	2	3	4	5
	1 - highly undesired / 2 - undesired / 3 - neutral / 4 - desired / 5 - highly desired	1	2	3	4	5
5	How desired is the visualization of the additional organs besides the vessel?	☐	☐	☐	☐	☐

The user can increase the vessel radius if it is not sufficient enough. This offers the possibility to view pathologies which have initially been hidden or are not visible.

(a) original vessel radius   **(b)** increased vessel radius

6	Which image depicts the calcifications best?	a☐		x☐		b☐
	1 - highly undesired / 2 - undesired / 3 - neutral / 4 - desired / 5 - highly desired	1	2	3	4	5
7	Is it desired to increase the vessel radius manually?	☐	☐	☐	☐	☐

A.2 Multiple Vessel Visualization

Multipath Curved Planar Reformation (mpCPR) was initially designed to visualize the vessel lumen of the human lower extremities. This technique splits the image into parts according to the branches of the vessel tree. Then for each part the CPR is visualized and finally all parts are combined to the final image. The following images show the peripheral vessel which split into femoral arteries left and right (a, b), cervical vessels (c, d), a peripheral pulmonary vessel tree (e, f) and an aneurysm (g, h).

8	Which image depicts the vessels best?	a ☐	x ☐	b ☐
9	Which image depicts the vessels best?	c ☐	x ☐	d ☐
10	Which image depicts the vessels best?	e ☐	x ☐	f ☐
11	Which image depicts the vessels best?	g ☐	x ☐	h ☐
12	Which image depicts the depth perception best? *(Anterior vessels vs. posterior vessels)*	a ☐	x ☐	b ☐
13	Which image depicts the depth perception best? *(Anterior vessels vs. posterior vessels)*	c ☐	x ☐	d ☐
14	Which image depicts the depth perception best? *(Anterior vessels vs. posterior vessels)*	e ☐	x ☐	f ☐
15	Which image depicts the depth perception best? *(Anterior vessels vs. posterior vessels)*	g ☐	x ☐	h ☐

		1	2	3	4	5
	1 - highly undesired / 2 - undesired / 3 - neutral / 4 - desired / 5 - highly desired	1	2	3	4	5
16	Do you consider the surrounding parts as visualized in (a, c, e, g) as desired?	☐	☐	☐	☐	☐

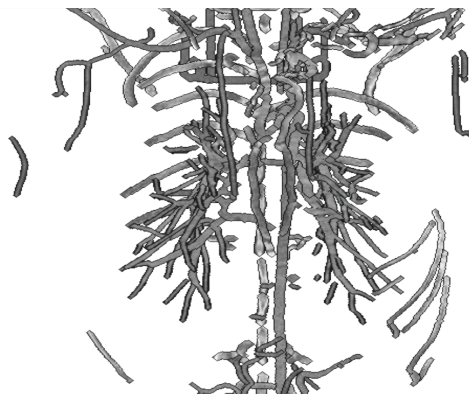|		1	2	3	4	5
	1 - totally not helpful / 2 - not helpful / 3 - neutral / 4 - helpful / 5 - very helpful	1	2	3	4	5
17	How clinically helpful is the visualization of vessels of any orientation?	☐	☐	☐	☐	☐
18	Is this helpful when detecting pathologies?	☐	☐	☐	☐	☐
19	Is this helpful to detect pathologies faster?	☐	☐	☐	☐	☐
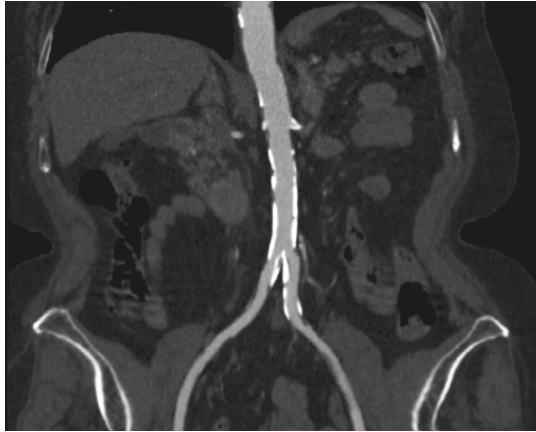
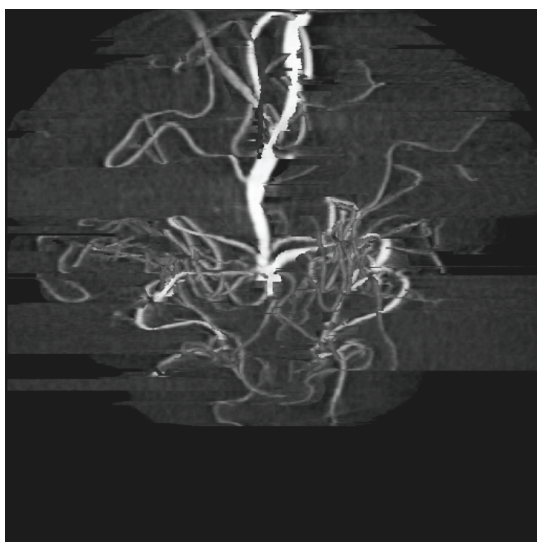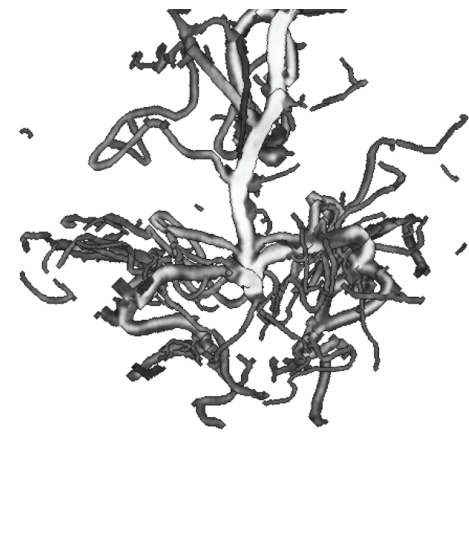**(a)**

(b)
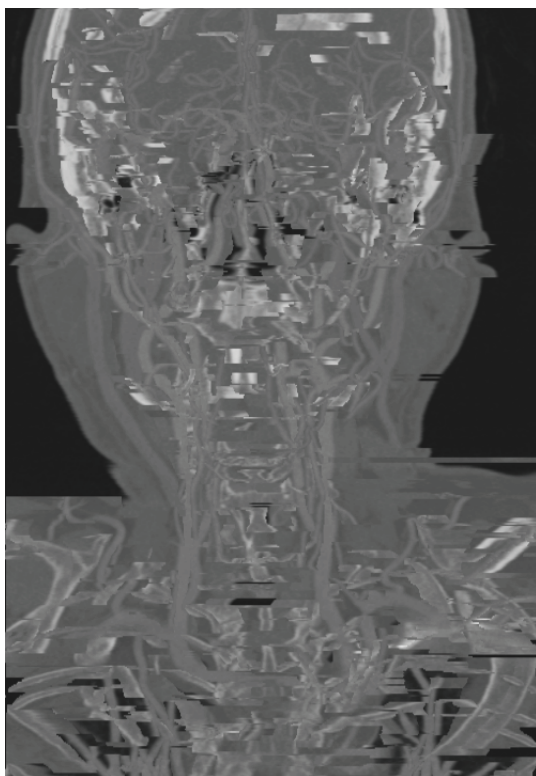
(c)
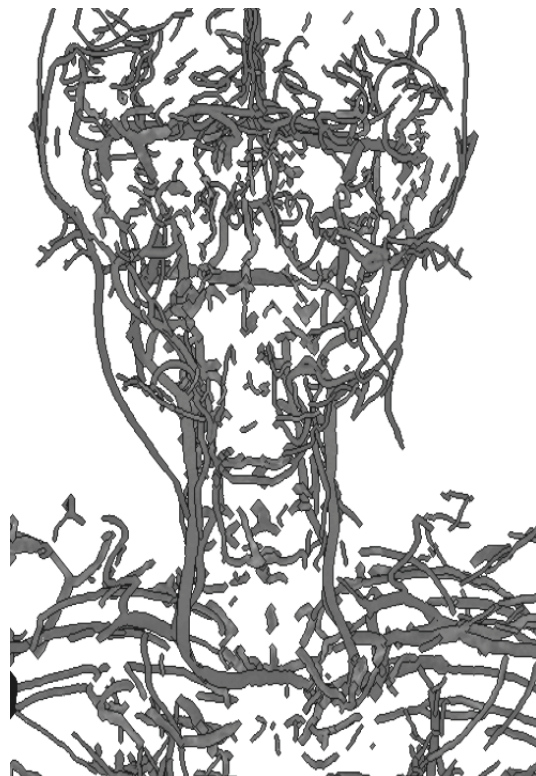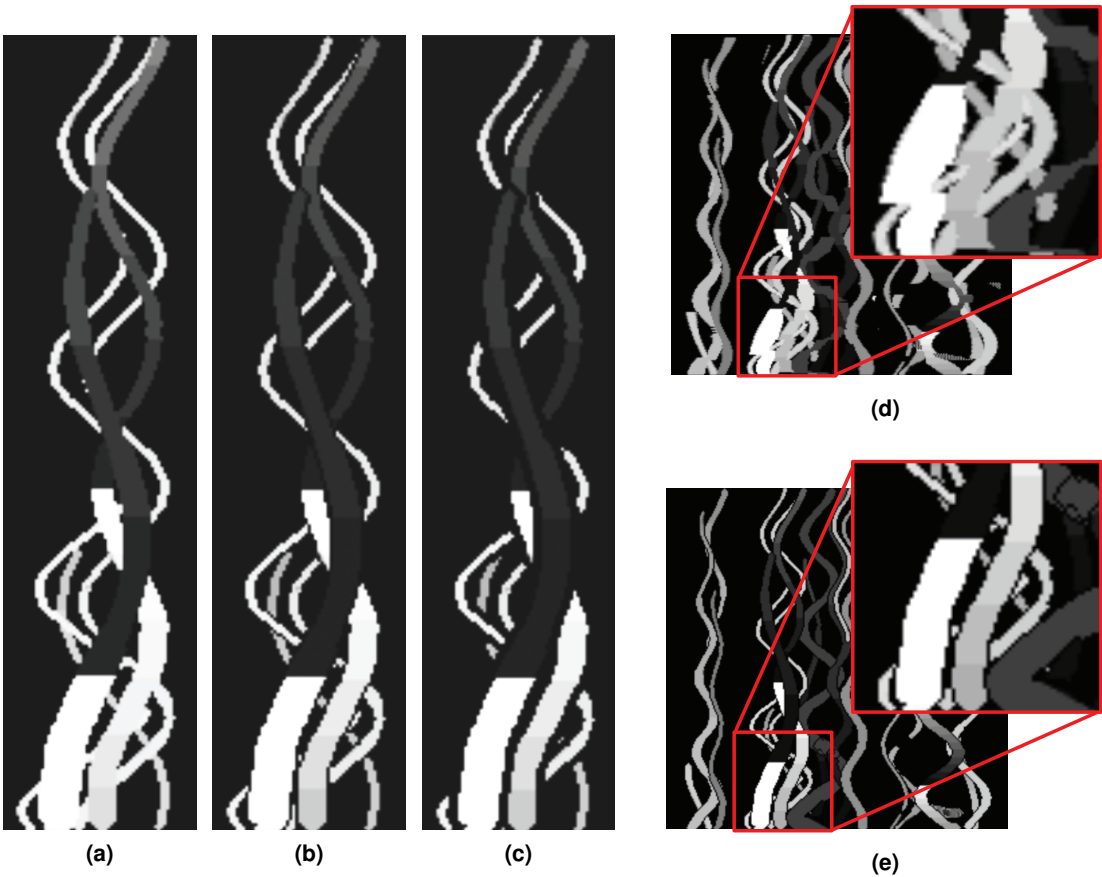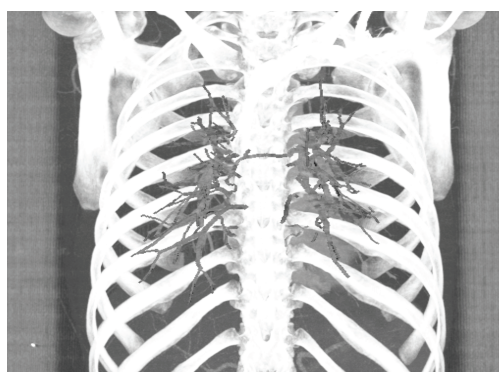

(d)
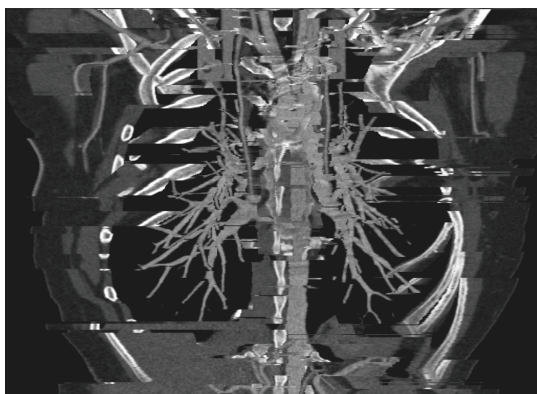
(e)

(f)

(g)

(h)

A.3 Halos

To enhance spatial relations and depth perception, a gap, called halo, can be optionally added around the lumen visualization. The user is able to specify the width of the halo. The images shown below are from an artificial data set, which contains several differently sized helices with various color gradients.
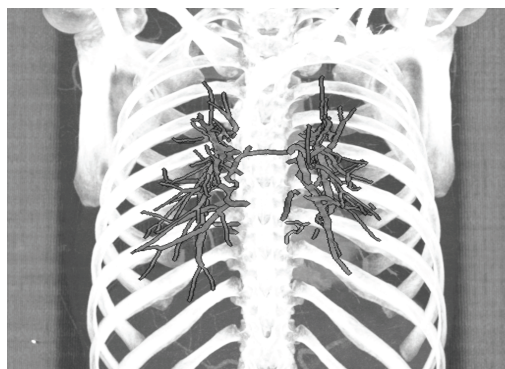

(a) (b) (c)

(d)

(e)

20	Which image depicts the vessels best?	a☐	b☐	c☐
21	Which image depicts the depth perception best? *(Anterior vessels vs. posterior vessels)*	a☐	b☐	c☐
22	Which image depicts the vessels best?	d☐	x☐	e☐
23	Which image depicts the depth perception best? *(Anterior vessels vs. posterior vessels)*	d☐	x☐	e☐

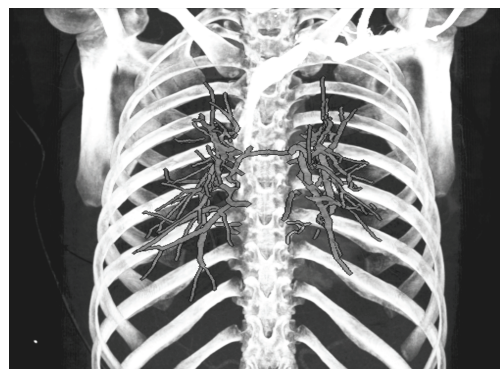|	1 - totally not helpful / 2 - not helpful / 3 - neutral / 4 - helpful / 5 - very helpful	1	2	3	4	5
24	Is it helpful to adjust the width of the halo?	☐	☐	☐	☐	☐

A.4 Context Rendering

Since the vessel lumen shows no further information concerning the spatial orientation and position of the vessels, context/surrounding information can be created around the lumen. Since rendering a context may reduce the focus and/or perception of the vessel lumen, halos can be added. The following images show two different types of surrounding parts together with the vessel lumen as overlay.

(a)

(b)

(c)

		a	b	c
25	Which image depicts the surrounding parts qualitatively best?	a☐	b☐	c☐
26	Which image depicts the vessels best?	a☐	b☐	c☐
27	Which image depicts the lumen best?	a☐	b☐	c☐
28	Which image depicts the surrounding parts qualitatively best?	b☐	x☐	c☐
29	Which image depicts the vessels best?	b☐	x☐	c☐
30	Which image depicts the depth perception best? *(Anterior vessels vs. posterior vessels)*	b☐	x☐	c☐

	1 - totally not helpful / 2 - not helpful / 3 - neutral / 4 - helpful / 5 - very helpful	1	2	3	4	5
31	Are halos helpful when investigating dense vascular structures?	☐	☐	☐	☐	☐

The following images show specific vessels of interest. In order to delineate the lumen from the context, halos in yellow are added.
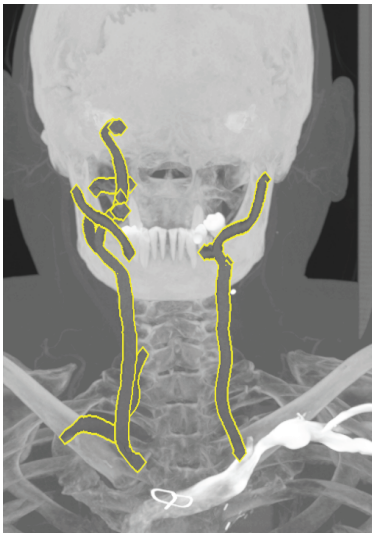
(a) Vessels of a carotis data set
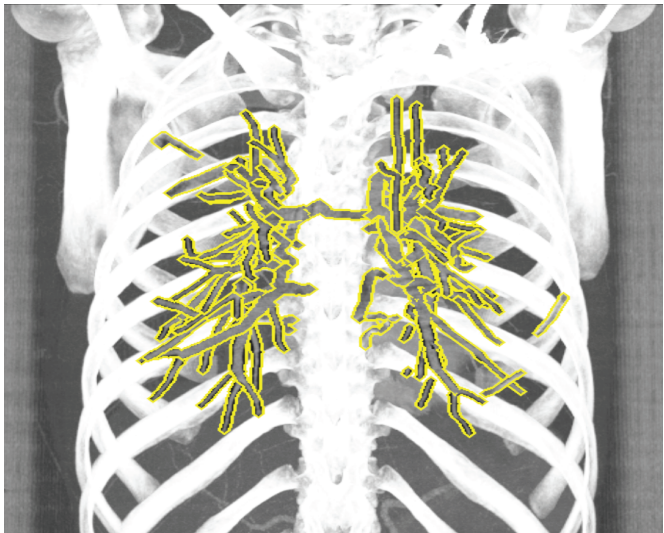
(b) Peripheral pulmonary vessels

	1 - totally not helpful / 2 - not helpful / 3 - neutral / 4 - helpful / 5 - very helpful	1	2	3	4	5
32	How clinically helpful is the visualization of specific vessels of interest?	☐	☐	☐	☐	☐
33	Is this helpful when detecting pathologies?	☐	☐	☐	☐	☐
34	Is this helpful to detect pathologies faster?	☐	☐	☐	☐	☐

APPENDIX **B**

Questionnaire of Curved Surface Reformation

I N this questionnaire several aspects of the proposed visualization technique Curved Surface Reformation (CSR) will be investigated and evaluated. The method will be compared to existing and well established visualization approaches such as Curved Planar Reformation (CPR), Multipath Curved Planar Reformation (mpCPR) and Centerline Reformation (CR). Throughout this questionnaire please give a **single** or **no** answer for each question in the ☐ field, i.e., no question allows multiple answers. If you want to correct an answer, please indicate this explicitly and tick your new answer. For several questions it would be highly beneficial for us if you could elaborate on the reasons for your answer; these questions are marked with the following text: *(please justify your decision in the comments)*. By doing so you allow us to benefit from your expert opinion, enhance this evaluation and provide us essential information for future improvements of relevant software tools. In case of any other comments, please feel free to write them into the provided comment field as well. All comments are very appreciated and will help us to strengthen this evaluation.

B.1   General Assessment

In this section, general aspects of the three methods (CPR, CR and CSR) should be anonymously evaluated. Several images are shown on the next page, without knowing which particular technique has been used.

Vessel Lumen — images (a)-(c)

---

*The **vessel lumen** is defined as the cut through the vessel along its centerline which covers the full width of the vessel. As this is the most important region to assess pathologies, e.g., calcifications, the visualization technique has to depict it as precise as possible.*

1	Which image depicts the vessels best?	a☐	b☐	c☐
2	Which image shows the flow channels qualitatively better?	a☐	b☐	c☐
				none☐

Surrounding Parts — images (a)-(c)

---

*The **surrounding parts** of a vessel are the tissues and organs around the vessel lumen. They show additional information that might be useful for spotting pathologies not necessarily related to the vessels themselves. Some CPRs show artifacts in these regions. Open questions such as if the surrounding parts are desired or if they should smoothly extend to the borders of the image are investigated here.*


|				
3	Which image shows the organs around the vessels with the lowest number of artifacts?	a☐	b☐	c☐
4	Is the visualization of the organs around the vessels desired? *(please justify your decision in the comments)*	YES☐		NO☐
5	Is the visualization of the organs around the vessels helpful? *(please justify your decision in the comments)*	YES☐		NO☐

Visibility — images (d)-(f)

---

*Finally, the correct **visibility** of the cuts through multiple vessels within one image will be assessed on the example of cervical vessels. Visibility refers to the depiction of correct obstructions of multiple vessels, i.e., which vessel is in front of another one.*

|				
6	Which image has the best visibility of all vessel lumen?	d☐	e☐	f☐
7	Which image preserves the relative location of the vessels to each other best?	d☐	e☐	f☐
8	Is the three dimensional visibility of several vessels in one image desired? *(please justify your decision in the comments)*	YES☐		NO☐
9	Which vessel is closer to the viewer in image (d)?	1☐		2☐
10	Which vessel is closer to the viewer in image (e)?	1☐		2☐
11	Which vessel is closer to the viewer in image (f)?	1☐		2☐

Comments:
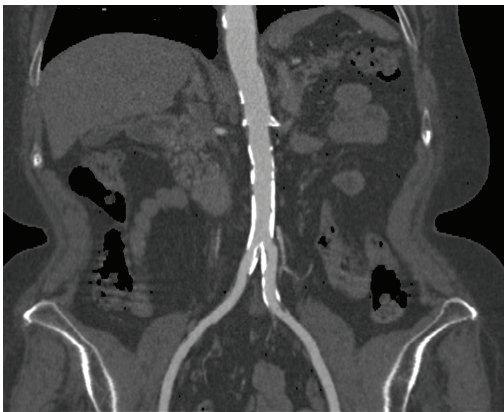
(a)
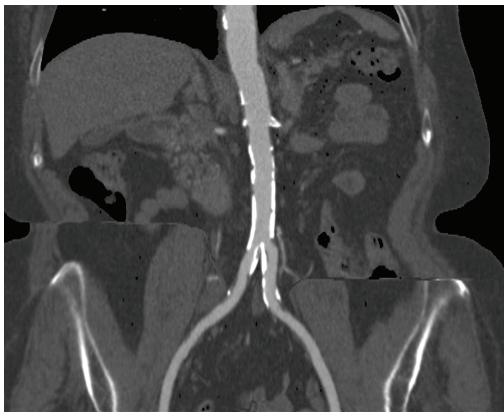
(b)
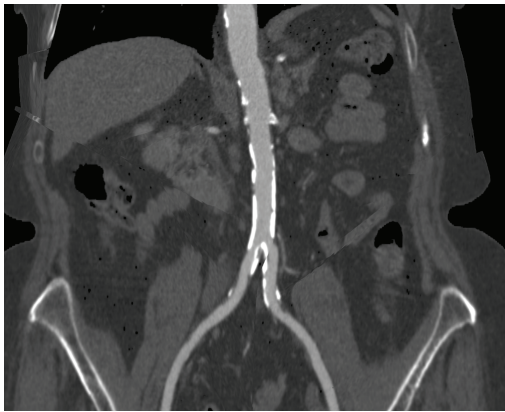
(c)
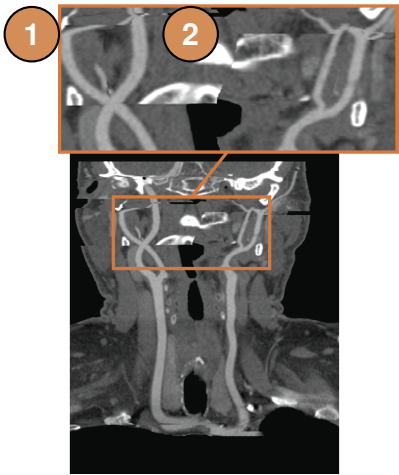
(d)
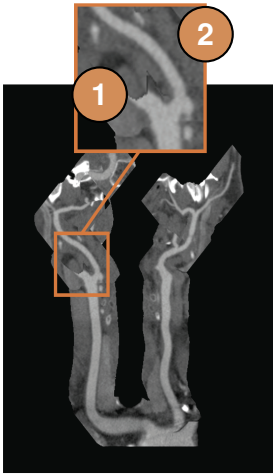
(e)
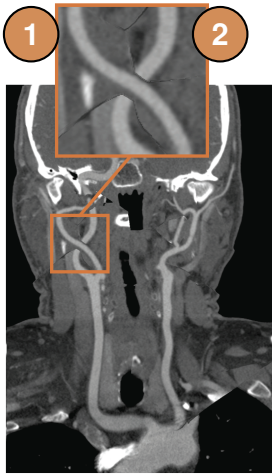
(f)

B.2 Perception

In this section we investigate perceptual issues of various vessel visualization methods. Several images on the next page show the abdominal aorta with its first branches. Your task is to decide, which vessel branch is closer to the viewer (i.e., in front of the other vessel branch).

Questions — images (a)-(f)

12	Which vessel is closer to the viewer in image (a)?	1☐	2☐
13	Which vessel is closer to the viewer in image (b)?	1☐	2☐
14	Which vessel is closer to the viewer in image (c)?	1☐	2☐
15	Which vessel is closer to the viewer in image (d)?	1☐	2☐
16	Which vessel is closer to the viewer in image (e)?	1☐	2☐
17	Which vessel is closer to the viewer in image (f)?	1☐	2☐

Silhouettes — images (g) and (h)

*The **yellow silhouettes** in the images (g) and (h) mark the boundaries between regions with different distances from the viewer.*

|			
18	Which vessel is closer to the viewer in image (g)?	1☐	2☐
19	Which vessel is closer to the viewer in image (h)?	1☐	2☐
20	Are silhouettes helpful for perceiving the vessel orientation in 3D space? *(please justify your decision in the comments)*	YES☐	NO☐
21	Are silhouettes helpful for perceiving the boundaries of regions with different distances from the viewer? *(please justify your decision in the comments)*	YES☐	NO☐

Comments:

(a)

(b)

(c)

(d)

(e)

(f)
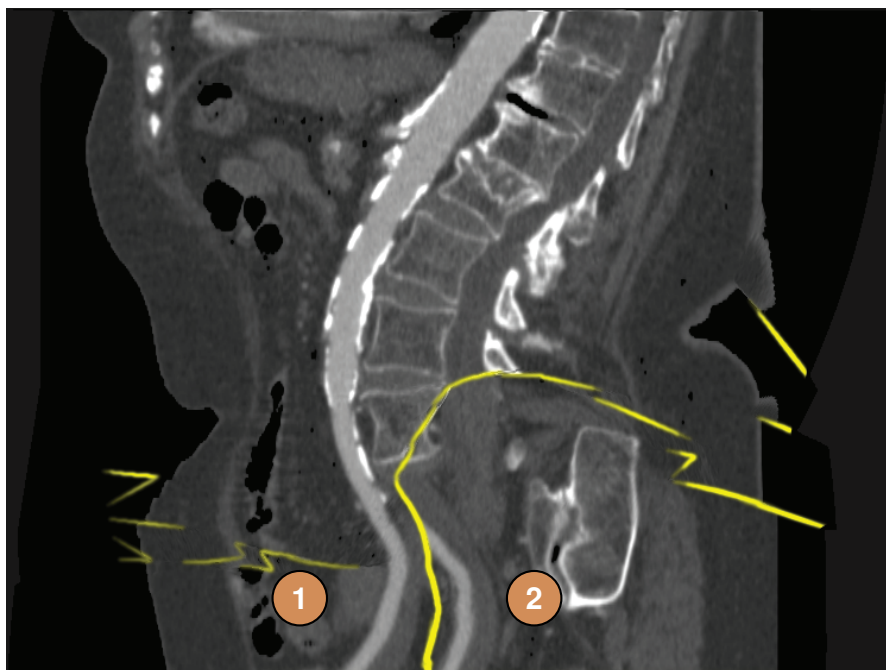
(g)

(h)

APPENDIX **C**

Fuzzy Inference System Rules of Smart Super Views

THIS chapter provides an outline of the complete rule base for the Fuzzy Inference System (FIS) that has been used to create the Smart Super Views (cf. Chapter 4). We distinguish between two different linguistic output variables, namely *Method* and *Slice*. The former encodes the result for the *vessel*, *bone* and *tissue* views, whereas the latter describes the slice views to present. The idea behind differentiating between these two categories of visualizations is that slice views should always be presented to the user to achieve a higher confidence in reporting [113]. Nevertheless, both could have been fused by adapting the subsequent rules accordingly, but one should be aware of the factors that are required to show a specific view.

The following two sections describe the rules for the *Method* and *Slice* linguistic output variables. Both are presented in the form of a table together with their linguistic input variables. The logical operation between the input variables is *and* and between output variables *or*. To convey the output more clearly, the logical operations are always stated for the output. One should keep in mind that the logical operators are *fuzzy* operators. In addition, these tables have to be transformed into *if-then* rules in order to feed them into the FIS. The order of the rules and of the input variables has no consequence and effect on the results.

C.1   Rules for Vessel, Bone, and Tissue Views

For the vessel, bone, and tissue views, the semantic layers of the vessel mask, the bone mask, and vessel tree are used. If a small or no part of the vessel tree is covered by the ROI, only bone or tissue can be suggested. If more vessel tree is successively included in the ROI, the vessel view gains importance, since the user expects to get a vessel related view, due to hovering over a vessel. The subsequent table presents all rules for the *Method* output variable that correspond to the views described. The vessel view presents a CPR of the currently selected vessel segment, the bone view shows only the bone mask using a DVR, and the tissue view displays vessel

together with bone in a DVR. The tissue view is shown if there is no clear distinction between vessel and bone, or in case no vessel tree is available for the particular ROI.

Input			Output
Vessel	Bone	Vessel Tree	*Method*
Low	Low	Low	Tissue
Low	Medium	Low	Bone
Low	High	Low	Bone
Medium	Low	Low	Tissue
Medium	Medium	Low	Tissue
Medium	High	Low	Bone
High	Low	Low	Tissue
High	Medium	Low	Tissue
High	High	Low	Tissue
Low	Low	Medium	Vessel
Low	Medium	Medium	Vessel
Low	High	Medium	Tissue
Medium	Low	Medium	Vessel
Medium	Medium	Medium	Vessel
Medium	High	Medium	Vessel
High	Low	Medium	Vessel
High	Medium	Medium	Vessel
High	High	Medium	Vessel
Low	Low	High	Vessel
Low	Medium	High	Vessel
Low	High	High	Vessel
Medium	Low	High	Vessel
Medium	Medium	High	Vessel
Medium	High	High	Vessel
High	Low	High	Vessel
High	Medium	High	Vessel
High	High	High	Vessel

C.2   Rules for Slice Views

The axis-aligned slice views depend on the slice semantic layer that encodes their importance. To model the special oblique slice, the information of the vessel tree is required, since we have to know the underlying selected vessel segment. Sometimes it would be appropriate to show more than one slice view, which can be encoded by the fuzzy logic *or* operation. The vessel tree has a high impact on the type of slice to show, since the user expects a corresponding response if hovering over a vessel. Hence, in case most of the ROI is covered by the vessel tree, the oblique slice is presented, together with the vessel view displaying a CPR. If all axis-aligned slices exhibit the same importance within the ROI, the axial slice view is preferred.

Input				Output
Vessel Tree	Axial	Sagittal	Coronal	*Slice*
Low	Low	Low	Low	Axial
Low	Low	Low	Medium	Coronal
Low	Low	Low	High	Coronal
Low	Low	Medium	Low	Sagittal
Low	Low	Medium	Medium	Sagittal or Coronal
Low	Low	Medium	High	Coronal
Low	Low	High	Low	Sagittal
Low	Low	High	Medium	Sagittal
Low	Low	High	High	Sagittal or Coronal
Low	Medium	Low	Low	Axial
Low	Medium	Low	Medium	Axial or Coronal
Low	Medium	Low	High	Coronal
Low	Medium	Medium	Low	Axial or Sagittal
Low	Medium	Medium	Medium	Axial
Low	Medium	Medium	High	Coronal
Low	Medium	High	Low	Sagittal
Low	Medium	High	Medium	Sagittal
Low	Medium	High	High	Sagittal or Coronal
Low	High	Low	Low	Axial
Low	High	Low	Medium	Axial
Low	High	Low	High	Axial or Coronal
Low	High	Medium	Low	Axial
Low	High	Medium	Medium	Axial
Low	High	Medium	High	Axial or Coronal
Low	High	High	Low	Axial or Sagittal
Low	High	High	Medium	Axial or Sagittal
Low	High	High	High	Axial
Medium	Low	Low	Low	Oblique
Medium	Low	Low	Medium	Oblique
Medium	Low	Low	High	Oblique or Coronal
Medium	Low	Medium	Low	Oblique or Sagittal
Medium	Low	Medium	Medium	Oblique
Medium	Low	Medium	High	Oblique or Coronal
Medium	Low	High	Low	Oblique or Sagittal
Medium	Low	High	Medium	Oblique or Sagittal
Medium	Low	High	High	Oblique or Sagittal or Coronal
Medium	Medium	Low	Low	Oblique or Axial
Medium	Medium	Low	Medium	Oblique or Axial
Medium	Medium	Low	High	Oblique or Coronal
Medium	Medium	Medium	Low	Oblique or Axial
Medium	Medium	Medium	Medium	Oblique or Axial
Medium	Medium	Medium	High	Oblique or Coronal

|				
Medium	Medium	High	Low	Oblique or Sagittal
Medium	Medium	High	Medium	Oblique or Sagittal
Medium	Medium	High	High	Oblique or Sagittal or Coronal
Medium	High	Low	Low	Oblique or Axial
Medium	High	Low	Medium	Oblique or Axial
Medium	High	Low	High	Oblique or Axial or Coronal
Medium	High	Medium	Low	Oblique or Axial
Medium	High	Medium	Medium	Oblique or Axial
Medium	High	Medium	High	Oblique or Axial or Coronal
Medium	High	High	Low	Oblique or Axial or Sagittal
Medium	High	High	Medium	Oblique or Axial or Sagittal
Medium	High	High	High	Oblique or Axial
High	Low	Low	Low	Oblique
High	Low	Low	Medium	Oblique
High	Low	Low	High	Oblique
High	Low	Medium	Low	Oblique
High	Low	Medium	Medium	Oblique
High	Low	Medium	High	Oblique
High	Low	High	Low	Oblique
High	Low	High	Medium	Oblique
High	Low	High	High	Oblique
High	Medium	Low	Low	Oblique
High	Medium	Low	Medium	Oblique
High	Medium	Low	High	Oblique
High	Medium	Medium	Low	Oblique
High	Medium	Medium	Medium	Oblique
High	Medium	Medium	High	Oblique
High	Medium	High	Low	Oblique
High	Medium	High	Medium	Oblique
High	Medium	High	High	Oblique
High	High	Low	Low	Oblique
High	High	Low	Medium	Oblique
High	High	Low	High	Oblique
High	High	Medium	Low	Oblique
High	High	Medium	Medium	Oblique
High	High	Medium	High	Oblique
High	High	High	Low	Oblique
High	High	High	Medium	Oblique
High	High	High	High	Oblique

138

APPENDIX **D**

Questionnaire of Curvicircular Feature Aggregation

T HE aim of this questionnaire is the evaluation of a visualization technique, called Curvicircular Feature Aggregation (CFA). This approach is an extension of the commonly used method Maximum Intensity Projection (MIP). The difference lies in the way how the data is sampled along a given centerline of a vessel. It can be seen as a MIP *around* a vessel. MIP determines the maximum of the data along a viewing ray and shows this in the final image, whereas CFA samples the data along circular rays around the centerline of a vessel, as shown in the illustration on top of the next page. Different methods can be applied to these circular rays, such as determining the maximum or the minimum data value along them. The motivation behind this approach is the aggregation of features into a single image. It can be seen as a combination of multiple Curved Planar Reformation (CPR) images of different viewing angles. This is suitable for inspecting vessels, since they have a cylindrical shape. The circular rays start at a centerline point and go around the vessel. In the following pages, we evaluate the advantages and disadvantages of this proposed technique, compared to CPR and MIP. In every subsequent question, you can only tick one answer. The following main questions will be investigated throughout this questionnaire.

Q1 Location of a pathology

Q2 Size of a pathology

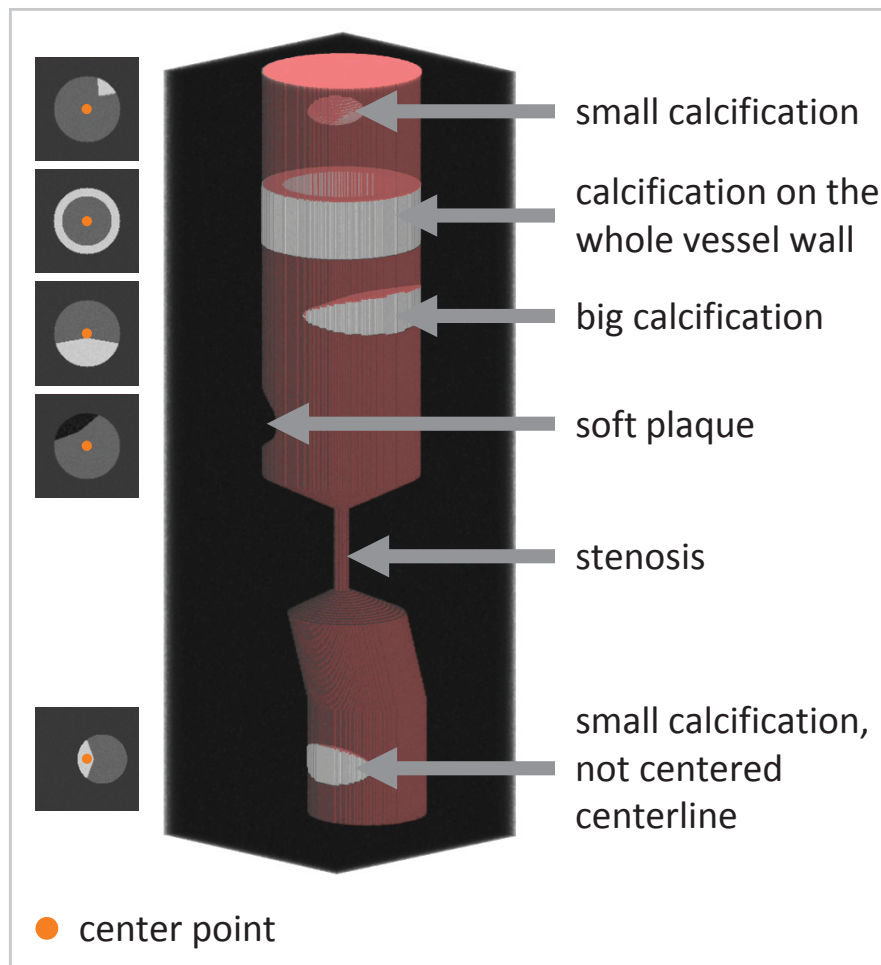Q3 Centeredness of the centerline of a vessel
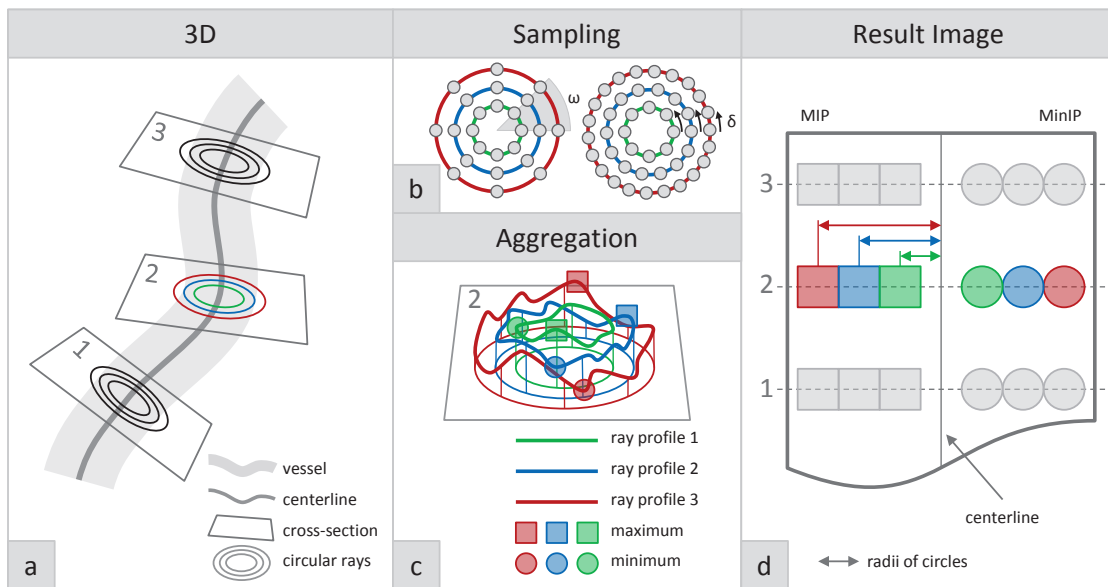
D.1 Phantom Data

A phantom data set showing a vessel with several pathologies should give an overview and a demonstration of MIP, CPR and CFA. It covers the following important cases that need to be evaluated throughout this questionnaire:

1. Small calcification

2. A ring-like calcification around the whole vessel wall

3. Big calcification

4. Soft plaque

5. Stenosis

6. Non-centered centerline with small calcification

The figure on the next page shows a 3D visualization of the phantom data set with axial slice images on the left, corresponding to the above mentioned cases, apart from the stenosis.

Three pages farther, a comparison of Maximum Intensity Projection (MIP), Curved Planar Reformation (CPR) and Curvicircular Feature Aggregation (CFA) will be presented based on the phantom data set. On the top-left, the MIP image is shown, where the centerline is highlighted in green. The top-right images show the axial slices of the important cases given above (except the stenosis). Several CPR images are presented in the middle, from $-90°$ to $90°$ with a step of $9°$ and 20 images in total. The bottom image demonstrates the CFA with showing the maximum data values (Maximum Intensity Projection (MIP)) on its left side and the minimum data values (MinIP) on its right side. These two sides are delineated by a thin black line. Please answer the following questions according to these images. If you have any comments or remarks, please fill them in below the questions.

small calcification

calcification on the
whole vessel wall

big calcification

soft plaque

stenosis

small calcification,
not centered
centerline

● center point

General

		MIP	CPR	CFA
1	Which method depicts the *small calcification* (1) best?	☐	☐	☐
2	Which method depicts the *ring-like calcification* (2) best?	☐	☐	☐
3	Which method depicts the *big calcification* (3) best?	☐	☐	☐
4	Which method depicts the *soft plaque* (4) best?	☐	☐	☐
5	Which method depicts the *stenosis* (5) best?	☐	☐	☐
6	Which method depicts the *non-centered small calcification* (6) best?	☐	☐	☐
7	Which method do you prefer solely for investigating pathologies?	☐	☐	☐
8	Which method do you prefer together with axial images for investigating pathologies?	☐	☐	☐
9	Which method is the least intuitive one?	☐	☐	☐
10	Which method is the most intuitive one?	☐	☐	☐

Size of Pathology

		Yes		No
11	Is it helpful to know the size of a pathology?	☐		☐
12	Is it required to know the size of a pathology?	☐		☐

		MIP	CPR	CFA
13	Which method depicts the size of a pathology best?	☐	☐	☐
14	Which method do you prefer together with axial images to determine the size?	☐	☐	☐

Location of Pathology

		Yes		No
15	Is it helpful to know the location of a pathology regarding the vessel diameter?	☐		☐
16	Is it required to know the location of a pathology regarding the vessel diameter?	☐		☐

		MIP	CPR	CFA
17	Which method depicts the location of a pathology best?	☐	☐	☐
18	Which method do you prefer together with axial images to determine the location?	☐	☐	☐

Centeredness of Centerline

		Yes		No
19	Is it helpful to visually perceive if a centerline is not centered properly?	☐		☐
20	Is it required to visually perceive if a centerline is not centered properly?	☐		☐

		MIP	CPR	CFA
21	Which method depicts the non-centeredness of the centerline best?	☐	☐	☐
22	Which method do you prefer together with axial images to verify and correct this?	☐	☐	☐

Remarks:

MIP

Slices

(1) (2) (3) (4) (6)

CPR

CFA

left: MIP **right:** MinIP
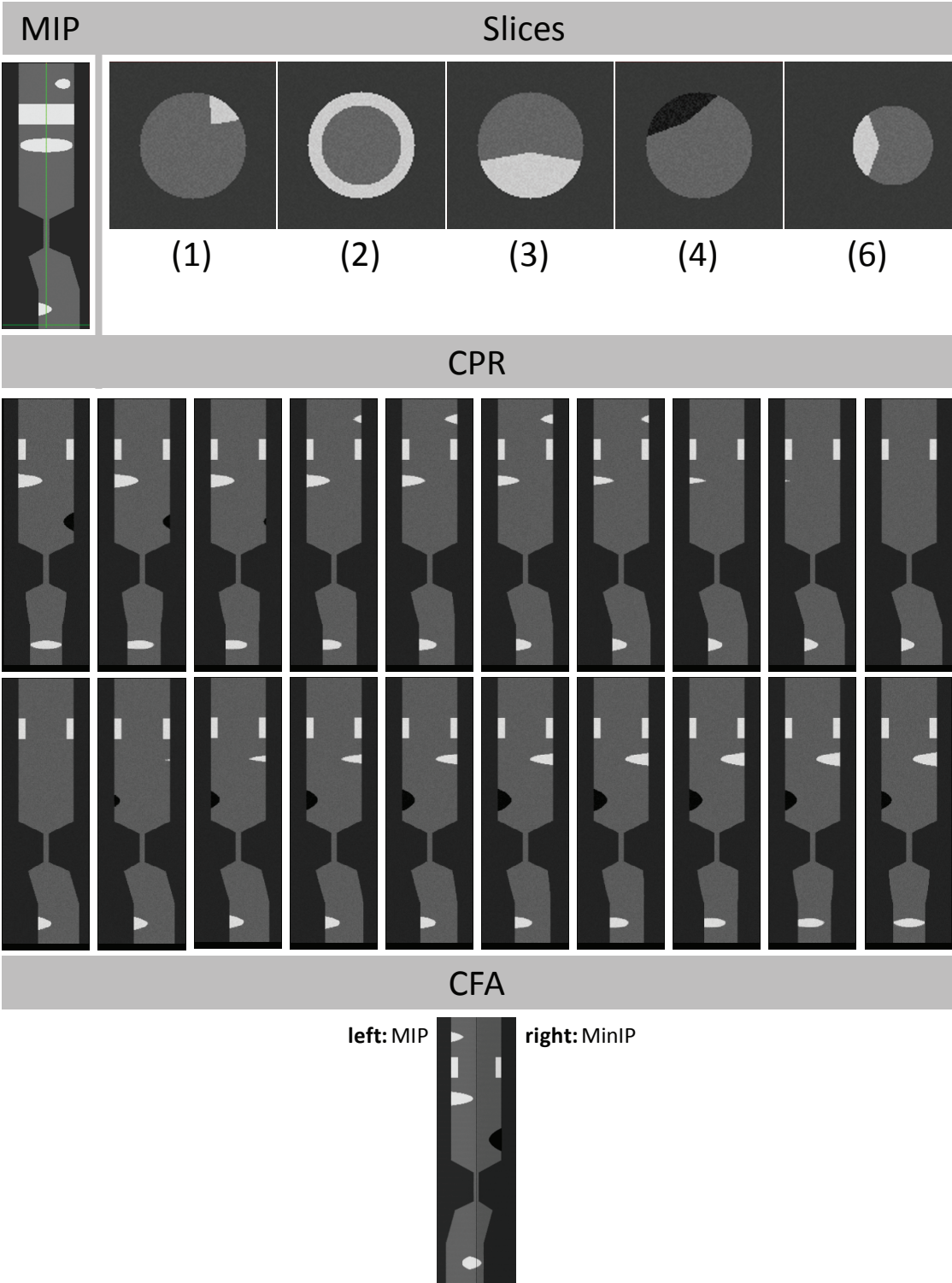
D.2 Vessel Stenosis

The following images show a stenosis pointed out by white arrows. CPR images (from $-90°$ to $90°$, 10 images) are shown on the left side, top-right a MIP and bottom-right a CFA. The CFA shows the maximum (MIP) on its left side and the minimum (MinIP) on the right side. The axial slice images show at the top the start of the stenosis, in the middle the center of the stenosis and at the bottom the end of the stenosis. The vessel of interest is pointed out by arrows. Please answer the questions below according to the images on the next page. If you have any comments or remarks, please fill them in below the questions.

General

		MIP	CPR	CFA
23	Which method depicts the stenosis best?	☐	☐	☐
24	Which method do you prefer solely for investigating the stenosis?	☐	☐	☐
25	Which method do you prefer together with axial images for investigating the stenosis?	☐	☐	☐
26	Which method is the least intuitive one?	☐	☐	☐
27	Which method is the most intuitive one?	☐	☐	☐

Size of the Stenosis

		Yes		No
28	Is it helpful to know the size of the stenosis?	☐		☐
29	Is it required to know the size of the stenosis?	☐		☐

		MIP	CPR	CFA
30	Which method depicts the size of the stenosis best?	☐	☐	☐
31	Which method do you prefer together with axial images to determine the size?	☐	☐	☐

Location of the Stenosis

		Yes		No
32	Is it helpful to know the location of the stenosis regarding the vessel diameter?	☐		☐
33	Is it required to know the location of the stenosis regarding the vessel diameter?	☐		☐

		MIP	CPR	CFA
34	Which method depicts the location of the stenosis best?	☐	☐	☐
35	Which method do you prefer together with axial images to determine the location?	☐	☐	☐

Remarks:
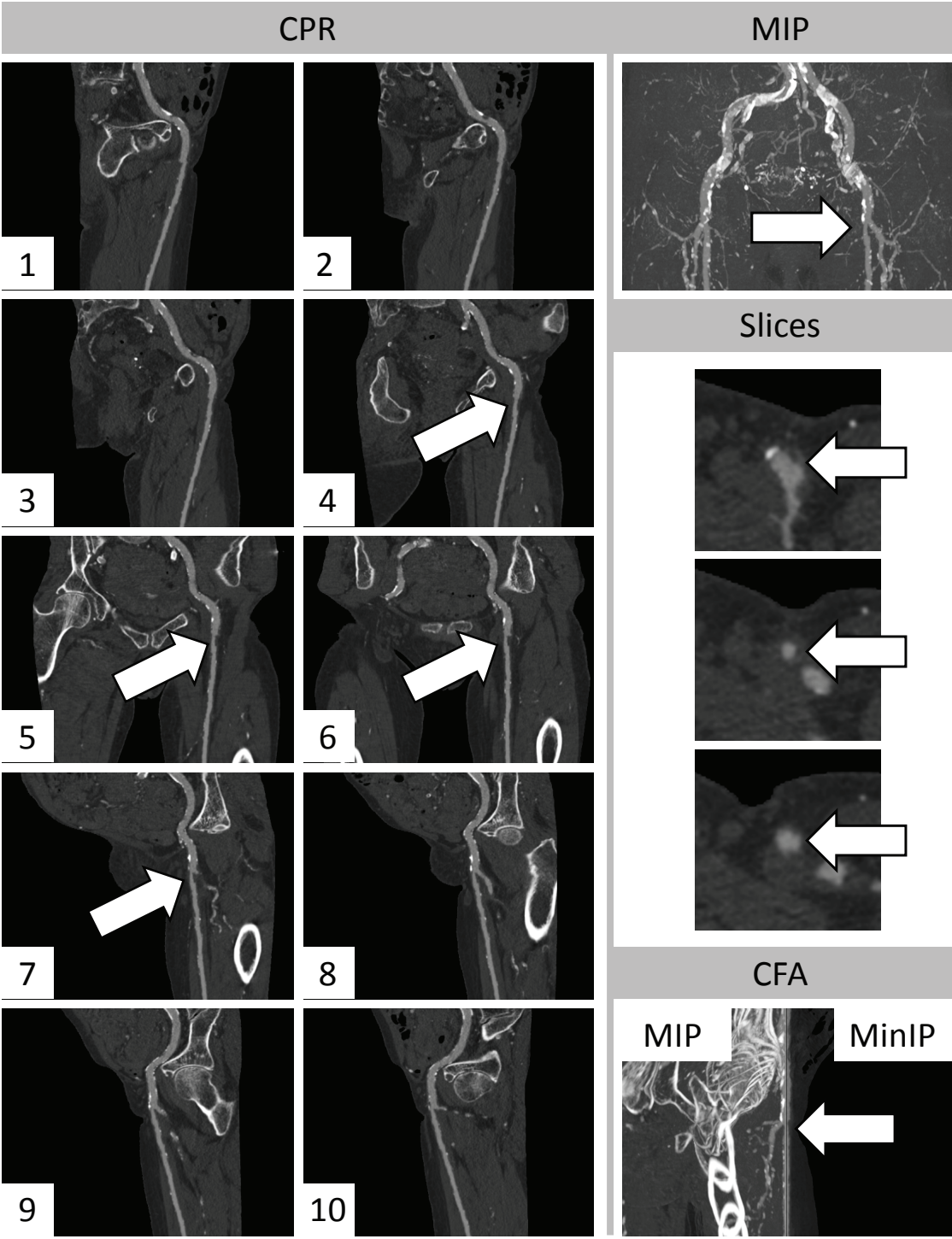
D.3 Vessel Occlusion

The following images show an occlusion pointed out by an arrow and a bracket. CPR images (from $-90°$ to $90°$, 10 images) are shown on the left side, top-right a MIP and bottom-right a CFA. The CFA shows the maximum (MIP) on its left side and the minimum (MinIP) on the right. The occlusion starts immediately after the aorta branch. Please answer the subsequent questions to the images on the next page. If you have any comments or remarks, please fill them in below the questions.

General

		MIP	CPR	CFA
36	Which method depicts the occlusion best?	☐	☐	☐
37	Which method do you prefer solely for investigating the occlusion?	☐	☐	☐
38	Which method do you prefer together with axial images for investigating the occlusion?	☐	☐	☐
39	Which method is the least intuitive one?	☐	☐	☐
40	Which method is the most intuitive one?	☐	☐	☐

Length of the Occlusion

		Yes		No
41	Is it helpful to know the length of the occlusion?	☐		☐
42	Is it required to know the length of the occlusion?	☐		☐

		MIP	CPR	CFA
43	Which method depicts the length of the occlusion best?	☐	☐	☐
44	Which method do you prefer together with axial images to determine the length?	☐	☐	☐

Location of the Occlusion

		Yes		No
45	Is it helpful to know the location of the occlusion regarding the vessel diameter?	☐		☐
46	Is it required to know the location of the occlusion regarding the vessel diameter?	☐		☐

		MIP	CPR	CFA
47	Which method depicts the location of the occlusion best?	☐	☐	☐
48	Which method do you prefer together with axial images to determine the location?	☐	☐	☐

Remarks:

CPR		MIP
1	2	
3	4	
5	6	**CFA**
7	8	MIP MinIP
9	10	
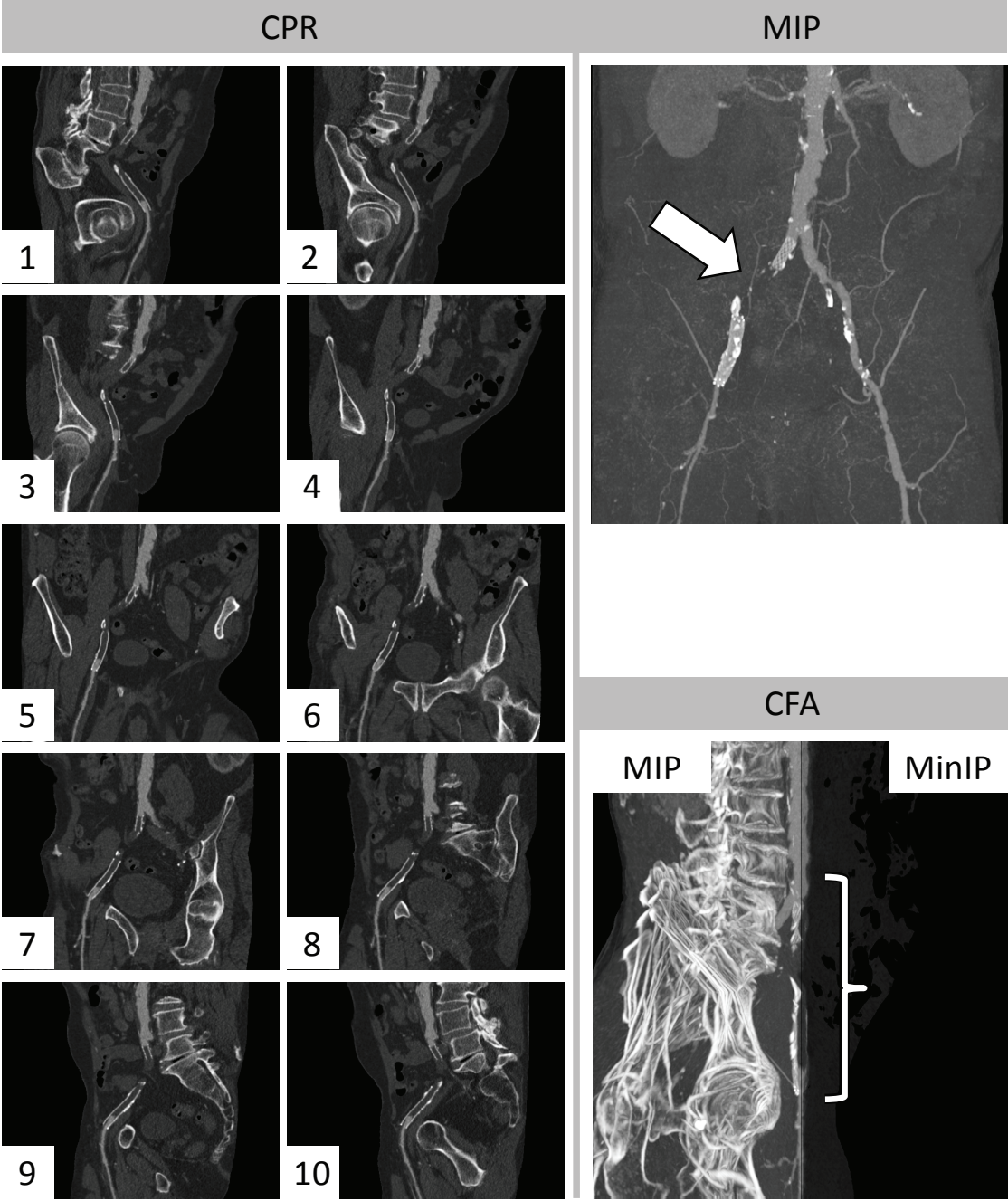
Bibliography

[1]   K. Andrews and H. Heidegger. Information slices: Visualising and exploring large hierarchies using cascading, semi-circular discs. In *Proceedings of IEEE Symposium on Information Visualization 1998*, pages 9–12, 1998.

[2]   AngioVis. www.angiovis.org, 2013.

[3]   S. R. Aylward and E. Bullitt. Initialization, noise, singularities and scale in height ridge traversal for tubular object centerline extraction. *IEEE Transactions on Medical Imaging*, 21(2):61–75, 2002.

[4]   K. T. Bae, H. Q. Tran, and J. P. Heiken. Multiphasic injection method for uniform prolonged vascular enhancement at CT angiography: pharmacokinetic analysis and experimental porcine model. *Radiology*, 216(3):872–880, 2000.

[5]   J.-P. Balabanian, I. Viola, and M. E. Gröller. Interactive illustrative visualization of hierarchical volume data. In *Proceedings of Graphics Interface 2010*, pages 137–144, 2010.

[6]   A. V. Bartrolí, R. Wegenkittl, A. König, and M. E. Gröller. Nonlinear virtual colon unfolding. In *Proceedings of IEEE Visualization 2001*, pages 411–420, 2001.

[7]   J. Berberich and S. Hirsch. Die Röntgenographische Darstellung der Arterien und Venen am Lebenden Menschen. *Klinische Wochenschrift*, 2(49):2226–2228, 1923.

[8]   E. A. Bier, M. C. Stone, K. Pier, W. Buxton, and T. D. DeRose. Toolglass and magic lenses: the see-through interface. In *Proceedings of ACM SIGGRAPH 1993*, pages 73–80, 1993.

[9]   Å. Birkeland, S. Bruckner, A. Brambilla, and I. Viola. Illustrative membrane clipping. *Computer Graphics Forum*, 31(3):905–914, 2012.

[10]   R. Blanch and E. Lecolinet. Browsing zoomable treemaps: Structure-aware multi-scale navigation techniques. *IEEE Transactions on Visualization and Computer Graphics*, 13(6):1248–1253, 2007.

[11]   J. Bloomenthal and K. Shoemake. Convolution surfaces. *SIGGRAPH Computer Graphics*, 25(4):251–256, 1991.

[12] M. A. Borkin, K. Z. Gajos, A. Peters, D. Mitsouras, S. Melchionna, F. J. Rybicki, C. L. Feldman, and H. Pfister. Evaluation of artery visualizations for heart disease diagnosis. *IEEE Transactions on Visualization and Computer Graphics*, 17(12):2479–2488, 2011.

[13] B. Brooks. Intra-arterial injection of sodium iodid: Preliminary report. *Journal of the American Medical Association*, 82(13):1016–1019, 1924.

[14] S. Bruckner. *Interactive Illustrative Volume Visualization*. PhD thesis, Vienna University of Technology, Austria, 2008.

[15] S. Bruckner and M. E. Gröller. VolumeShop: an interactive system for direct volume illustration. In *Proceedings of IEEE Visualization 2005*, pages 671–678, 2005.

[16] S. Bruckner and M. E. Gröller. Enhancing depth-perception with flexible volumetric halos. *IEEE Transactions on Visualization and Computer Graphics*, 13(6):1344–1351, 2007.

[17] S. Bruckner and M. E. Gröller. Style transfer functions for illustrative volume rendering. *Computer Graphics Forum*, 26(3):715–724, 2007.

[18] S. Bruckner and M. E. Gröller. Instant volume visualization using maximum intensity difference accumulation. *Computer Graphics Forum*, 28(3):775–782, 2009.

[19] K. Bühler, P. Felkel, and A. La Cruz. Geometric methods for vessel visualization and quantification - a survey. In G. Brunnett, B. Hamann, H. Müller, and L. Linsen, editors, *Geometric Modeling for Scientific Visualization*, Mathematics and Visualization, pages 399–419. Springer Berlin Heidelberg, 2004.

[20] M. Burns and A. Finkelstein. Adaptive cutaways for comprehensible rendering of polygonal scenes. *ACM Transactions on Graphics*, 27(5):154:1–154:7, 2008.

[21] M. Burns, M. Haidacher, W. Wein, I. Viola, and M. E. Gröller. Feature emphasis and contextual cutaways for multimodal medical visualization. In *Proceedings of the Eurographics / IEEE VGTC Symposium on Visualization 2007*, pages 275–282, 2007.

[22] J. Canny. A computational approach to edge detection. *IEEE Transactions on Pattern Analysis and Machine Intelligence*, 8(6):679–698, 1986.

[23] J. Cebral and R. Lohner. From medical images to CFD meshes. In *Proceedings 8th International Meshing Roundtable 1999*, pages 321–331, 1999.

[24] M. Chen, D. Ebert, H. Hagen, R. Laramee, R. van Liere, K.-L. Ma, W. Ribarsky, G. Scheuermann, and D. Silver. Data, information, and knowledge in visualization. *IEEE Computer Graphics and Applications*, 29(1):12–19, 2009.

[25] C. Chuon, S. Guha, P. Janecek, and N. D. C. Song. Simplipoly: Curvature-based polygonal curve simplification. *International Journal of Computational Geometry & Applications*, 21(4):417–429, 2011.

[26] N. D. Cornea, D. Silver, and P. Min. Curve-skeleton applications. In *Proceedings of IEEE Visualization 2005*, pages 95–102, 2005.

[27] N. D. Cornea, D. Silver, and P. Min. Curve-skeleton properties, applications and algorithms. *IEEE Transactions on Visualization and Computer Graphics*, 13(3):530–548, 2007.

[28] C. Correa and K.-L. Ma. Size-based transfer functions: A new volume exploration technique. *IEEE Transactions on Visualization and Computer Graphics*, 14(6):1380–1387, 2008.

[29] C. Correa, P. Lindstrom, and P.-T. Bremer. Topological spines: A structure-preserving visual representation of scalar fields. *IEEE Transactions on Visualization and Computer Graphics*, 17(12):1842–1851, 2011.

[30] J. Cui, P. Rosen, V. Popescu, and C. Hoffmann. A curved ray camera for handling occlusions through continuous multiperspective visualization. *IEEE Transactions on Visualization and Computer Graphics*, 16(6):1235–1242, Nov. 2010.

[31] D. DeCarlo, A. Finkelstein, S. Rusinkiewicz, and A. Santella. Suggestive contours for conveying shape. *ACM Transactions on Graphics*, 22(3):848–855, 2003.

[32] T. DeRose, M. Kass, and T. Truong. Subdivision surfaces in character animation. In *Proceedings of ACM SIGGRAPH 1998*, pages 85–94, 1998.

[33] C. Diehm, A. Schuster, J. R. Allenberg, H. Darius, R. Haberl, S. Lange, D. Pittrow, B. von Stritzky, G. Tepohl, and H.-J. Trampisch. High prevalence of peripheral arterial disease and co-morbidity in 6880 primary care patients: cross-sectional study. *Atherosclerosis*, 172(1):95–105, 2004.

[34] S. Diepenbrock, T. Ropinski, and K. Hinrichs. Context-aware volume navigation. In *Proceedings of IEEE Pacific Visualization Symposium 2011*, pages 11–18, 2011.

[35] S. Diepenbrock, S. Hermann, M. Schäfers, M. Kuhlmann, and K. H. Hinrichs. Comparative visualization of tracer uptake in In Vivo small animal PET/CT imaging of the carotid arteries. *Computer Graphics Forum*, 32(3):241–250, 2013.

[36] J. Diepstraten, D. Weiskopf, and T. Ertl. Interactive cutaway illustrations. *Computer Graphics Forum*, 22(3):523–532, 2003.

[37] D. H. Douglas and T. K. Peucker. Algorithms for the reduction of the number of points required to represent a digitized line or its caricature. *Cartographica*, 10(2):112–122, 1973.

[38] M. H. Everts, H. Bekker, J. B. Roerdink, and T. Isenberg. Depth-dependent halos: Illustrative rendering of dense line data. *IEEE Transactions on Visualization and Computer Graphics*, 15(6):1299–1306, 2009.

[39] P. Felkel, R. Wegenkittl, and K. Bühler. Surface models of tube trees. In *Proceedings of Computer Graphics International 2004*, pages 70–77, 2004.

[40] D. Fleischmann. Use of high concentration contrast media: principles and rationale—vascular district. *European Radiology*, 45(1):88–93, 2003.

[41] D. Fleischmann. Contrast medium delivery for vascular MDCT: Principles and rationale. In *Multislice CT*, Diagnostic Imaging, pages 27–33. Springer Berlin Heidelberg, 2004.

[42] D. Fleischmann and K. Hittmair. Mathematical analysis of arterial enhancement and optimization of bolus geometry for CT angiography using the discrete fourier transform. *Computer Assisted Tomography*, 23(3):474–484, 1999.

[43] D. Fleischmann and G. D. Rubin. Quantification of intravenously administered contrast medium transit through the peripheral arteries: implications for ct angiography. *Radiology*, 236(3):1076–1082, 2005.

[44] D. Fleischmann, G. D. Rubin, A. A. Bankier, and K. Hittmair. Improved uniformity of aortic enhancement with customized contrast medium injection protocols at CT angiography. *Radiology*, 214(2):363–371, 2000.

[45] A. F. Frangi, W. J. Niessen, K. L. Vincken, and M. A. Viergever. Multiscale vessel enhancement filtering. *Lecture Notes in Computer Science*, 1496:130–137, 1998.

[46] S. Z. Goldhaber. Pulmonary embolism. *The Lancet*, 363(9417):1295–1305, 2004.

[47] S. Z. Goldhaber and H. Bounameaux. Pulmonary embolism and deep vein thrombosis. *The Lancet*, 379(9828):1835–1846, 2012.

[48] M. E. Gröller. Nonlinear raytracing - visualizing strange worlds. *Visual Computer*, 11(5): 263–274, 1995.

[49] J. Gudmundsson, G. Narasimhan, and M. Smid. Distance-preserving approximations of polygonal paths. *Computational Geometry*, 36(3):183–196, 2007.

[50] H. K. Hahn, B. Preim, D. Selle, and H.-O. Peitgen. Visualization and interaction techniques for the exploration of vascular structures. In *Proceedings of IEEE Visualization 2001*, pages 395–402, 2001.

[51] E. Haschek and O. Lindenthal. Ein Beitrag zur praktischen Verwerthung der Photographie nach Röntgen. *Wiener Klinische Wochenschrift*, 9(4):63–64, 1896.

[52] M. Hochbruck and J.-M. Sautter. Mathematik fürs Leben am Beispiel der Computertomographie. *Mathematische Semesterberichte*, 49(1):95–113, 2002.

[53] K. E. Hoff, III, J. Keyser, M. Lin, D. Manocha, and T. Culver. Fast computation of generalized Voronoi diagrams using graphics hardware. In *Proceedings of ACM SIGGRAPH 1999*, pages 277–286, 1999.

[54] W. Hong, X. Gu, F. Qiu, M. Jin, and A. Kaufman. Conformal virtual colon flattening. In *Proceedings of the ACM Symposium on Solid and Physical Modeling 2006*, pages 85–93. ACM, 2006.

[55] W.-H. Hsu, K.-L. Ma, and C. Correa. A rendering framework for multiscale views of 3d models. *ACM Transactions on Graphics*, 30(6):131:1–131:10, 2011.

[56] H. Imai and M. Iri. Computational-geometric methods for polygonal approximations of a curve. *Computer Vision, Graphics, and Image Processing*, 36(1):31–41, 1986.

[57] H. Imai and M. Iri. *Computational Morphology*, chapter Polygonal approximations of a curve – formulations and algorithms, pages 87–95. North-Holland, 1988.

[58] V. Interrante and C. Grosch. Strategies for effectively visualizing 3D flow with volume LIC. In *Proceedings of Visualization 1997*, pages 421–424, 1997.

[59] M. Jankun-Kelly, M. Jiang, D. Thompson, and R. Machiraju. Vortex visualization for practical engineering applications. *IEEE Transactions on Visualization and Computer Graphics*, 12(5):957–964, 2006.

[60] R. Jianu, C. Demiralp, and D. H. Laidlaw. Exploring brain connectivity with two-dimensional neural maps. *IEEE Transactions on Visualization and Computer Graphics*, 18(6):978–987, 2012.

[61] B. Johnson and B. Shneiderman. Tree-maps: A space-filling approach to the visualization of hierarchical information structures. In *Proceedings of Visualization 1991*, pages 284–291, 1991.

[62] M. W. Jones, J. A. Bærentzen, and M. Šrámek. 3D distance fields: A survey of techniques and applications. *IEEE Transactions on Visualization and Computer Graphics*, 12(4):581–599, 2006.

[63] A. Joshi, X. Qian, D. Dione, K. Bulsara, C. Breuer, A. Sinusas, and X. Papademetris. Effective visualization of complex vascular structures using a non-parametric vessel detection method. *IEEE Transactions on Visualization and Computer Graphics*, 14(6):1603–1610, 2008.

[64] B. Kadlec, H. Tufo, and G. Dorn. Knowledge-assisted visualization and segmentation of geologic features. *IEEE Computer Graphics and Applications*, 30(1):30–90, 2010.

[65] W. A. Kalender. *Computed Tomography*. Publicis MCD Verlag, 2000.

[66] A. Kanitsar. *Curved Planar Reformation for Vessel Visualization*. PhD thesis, Vienna University of Technology, Austria, 2004.

[67] A. Kanitsar, D. Fleischmann, R. Wegenkittl, D. Sandner, P. Felkel, and E. Gröller. Computed tomography angiography: a case study of peripheral vessel investigation. In *Proceedings of IEEE Visualization 2001*, pages 477–593, 2001.

[68] A. Kanitsar, D. Fleischmann, R. Wegenkittl, P. Felkel, and M. E. Gröller. CPR - curved planar reformation. In *Proceedings of IEEE Visualization 2002*, pages 37–44, 2002.

[69] A. Kanitsar, R. Wegenkittl, D. Fleischmann, and E. Gröller. Advanced curved planar reformation: Flattening of vascular structures. In *Proceedings of IEEE Visualization 2003*, pages 43–50, 2003.

[70] A. Kanitsar, D. Fleischmann, R. Wegenkittl, and M. E. Gröller. Diagnostic relevant visualization of vascular structures. In G.-P. Bonneau, T. Ertl, and G. Nielson, editors, *Scientific Visualization: The Visual Extraction of Knowledge from Data 2006*, Mathematics and Visualization, pages 207–228. Springer Berlin Heidelberg, 2006. ISBN 978-3-540-30790-7.

[71] H. Katayama, K. Yamaguchi, T. Kozuka, T. Takashima, P. Seez, and K. Matsuura. Adverse reactions to ionic and nonionic contrast media. A report from the Japanese Committee on the Safety of Contrast Media. *Radiology*, 175(3):621–628, 1990.

[72] D. N. Kenwright and R. Haimes. Automatic vortex core detection. *IEEE Computer Graphics and Applications*, 18(4):70–74, 1998.

[73] M.-S. Kim, E.-J. Park, and H.-Y. Lee. Modeling and animation of generalized cylinders with variable radius offset space curves. *Journal of Visualization and Computer Animation*, 5(4):189–207, 1994.

[74] G. Kindlmann. Superquadric tensor glyphs. In *Proceedings of the Eurographics / IEEE TCVG Symposium on Visualization 2004*, pages 147–154, 2004.

[75] J. Klein, D. Bartz, O. Friman, M. Hadwiger, B. Preim, F. Ritter, A. Vilanova, and G. Zachmann. Advanced algorithms in medical computer graphics. In *Proceedings of Eurographics 2008*, pages 25–44, 2008.

[76] P. Kohlmann, S. Bruckner, A. Kanitsar, and M. E. Gröller. LiveSync: deformed viewing spheres for knowledge-based navigation. *IEEE Transactions on Visualization and Computer Graphics*, 13(6):1544–1551, Oct. 2007.

[77] P. Kohlmann, S. Bruckner, A. Kanitsar, and M. E. Gröller. LiveSync++: enhancements of an interaction metaphor. In *Proceedings of Graphics Interface 2008*, pages 81–88, 2008.

[78] P. Kohlmann, S. Bruckner, A. Kanitsar, and M. E. Gröller. Contextual picking of volumetric structures. In *Proceedings of IEEE Pacific Visualization Symposium 2009*, pages 185–192, 2009.

[79] O. Konrad-Verse, B. Preim, and A. Littmann. Virtual resection with a deformable cutting plane. In *Proceedings of SimVis 2004*, pages 203–214, 2004.

[80] K. Krissian, G. Malandain, N. Ayache, R. Vaillant, and Y. Trousset. Model-based detection of tubular structures in 3D images. *Comput. Vis. Image Underst.*, 80(2):130–171, 2000.

[81] R. A. Kruger, C. A. Mistretta, J. Lancaster, T. L. Houk, M. Goodsitt, C. G. Shaw, S. J. Riederer, J. Hicks, J. Sackett, A. B. Crummy, and D. Fleming. A digital video image processor for real-time x-ray subtraction imaging. *Optical Engineering*, 17(6):652–657, 1978.

[82] Y. Kurzion and R. Yagel. Space deformation using ray deflectors. In *Proceedings of the 6th Eurographics Workshop on Rendering 1995*, pages 21–32. Springer, 1995.

[83] E. LaMar, B. Hamann, and K. I. Joy. A magnification lens for interactive volume visualization. In *Proceedings of the Pacific Conference on Computer Graphics and Applications 2001*, pages 223–232, 2001.

[84] O. D. Lampe, C. Correa, K.-L. Ma, and H. Hauser. Curve-centric volume reformation for comparative visualization. *IEEE Transactions on Visualization and Computer Graphics*, 15(6):1235–1242, 2009.

[85] G. Läthén, S. Lindholm, R. Lenz, and M. Borga. Automatic tuning of spatially varying transfer functions for blood vessel visualization. *IEEE Transactions on Visualization and Computer Graphics*, 18(12):2345–2354, 2012.

[86] C. C. Law, W. J. Schroeder, K. M. Martin, and J. Temkin. A multi-threaded streaming pipeline architecture for large structured data sets. In *Proceedings of Visualization 1999*, pages 225–232, 1999.

[87] N. Lee and M. Rasch. Tangential curved planar reformation for topological and orientation invariant visualization of vascular trees. In *Engineering in Medicine and Biology Society, 2006. EMBS '06. 28th Annual International Conference of the IEEE*, pages 1073–1076, 2006.

[88] T.-C. Lee, R. L. Kashyap, and C.-N. Chu. Building skeleton models via 3-D medial surface/axis thinning algorithms. *Graphical Models and Image Processing*, 56(6):462–478, 1994.

[89] D. Lesage, E. D. Angelini, I. Bloch, and G. Funka-Lea. A review of 3D vessel lumen segmentation techniques: Models, features and extraction schemes. *Medical Image Analysis*, 13(6):819–845, 2009.

[90] W. Li, L. Ritter, M. Agrawala, B. Curless, and D. Salesin. Interactive cutaway illustrations of complex 3D models. *ACM Transactions on Graphics*, 26(3):31:1–31:11, 2007.

[91] E. M. Lidal, H. Hauser, and I. Viola. Design principles for cutaway visualization of geological models. In *Proceedings of the Spring Conference on Computer Graphics 2012*, pages 47–54. ACM, 2012.

[92] T. Lindeberg. *Scale-Space Theory in Computer Vision*. Kluwer Academic Publishers, Norwell, MA, USA, 1993. ISBN 0792326369.

[93] H. Löffelmann and E. Gröller. Ray tracing with extended cameras. *The Journal of Visualization and Computer Animation*, 7(4):211–227, 1996.

[94] W. E. Lorensen and H. E. Cline. Marching cubes: A high resolution 3d surface construction algorithm. *SIGGRAPH Computer Graphics*, 21(4):163–169, 1987.

[95] X. Lou, S. Liu, and T. Wang. Fanlens: A visual toolkit for dynamically exploring the distribution of hierarchical attributes. In *Proceedings of IEEE Pacific Visualization Symposium 2008*, pages 151–158, 2008.

[96] E. Mahmud, J. J. Cavendish, and A. Salami. Current treatment of peripheral arterial disease. *Journal of the American College of Cardiology*, 50(6):473–490, 2007.

[97] E. Mamdani. Application of fuzzy logic to approximate reasoning using linguistic synthesis. *IEEE Transactions on Computers*, C-26(12):1182–1191, dec. 1977.

[98] M. J. McGuffin, L. Tancau, and R. Balakrishnan. Using deformations for browsing volumetric data. In *Proceedings of IEEE Visualization 2003*, pages 401–408, 2003.

[99] T. McInerney and P. Crawford. Ribbonview: interactive context-preserving cutaways of anatomical surface meshes. In *Proceedings of the International Conference on Advances in visual computing 2010 - Volume Part II*, ISVC'10, pages 533–544, 2010.

[100] E. Meijering. *Image Enhancement in Digital X-Ray Angiography*. PhD thesis, University Medical Center Utrecht, The Netherlands, 2000.

[101] G. Mistelbauer. Automated processing and visualization of vessel trees. Master's thesis, Vienna University of Technology, Austria, 2010.

[102] A. Motro. Superviews: Virtual integration of multiple databases. *IEEE Transactions on Software Engineering*, SE-13(7):785–798, july 1987.

[103] J. Nam, M. Maurer, and K. Mueller. A high-dimensional feature clustering approach to support knowledge-assisted visualization. *Computers & Graphics*, 33(5):607–615, Oct. 2009.

[104] F. Natterer. *The Mathematics of Computerized Tomography*. John Wiley & Sons Ltd, 1986.

[105] A. Nealen, M. Müller, R. Keiser, E. Boxerman, and M. Carlson. Physically based deformable models in computer graphics. *Computer Graphics Forum*, 25(4):809–836, 2006.

[106] R. Netzer. http://www.herz-praxis.ch/, 2013. Accessed: 2013-09-02.

[107] L. Norgren, W. Hiatt, J. Dormandy, M. Nehler, K. Harris, and F. Fowkes. Inter-society consensus for the management of peripheral arterial disease (TASC II). *Journal of Vascular Surgery*, 45(1):5–67, 2007.

[108] M. Northam, J. Koonce, and J. G. Ravenel. Pulmonary nodules detected at cardiac CT: comparison of images in limited and full fields of view. *American Journal of Roentgenology*, 191(3):878–881, Sep 2008.

[109] Y. Ohtake, A. Belyaev, M. Alexa, G. Turk, and H.-P. Seidel. Multi-level partition of unity implicits. *ACM Transactions on Graphics*, 22(3):463–470, 2003.

[110] H. Ota, K. Takase, K. Igarashi, Y. Chiba, K. Haga, H. Saito, and S. Takahashi. MDCT compared with digital subtraction angiography for assessment of lower extremity arterial occlusive disease: Importance of reviewing cross-sectional images. *American Journal of Roentgenology*, 182(1):201–209, Jan 2004.

[111] T. Pock, R. Beichel, and H. Bischof. A novel robust tube detection filter for 3D centerline extraction. In *Lecture Notes in Computer Science*, volume 3540, pages 481–490, 2005.

[112] A. Pommert, K. H. Höhne, B. Pflesser, E. Richter, M. Riemer, T. Schiemann, R. Schubert, U. Schumacher, and U. Tiede. Creating a high-resolution spatial/symbolic model of the inner organs based on the visible human. *Medical Image Analysis*, 5(3):221–228, 2001.

[113] H. R. Portugaller, H. Schoellnast, K. A. Hausegger, K. Tiesenhausen, W. Amann, and A. Berghold. Multislice spiral CT angiography in peripheral arterial occlusive disease: a valuable tool in detecting significant arterial lumen narrowing? *European Radiology*, 14 (9):1681–1687, Sep 2004.

[114] K. Pöthkow, B. Weber, and H.-C. Hege. Probabilistic marching cubes. *Computer Graphics Forum*, 30(3):931–940, 2011.

[115] B. Preim and D. Bartz. *Visualization in Medicine*. Elsevier, Morgan Kaufmann Publishers, 2007.

[116] B. Preim and S. Oeltze. 3D visualization of vasculature: An overview. In L. Linsen, H. Hagen, and B. Hamann, editors, *Visualization in Medicine and Life Sciences*, Mathematics and Visualization, pages 39–59. Springer Berlin Heidelberg, 2008.

[117] M. Prokop. CT angiography of the abdominal arteries. *Abdominal Imaging*, 23(5):462–468, 1998.

[118] C. Pudney. Distance–ordered homotopic thinning: A skeletonization algorithm for 3D digital images. *Computer Vision and Image Understanding*, 72(3):404–413, 1998.

[119] J. Rada-Vilela. fuzzylite: a fuzzy logic control library in C++, 2013. URL `http://www.fuzzylite.com`.

[120] A. Radloff, M. Luboschik, and H. Schumann. Smart views in smart environments. In *Proceedings of Smart Graphics 2011*, pages 1–12, 2011.

[121] U. Ramer. An iterative procedure for the polygonal approximation of plane curves. *Computer Graphics and Image Processing*, 1(3):244–256, 1972.

[122] P. Rautek, S. Bruckner, and M. E. Gröller. Semantic layers for illustrative volume rendering. *IEEE Transactions on Visualization and Computer Graphics*, 13(6):1336–1343, 2007.

[123] P. Rautek, S. Bruckner, and M. E. Gröller. Interaction-dependent semantics for illustrative volume rendering. *Computer Graphics Forum*, 27(3):847–854, 2008.

[124] E. M. Reingold and J. S. Tilford. Tidier drawings of trees. *IEEE Transactions on Software Engineering*, 7(2):223–228, 1981.

[125] C. Rezk-Salama, M. Keller, and P. Kohlmann. High-level user interfaces for transfer function design with semantics. *IEEE Transactions on Visualization and Computer Graphics*, 12(5):1021–1028, 2006.

[126] F. Ritter, C. Hansen, V. Dicken, O. Konrad, B. Preim, and H.-O. Peitgen. Real-time illustration of vascular structures. *IEEE Transactions on Visualization and Computer Graphics*, 12(5):877–884, 2006.

[127] J. C. Roberts. State of the art: Coordinated & multiple views in exploratory visualization. In *Proceedings of the International Conference on Coordinated & Multiple Views in Exploratory Visualization 2007*, pages 61–71, 2007.

[128] W. C. Röntgen. Über eine neue Art von Strahlen. In *Aus den Sitzungsberichten der Würzburger Physik.-medic. Gesellschaft Würzburg*, volume 137, pages 132–141, 1895.

[129] J. E. Roos, D. Fleischmann, A. Köchl, T. Rakshe, M. Straka, A. Napoli, A. Kanitsar, M. Šrámek, and E. Gröller. Multi-path curved planar reformation (mpCPR) of the peripheral arterial tree in CT angiography (CTA). *Radiology*, 244(1):281–290, 2007.

[130] T. Ropinski and B. Preim. Taxonomy and usage guidelines for glyph-based medical visualization. In *Proceedings of SimVis 2008*, pages 121–138, 2008.

[131] T. Ropinski, I. Viola, M. Biermann, H. Hauser, and K. Hinrichs. Multimodal visualization with interactive closeups. In *Proceedings of the Conference on Theory and Practice of Computer Graphics 2009*, pages 17–24, 2009.

[132] L. Saroul, S. Gerlach, and R. D. Hersch. Exploring curved anatomic structures with surface sections. In *Proceedings of IEEE Visualization 2003*, pages 27–34, 2003.

[133] L. Saroul, O. Figueiredo, and R.-D. Hersch. Distance preserving flattening of surface sections. *IEEE Transactions on Visualization and Computer Graphics*, 12(1):26–35, 2006.

[134] R. Schernthaner, D. Fleischmann, F. Lomoschitz, A. Stadler, J. Lammer, and C. Loewe. Effect of MDCT angiographic findings on the management of intermittent claudication. *American Journal of Roentgenology*, 189(5):1215–1222, 2007.

[135] R. Schernthaner, A. Stadler, F. Lomoschitz, M. Weber, D. Fleischmann, J. Lammer, and C. Loewe. Multidetector CT angiography in the assessment of peripheral arterial occlusive disease: accuracy in detecting the severity, number, and length of stenoses. *European Radiology*, 18(4):665–671, 2008.

[136] R. Schernthaner, D. Fleischmann, A. Stadler, M. Schernthaner, J. Lammer, and C. Loewe. Value of MDCT angiography in developing treatment strategies for critical limb ischemia. *American Journal of Roentgenology*, 192(5):1416–1424, 2009.

[137] T. Schertler, T. Frauenfelder, P. Stolzmann, H. Scheffel, L. Desbiolles, B. Marincek, V. Kaplan, N. Kucher, and H. Alkadhi. Triple rule-out CT in patients with suspicion of acute pulmonary embolism: Findings and accuracy. *Academic Radiology*, 16(6):708–717, Jun 2009.

[138] C. Schumann, S. Oeltze, R. Bade, B. Preim, and H.-O. Peitgen. Model-free surface visualization of vascular trees. In *Proceedings of the Eurographics / IEEE VGTC Symposium on Visualization 2007*, pages 283–290, 2007.

[139] D. Selle, B. Preim, A. Schenk, and H.-O. Peitgen. Analysis of vasculature for liver surgical planning. *IEEE Transactions on Medical Imaging*, 21(11):1344–1357, 2002.

[140] J. A. Sethian. *Level Set Methods and Fast Marching Methods*. Cambridge University Press, 1999. ISBN 0521645573.

[141] J. A. Sethian. Fast marching methods. *SIAM Review*, 41(2):199–235, 1999.

[142] S. Sigg, R. Fuchs, R. Carnecky, and R. Peikert. Intelligent cutaway illustrations. In *Proceedings of IEEE Pacific Visualization Symposium 2012*, pages 185–192, 2012.

[143] Society of Interventional Radiology Standards of Practice Committee. Guidelines for percutaneous transluminal angioplasty. *Journal of Vascular and Interventional Radiology*, 14:209–217, 2003.

[144] M. Steinberger, M. Waldner, M. Streit, A. Lex, and D. Schmalstieg. Context-preserving visual links. *IEEE Transactions on Visualization and Computer Graphics*, 17(12):2249–2258, Dec. 2011.

[145] M. Straka. *Processing and Visualization of Peripheral CT-Angiography Datasets*. PhD thesis, Vienna University of Technology, Austria, 2006.

[146] M. Straka, A. Köchl, M. Cervenansky, M. Šrámek, D. Fleischmann, A. La Cruz, and E. Gröller. The VesselGlyph: Focus & Context Visualization in CT-Angiography. In *Proceedings of IEEE Visualization 2004*, pages 385–392, 2004.

[147] S. Svensson, I. Nystrom, and G. Sanniti di Baja. Curve skeletonization of surface-like objects in 3D images guided by voxel classification. *Pattern Recognition Letters*, 23(12): 1419–1426, October 2002.

[148] T. Taerum, M. Sousa, F. Samavati, S. Chan, and J. Mitchell. Real-time super resolution contextual close-up of clinical volumetric data. In *Proceedings of the Eurographics / IEEE VGTC Symposium on Visualization 2006*, pages 347–354, 2006.

[149] A. Tagliasacchi, H. Zhang, and D. Cohen-Or. Curve skeleton extraction from incomplete point cloud. *ACM Transactions on Graphics*, 28:71:1–71:9, July 2009.

[150] A. Telea and J. J. van Wijk. An augmented fast marching method for computing skeletons and centerlines. In *Proceedings of the Symposium on Data Visualisation 2002*, pages 251–259. Eurographics Association, 2002.

[151] M. Termeer, J. Oliván Bescós, M. Breeuwer, A. Vilanova, F. Gerritsen, and E. Gröller. CoViCAD: Comprehensive visualization of coronary artery disease. *IEEE Transactions on Visualization and Computer Graphics*, 13(6):1632–1639, 2007.

[152] C. Tietjen, B. Meyer, S. Schlechtweg, B. Preim, I. Hertel, and G. Strauß. Enhancing slice-based visualizations of medical volume data. In *Proceedings of the Eurographics / IEEE VGTC Symposium on Visualization 2006*, pages 123–130, 2006.

[153] F.-Y. Tzeng, E. Lum, and K.-L. Ma. An intelligent system approach to higher-dimensional classification of volume data. *IEEE Transactions on Visualization and Computer Graphics*, 11(3):273–284, 2005.

[154] R. Uflacker. *Atlas of Vascular Anatomy: An Angiographic Approach*. Lippincott Williams and Wilkins, 2006. ISBN 078176081X.

[155] H. A. F. G. van Andl, E. H. W. Meijering, A. van der Lugt, H. A. Vrooman, and R. Stokking. Vampire: Improved method for automated center lumen line definition in atherosclerotic carotid arteries in CTA data. In *Proceedings of the Conference on Medical Image Computing and Computer-Assisted Intervention 2004*, pages 525–532, 2004.

[156] F. van Ham and J. van Wijk. Beamtrees: Compact visualization of large hierarchies. *Information Visualization*, 2(1):31–39, 2003.

[157] J. van Wijk and H. van de Wetering. Cushion treemaps: Visualization of hierarchical information. In *Proceedings of IEEE Symposium on Information Visualization 1999*, pages 73–78, 1999.

[158] A. Varchola, A. Vaško, V. Solčány, L. I. Dimitrov, and M. Šrámek. Processing of volumetric data by slice- and process-based streaming. In H. Slay and S. Bangay, editors, *Proceedings of the International Conference on Computer graphics, virtual reality, visualisation and interaction in Africa (Afrigraph) 2007*, pages 101–110. ACM Siggraph, 2007.

[159] I. Viola. *Importance-Driven Expressive Visualization*. PhD thesis, Vienna University of Technology, Austria, 2005.

[160] I. Viola, A. Kanitsar, and M. E. Gröller. Importance-driven feature enhancement in volume visualization. *IEEE Transactions on Visualization and Computer Graphics*, 11(4): 408–418, 2005.

[161] I. Viola, M. Feixas, M. Sbert, and M. E. Gröller. Importance-driven focus of attention. *IEEE Transactions on Visualization and Computer Graphics*, 12(5):933–940, 2006.

[162] L. Wang, Y. Zhao, K. Mueller, and A. Kaufman. The magic volume lens: An interactive focus+context technique for volume rendering. In *Proceedings of IEEE Visualization 2005*, pages 367–374, 2005.

[163] L. Wang, Y. Zhao, K. Mueller, and A. Kaufman. The magic volume lens: An interactive focus+context technique for volume rendering. In *Proceedings of IEEE Visualization 2005*, pages 367–374, 2005.

[164] S. W. Wang and A. E. Kaufman. Volume sculpting. In *Proceedings of the Symposium on Interactive 3D Graphics 1995*, pages 151–156, 1995.

[165] W. Wang, B. Jüttler, D. Zheng, and Y. Liu. Computation of rotation minimizing frames. *ACM Transactions on Graphics*, 27(1):2:1–2:18, 2008.

[166] X. Wang, D. H. Jeong, W. Dou, S.-W. Lee, W. Ribarsky, and R. Chang. Defining and applying knowledge conversion processes to a visual analytics system. *Computers & Graphics*, 33(5):616–623, Oct. 2009.

[167] D. Weiskopf, K. Engel, and T. Ertl. Interactive clipping techniques for texture-based volume visualization and volume shading. *IEEE Transactions on Visualization and Computer Graphics*, 9(3):298–312, 2003.

[168] D. Weiskopf, T. Schafhitzel, and T. Ertl. GPU-based nonlinear ray tracing. *Computer Graphics Forum*, 23(3):625–634, 2004.

[169] A. Wenger, D. F. Keefe, S. Zhang, and D. H. Laidlaw. Interactive volume rendering of thin thread structures within multivalued scientific data sets. *IEEE Transactions on Visualization and Computer Graphics*, 10(6):664–672, November 2004.

[170] D. Williams, S. Grimm, E. Coto, A. Roudsari, and H. Hatzakis. Volumetric curved planar reformation for virtual endoscopy. *IEEE Transactions on Visualization and Computer Graphics*, 14(1):109–119, 2008.

[171] J. K. Willmann, S. Wildermuth, T. Pfammatter, J. E. Roos, B. Seifert, P. R. Hilfiker, B. Marincek, and D. Weishaupt. Aortoiliac and renal arteries: Prospective intraindividual comparison of contrast-enhanced three-dimensional MR angiography and multi–detector row CT angiography. *Radiology*, 226(3):798–811, 2003.

[172] J. Wua, R. Maa, X. Maa, F. Jia, and Q. Hua. Curvature-dependent surface visualization of vascular structures. *Computerized Medical Imaging and Graphics*, 34:651–658, 2010.

[173] L. Zadeh. Fuzzy sets. *Information and Control*, 8(3):338–353, 1965.

[174] L. Zadeh. The concept of a linguistic variable and its application to approximate reasoning. *Information Sciences*, 8(3):199–249, 1975.

[175] L. Zadeh. Fuzzy logic, neural networks, and soft computing. *Communications of the ACM*, 37(3):77–84, 1994.

[176] Q. Zhang, R. Eagleson, and T. Peters. Rapid scalar value classification and volume clipping for interactive 3D medical image visualization. *The Visual Computer*, 27(1):3–19, 2011.

[177] S. Zhao, M. J. McGuffin, and M. H. Chignell. Elastic hierarchies: Combining treemaps and node-link diagrams. In *Proceedings of IEEE Symposium on Information Visualization 2005*, pages 57–64, 2005.

[178] L. Zhu, S. Haker, and A. Tannenbaum. Flattening maps for the visualization of multi-branched vessels. *IEEE Transactions on Medical Imaging*, 24(2):191–198, 02 2005.

Curriculum Vitae

Personal Details

Name	Gabriel Mistelbauer
Date of Birth	February 23rd, 1985
Place of Birth	Vienna, Austria
Citizenship	Austrian
Languages	German, English
Military Service	Fulfilled

Education

Sep. 1991 – Jun. 1995	Elementary School *Galileigasse*, Vienna, Austria
Sep. 1995 – Jun. 2003	High School *Wasagasse*, Vienna, Austria
Oct. 2003 – Jun. 2007	Vienna University of Technology, Austria **Bachelor's studies** (computer science).
Oct. 2007 – Jun. 2010	Vienna University of Technology, Austria **Master's studies** (computer science). Completed with the master's thesis *Automated Processing and Visualization of Vessel Trees* at the Institute of Computer Graphics and Algorithms.
since Oct. 2010	Vienna University of Technology, Austria **Doctoral studies** (computer science). Working on the dissertation *Smart Interactive Vessel Visualization in Radiology* at the Institute of Computer Graphics and Algorithms.

Teaching Related Activities

Oct. 2006 – Jan. 2007 Oct. 2007 – Jan. 2008	Teaching assistant (Tutor) at the Institute of Software Technology and Interactive Systems, Vienna University of Technology, for the lab *Multimedia 1*
Mar. 2007 – Jun. 2007 Mar. 2008 – Jun. 2008 Mar. 2009 – Jun. 2009	Teaching assistant (Tutor) at the Institute of Computer Engineering, Vienna University of Technology, for the lab *Object-Oriented Programming in C++*

Reviewing Activities

Journals	Computers & Graphics, Computerized Medical Imaging and Graphics
Conferences	IEEE Visualization, IEEE Pacific Visualization, Computational Aesthetics, Computer Graphics Theory and Applications, SIGRAD, CLEI

Publications

Gabriel Mistelbauer, Andrej Varchola, Hamed Bouzari, Juraj Starinsky, Arnold Köchl, Rüdiger Schernthaner, Dominik Fleischmann, Meister Eduard Gröller, and Miloš Šrámek. Centerline Reformations of Complex Vascular Structures. In *Proceedings of IEEE Pacific Visualization Symposium 2012*, pages 233–240, 2012

Gabriel Mistelbauer, Hamed Bouzari, Rüdiger Schernthaner, Ivan Baclija, Arnold Köchl, Stefan Bruckner, Miloš Šrámek and Meister Eduard Gröller. Smart Super Views — A Knowledge-Assisted Interface for Medical Visualization. In *Proceedings of IEEE Conference on Visual Analytics Science and Technology*, pages 163–172, 2012

Gabriel Mistelbauer, Anca Morar, Andrej Varchola, Rüdiger Schernthaner, Ivan Baclija, Arnold Köchl, Armin Kanitsar, Stefan Bruckner, and Meister Eduard Gröller. Vessel Visualization using Curvicircular Feature Aggregation. *Computer Graphics Forum*, 32(3):231–240, 2013

Thomas Auzinger*, Gabriel Mistelbauer*, Ivan Baclija, Rüdiger Schernthaner, Arnold Köchl, Michael Wimmer, M. Eduard Gröller, and Stefan Bruckner. Vessel Visualization using Curved Surface Reformation. *IEEE Transactions on Visualization and Computer Graphics*, accepted for publication, 2013, (*contributed equally)